eman ta zabal zazu
Universidad del País Vasco
Euskal Herriko Unibertsitatea

INGENIARITZA MEKANIKOA SAILA
DEPARTAMENTO DE INGENIERÍA MECÁNICA

Ph.D. Thesis

Four-point contact slewing bearings for wind turbines: advances in structural modelling and friction torque calculation

Presented by:

Iker Heras Miguel

Belonging to the:

Mechanical Engineering Department
Faculty of Engineering of Bilbao
University of the Basque Country (UPV/EHU)
Spain

To obtain the degree of:

Doctor of Philosophy in Mechanical Engineering

Thesis Advisors:

Dr. Josu Aguirrebeitia Celaya
Dr. Mikel Abasolo Bilbao

Bilbao, February 2018

A Ricardo Heras

Agradecimientos

Mi principal agradecimiento va dirigido a Josu Aguirrebeitia y Mikel Abasolo, directores de la tesis. Durante estos últimos tres años en los que hemos trabajado juntos, me han hecho sentir como un miembro más del equipo. Gracias por la oportunidad, vuestra disposición y el reconocimiento. Gracias también a todo el grupo de Análisis y Diseño Mecánico (ADM), en particular a Gorka Urkullu, Ibai Coria e Iñigo Martín, compañeros de trabajo y tontería. Quiero extender el agradecimiento a todos los colegas de la sala de doctorandos, doctorandos y no doctorandos, que me han sabido soportar durante tanto tiempo. Como no, agradezco asimismo la diligencia y el buen trato recibido por Mari Jose Maestu, María Fernández y Pilar Furones.

No me puedo olvidar de toda la gente que ha contribuido, con su interés, trabajo e ideas, al desarrollo de esta tesis. Merecen una mención especial Eneko Goikolea, Rocío Olaguibel, Xabier Benito, Mikel Torre y Alex Rementeria. Gracias por vuestra dedicación y aportaciones, que han enriquecido la tarea investigadora que se plasma en esta tesis.

Sin duda, este trabajo no se habría podido realizar sin la colaboración existente entre el grupo de investigación e Iraundi S.A. A ellos debemos agradecer el material y las herramientas cedidas para los diferentes ensayos y mediciones realizadas. Gracias a Albert Fernández por hacernos saber de primera mano las necesidades y retos a los que se enfrentan en la actualidad las empresas fabricantes de rodamientos de vuelco. Y gracias también a Unai Lonbide y Carlos Aristi por su tiempo y ayuda.

Je voudrais remercier en particulier Professeur Daniel Nélias, directeur du LaMCoS (INSA-Lyon), de m'avoir donné l'opportunité d'utiliser le matériel disponible dans les locaux du laboratoire. Merci à lui, Lionel Lafarge et Sylvie Descartes pour leur temps, leur aide et leurs conseils. Merci aussi à Zahia et Théo, qui m'ont aidé à ne pas perdre la raison durant les derniers mois particulièrement durs de la thèse pendant mon séjour à Lyon.

Y reservo mis últimas palabras a la gente más merece mi gratitud. A mis padres, Araceli y Jose Antonio, por su apoyo incondicional, cualquiera que sea la aventura en la que me embarque. A mi abuela Feli, por cuidar siempre de mí. Y en especial y sobre todo a ti, Goiz. Por compartir la carga y por ofrecerme las palabras que necesitaba. Gracias por estar a mi lado.

Iker

Abstract

Slewing bearings are large sized rolling bearings used for orientation purposes. Due to their working conditions, these components are designed to support axial and radial loads and a tilting moment. They are employed in a wide variety of applications like tower cranes, radio telescopes or solar trackers. Furthermore, slewing bearings are used for yaw and pitch rotations in wind turbine generators. Wind Energy has been experiencing a constant growth in importance over recent years, and nowadays is the second largest form of power generation capacity in Europe after Natural Gas. The current tendency in wind turbines is to increase the dimensions in order to obtain the maximum possible energy. This involves more demanding working conditions, and therefore a better understanding of the components is required in order to conceive new reliable and competitive designs. For that reason, the renewable energy industry is demanding a deeper knowledge on slewing bearings.

This Doctoral Thesis is focused on four-point contact slewing bearings. In this context, state of the art models for their mechanical characterization have several limitations. For instance, manufacturing errors have been demonstrated to have a significant effect on the load distribution among the balls, but no analytical approach has been developed yet to consider this fact. Moreover, including ring flexibility always requires computationally expensive Finite Element simulations. As regards friction torque, simple linear formulas are usually employed, while the latest analytical models make assumptions that may have important limitations when calculating friction forces and shear stresses at the contact.

In this Doctoral Thesis, new approaches are proposed to deal with such limitations. Firstly, a novel analytical model is presented to solve the load distribution problem considering manufacturing errors. In this model, ring flexibility can be easily implemented though a simple Finite Element model. A

practical engineering formulation was also reached to account for ring elasticity in the analytical approach for the calculation of the stiffness curves. To study the friction forces while the bearing is rotating, a different analytical model was developed. This model, contrary to state of the art analytical approaches for ball bearings, considers the stick regions in the ball-raceway contact. Several Finite Element models are presented as well, which were used for a first approach or for validation purposes. Additionally, some preliminary tests were performed and compared with analytical simulations.

Apart from developing and validating the mentioned new models, they were employed to perform different calculations, from which several conclusions can be drawn. Both manufacturing errors and ring deformability were demonstrated to have a significant effect on the load distribution and idling friction torque. Therefore, not considering them will lead to inaccurate results. Moreover, ring flexibility was evinced to have a great effect on the global stiffness of the bearing as well. It was also proved that global displacements due to contact deformations and those coming from the flexibility of the rings can be considered separately. In addition, the stick regions were found to have an important effect on the shear stresses of the contact area, but not on the resulting friction torque.

It is worth pointing out that, although the research work developed in this Doctoral Thesis is focused on four-point contact slewing bearings, the proposed approaches and procedures can be adapted or reproduced for other types of slewing bearings, such as eight-point contact bearings or crossed roller bearings. Moreover, further work can be done either to improve the proposed models or to simplify them to obtain more practical engineering approaches.

Resumen

Este resumen sintetiza el contenido de la presente tesis doctoral y su objetivo es el de ofrecer una visión general de la misma para aquellos lectores que no hablen inglés. A lo largo de las siguientes líneas se explican brevemente el objeto de la tesis, los trabajos realizados y las conclusiones derivadas de los mismos. El contenido de este resumen no coincide con el del *Abstract* (resumen en inglés), en el cual se exponen las líneas principales de la tesis de manera más superflua.

Los rodamientos de vuelco (*slewing bearings* en inglés) son elementos de máquina enfocados a aplicaciones de orientación. Estos componentes se emplean en máquinas de muy diferente naturaleza, como grúas, brazos robóticos, centros de mecanizado, tuneladoras, tomógrafos computarizados, radiotelescopios o seguidores solares. Además de en las máquinas mencionadas, los rodamientos de vuelco también cumplen un papel fundamental en los aerogeneradores. En este último caso, se requiere de cuatro rodamientos de este tipo: uno para la orientación de la góndola y tres para permitir el giro de las palas. La función del primero es la de encarar la turbina contra el viento, mientras que los otros tres son responsables del ángulo de paso de las palas, y por lo tanto de la energía a extraer del viento. Así pues, han de soportar cargas importantes y de distinta naturaleza debidas fundamentalmente al peso propio de los componentes, el empuje del viento y las fuerzas centrífugas.

Los rodamientos de vuelco son, por lo tanto, elementos de grandes dimensiones que han de soportar combinaciones de cargas axiales y radiales junto con un importante momento de vuelco. Asimismo, su modo de trabajo implica rotaciones oscilatorias a bajas velocidades en torno a una posición, como contraste al giro continuo y de altas revoluciones común en los rodamientos convencionales. Debido a su naturaleza, son componentes cuya sección transversal tiene dimensiones muy inferiores a las dimensiones

globales. Se trata por ende de un componente de gran esbeltez, donde la flexibilidad de los anillos adquiere una relevancia especial. Otra diferencia respecto a los rodamientos convencionales es que no van montados sobre un eje, sino que se ensamblan a las estructuras adyacentes mediante uniones atornilladas.

Los aerogeneradores constituyen una fuente de energía limpia y renovable que viene experimentando un crecimiento constante durante los últimos años. Su presencia en el mix energético ha adquirido tal relevancia que, de acuerdo con los últimos informes de WindEurope, a finales de 2016 se alcanzó una capacidad total instalada de 153.7GW en Europa. Esto sitúa a la energía eólica como la segunda fuente de electricidad del continente, sólo por detrás del Gas Natural. La relevancia del sector eólico implica una gran demanda de rodamientos de vuelco, que se ve reflejada en la cantidad de multinacionales dedicadas a su manufactura, como la sueca SKF; las alemanas Rothe Erde, Schaefler, e IMO; las americanas Kaydon y Timken; la francesa Rollix; o la japonesa NSK. Este sector también está presente en el País Vasco, donde las empresas Iraundi S.A. y Laulagun Bearings S.L. tienen su sede principal. Dada la competencia en el sector y las condiciones de trabajo cada vez más exigentes a las que se ven sometidos los rodamientos de vuelco, debidas principalmente al aumento de las dimensiones de los aerogeneradores y a su emplazamiento en entornos hostiles, existe una demanda para el mejor conocimiento del comportamiento de estos.

Existen normas enfocadas al diseño de rodamientos que ofrecen métodos y formulaciones simples para garantizar su integridad estructural frente a cargas estáticas y dinámicas. No obstante, estas normas están enfocadas a rodamientos convencionales, y no contemplan las particularidades de los rodamientos de vuelco, cuya geometría y condiciones de trabajo son notablemente diferentes. Para cubrir el hueco de estas normas, la NREL (National Renewable Energy Laboratory) publicó una guía de diseño enfocada a rodamientos de vuelco para aerogeneradores, que es ampliamente reconocida y utilizada por los fabricantes no sólo para aplicaciones eólicas. No obstante, esta guía no contempla aspectos tan relevantes como la flexibilidad de los anillos o la precarga. Asimismo, el par de fricción se plantea como una función lineal de las fuerzas aplicadas, formulación ampliamente utilizada pero que demuestra tener importantes limitaciones.

Debido a la demanda de conocimiento en el área y las limitaciones previamente mencionadas, actualmente existe un gran interés por parte de los

investigadores por avanzar en la capacidad predictiva del comportamiento de estos rodamientos, interés que se ve reflejado en la gran cantidad de publicaciones relacionadas. Estas publicaciones van más allá de la norma o la guía de diseño de la NREL y estudian aspectos como la influencia del templado por inducción en el fallo estático o desarrollan nuevos métodos para el cálculo a fatiga. No obstante, todavía existen importantes lagunas en la caracterización y simulación de los rodamientos de vuelco.

Esta tesis se centra en los rodamientos de vuelco de cuatro puntos de contacto. Estos son rodamientos de bolas que, a diferencia de los rodamientos convencionales, contactan con cada anillo en dos puntos en lugar de en uno sólo. Este tipo de rodamientos es el más comúnmente utilizado por su versatilidad y bajo coste. A pesar de que los desarrollos presentados en este documento están enfocados a este tipo concreto de rodamientos, estos pueden ser adaptados o reproducidos para otros tipos como los de rodillos cruzados o los de dos hileras de bolas (o de 8 puntos de contacto), ampliamente utilizados estos últimos en los aerogeneradores de mayores dimensiones.

En lo referente a los rodamientos de cuatro puntos de contacto, existen trabajos recientes que demuestran la relevancia que los errores de fabricación pueden tener en la distribución de carga. No obstante, dichos trabajos están basados en modelos de Elementos Finitos e introducen variaciones aleatorias en la geometría, de manera que no existe un planteamiento analítico para la simulación de estos errores ni una estimación real de su influencia. En esta tesis se plantea un modelo analítico para tal fin, que requiere como dato la geometría real del rodamiento. Además, se desarrolla un sencillo modelo paramétrico de Elementos Finitos para el cálculo de las matrices de rigidez de los anillos, que pueden ser implementadas de manera directa en el planteamiento analítico. Iraundi S.A. cedió un rodamiento y prestó sus instalaciones para medir las pistas mediante una máquina de medir por coordenadas. Utilizando estos datos, se demuestra que los errores de fabricación existentes en un rodamiento real pueden ser del mismo orden de magnitud que la propia precarga de las bolas, de manera que no considerarlos puede incurrir en resultados poco fiables o imprecisos.

El par de fricción también es un parámetro indispensable, dado que su valor es necesario para el dimensionamiento del sistema de actuación correspondiente. A este respecto, existen formulaciones más precisas que las planteadas por la NREL. No obstante, los modelos más avanzados para

rodamientos de cuatro puntos de contacto consideran que existe deslizamiento puro entre la bola y la pista. En esta tesis, se presentan diferentes modelos de Elementos Finitos para la caracterización del contacto cuando el rodamiento está girando, así como el cálculo del par de fricción. Estos modelos demuestran que, para condiciones de funcionamiento normales, existen importantes regiones en adhesión en la elipse de contacto, lo que conlleva tensiones tangenciales menores que las predichas por los modelos analíticos existentes en dichas regiones, lo cual puede afectar al par de fricción. Dichos modelos son también utilizados junto con el modelo analítico previamente mencionado para realizar una serie de simulaciones de las que se concluye que tanto los errores de fabricación como la flexibilidad de los anillos afectan de manera importante al par en vacío. Adicionalmente, se demuestra que la influencia del número de bolas en el par en vacío es logarítmica.

Con el fin de incluir el efecto de las regiones en adhesión en un planteamiento analítico y poder eludir así las costosas simulaciones de Elementos Finitos, se desarrolla un nuevo modelo. Dicho modelo parte del planteamiento cinemático de los modelos que asumen deslizamiento puro, pero implementa una formulación más compleja para la caracterización del problema tangencial. Tras identificar los factores que influyen en la extensión de la región en adhesión, se realizan simulaciones para diferentes casos bajo cargas típicas de funcionamiento mediante el modelo analítico propuesto, el modelo que asume deslizamiento puro y modelos de Elementos Finitos de diferente precisión. Como resultado, se concluye que el nuevo modelo es capaz de determinar qué zonas de la elipse de contacto están en adhesión, lo que demuestra influir de manera importante en el mapa de tensiones, mientras que el par de fricción a penas se ve afectado. En comparación con el modelo de Elementos Finitos, el planteamiento analítico muestra una serie de ventajas, como el ínfimo coste computacional o la menor dependencia de la discretización. A pesar de la limitada ventaja que aporta el nuevo planteamiento respecto al cálculo del par de fricción, una precisa estimación del campo de tensiones en la huella puede ayudar a desarrollar procedimientos de cálculo enfocados a la fatiga o relacionados con modos de desgaste típicos que actualmente carecen de un método adecuado para su predicción.

Finalmente, se aborda el problema del cálculo de la rigidez del rodamiento. En este caso, las formulaciones analíticas existentes únicamente consideran las deformaciones locales del contacto bola-pista, suponiendo por lo tanto anillos

infinitamente rígidos. Como ya se ha señalado anteriormente, esta hipótesis no es asumible en el caso de los rodamientos de vuelco debido a su esbeltez, que da lugar a grandes deformaciones en los anillos. La implementación de la flexibilidad de estos últimos en los procedimientos existentes conlleva siempre, de un modo u otro, costosas simulaciones de Elementos Finitos. En esta tesis, y por medio también de un preciso modelo de Elementos Finitos, se realizan una serie de simulaciones considerando diferentes valores de las variables principales que definen el rodamiento. Como resultado, se obtiene una formulación ingenieril que permite calcular las curvas de rigidez axial, radial y de frente al momento de vuelco, formulación que permite un cálculo directo y rápido prescindiendo de simulaciones de Elementos Finitos. Se demuestra que esta nueva formulación reproduce de manera adecuada los efectos no sólo de las variables principales, sino también de los parámetros de contacto.

Adicionalmente, se presentan los resultados de unos ensayos preliminares realizados para la medición experimental del par de fricción. De la comparación de los resultados obtenidos con simulaciones realizadas mediante los modelos analíticos planteados en esta tesis, se concluye que existe una buena correlación para cargas altas, pero es necesario medir las pistas de los rodamientos ensayados para obtener conclusiones más sólidas para cargas bajas.

Esta tesis deja la puerta abierta a futuros desarrollos. Así, aprovechándose de los bajos costes computacionales que ofrecen los nuevos modelos analíticos, pueden realizarse numerosas simulaciones que puedan permitir obtener una fórmula sencilla pero más completa y precisa que la planteada por la NREL para el cálculo del par de fricción. Asimismo, se puede ir más allá en el estudio del contacto, analizando las tensiones subsuperficiales existentes mientras el rodamiento gira y evaluar el efecto de la capa templada. Además, el procedimiento desarrollado para el cálculo de la rigidez en rodamientos de cuatro puntos de contacto puede replicarse para otros tipos de rodamiento de vuelco. Igualmente, se pueden realizar simulaciones adicionales mediante Elementos Finitos de uniones reales de pala-buje o torre-góndola para evaluar las ventajas y limitaciones de sustituir los rodamientos de vuelco por matrices de rigidez calculadas mediante la formulación simplificada propuesta. Finalmente, queda realizar más ensayos experimentales con diferentes precargas y grasas para una validación definitiva de los modelos. Del mismo modo, falta por comprobar la relevancia de otros fenómenos como la

viscosidad de la grasa, la interacción entre bolas o entre bolas y espaciadores, o la contribución de los retenes al par de fricción.

Contents

List of Figures

List of Tables

1 Introduction

1.1 Context and motivation

Slewing bearings are large rolling bearings used for orientation purposes. This type of bearing is designed to support large tilting moments and loads in any axial or radial direction. Because of their orientation focused application, they rotate in an oscillatory way and work at slow speeds. Figure 1.1 shows a drawing of a conventional four-point contact slewing bearing and the involved loads in these components.

Slewing bearings are employed in a wide variety of applications. They are used in tower cranes, vertical lathe tables, precision robots, tunnelling machines, TC scanners, radio telescopes, solar trackers, sewage treatment plants and palletizers, among others (Figure 1.2). Besides, these components are employed in yaw and pitch systems in wind turbines. In these machines, four slewing bearings are required: three blade bearings for pitch rotations, and one for the orientation of the nacelle. The latter is used to face the turbine towards the wind, while the other three allow the regulation of the amount of energy to be taken from it. The loads to be supported by the bearings mainly come from the weight of the components, the thrust of the wind and the centrifugal forces. The combination of them results in the bearings being subjected to variable axial and radial forces and a large tilting moment.

According to the latest reports of WindEurope, wind energy is experiencing significant constant growth on the continent. The statistics for 2015 [1] and 2016 [2] show that 12.8GW and 12.5GW of gross additional wind capacity was installed in these years respectively. At the end of 2016, the total installed capacity in Europe was 153.7GW, which means that wind energy now overtakes coal as the second largest form of power generation capacity (see Figure 1.3). This growing rate has led the wind energy industry to demand a deeper knowledge of their machines, where slewing bearings constitute a very important component. As is known, the current tendency in this sector is to

increase the dimensions in order to obtain the maximum possible energy, which increases the involved loads as well. The more demanding work conditions, combined with the need to optimize the machines to make them competitive in the energy market, constitute a demand for a better understanding of the involved components.

The high demand for slewing bearings is also reflected in the number of multinationals that manufacture this product. Among the most well known are the Swedish SKF; the German Rothe Erde, Schaefler, and IMO; the American Kaydon and Timken; the French Rollix; and the Japanese NSK. This sector is also present in the Basque Country, where the slewing bearing manufacturers Iraundi S.A. and Laulagun Bearings S.L. have their headquarters.

Due to the importance of slewing bearings in wind energy generation and the demand for research in the field, the ADM group of the University of the Basque Country started a research line in this topic several years ago. Since the group published its first analytical approach for the static characterization of slewing bearings in 2010 [3], it has made important contributions regarding the mechanical modelling of slewing bearings. The group also has a close relationship with Iraundi S.A., with which it participates in different projects. This relationship means the ADM group is aware of the current interests of the industry. The research work presented in this Doctoral Thesis stems from the latest advances of the ADM group in the field.

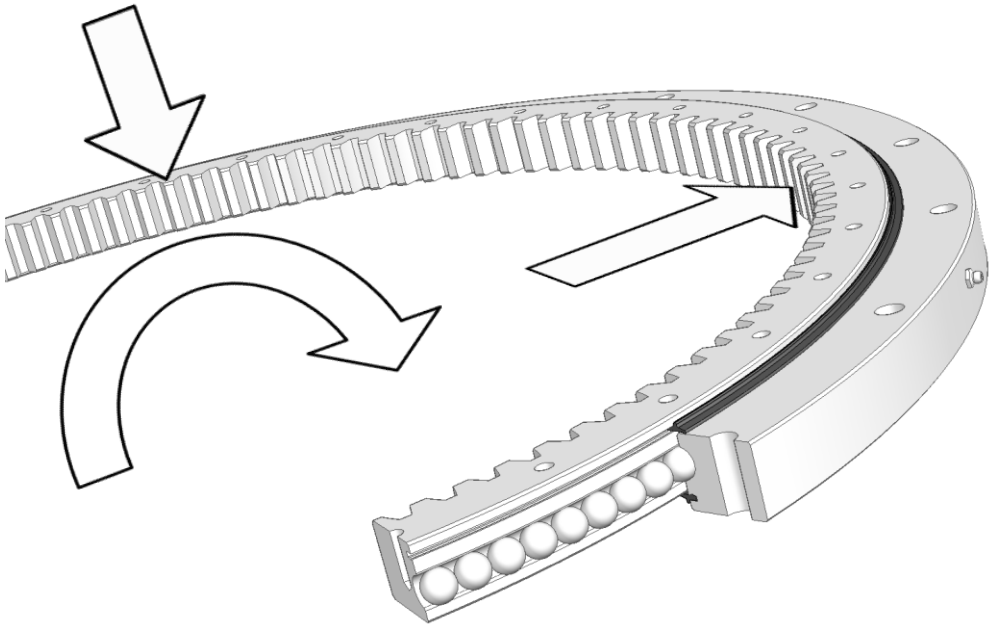

Figure 1.1. Four-point contact slewing bearing and acting loads.

Figure 1.2. Slewing bearing applications.

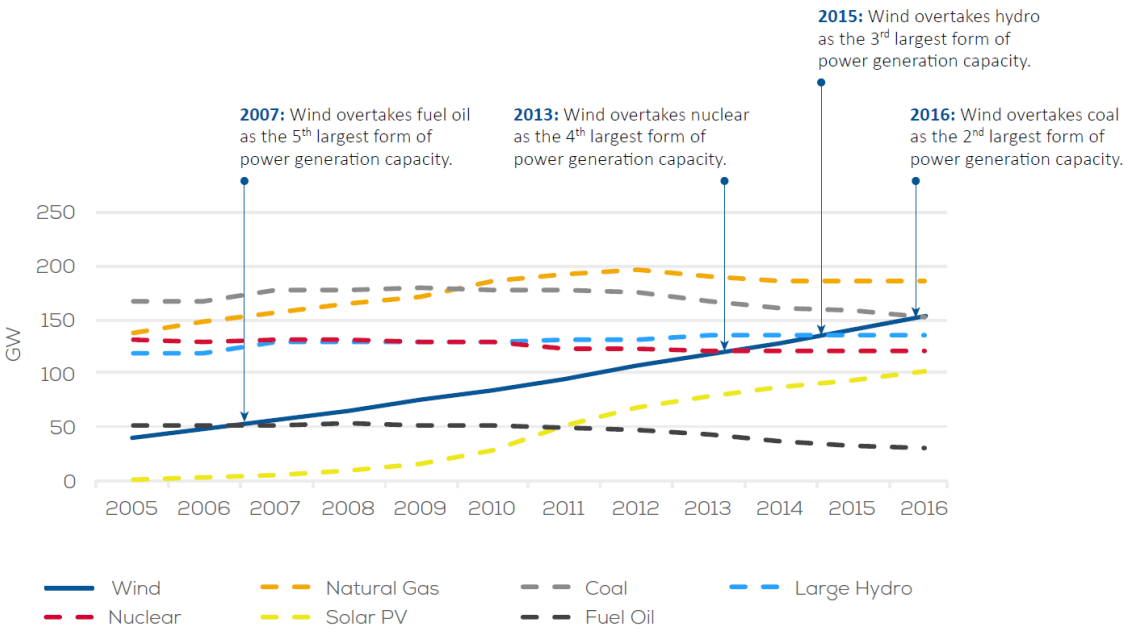

Figure 1.3. Cumulative power capacity in the European Union 2005-2016 [2].

1.2 Slewing bearing description

Before addressing more advanced aspects of the slewing bearings, a general description of these components is made in this section. In the first place, the different parts that most slewing bearings are composed of are going to be detailed (see Figure 1.4 and Figure 1.5):

- Rings: in slewing bearings, the mean diameter (D_{pw}, see Figure 1.5) is much greater than the diameter of the rolling element (D_w). Therefore, the rings are very slender in comparison with typical rolling bearings. This makes the rings more flexible, conditioning the structural behaviour of the bearing. Besides, the raceways are induction hardened (Figure 1.6), obtaining a contact surface with good wear properties. The material typically used for rings is mild carbon steel.
- Rolling elements: they can be balls or rollers. In the case of balls, the contact with the raceway takes place at a point (point contact) at a certain angle (α_0, see Figure 1.5). The relationship between the curvatures of the ball and the raceway (R_C, see Figure 1.5) is known as the osculation ratio ($s = D_w/2R_C < 1$). Conversely, the contact between a roller and the raceway takes place in a line (line contact). In any case, oversized rolling elements are used in most cases, introducing a preload to the bearing. This preload avoids clearances between rolling elements and raceways, eliminating vibrations [4], and thus favouring the life behaviour due to the

more regular working conditions. The preload also favours the accuracy and increases the stiffness of the bearing. As a drawback, it increases the friction at the contact, leading to higher friction torques and wear rates. A material typically used for rolling elements is hardened chrome alloy steel.

- Spacers: in most cases, spacers are used in order to avoid contact between rolling elements, so they fulfil the function the cage has in conventional rolling bearings. Spacers are usually made of a plastic material and therefore minimize the friction between rolling elements. In certain applications, no spacers are used, while in others smaller balls are employed instead (spacer balls).
- Mounting holes: unlike conventional rolling bearings, slewing bearings are not mounted on a shaft. Contrarily, they are linked to the surrounding structures by bolted joints. For this purpose, mounting holes are required in the rings. These holes can be through (outer ring in Figure 1.4) or threaded (inner ring in Figure 1.4).
- Gear: usually, the actuation system is driven by one or a series of electric gear motors. In this case, the driven ring must have a gear in order to make the transmission possible. Depending on the design of the machine, the driven ring can be the inner one or the outer one. Of course, the gear is not mandatory, since it can be manufactured in the adjacent structures, or different actuation systems can be employed.
- Load plug: the assembly in slewing bearings is typically done by introducing the rolling elements through a hole drilled radially in the non-geared ring. Once the assembly is complete, this hole is filled with a plug. This plug is then retained by a pin, which also ensures the correct alignment of the plug. Nonetheless, some bearings do not use a filler hole, so they need one of the rings be split to allow the assembly.
- Grease fitting: a small hole (or holes) is radially drilled in the non-geared ring for lubrication purposes. There are automated lubrication systems, which periodically provide lubricant inside the bearing, compensating possible leakages.
- Seals: seals are required to minimize lubricant leakage and prevent unwanted particles from entering the bearing. Wind turbines, for example, are installed in the most adverse environments, as offshore platforms and deserts. In such extreme environments, the role of the seals is highly relevant.

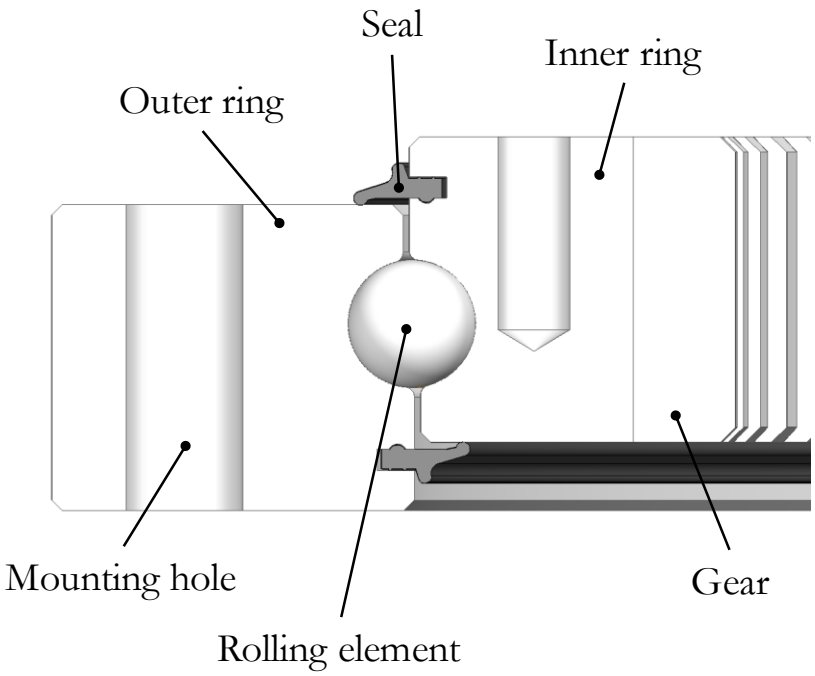

Figure 1.4. Parts of a four-point contact slewing bearing.

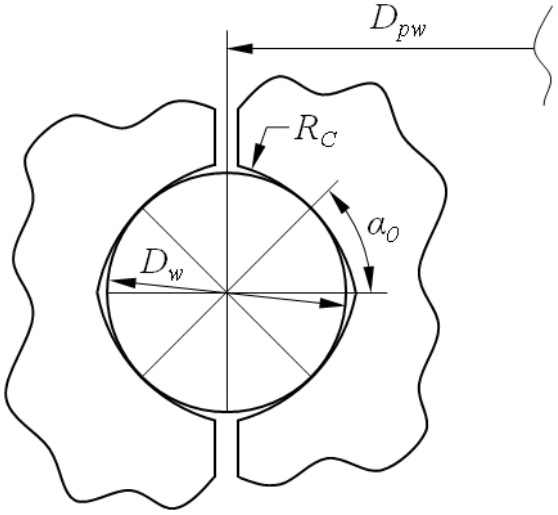

Figure 1.5. Contact parameters in four-point contact bearings.

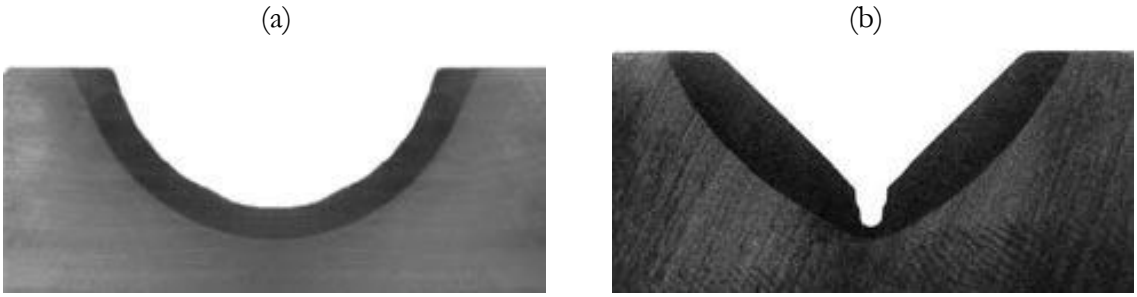

Figure 1.6. Hardened pattern for: (a) ball raceway; (b) roller raceway [5].

Based on the description of the different parts, it seems convenient to classify the slewing bearings according to the employed rolling element. Nevertheless, such a classification falls very short considering the number of existing slewing bearing types. Generally, the most common ones are the following two:

- Four-point contact slewing bearing: they are the most used due to their versatility, low friction torques and low costs in comparison with the other types. Bearings in Figure 1.1, Figure 1.4 and Figure 1.5 are of this type.
- Crossed roller slewing bearings: Figure 1.7a shows the configuration of these type of bearings. They offer a higher stiffness and load capacity, but involve larger friction torques and usually higher manufacturing costs.

Furthermore, there are a number of additional aspects to take into account, like the number of rows. More than one row of rolling elements can be used in order to increase the capacity of the bearing. In the case of rollers, the three-row roller slewing bearing is extensively used in applications where especially high loads are involved, for example. In this configuration (Figure 1.7b), two rows of horizontal rollers withstand axial and tilting loads, and a third row of vertical rollers supports radial loads. In the case of balls, two rows can be used with two contacts on each (Figure 1.8a), while the eight-point contact design (Figure 1.8b) is the most typical option employed for yaw and pitch systems in the latest wind turbines.

When the design specifications are more restrictive regarding the weight of the component and do not demand high stiffness values, the light series (also known as profile bearings) are more suitable (Figure 1.9). There exist several alternative solutions for slewing bearings, like double-row tapered roller bearings, four-row roller bearings or the less conventional combination bearings (Figure 1.10a). Nevertheless, since the objective of the current research work is to study the most conventional four-point contact slewing bearings, it is not pertinent to further extend the description of every slewing bearing type.

However, it is worth mentioning a particular solution for applications where important weight savings are required: the wire bearing. In these bearings, the rolling element runs over steel wires, which are fixed to the rings (Figure 1.10b and Figure 1.10c). This way, rings can be made of lighter materials like aluminium alloys, for example.

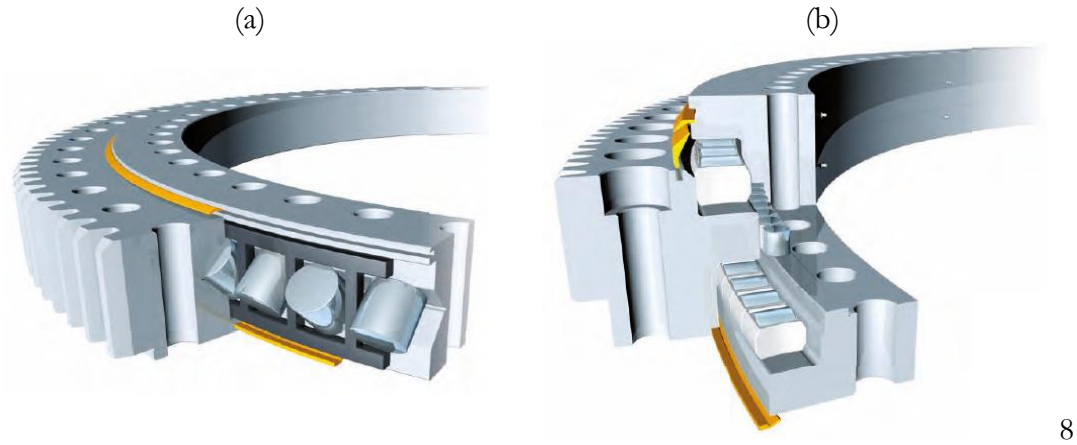

Figure 1.7. Roller slewing bearings: (a) crossed roller; (b) three-row roller [6].

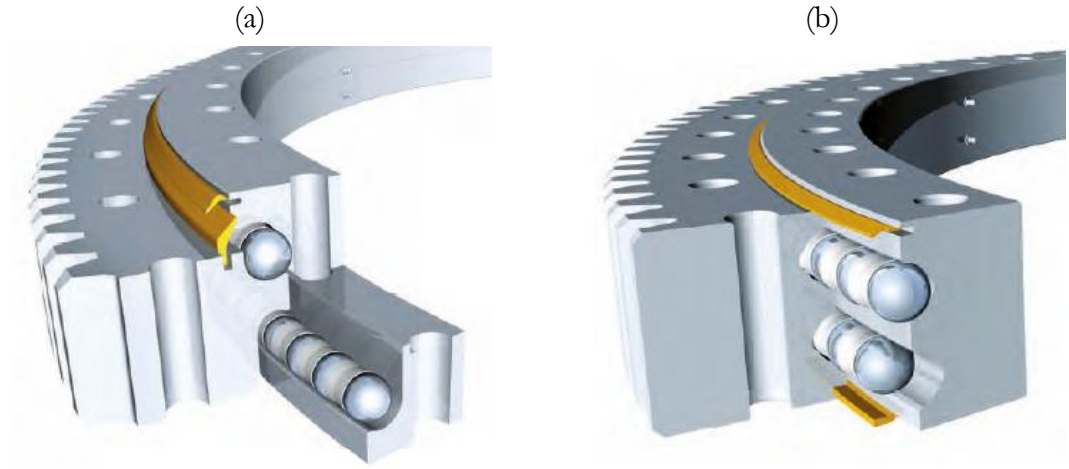

Figure 1.8. Double row ball slewing bearings: (a) 4-point contact; (b) 8-point contact [6].

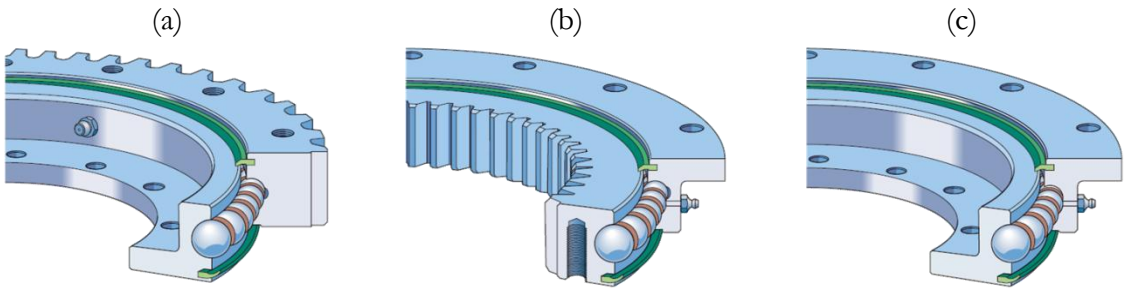

Figure 1.9. Light series four-point contact slewing bearings: (a) with an external gear; (b) with an internal gear; (c) without gear [7].

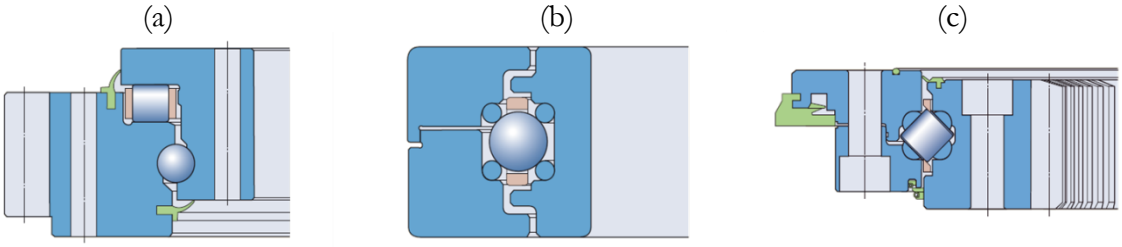

Figure 1.10. Non-conventional slewing bearings: (a) combined roller-ball bearing; (b) four-point wire race bearing; (c) crossed roller wire race bearing [7].

1.3 Slewing bearing selection criteria

When designing or selecting a slewing bearing, different aspects must be taken into consideration. In this section, these aspects and the corresponding criteria are succinctly described. The applicable standards are also presented.

1.3.1 Static capacity

The first dimensioning of the slewing bearing is made according the static loads to be supported by the component. According to the ISO standards for static load ratings in rolling bearings [8,9], *"Experience shows that a total permanent deformation of 0.0001 of the rolling element diameter, at the centre of the most heavily loaded rolling element/raceway contact, can be tolerated in most bearing applications without the subsequent bearing operation being impaired."* Therefore, it will be considered that static failure does not happen as long as this deformation is not reached in any ball for any load condition. The standard also establishes that, according to different tests, this deformation takes place when the maximum contact pressure at the contact is equal to the following values:

- 4600MPa for self-aligning ball bearings
- 4200MPa for all other ball bearings
- 4000MPa for all roller bearings

Consequently, the maximum allowable contact pressure in the case of four-point contact ball bearings in order to avoid static failure will be 4200MPa. Thus, the static load capacity is the applied load that causes this pressure in the most loaded ball. The ISO standard proposes a formulation to calculate the axial static capacity (C_{0a}), and also allows the consideration of radial forces, but does not propose any approach to consider the tilting moment. Moreover, the proposed formulation assumes that the initial contact angle does not change with the applied load and does not take into account the flexibility of the rings or the surrounding structures. In the literature review, different approaches are presented that address these limitations.

The criterion proposed in the ISO standard for the static capacity is thought to avoid indentation in conventional bearings, where the rings are thorough hardened. Nevertheless, this kind of hardening is not possible in slewing bearing rings due to the large dimensions. Therefore, only the raceways are treated by means of induction hardening. This fact leads to another possible static failure: core crushing. The difference in the material properties between

the hardened layer and the softer core underneath favours sub-superficial crack nucleation. This can affect the hardened layer, causing cracks on it. This phenomena was studied by Lai et al. for the ball-raceway contact [10] and Göncz et al. for the case of roller-raceway contact [11]. According to Lai et al., core crushing happens before indentation for thin hardened layers, while the latter is dominant from a certain hardened depth in advance (see Figure 1.11).

Apart from core crushing and indentation, there is a third possible way of static failure in ball bearings. Axial forces and tilting moments increase the contact angle, so the contact area approaches the edge of the raceways. For a large enough contact ellipse and angle, the contact area can reach this edge, causing the truncation of the ellipse. This truncation involves a great increment in the contact pressure (Figure 1.12), leading to unacceptable stresses. Thus, ellipse truncature is a phenomenon to be avoided. To evaluate if truncation happens for certain applied loads, analytical or Finite Element (FE) models like the ones presented in the literature review or the new approach proposed in Chapter 2 can be employed.

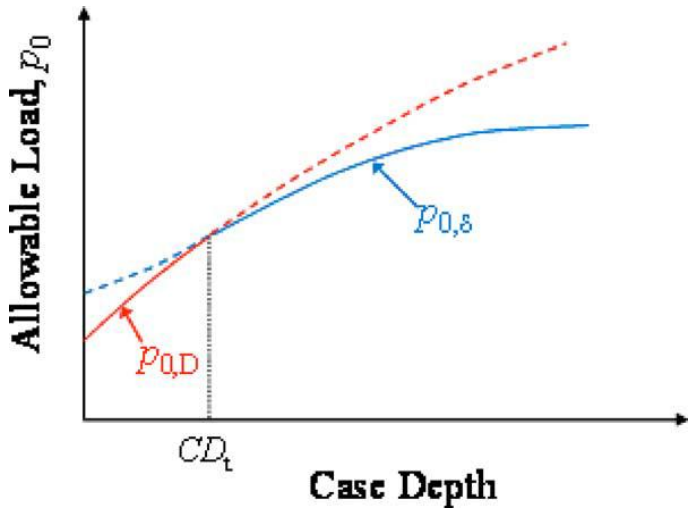

Figure 1.11. Core crushing (red line) and indentation (blue line) criteria for different hardened depths in ball bearings [10].

1.3.2 Stiffness

There is not a general criterion for the selection of the appropriate stiffness of the bearing for a general purpose. This parameter conditions the global deformations of the machine in which the bearing is installed, so high values of the stiffness are typically preferred in order to avoid excessive deformations that can lead to undesired conflicts between different parts. Thus, the stiffness

is subjected to a functional criterion, which will be different depending on the application.

When calculating the stiffness of slewing bearings, considering ring deformations is mandatory in order to obtain reliable results. Thus, not doing so can lead to underestimated deformations, resulting in unsafe designs. Nonetheless, state of the art models involve assuming rigid rings or performing FE calculations. The stiffness of slewing bearings considering ring flexibility can be approached in a simple and direct way by the formulation proposed in Chapter 5, where the ring flexibility is taken into account.

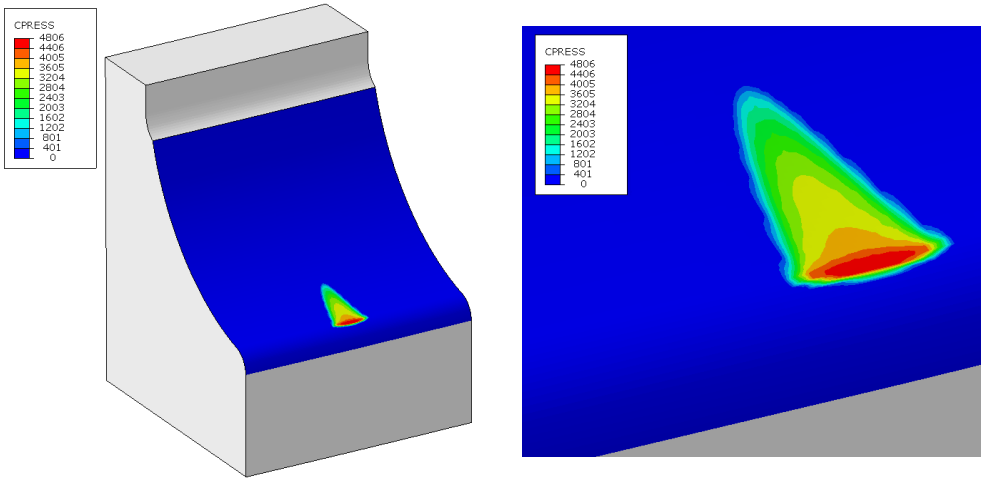

Figure 1.12. Contact pressure in a case with truncated ellipse [12].

1.3.3 Friction torque

The friction torque is the moment required by the bearing to rotate one of the rings with respect to the other. A low friction torque means smaller and cheaper actuation systems. Moreover, it also involves lower loads in the kinematic chain, resulting in more durable systems. Therefore, a low friction torque is typically preferred. However, the preload increases the friction torque, although it involves other positive effects on the structural behaviour of the bearing. Consequently, equilibrium is always sought between the advantages due to the preload and the desired friction torque. Moreover, an accurate estimation of the friction torque is not only valuable when designing the actuation system, but also to allow a better control of the rotation.

To deal with this issue, very simple formulations are usually recommended by manufacturers in their catalogues, which have many limitations. In the literature review, the most relevant research works in this field are presented. Furthermore, in Chapter 3 and Chapter 4, different innovative approaches are

proposed for the friction torque calculation, which deal with the limitations of state of the art models.

1.3.4 Dynamic capacity and fatigue

Of course, the capacity of bearings to withstand variable load conditions and the fatigue life must be studied. For this purpose, the ISO standard proposes a simplified procedure [13–16]. This procedure considers several parameters, such as the static load capacity, the geometry, the lubrication conditions, the surface finish, the variability of the loads and the environmental conditions. As in previous cases, the main limitation of the standard lies in the fact that it is focused on conventional bearings, so it is not directly applicable to slewing bearings. For example, in conventional bearings, hydrodynamic lubrication conditions are always sought to favour the fatigue behaviour, while this regime can rarely be reached in slewing bearings due to the slow speeds. Moreover, slewing bearings still lack a criterion which considers their particular characteristics and working conditions. For this reason, a lot of research is currently being done in this field, as is shown in the next section. Although dynamic and fatigue life calculations are beyond the scope of this Doctoral Thesis, the analytical model presented in Chapter 4 could be of great help to further research on this topic, since it allows an accurate estimation of the stresses at the contact.

1.4 Literature review

When describing the different selection criteria, the applicable ISO standards were mentioned [8,9,13–16]. Nevertheless, there exists more extensive literature of general acceptance for the design of slewing bearings. In this regard, the most recognised and commonly referenced work is by Harris and Kotzalas [17,18], where they deal with aspects not mentioned in the standards. Nevertheless, this work is still focused on conventional bearings, so it lacks specific approaches for the study of slewing bearings. For this reason, the National Renewable Energy Laboratory of the U.S. Department of Energy (NREL) published a guideline for the design of wind turbine yaw and pitch rolling bearings, written by Harris, Rumbarger and Butterfield [19]. Although the work was focused on wind turbines, the guideline is valid and usually employed for the design of slewing bearings that work in similar conditions. This report deals with some of the limitations of

the previously mentioned standards or books for such bearings. However, it still has several limitations. Among others, the most relevant ones are:

- Ring flexibility: ring deformation is not considered in any way. Moreover, this aspect is not even mentioned in the whole document.
- Tilting moment: this load is taken into account in the guideline, which is not in the standards. Nonetheless, it is considered in a simplified way, which has limitations for the static load capacity and friction torque estimation.
- Contact preloads and clearances: the ball preload or the possible contact clearances due to manufacturing errors are not considered. These parameters are common in the design of slewing bearings, and have a significant effect on the operation of the component.

In addition, manufacturers only provide the features and properties of their own products in the catalogues or web pages [5–7,20–26]. Companies do not offer general application methodologies or formulations, and they are very wary of sharing their know-how. The limitations of the standards and the literature of general acceptance and the lack of information about the design procedures of the main manufacturers by the academic environment encourage the researchers to study in this field.

In this section, the most relevant research works regarding slewing bearings are presented, especially on four-point contact slewing bearings. Moreover, the latest advances and trends are also introduced, as well as the limitations of state of the art models for their structural characterization.

1.4.1 Load distribution model

The load distribution problem seeks to find how the applied loads are distributed among the different rolling elements (see Figure 1.13). To do so, it is required to somehow simulate the normal behaviour of the contact between the rolling element and the raceway. The normal problem was first solved by Hertz [17,27,28], who considered the following assumptions:

- The deformations are within the elastic limit and small in comparison with the curvature radii of contacting surfaces.
- The dimensions of the contact area are very small in comparison with the dimensions of contacting bodies or the curvature radii of the surfaces.
- Contacting surfaces are non-conformal and smooth (with no roughness).

- There is no friction, so only normal forces are present in the contact.

The ball-raceway contact in slewing bearings contravenes some of the mentioned assumptions. This contact is not conformal in the circumferential direction, but can be pretty conformal in the radial plane (Figure 1.5). Therefore, the contact area is small in the circumferential direction, but it can be the order of the curvature radii in the other. Moreover, friction exists in the contact. Nevertheless, it was demonstrated by Pandiyarajan through FE calculations that the Hertz theory offers good results for large ball bearings [29]. Therefore, this formulation is commonly used to solve the normal problem in slewing bearings. Moreover, it is the basis of the load distribution analytical models presented in the following paragraph. Besides, Houpert proposed an engineering approach to the Hertz formulation [30], avoiding the elliptical integrals required by it. Later, Houpert also proposed a similar approach for non-hertzian contacts [31], although this formulation is not applied to slewing bearings.

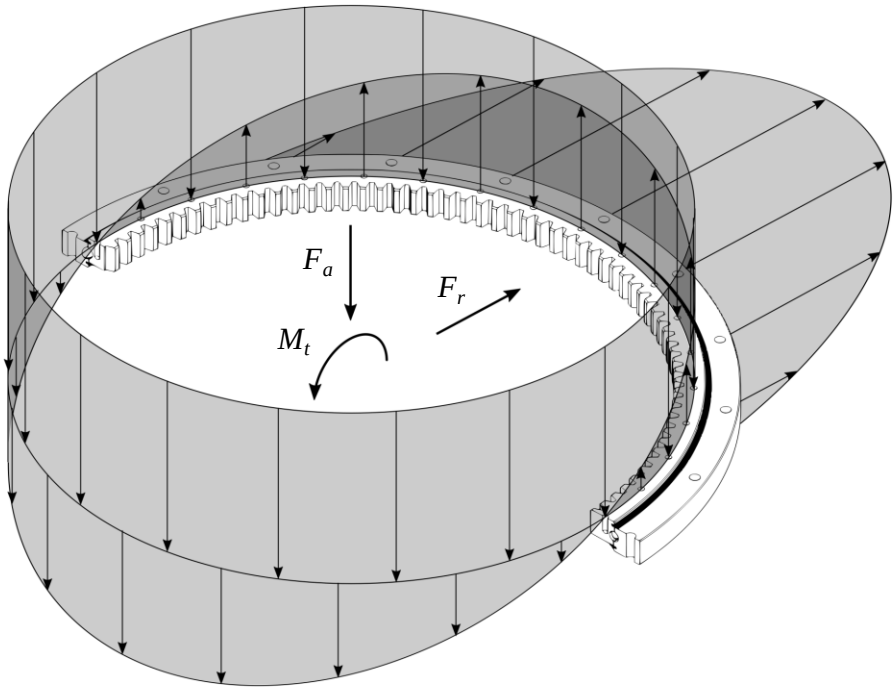

Figure 1.13. Simplified approach for the load distribution in a slewing bearing.

The first steps regarding the load distribution problem in conventional ball bearings were given by Stribeck [32–34]. Later, Sjoväll proposed a method to calculate the load among the balls when the bearing is subjected to a combination of axial and radial loads [35]. Then, Rumbarger presented an

approach considering the case of an axial load combined with a tilting moment [36]. Finally, Jones proposed a model to consider any load combination [37]. This model consists of a highly non-linear equation system, which requires numerical methods to find a solution. Zupan and Prebil applied the formulation proposed by Jones to four-point contact slewing bearings and studied the effect of some geometrical parameters and the stiffness of the bearing and surrounding structures in the static load capacity [38]. To consider ring deformations, an FE model was used to calculate equivalent stiffness values in axial and radial directions, which were implemented in the analytical model. Later, the approach of Jones was adapted by Amasorrain et al. for four-point contact bearings [39]. Then, a procedure was proposed by Olave et al. to implement ring deformations [40] in the model of Amasorrain et al.. Up to this point, mentioned models do not consider any initial preload or possible clearances. In the same line but with a different focus, Aguirrebeitia et al. proposed a procedure for calculating the load combinations that result in static failure in four-point contact slewing bearings [3]. A similar approach was done for crossed roller bearings [41] and three-row roller bearings [42]. Later, the model for four-point contact slewing bearings was improved to consider the variation of the ball-raceway contact [43] and ball preload [44]. All these models are based on the geometrical interference in the contact (see Figure 1.14, where δ_n is the ball-raceway interference).

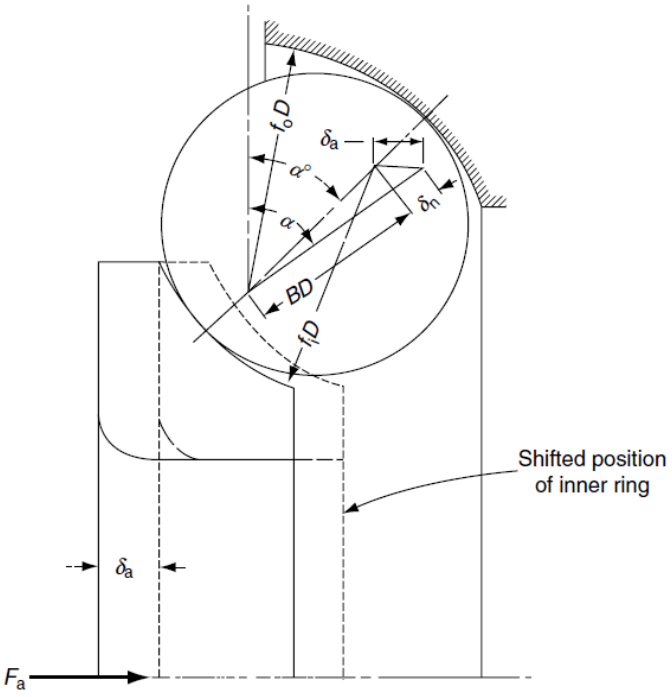

Figure 1.14. Angular-contact ball bearing under thrust load [17].

Finally, recent studies carried out by Starvin and Manisekar [45] and Aithal et al. [46] demonstrated via FE calculations that manufacturing errors can significantly affect the load distribution in large diameter angular contact ball bearings. Nonetheless, an analytical approach to consider manufacturing errors does not exist as yet.

1.4.2 Friction torque calculation

The most extended and simple way for the estimation of the friction torque is the formula proposed by the NREL [19]. This formula assumes that each applied load has a linear effect on the friction torque. Additionally, it includes a term to consider the friction torque after the bearing assembly and with no applied loads. This formulation is the one proposed by manufacturers in their catalogues and can be expressed as follows:

$$M_f = \mu \frac{D_{pw}}{2}\left(A \cdot \frac{M_t}{D_{pw}} + B \cdot F_a + C \cdot F_r\right) + M_{f0} \tag{1.1}$$

Where M_t is the tilting moment, F_a is the axial load, F_r is the radial load, μ is a generic friction coefficient and M_{f0} is the idling friction torque. Typical values of the coefficients A, B and C are 4.4, 1 and 3.8 respectively according to manufacturers [6,21,23], although the NREL proposes a value of 2.2 for C [19]. Despite this formulation being extended and commonly used, it does not consider many aspects, like ball preload or contact angle variation. Moreover, the contact area is a nonlinear function of the applied loads, and this will affect the friction torque. In the case of four-point contact bearings, this approximation will have more limitations. In this type of bearing and depending on applied loads, each ball can have only two contact points, or it can roll with respect to two points and slide with respect to the other two, or spinning can occur at the four points. This would imply having three different values of μ and would require knowing which one should be used under certain applied loads. Therefore, a more advanced model is required in order to obtain more accurate results.

In this way, Todd and Johnson proposed an approach for angular contact ball bearings, which takes into account contact nonlinearities and angle variations [47]. In his approach, Todd considered three components, which are calculated separately: the spin, the microslip due to the rolling and the hysteresis. Other interesting research works focused on two-point contact angular bearings, where the different components of the friction torque are

also calculated separately, were done by Houpert and Leenders [48] and Houpert [49,50]. In these works, simple and powerful formulas are proposed for the friction torque calculation. More recent publications based in Houpert's formulation offer new models, such as the works of Olaru [51] and Bălan [52,53].

Furthermore, Jones proposed a different approach for the study of the friction in angular contact ball bearings [54]. In this approach, bearing kinematics are formulated and solved by imposing the equilibrium of the forces and moments acting on the ball. To do so, the relative velocities and the frictional behaviour in the contact areas are studied. For the contact simulation, it is assumed that full sliding occurs, so the friction forces are directly computed by multiplying normal forces by the friction coefficient. This approach was later adapted by Hamrock for three-point contact bearings [55] and by Leblanc and Nélias for four-point contact bearings [56,57]. Later, several methods were proposed by Lacroix et al. to account for the flexibility of the rings [58]. All these works included inertial effects. Nevertheless, in slewing bearings for orientation purposes, the operational velocities are usually low and thus inertial effects are negligible. Consequently, the load distribution problem and the kinematics can be decoupled and therefore solved separately, which simplifies the solution of the equation system. This was done by Joshi et al., who particularized the problem for slow speed applications and formulated the friction torque calculation [59].

As in Jones' work, state of the art models for four-point contact bearings assume full sliding at the contact. However, in slewing bearings for wind turbines, there are only two points in contact in regular working conditions because of the large tilting moments, so balls roll in the same way as in a typical angular contact bearing, and consequently stick regions will exist in the contact area according to the Heathcote slip [60]. Due to the low velocities, the area of the stick regions can be significant in the contact ellipse, contravening the assumption of full sliding. Thus, it is expected that the described models may have certain limitations for the friction analysis in wind turbine slewing bearings.

1.4.3 Rolling contact

The rolling contact between two elastic bodies is a phenomenon that has been studied for a long time. The basis for the study of the friction forces at contacts was established by the Amontons-Coulomb laws of friction. Carter

[61] and Fromm [62] independently demonstrated that Amontons-Coulomb equations are not applicable when rolling exists. Most contact models for the study of the shear stresses in the rolling contact are based on the Hertz theory. When a contact can be solved by applying the Hertz theory, it is called a hertzian contact. Among the most relevant publications regarding hertzian contacts, there are the works from Carter [61], Johnson [63], Vermeulen and Johnson [64] and Kalker. The last developed the linear theory for the study of rolling contacts in full adhesion [65]. Kalker used this approach to develop the simplified theory [66], which was later computationally implemented through the FASTSIM algorithm [67]. For the non-hertzian contacts, Kalker developed the exact theory, which was implemented through the CONTACT algorithm [68]. The FASTSIM algorithm has been widely used for the study of the wheel-rail contact, and it is still a useful tool for dynamic simulations due to its low computational cost. On the other hand, the CONTACT algorithm is more rigorous and offers better results for non-hertzian contacts. In return, the CONTACT algorithm is around 1000 times slower than the FASTSIM [69]. Nevertheless, neither one nor the other has ever been used for the analysis of the contact in bearings. Allegedly, such formulations would provide more accurate and reliable results for the friction torque than the state of the art models for four-point contact slewing bearings, where full sliding is assumed. However, this remains to be demonstrated.

Although Kalker's theories are widely accepted and used, they continue publishing relevant works in the field. For example, Al-Bender and De Moerlooze [70] developed a new theory to study the transient behaviour of rolling contacts. More recently, Blanco-Lorenzo et al. studied the influence of the conformity on the wheel-rail contact using the exact theory of Kalker and FE calculations [71].

1.4.4 Stiffness

As stated in the previous section, stiffness is a functional criterion for the selection of the appropriate slewing bearings for a particular application. However, unlike with the static capacity or the friction torque, no procedure or methodology can be found in the standards or in the NREL guideline [19]. In addition, manufacturers commonly provide stiffness curves, but they do not explain the calculation procedure. The lack of a standardized methodology to obtain stiffness curves means it is unfeasible to make direct comparisons between data provided by different manufacturers.

Several works studied the matter of the stiffness for two-point angular contact bearings. Houpert [72], Lim and Singh [73], Hernot et al. [74], Liew and Lim [75] and Noel [76] for example dealt with this issue, but always assuming rigid rings, thus considering only ball-raceway contact deformations. Guo and Parker [77] considered ring deformations through the FE analysis and proposed a numerical method to compute the stiffness matrix of any rolling element bearing.

Some approaches were developed by Jones and Harris [78], Harris and Broschard [79] and Mignot et al. [80] regarding planetary gear-transmission bearings. In these approaches the stiffness of the structures is considered. Nevertheless, this type of bearing allows such approaches to be developed because they are always subjected to the same boundary conditions and load type. Contrarily, the conditions change from one application to another in slewing bearings. An analytical approach does not seem therefore so straightforward in this case.

To obtain stiffness curves in four-point contact slewing bearings, the models for the load distribution calculation described in 1.4.1 can be used, like the analytical model in [39] for rigid rings, or the semi-analytical methodology in [40] to consider global deformations. For instance, Aguirrebeitia et al. studied the effect of the preload on the stiffness of four-point contact slewing bearings using their analytical model [44]. Nevertheless, these models require numerical methods to find a solution and are hard to implement. Moreover, they need FE calculations to consider ring flexibility. A simple engineering formulation for the calculation of the stiffness of four-point slewing bearings considering ring deformations is still to be developed.

1.4.5 Finite Element models

The Finite Element modelling of slewing bearings entails several difficulties. One of the main problems is the large amount of Degrees of Freedom (DoF) required by the model, which involves high computational costs. The large amount of required elements is due to two reasons: the slenderness of the rings and the need of refinement in the ball-raceway contact. Another main problem resides in the high nonlinearity of the simulation. There exist two sources of nonlinearities: frictional contacts and large displacements. Frictional contacts are required between balls and raceways and between rings and adjacent structures to simulate the sliding or opening of the bolted joint. Large displacements are to be considered in order to correctly reproduce the

variation of the contact angle. The most challenging aspect to reach the convergence of such simulations resides in the ball-raceway contacts because they take place in a small area and it changes during the simulation. This is the reason for the mesh refinement in this contact region.

There exist simulation techniques based on substituting rolling elements by mechanisms composed of rigid elements and traction only springs. The responsibility for simulating the elastic behaviour of the ball-raceway contact and the angle variation corresponds to these mechanisms. Smolnicki and Rusiński proposed such a mechanism in the first place [81,82]. Soon after, Daidié et al. developed and validated a similar method [83] (Figure 1.15a). Although the traction only spring mechanism is still nonlinear, it avoids the convergence problems due to rigid body motions in balls caused by the loss of contact. Moreover, such techniques avoid simulating solid balls and do not require a mesh refinement in the raceways, resulting in an important decrease of the total DoF of the model. These techniques are commonly used for the FE modelling of slewing bearings. For instance, Aguirrebeitia et al. used Daidié's approach to validate their analytical model [84] (Figure 1.15b), and also proposed a method to consider ball preload by changing the length of the nonlinear spring [44]. These mechanisms were also used for two-row ball slewing bearings by Śpiewak [85] (Figure 1.15c).

To tackle the issue of the flexibility of the rings, FE simulations are usually employed, although there also exist other approaches like the one proposed by Yao et al. [86]. As mentioned before, Zupan and Prebil [38] or Guo and Parker [77] used a FE model to calculate the stiffness values. On the other hand, Olave et al. employed FE model reduction techniques to calculate a more comprehensive stiffness matrix of the rings and the surrounding structures [40]. Model reduction techniques were also demonstrated as a cost effective tool that significantly reduces the computational cost with a negligible accuracy loss to solve the load distribution problem of a particular wind turbine generator by Plaza et al. [87].

As stated before, manufacturing errors were proved to significantly affect the load distribution in large diameter slewing bearings by Starvin and Manisekar [45] and Aithal et al. [46]. To do so, they propose approaches based on different FE modelling techniques. Finally, the growing relevance of wire race bearings is evinced by the recent work of Gunia and Smolnicki, where they offer a first approach to this type of bearings through FE calculations [88].

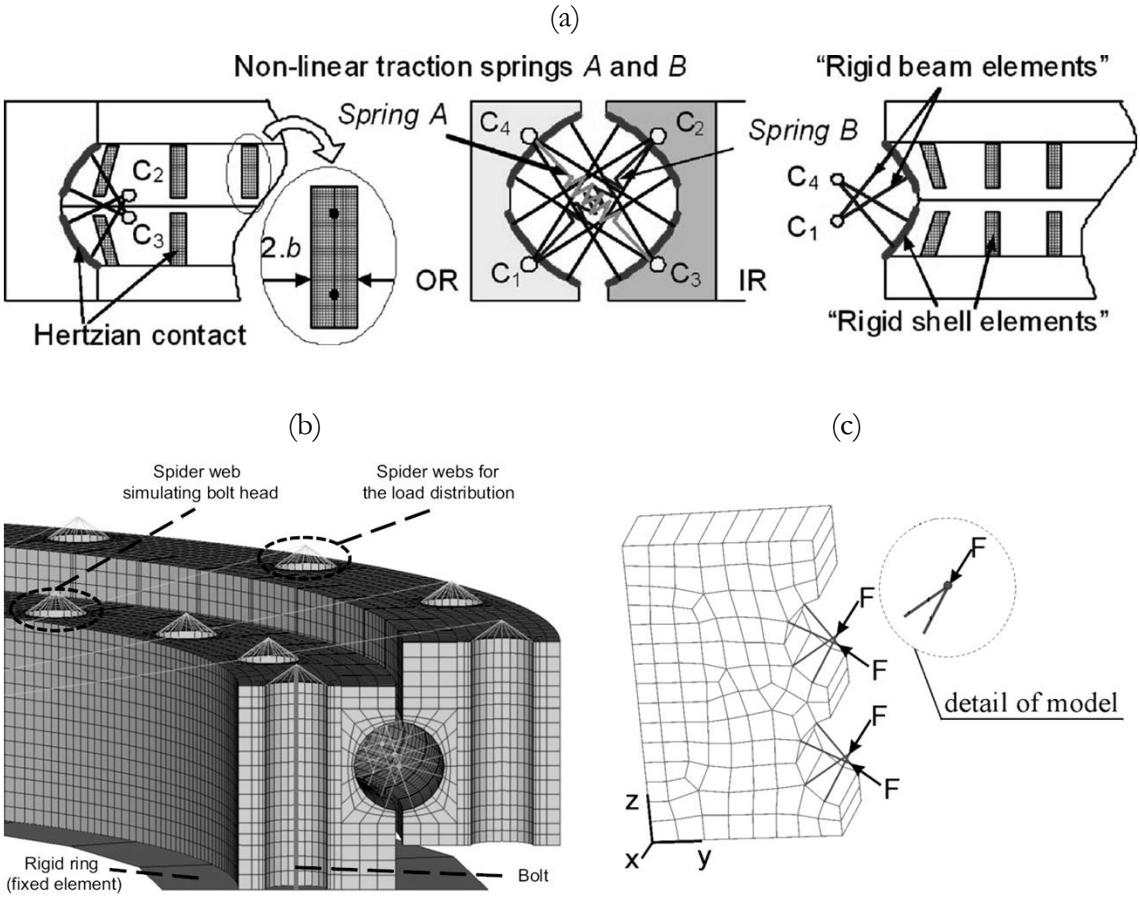

Figure 1.15. Daidie's mechanism: (a) graphical representation [83]; (b) application in one row ball bearing [84]; (c) application in two row ball bearing [85].

Despite the large amount of publications regarding FE modelling to compute the load distribution, study the normal contact problem or for the stiffness calculation, an FE model has not been developed for the friction torque calculation or the study of the tangential contact problem yet.

1.4.6 Fatigue calculation

The NREL [19] proposed a procedure for the fatigue life calculation for yaw and pitch wind turbine bearings. Nevertheless, the limitations of this guideline listed in the beginning of the literature review encourage researches to conceive novel and more accurate methodologies for the case of slewing bearings. In this sense, new calculation procedures involving analytical and FE calculations where proposed by Sawicki et al. for four-point contact slewing bearings [89] and Potočnik et al. for double row eight-point contact bearings [90]. The latter takes into account possible geometrical irregularities caused by manufacturing errors or the deformation of the rings. To consider the induction hardened layer in the raceways, Göncz and Glodež presented an FE

based method for the assessment of the rolling contact fatigue life for roller bearings [91]. For the case of ball-raceway contact, Londhe et al. [92] studied the subsurface stress variation due to the raceway induction hardening and discussed its implications on bearing fatigue life. Nevertheless, an approach for the contact stress calculation when the bearing is rotating remains to be developed.

Further, Žvokelj et al. proposed a method for predictive damage detection and diagnosis in slewing bearings [93]. From a more generalist point of view, Portugal et al. recently developed a fatigue model for multiaxial random loading cases [94]. This new approach was aimed at machine components which lack a specific procedure for fatigue life calculations due to their particular working conditions, like slewing bearings. Finally, Schwack et al. compared fatigue life results obtained by four different approaches applied to a blade bearing under individual pitch control [95].

However, from the literature review it is concluded that there is not a generally accepted procedure for the fatigue life calculation of slewing bearings yet. Moreover, phenomena like false brinelling or fretting corrosion require further research in order to obtain a reliable prediction of fatigue life in such components.

1.4.7 Experimental testing

There are plenty of research works involving experimental tests with conventional bearings. Previously mentioned manuscripts like the ones by Todd and Johnson [47] and Houpert [50] offer experimental results of the friction torque for angular contact ball bearings. For the case of four-point contact bearings, Joshi et al. [59] performed tests for two different preloads and two grease types under axial load and contrasted measured results with those from their analytical approach. More recently, Stammler et al. compared the results of torque from experimental measurements with those obtained using different calculation models [96]. In this case, a four-point contact pitch bearing was tested under an applied tilting moment in the blade bearing test stand from the Fraunhofer Institute for Wind Energy and Energy System Technology (IWES). This rig (Figure 1.16) was designed for the entire hub-bearing-blade group testing of turbines up to 3MW.

Figure 1.16. Pitch bearing test rig at Fraunhofer IWES [96].

1.5 Objectives

Considering the limitations of state of the art simulation methods and techniques for the structural characterization of four-point contact slewing bearings, the following objectives were defined for the research work presented in this Doctoral Thesis:

- Load distribution analytical modelling:
  - Develop a methodology to consider the manufacturing errors.
  - Implement the deformability of the rings in the new methodology.
- Friction torque and tangential contact problem modelling:
  - Develop an analytical model for the calculation of the friction torque and the analysis of the ball-raceway contact, considering the stick regions.
  - Study the effect of manufacturing errors and ring stiffness in the idling friction torque.
- Stiffness calculation formulation:
  - Reach an engineering formulation for the calculation of the stiffness, considering ring flexibility.

- Finite Element modelling:
  - Develop a robust multiparametric FE model to simulate the rotation of the bearing and obtain reliable results of the torque, the kinematics and the contact results, especially the shear stress.
  - Obtain a robust multiparametric FE model for the calculation of the stiffness matrices for its implementation in the load distribution model.
  - Advance in the entire bearing modelling, obtaining a multiparametric robust FE model which includes the balls as solid elements.
- Experimental validation:
  - Validate the analytical models through experimental testing.

Except for the experimental validation, all the objectives were satisfactorily fulfilled. Regarding this last goal, some preliminary tests were performed, but a more intensive experimental campaign will be necessary in order to proceed to a proper empirical validation of the analytical models.

1.6 General overview of the proposed methodology

In this Doctoral Thesis, different novel approaches are developed and evaluated in order to meet all the objectives. This section provides a general overview of the research work to be presented in the following chapters. Given that the Doctoral Thesis covers different problems, each of which is studied by means of different approaches, it is important to give a first general view. The reader may feel it convenient to come back to this point during the reading of the document as a reminder of which problem is being addressed in each chapter.

In Chapter 2, a new analytical model is presented for the calculation of the load distribution among the balls. Contrary to state of the art analytical approaches, this model envisages the possibility of considering manufacturing errors. To account for these errors, the model requires experimental measurements of the raceways. Additionally, it also allows a direct way for the implementation of the stiffness matrices of the rings. As explained in the chapter, these matrices can be easily calculated by an ad hoc developed parametric FE model.

The basis of the different approaches presented in Chapter 3 and Chapter 4 for the friction torque calculation and the ball-raceway contact analysis resides in the fact that the normal contact problem and the tangential contact problem can be decoupled and solved independently. This assumption is

adequate for slewing bearings mainly due to the slow rotation speeds involved in orientation applications. Therefore, a novel FE model is presented in Chapter 3, which offers detailed results of the contact while the bearing is rotating. The input of this model is the solution of the load distribution problem. By using the analytical model of Chapter 2 and the FE model of Chapter 3, different possibilities are explored and compared in order to find an accurate and cost effective way for solving the problem. Moreover, the effect of manufacturing errors, ring stiffness and ball number in the friction torque is studied in this chapter.

In Chapter 4, an analytical alternative is presented to solve the friction problem. The objective of this analytical approach is to substitute the FE model in the calculation procedure. This new model offers a more robust calculation option with a much lower computational cost. The proposed approach stems from the formulation for the kinematics done by Leblanc and Nélias, but does not assume full sliding at the contact. Conversely, Kalker's formulations are implemented in order to consider the stick regions of the contact area. At the end of the chapter, different cases for regular working conditions are studied by means of the new model, the model of Leblanc and Nélias and the FE model. The results are compared and the capabilities and limitations of each approach are discussed.

In Figure 1.17 the different models used in Chapter 2 to Chapter 4 are schematically represented. This figure shows a global view of the proposed procedure for the friction torque calculation and the study of the ball-raceway contact. BIME and FRANC are the names of the new proposed analytical models to solve load distribution and friction problems, respectively. This schema may be of a great help while reading Chapter 3, where several calculation alternatives are explored.

Chapter 5 deals with the calculation of the global stiffness of the bearing. Although this issue is related with the load distribution problem, it is focused from a different point of view. A parametric FE model is developed to calculate the stiffness curves of the bearing, and then a number of calculations are performed, varying the main parameters of the problem. The results are approximated by means of simple functions, finally leading to a practical engineering formulation. The resulting approach is then demonstrated to satisfactorily reproduce the influence of the main geometric variables and contact parameters in the stiffness curves.

In Chapter 6 some preliminary tests for the friction torque experimental measurement are presented. The objective of the tests is to assess the capabilities and limitations of developed analytical models. The experimental measurements of this chapter are a first step of a more extensive test campaign to be carried out in future works. Nevertheless, some interesting conclusions are drawn.

Finally, in Chapter 7 the main conclusions that arise from the current work are presented and the future work to be done in the same line is suggested.

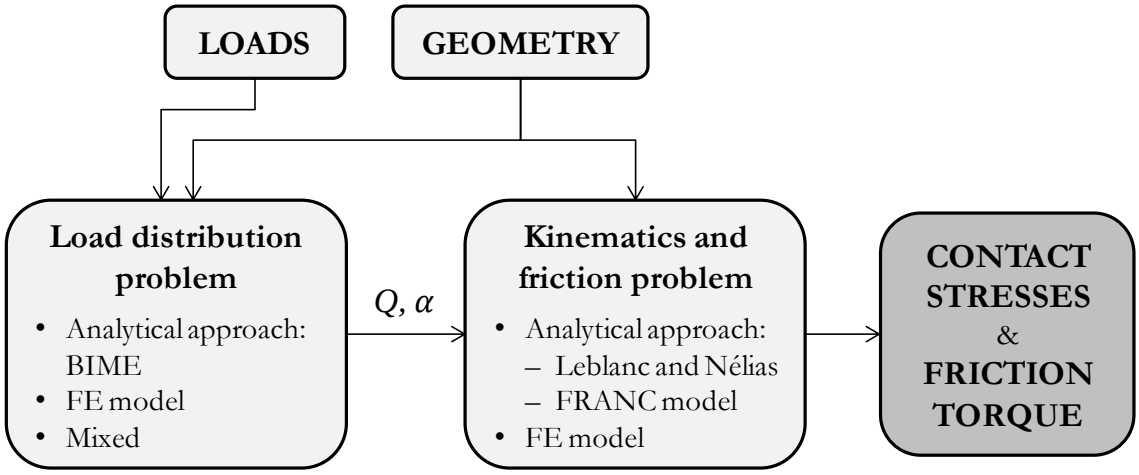

Figure 1.17. Schematic representation of the procedure for the friction torque calculation and contact analysis.

2 Load distribution model

2.1 Introduction

In this chapter, a novel analytical model for the determination of the load distribution among the balls is presented. The novelty of the model resides in its capability to consider the effect of manufacturing errors. Manufacturing errors can significantly affect the load distribution in large diameter slewing bearings, as demonstrated by Starvin and Manisekar [45] and Aithal et al. [46] through FE calculations. Nevertheless, none of the analytical models mentioned in Chapter 1 [38,39,43,44,84] considered this issue.

The errors to be considered are those due to the manufacturing process of the raceways, but not the balls. Of course, there also exist errors when balls are manufactured, but they can be measured very accurately later and classified according to their real dimension. Therefore, the uncertainty of the calculations comes only from the raceways.

Manufacturing errors do not only affect the load distribution but also the friction torque, specially the idling friction torque. The idling friction torque is the moment required to rotate the bearing under no external loads. It is easily measurable and commonly used by bearing manufacturers as a straightforward way to adjust the preload level required for a particular application. Along with the starting and the running torque under external loads, the idling torque is usually demanded by the customers, and thus it is a very relevant parameter. With the model presented in this chapter, it will be possible to accurately calculate the required ball diameter to achieve the desired preload level. Moreover, the results from the load distribution after the assembly of the bearing, and before applying any external load, can be calculated through the proposed model. The resulting contact loads and angles can be later introduced in any of the models presented in the next chapter for the idling friction torque calculation.

In a first approach, the model is developed to calculate the ball-raceway interferences after the assembly and considering rigid rings. Later, the flexibility of the rings is implemented by means of stiffness matrices. The Guyan reduction method is applied to condense the stiffness matrix of a full FE model of the rings to certain points [97]. This procedure is similar to the one proposed by Olave et al. [40], but the selection of the condensation points and their corresponding degrees of freedom differs, which shows some advantages as is later explained. Finally, the model is extended to consider external loads.

To sum up, the proposed model calculates ball-raceway interferences and contact forces and angles of every ball of the bearing after the assembly or under certain external loads, considering manufacturing errors and ring stiffness. Thus, it can be used to calculate the stiffness curve of a bearing and its static capacity, or to obtain the input data required by a model for the friction torque calculation. For future reference, the new model is called BIME due to its capability to consider manufacturing errors (Bearing Interferences due to Manufacturing Errors).

The BIME model was applied to a particular bearing (see Figure 2.1) in order to evaluate the effect of manufacturing errors and ring stiffness on the load distribution, and later also on the friction torque (Chapter 3). The bearing was provided by Iraundi S.A., and its nominal dimensions are reported in Table 2.1.

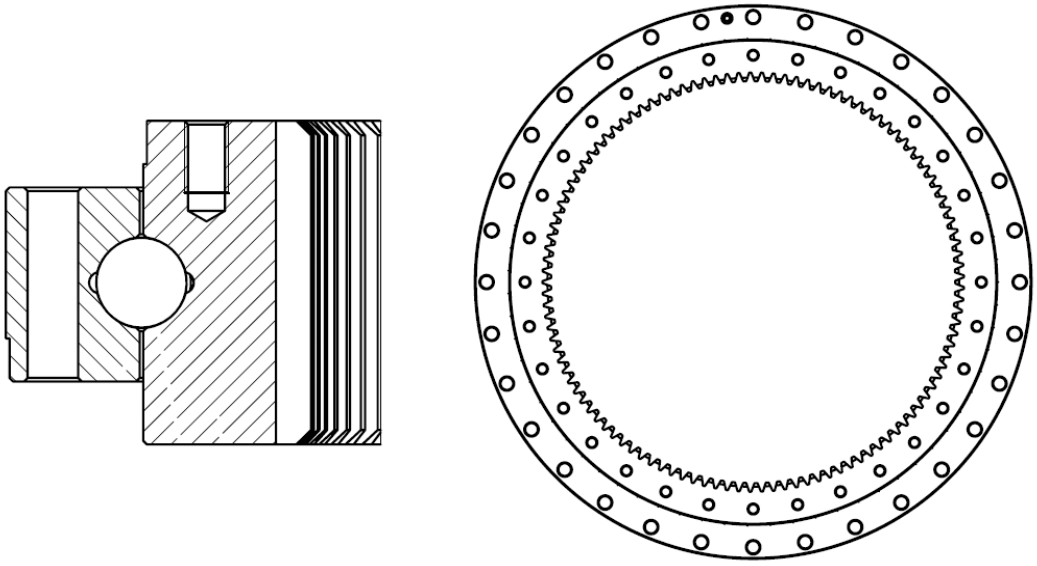

Figure 2.1. Measured bearing for initial results, courtesy of Iraundi S.A..

2.2 Calculation of the interferences due to manufacturing errors. The BIME model

In this section, the procedure for the determination of the interferences between balls and the raceways due to manufacturing errors is described. This procedure involves the need to accurately measure the raceways in a first step in order to know their real shape. Then, the BIME model is presented and applied to estimate the interferences.

2.2.1 Measurement of the raceway

A coordinate-measuring machine (CMM) is required for the measurement of the raceways due to the geometry and the required accuracy. Iraundi S.A. offered its measuring machine for this purpose (DEA Global Silver 12.15.10, see Figure 2.2), available in their facilities at Bergara, Spain.

Bearing mean diameter (D_{pw})	Ball diameter (D_w)	Raceway radius (R_C)	Initial contact angle (α_0)
541.00 mm	25.00 mm	13.25 mm	45°

Table 2.1. Nominal dimensions of the measured bearing.

Figure 2.2. Coordinate-measuring machine and measured rings.

To determine the real shape of a raceway, a minimum set of three points is required per each circumferential position under study. This way, the circumference that defines the centre and the radius of the raceway can be calculated. For a double arched ring, at least 6 points are needed per each circumferential position (see Figure 2.3b). To obtain the general shape of a ring, these measurements must be taken in several circumferential positions. These measurements were taken for 32 positions and with the minimum points required, but for a higher accuracy and to consider hypothetical shape irregularities of each arc, more points are required. Nevertheless, the goal of these first measurements is to obtain the magnitude order of the phenomena and justify the relevance of manufacturing errors.

Since the measurements are taken for each ring separately, the relative position between them once the bearing is assembled, i.e. when the balls are inserted, is unknown. The BIME model described in the next section aims to determine this position, from which the ball-raceway interferences will be calculated.

As shown in Figure 2.3c, special attention must be taken when measuring surfaces that are neither flat nor normal to the approach direction of the sensor probe. For the particular case which this work concerns, the CMM was programmed to report point R, as shown in Figure 2c. From the reported coordinates, it is straightforward to place the location of the centre of the probe (point O), from which the coordinates of each raceway centre can be obtained, as well as its radius.

In order to check for repeatability, the measurements were taken twice for each ring. It was also checked that the different measurements from the same raceway were coherent between them.

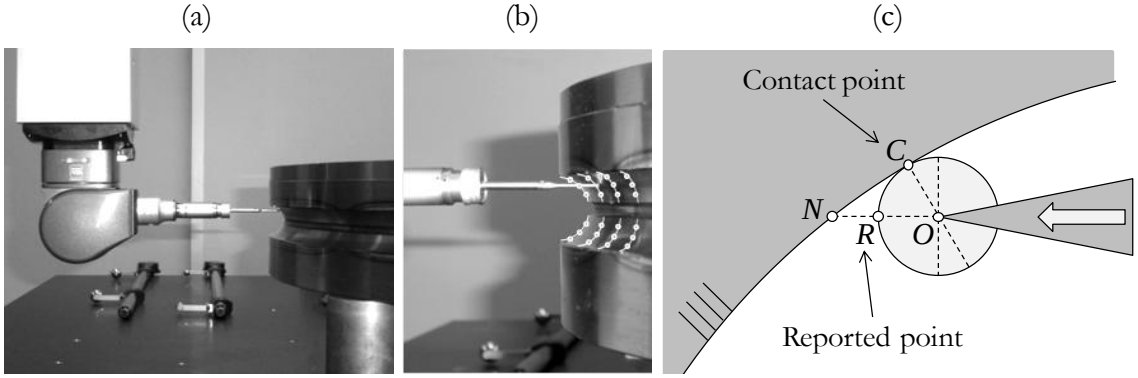

Figure 2.3. Experimental measurements: (a) coordinate-measuring machine; (b) measured points (c); graphical representation of the probe in contact with the raceway meter.

2.2.2 Analytical approach for the calculation of the interferences: the BIME model

The next step in calculating the ball-raceway interferences is to assess the relative position between the inner and the outer ring once the balls are inserted and equilibrium is reached. In this regard, the final spatial configuration will be that with the minimum associated elastic deformation potential energy. Therefore, the key of the proposed method lies in the formulation and the minimization of the energy of the system.

For this purpose, the ball-raceway contact model developed and validated by Daidié et al. [83] is used. Taking advantage of this technique, the centres of the raceways from the different rings are linked to each other by traction-only springs that simulate the stiffness of the contacts, as shown in Figure 2.4. Moreover, the centres from the same ring are rigidly connected, assuming rigid rings. This way, each pair of springs represents the four contacts of each ball of the bearing, so the elastic contact problem is simplified by means of the deformable mechanism represented in the figure.

For the formulation of the potential energy, the outer ring is fixed, while the position of the inner ring will be a function of the relative displacements and rotations between both rings. Hence, points O^1 and O^4 of the mechanism are fixed, while the coordinates of points O^2 and O^3 are a function of the parameters X_D, Y_D, Z_D, α and β, represented in Figure 2.5, which define the position of the inner ring with respect to the outer.

As a first step, the coordinates of the centres of the raceways, obtained from the experimental measurements, are changed from the Cartesian coordinate system (x, z) to a cylindrical system (R, φ, z). Following the nomenclature in Figure 2.5:

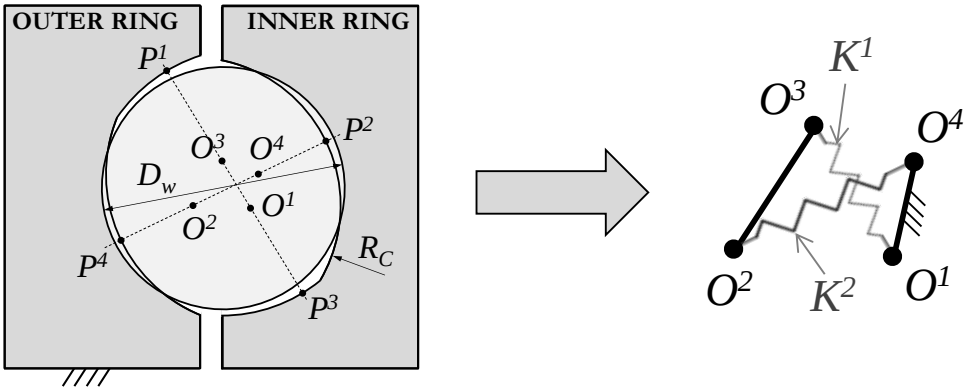

Figure 2.4. Graphical representation of the mechanism of the analytical model.

$$R^i_{Oini} = \sqrt{\left(x^i_{Oini}\right)^2 + \left(y^i_{Oini}\right)^2}$$
$$\varphi^i_{Oini} = atan\left(\frac{y^i_{Oini}}{x^i_{Oini}}\right) \qquad \text{where } i \in [1,4] \tag{2.1}$$

The outer ring is fixed and thus the position of points O^1 and O^4 remain constant. Conversely, the final coordinates of points O^2 and O^3 will be given by the following expressions in Cartesian coordinates:

$$\begin{aligned} x^i_O &= x^i_{Oini}cos\beta + z^i_{Oini}sin\beta + X_D \\ y^i_O &= y^i_{Oini}cos\alpha - z^i_{Oini}sin\alpha + Y_D \\ z^i_O &= z^i_{Oini}cos\alpha cos\beta - x^i_{Oini}sin\beta + y^i_{Oini}sin\alpha + Z_D \end{aligned} \qquad \text{where } i \in [2,3] \tag{2.2}$$

These expressions are changed into cylindrical coordinates:

$$\begin{aligned} R^i_O = R^i_{Oini}&\left(cos\alpha sin^2\varphi^i_O + cos\beta cos^2\varphi^i_O\right) \\ &+ \left(X_D + z^i_{Oini}sin\beta\right)cos\varphi^i_O \\ &+ \left(Y_D - z^i_{Oini}sin\alpha\right)sin\varphi^i_O \\ z^i_O = z^i_{Oini}&cos\alpha cos\beta \\ &+ R^i_{Oini}\left(sin\alpha sin\varphi^i_O - sin\beta cos\varphi^i_O\right) \\ &+ Z_D \end{aligned} \qquad \text{where } i \in [2,3] \tag{2.3}$$

Note that all the displacements occur in the radial plane, so the angular coordinate (φ) will remain constant:

$$\varphi^i_O = \varphi^i_{Oini} \quad \text{where } i \in [1,4] \tag{2.4}$$

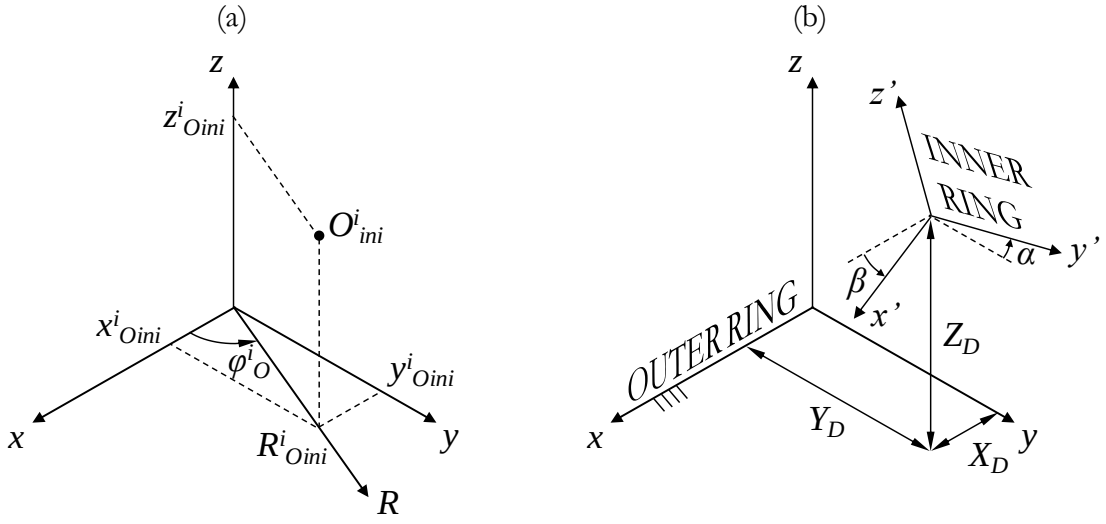

Figure 2.5. Coordinate systems: (a) cartesian and cylindrical coordinates; (b) parameters for the relative position definition of the inner ring.

Since manufacturing errors are being considered, the natural lengths of the springs can be different from each other. For a given circumferential position, and according to the numbering used in Figure 2.4, the natural length of spring i is given by:

$$l_N^i = R_C^i + R_C^{i+2} - D_w = R_C^i + R_C^{i+2} - (D_w^{nom} + \delta_P) \quad \text{where } i \in [1,2] \tag{2.5}$$

Where D_w is the diameter of the ball, equal to the nominal diameter D_w^{nom} plus the preload δ_P, and R_C^i the radius of the raceway. On the other hand, the real length (l) will be a function of the position of the inner ring:

$$l^i = \sqrt{\left(R_0^i - R_0^{i+2}\right)^2 + \left(z_0^i - z_0^{i+2}\right)^2} \quad \text{where } i \in [1,2] \tag{2.6}$$

Having both natural and real lengths, the summation of the interferences corresponding to each contact pair linked by each spring will be calculated according to the following expression:

$$\delta_{Tot}^i = \delta^i + \delta^{i+2} = l^i - l_N^i \quad \text{where } i \in [1,2] \tag{2.7}$$

In the ball-raceway hertzian-type contact, the relationship between the ball normal load (Q) and its deformation (δ) is formulated as follows [17]:

$$Q = K\delta^{3/2} \tag{2.8}$$

This formula is valid for elastic deformations with no truncation of the contact ellipse. The exact solution of the formula above requires the use of elliptic integrals [17], but Houpert offers functional approximations for different ranges of the osculation ratio (s) [30], which are a good approach for engineering applications. For osculation ratios in the range of $0.89 < s < 0.99$:

$$\delta = 1.8586\,(1-s)^{0.2414}\left(\frac{1-\nu^2}{E}\right)^{2/3}\left(\frac{2}{D_w}\right)^{1/3} Q^{2/3} \tag{2.9}$$

Where E and ν are the Young's modulus and Poisson's ratio, assuming the same material in both ball and raceway. Particularizing for the case of steel and assuming typical values of $E = 2 \cdot 10^5 MPa$ and $\nu = 0.3$, the next expression is obtained:

$$\delta = 5.046 \cdot 10^{-4}(1-s)^{0.2414}\frac{Q^{2/3}}{D_w^{1/3}} \tag{2.10}$$

By reordering the terms according to (2.8), the value of the coefficient K can be formulated:

$$K^i = \begin{cases} \dfrac{88220\, D_w^{1/2}}{(1-s^i)^{0.3621}} & \text{if} \quad \delta^i > 0 \\ 0 & \text{if} \quad \delta^i \leq 0 \end{cases} \qquad \text{where } i \in [1,4] \tag{2.11}$$

Where $s^i = D_w/\left(2R_C^i\right)$ is the osculation ratio of the contact i. It is important to point out that, as the springs are traction-only, they do not offer any resistance for the $\delta^i < 0$ case, which represents a gap between the contacting bodies. From (2.7) and (2.8), the total stiffness of the spring i that links the raceway centres i and $(i+2)$ is obtained:

$$\frac{1}{\left(K_{Tot}^i\right)^{2/3}} = \frac{1}{\left(K^i\right)^{2/3}} + \frac{1}{\left(K^{i+2}\right)^{2/3}} \quad \text{where } i \in [1,2] \tag{2.12}$$

Finally, the expression for the potential energy can be obtained by integrating (2.8). For the entire system formed by B balls, the total potential energy will be given by:

$$U = \frac{2}{5}\sum_{b=1}^{B}\left[K_{Tot}^{1b}(\delta_{Tot}^{1b})^{5/2} + K_{Tot}^{2b}(\delta_{Tot}^{2b})^{5/2}\right] \tag{2.13}$$

Inasmuch as the interferences depend on the five parameters that define the final position of the inner ring, so will the potential energy. The proposed formulation was implemented in Matlab® and the minimization of the potential energy was performed by means of a gradient based algorithm. No convergence problems were found because the potential energy function is continuous and derivable with no local minima; when the function is null (no interferences case), it is not derivable, but that point would directly be the solution. From the minimization, the relative position of one ring with respect to the other is obtained, and therefore the interferences distribution and final contact angles. From the interferences distribution and through equations (2.8) and (2.11), contact forces can be also obtained.

2.2.3 Results for a particular bearing

For the particular case studied in this chapter (see Table 2.1), the calculated interferences are shown in Figure 2.6. For the calculations, 32 balls were considered, namely the number of measured circumferential positions. As rigid rings are being considered, the final relative position of the rings will not be affected by the number of balls, so neither will be the interferences distribution calculated with the analytical model. In the plots, the interferences for the nominal ball and for preloads of 10μm and 20μm are shown. For the nominal ball, maximum interferences of 10μm and minimum of -4μm (which represents a gap) are observed, with an average around 5μm. Since no deformations of the rings are allowed, a certain increment in the ball diameter supposes an equal increment in the interferences, as is shown for preloads of 10μm (average interference of 15μm) and 20μm (average interference of 25μm). Additionally, calculations for different relative circumferential positions were made (rotating one ring with respect to the other), achieving similar results.

From these plots, a significant conclusion arises. The interferences due to manufacturing errors are demonstrated to be of the order of the preloads, so they are as relevant to the calculations as the preloads themselves.

2.3 Interference calculation with deformable rings

The flexibility of the rings has a large influence in the load distribution of slewing bearings, as demonstrated both by Aguirrebeitia et al. [43,44,84] and Olave et al. [40]. For this reason, it must be somehow considered in order to achieve accurate results. In this section, the FE model used for the calculation of the stiffness matrices of the rings is described, and then the formulation for their implementation in the BIME model is presented. Finally, the effect the ring flexibility has on the interferences is studied for the case of the measured bearing.

2.3.1 Finite Element models for ring stiffness matrix calculation

For the calculation of the stiffness matrices of the rings, the FE static condensation method is used. This technique was firstly developed by Guyan for static analysis [97], and it allows the condensation of the stiffness matrix of a component to selected Degrees of Freedom (DoF). Of course, the selected DoF are those subjected to boundary conditions or those where loads are

applied, thus avoiding unloaded DoF. The resulting condensed matrix can be then used to perform faster simulations. When a component (or a set of components) is condensed by means of this technique, it is usually called a superelement in its reduced form. The nodes that contain the selected DoF are called master nodes.

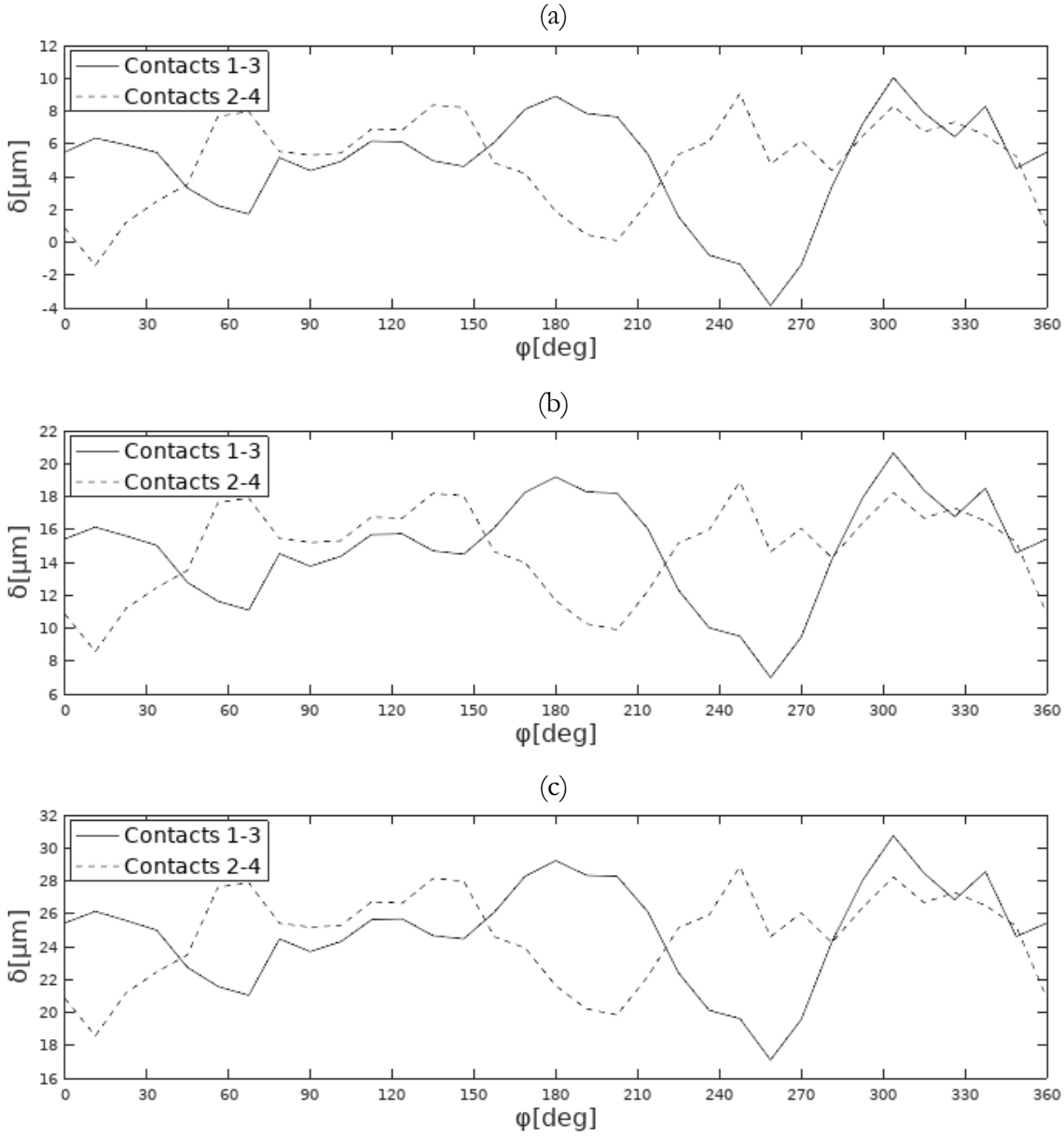

Figure 2.6. Interferences in the measured bearing with different ball preloads: (a) nominal ball; (b) +10μm; (c) +20μm.

In order to obtain the stiffness matrix of any ring, a fully parametric FE model was built in ANSYS®. Although the model is framed in the Workbench environment, the calculation of the superelements requires APDL commands because condensation methods have not been implemented in this interface yet. Nevertheless, Workbench allows the introduction of APDL scripts. The

geometry is entirely modelled in Design Modeller (the geometry module of the Workbench environment) and assumes no gear or holes, since they have little effect on the ring stiffness. As can be seen in Figure 2.7, the geometry is divided into different bodies to improve the meshing process. Then, the model is imported into the mechanical module and a highly regular mesh formed entirely by second order hexahedrons (SOLID186 in ANSYS®) is built. The mesh size is also parameterized as a function of ball diameter (see Figure 2.8).

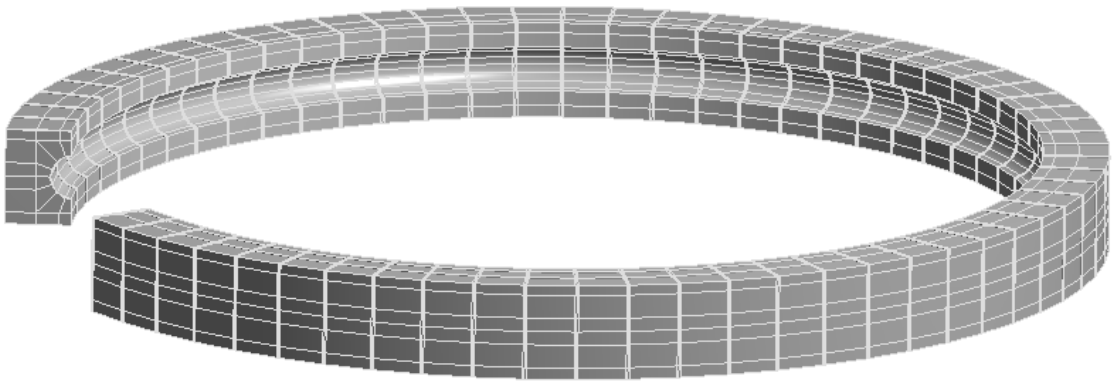

Figure 2.7. Geometry of the outer ring for the FE model.

The key of the condensation procedure lies in the selection of the master nodes and their DoF. In this regard, Olave et al. [40] selected the ball-raceway contact points as master nodes. The main drawback of this procedure is that a fixed contact point is assumed, as happens with Smolnicki's mechanism [81], so the contact angle variation is not appropriately simulated. On the other hand, Plaza et al. [87] used Daidié's mechanism [83], which is more suitable to catch the effect of the contact angle change. Daidié links, via rigid beams, the centre of each raceway to a rigid shell with the dimensions of the contact ellipse, simplified to a curved rectangle, as shown in Figure 2.8. Plaza reduced the stiffness of the rings to the nodes of these shells, so the mechanism can be later attached to the superelement. In this procedure, a different approach is proposed. Instead of selecting the nodes from the contact surface, raceway centres are directly chosen as the master nodes (see Figure 2.8). The rigid shells and beams of Daidié's mechanism are added to the rings through a parameterized APDL script before the model reduction, and they are taken as part of the ring itself when calculating the superelement. Moreover, since balls do not transmit circumferential forces to the raceways in static load conditions, only axial and radial DoF are considered. This way, a more compact stiffness matrix is obtained in comparison with those proposed by Olave or Plaza, with the same capabilities of Daidié's mechanism.

Furthermore, and as later explained, the proposed model solves the mechanism misalignment when radial loads are applied because the circumferential DoF is not considered. Note that selected master nodes are points O^1, O^2, O^3 and O^4 from figure Figure 2.4, so the obtained stiffness matrices could be implemented in a direct way in the BIME model.

FE analysis involving superelements usually requires the next three steps:

- Generation pass: the superelement is created.
- Use pass: the superelement is introduced in the FE model substituting the original component and the analysis is performed.
- Expansion pass: the results are expanded to the entire component from the results at the master nodes.

In our case, only the generation pass is carried out in ANSYS®, since the use pass is derived to Matlab®, where the BIME is programmed. To export the condensed stiffness matrices, they are written in a text file, which can be later read in Matlab®. No expansion pass is required since only the forces at master nodes are wanted to be known, that is, contact forces.

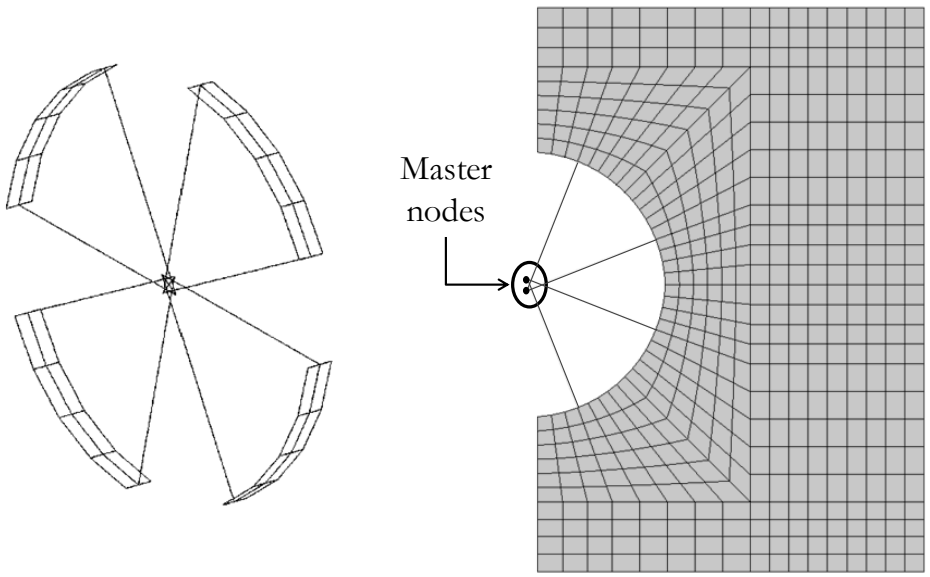

Figure 2.8. Daidie's mechanism in the FE model..

If the stiffness matrices are condensed only to the centres of the raceways, the rings will displace and deform freely. Additional master nodes can be therefore selected if boundary conditions or loads are wanted to be imposed. These additional nodes can also be used to link rings to the supports, which could be superelements or not. Moreover, superelements composed of different components can be calculated. For example, for wind turbine

generators, a superelement can be made with the upper part of the tower joined to the inner ring, and the nacelle can be included in a second superelement together with the outer ring. Nevertheless, it must be pointed out that the calculated matrix is constant, so nonlinearities can not be considered inside a superelement.

In the next sections, no additional components are considered, and raceways centres are selected as the unique master nodes. Nevertheless, it must be made clear that this is not a limitation of the model, since as many additional master nodes as wanted can be selected for whatever application, or more components considered in each superelement. Figure 2.9 shows the model for the sector corresponding to one ball. This figure shows how the span angle for each ball changes with the number of balls.

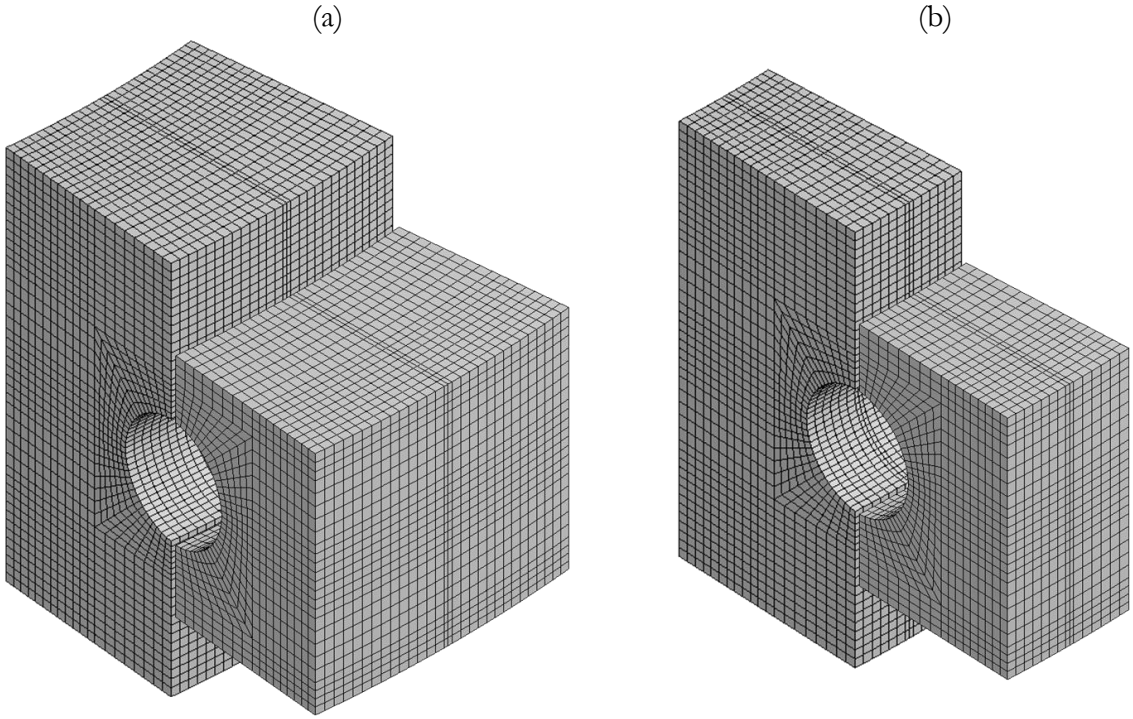

Figure 2.9. Sector of the FE model of the measured rings corresponding to each ball: (a) for 32 balls; (b) for 67 balls.

2.3.2 Implementation of the ring stiffness in the BIME model

Once the stiffness matrices of the rings are obtained, they must be implemented in the BIME model. For each ball there are two nodes per ring (see Figure 2.8), and each node has two degrees of freedom, the displacements in the axial (z) and radial (R) directions. Thus, for a bearing with B balls, the dimensions of the stiffness matrix of each ring will be $[4B \times 4B]$. The structure of these matrices is shown below, where $K_{D_2 i_2 b_2}^{D_1 i_1 b_1}$ is the component

that relates the degree of freedom D_1 (R or z) of the raceway centre of the contact point i_1 (1 or 4 for the outer ring and 2 or 3 for the inner ring) and the ball b_1, with the degree of freedom D_2 of the raceway centre of the contact point i_2 and the ball b_2. Thus, the stiffness matrix for the outer ring is defined as follows:

$$[K_{out}] = \begin{bmatrix} K_{R11}^{R11} & K_{Z11}^{R11} & K_{R41}^{R11} & K_{Z41}^{R11} & \cdots & K_{R1B}^{R11} & K_{Z1B}^{R11} & K_{R4B}^{R11} & K_{Z4B}^{R11} \\ K_{R11}^{Z11} & K_{Z11}^{Z11} & K_{R41}^{Z11} & K_{Z41}^{Z11} & & K_{R1B}^{Z11} & K_{Z1B}^{Z11} & K_{R4B}^{Z11} & K_{Z4B}^{Z11} \\ K_{R11}^{R41} & K_{Z11}^{R41} & K_{R41}^{R41} & K_{Z41}^{R41} & & K_{R1B}^{R41} & K_{Z1B}^{R41} & K_{R4B}^{R41} & K_{Z4B}^{R41} \\ K_{R11}^{Z41} & K_{Z11}^{Z41} & K_{R41}^{Z41} & K_{Z41}^{Z41} & & K_{R1B}^{Z41} & K_{Z1B}^{Z41} & K_{R4B}^{Z41} & K_{Z4B}^{Z41} \\ \vdots & & \vdots & & \ddots & & \vdots & & \\ K_{R11}^{R1B} & K_{Z11}^{R1B} & K_{R41}^{R1B} & K_{Z41}^{R1B} & & K_{R1B}^{R1B} & K_{Z1B}^{R1B} & K_{R4B}^{R1B} & K_{Z4B}^{R1B} \\ K_{R11}^{Z1B} & K_{Z11}^{Z1B} & K_{R41}^{Z1B} & K_{Z41}^{Z1B} & \cdots & K_{R1B}^{Z1B} & K_{Z1B}^{Z1B} & K_{R4B}^{Z1B} & K_{Z4B}^{Z1B} \\ K_{R11}^{R4B} & K_{Z11}^{R4B} & K_{R41}^{R4B} & K_{Z41}^{R4B} & & K_{R1B}^{R4B} & K_{Z1B}^{R4B} & K_{R4B}^{R4B} & K_{Z4B}^{R4B} \\ K_{R11}^{Z4B} & K_{Z11}^{Z4B} & K_{R41}^{Z4B} & K_{Z41}^{Z4B} & & K_{R1B}^{Z4B} & K_{Z1B}^{Z4B} & K_{R4B}^{Z4B} & K_{Z4B}^{Z4B} \end{bmatrix} \quad (2.14)$$

Analogously, the structure of the inner ring stiffness matrix will be:

$$[K_{in}] = \begin{bmatrix} K_{R21}^{R21} & K_{Z21}^{R21} & K_{R31}^{R21} & K_{Z31}^{R21} & \cdots & K_{R2B}^{R21} & K_{Z2B}^{R21} & K_{R3B}^{R21} & K_{Z3B}^{R21} \\ K_{R21}^{Z21} & K_{Z21}^{Z21} & K_{R31}^{Z21} & K_{Z31}^{Z21} & & K_{R2B}^{Z21} & K_{Z2B}^{Z21} & K_{R3B}^{Z21} & K_{Z3B}^{Z21} \\ K_{R21}^{R31} & K_{Z21}^{R31} & K_{R31}^{R31} & K_{Z31}^{R31} & & K_{R2B}^{R31} & K_{Z2B}^{R31} & K_{R3B}^{R31} & K_{Z3B}^{R31} \\ K_{R21}^{Z31} & K_{Z21}^{Z31} & K_{R31}^{Z31} & K_{Z31}^{Z31} & & K_{R2B}^{Z31} & K_{Z2B}^{Z31} & K_{R3B}^{Z31} & K_{Z3B}^{Z31} \\ \vdots & & \vdots & & \ddots & & \vdots & & \\ K_{R21}^{R2B} & K_{Z21}^{R2B} & K_{R31}^{R2B} & K_{Z31}^{R2B} & & K_{R2B}^{R2B} & K_{Z2B}^{R2B} & K_{R3B}^{R2B} & K_{Z3B}^{R2B} \\ K_{R21}^{Z2B} & K_{Z21}^{Z2B} & K_{R31}^{Z2B} & K_{Z31}^{Z2B} & \cdots & K_{R2B}^{Z2B} & K_{Z2B}^{Z2B} & K_{R3B}^{Z2B} & K_{Z3B}^{Z2B} \\ K_{R21}^{R3B} & K_{Z21}^{R3B} & K_{R31}^{R3B} & K_{Z31}^{R3B} & & K_{R2B}^{R3B} & K_{Z2B}^{R3B} & K_{R3B}^{R3B} & K_{Z3B}^{R3B} \\ K_{R21}^{Z3B} & K_{Z21}^{Z3B} & K_{R31}^{Z3B} & K_{Z31}^{Z3B} & & K_{R2B}^{Z3B} & K_{Z2B}^{Z3B} & K_{R3B}^{Z3B} & K_{Z3B}^{Z3B} \end{bmatrix} \quad (2.15)$$

According to these matrices, the deformation vectors are defined as follows:

$$\begin{aligned} \{D_{out}\} &= \{D^{R11} \quad D^{Z11} \quad D^{R41} \quad D^{Z41} \quad \cdots \quad D^{R11} \quad D^{Z11} \quad D^{R41} \quad D^{Z41}\}^T \\ \{D_{in}\} &= \{D^{R21} \quad D^{Z21} \quad D^{R31} \quad D^{Z31} \quad \cdots \quad D^{R21} \quad D^{Z21} \quad D^{R31} \quad D^{Z31}\}^T \end{aligned} \quad (2.16)$$

Since now the rings can deform, the coordinates of points O^1 and O^4 are no longer fixed. Therefore, the final location of these points will be obtained by adding the corresponding elastic deformation to the initial coordinates. So, the final coordinates of each ball are expressed as follows:

$$\begin{aligned} R_O^i &= R_{Oini}^i + D^{Ri} \\ z_O^i &= z_{Oini}^i + D^{zi} \end{aligned} \quad \text{where } i \in [1,4] \quad (2.17)$$

Similarly, the location of points O^2 and O^3 of the inner ring are not only a function of rigid body motion displacements (X_D, Y_D, Z_D, α and β, see Figure

2.5), but they must consider the corresponding elastic deformations too. Thus, adding these components to formula (2.3):

$$\begin{aligned} R_O^i &= R_{Oini}^i\left(cos\alpha sin^2\varphi_O^i + cos\beta cos^2\varphi_O^i\right) \\ &\quad + \left(X_D + z_{Oini}^i sin\beta\right)cos\varphi_O^i \\ &\quad + \left(Y_D - z_{Oini}^i sin\alpha\right)sin\varphi_O^i + D^{Ri} \\ z_O^i &= z_{Oini}^i cos\alpha cos\beta \\ &\quad + R_{Oini}^i\left(sin\alpha sin\varphi_O^i - sin\beta cos\varphi_O^i\right) \\ &\quad + Z_D + D^{zi} \end{aligned} \qquad \begin{matrix} \text{where} \\ i \in [2,3] \end{matrix} \qquad (2.18)$$

Finally, the elastic potential energy must be also reformulated. By adding the potential energy gained due to the elastic deformation of the rings (2.13), the next formula is obtained.

$$\begin{aligned} U = \frac{2}{5}\sum_{b=1}^{B}\Big[K_{Tot}^{1b}(\delta_{Tot}^{1b})^{5/2} + K_{Tot}^{2b}(\delta_{Tot}^{2b})^{5/2}\Big] \\ + \frac{1}{2}[\{D_{out}\}^T[K_{out}]\{D_{out}\} + \{D_{in}\}^T[K_{in}]\{D_{in}\}] \end{aligned} \qquad (2.19)$$

Note there are far more variables in the problem than in formula (2.13) for rigid rings. For the case of flexible rings, $5+8B$ variables are unknown for the minimization (5 for solid body motion plus $8B$ for the elastic deformations of the rings), so computational costs rise from seconds to minutes. Nevertheless, and as happens for rigid rings, no convergence problems were found.

2.3.3 Effect of the ring stiffness on the interferences

To evaluate the effect of ring stiffness on the interferences, the calculations done for the case of the rigid rings are repeated. The results for the three different preloads are shown in Figure 2.10, which can be directly compared with those previously obtained for rigid rings in Figure 2.6. From the comparison, it is clear that ring flexibility has a large effect, even when no external loads are applied. For the nominal ball, the average interference decreases from 5μm for rigid rings to 3μm for deformable rings. Moreover, the difference between the maximum and the minimum interferences also decreases, from 14μm for rigid rings to 12μm for deformable rings. Thus, by considering ring flexibility lower interferences are obtained, and the distribution is also smoother. This happens because the rings are deformed due to ball-raceway contact loads.

When the ball preload increases, the effect is more noticeable. Thus, for the preload of +20μm, the average interference decreases from 25μm for rigid rings to 14μm for deformable rings. With deformable rings, an increment in the preload does not mean an equal increment in the interferences, as happens with rigid rings, because the higher the preload is, the higher the contact loads are, and therefore the more the rings are deformed. Moreover, with higher preloads the interferences distribution becomes even smoother.

Up to this point, interferences have been calculated by considering 32 balls. For the case of rigid rings, the interferences distribution after the assembly does not depend sensibly on the number of balls. Nonetheless, more balls imply more loads, and if ring flexibility is considered, also larger ring deformations, resulting in smaller interferences. This can be seen in Figure 2.11, where the interferences were calculated for a preload of +20μm and 67 balls, which is the maximum number of balls for this bearing. This interference distribution showed values 2μm smaller than those for 32 balls in Figure 2.10c, supporting previous reasoning. Moreover, the pattern is mostly the same, which is also consistent.

2.4 External load application

Calculating interferences and load distribution after the assembly of the bearing is required to accurately select the desired preload level or calculate the idling friction torque. These two parameters are very important in four-point contact slewing bearings. Nevertheless, bearings are designed to support external loads. For this reason, and in order to bring the model to completion, external loads are to be included in the BIME model.

Slewing bearings can bear axial and radial loads and a tilting moment (F_a, F_r and M_t respectively). These loads produce certain displacements in one ring with respect to the other (δ_a, δ_r, and θ_t), taking the equilibrium position after the assembly of the bearing as the initial position. The axial displacement δ_a is in the z axis, while the radial displacement takes place in the xy plane for a certain φ_r (see Figure 2.12). The rotation axis for θ_t is perpendicular to the radial displacement. Of course, the final position of the raceway centres of the mobile ring (the inner one) will be a function of these displacements, affecting contact interferences and loads. Thus, adding these new parameters to equation (2.18) the next expression is obtained:

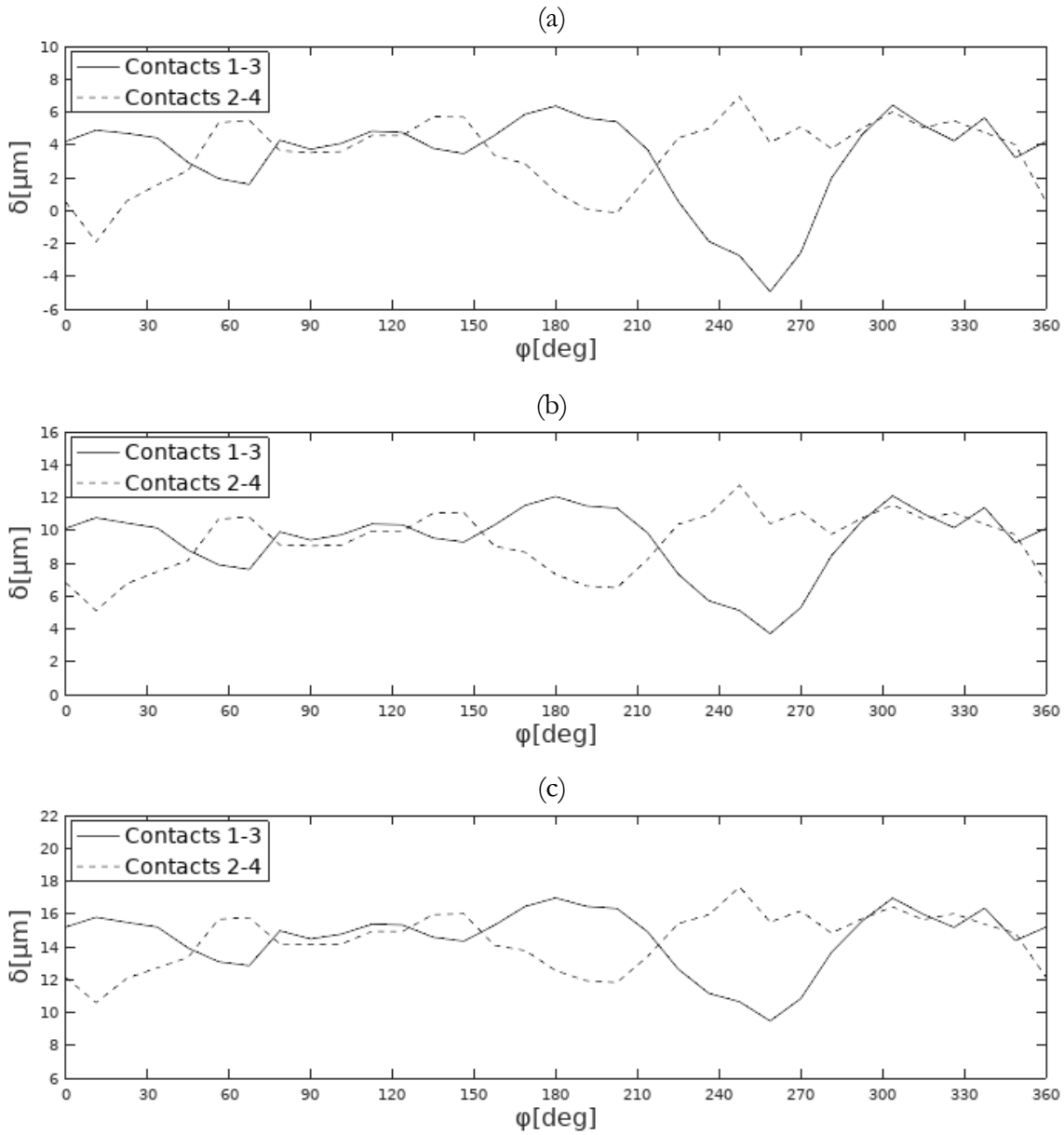

Figure 2.10. Interferences in the measured bearing with different ball preloads, considering deformable rings with 32 balls: (a) nominal ball; (b) +10μm; (c) +20μm.

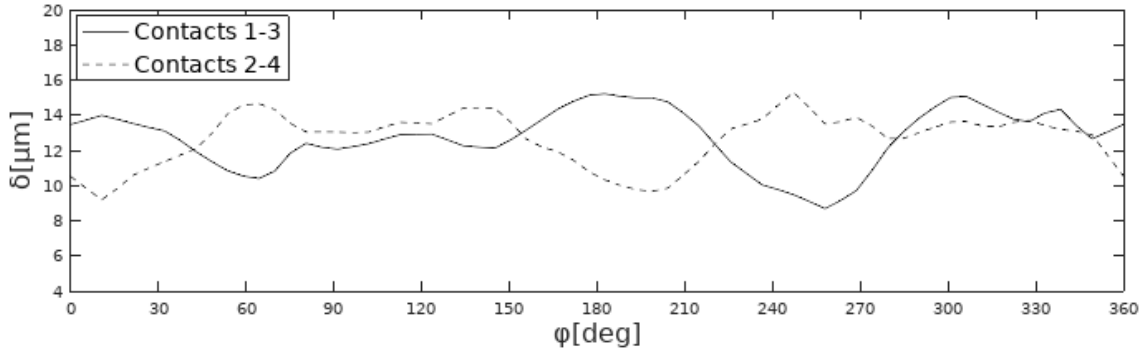

Figure 2.11. Interferences in the measured bearing with a ball preload of +20μm, considering deformable rings with 67 balls.

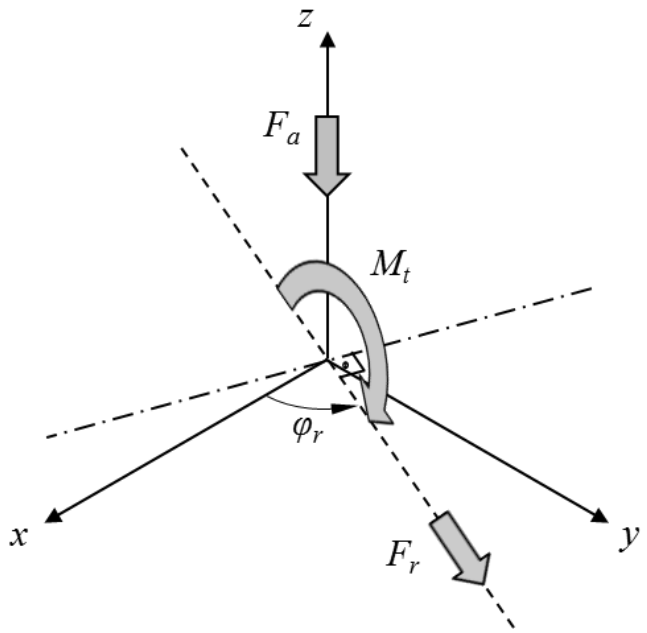

Figure 2.12. Applied external loads.

$$\begin{aligned} R_O^i &= R_{Oini}^i\left(cos\alpha' sin^2\varphi_O^i + cos\beta' cos^2\varphi_O^i\right) \\ &\quad + \left(X_D + z_{Oini}^i sin\beta'\right)cos\varphi_O^i \\ &\quad + \left(Y_D - z_{Oini}^i sin\alpha'\right)sin\varphi_O^i \\ &\quad + \delta_r cos\left(\varphi_r - \varphi_O^i\right) + D^{Ri} \\ z_O^i &= z_{Oini}^i cos\alpha' cos\beta' \\ &\quad + R_{Oini}^i\left(sin\alpha' sin\varphi_O^i - sin\beta' cos\varphi_O^i\right) \\ &\quad + Z_D - \delta_a + D^{zi} \end{aligned} \qquad \begin{matrix} \text{where} \\ i \in [2,3] \end{matrix} \qquad (2.20)$$

Where the rotations α' and β' will be a function of θ_t:

$$\begin{aligned} \alpha' &= \alpha - \theta_t \sin\varphi_r \\ \beta' &= \beta + \theta_t \cos\varphi_r \end{aligned} \qquad (2.21)$$

To avoid such long expressions, small displacements can be assumed. This way, formulas (2.20) can be simplified as follows:

$$\begin{aligned} R_O^i &= R_{Oini}^i + \left(X_D + z_{Oini}^i \beta'\right)cos\varphi_O^i \\ &\quad + \left(Y_D - z_{Oini}^i \alpha'\right)sin\varphi_O^i \\ &\quad + \delta_r cos\left(\varphi_r - \varphi_O^i\right) + D^{Ri} \\ z_O^i &= z_{Oini}^i + R_{Oini}^i\left(\alpha' sin\varphi_O^i - \beta' cos\varphi_O^i\right) + Z_D - \delta_a \\ &\quad + D^{zi} \end{aligned} \qquad \begin{matrix} \text{where} \\ i \in [2,3] \end{matrix} \qquad (2.22)$$

The potential energy of the system will now be reformulated for cases with external loads. It is known that the change in the potential energy of a system

due to an applied conservative load is equal to the negative of the work done by it. For a load F applied along a displacement δ:

$$F = -\frac{dU}{d\delta} \quad \rightarrow \quad dU = -F\, d\delta \quad \rightarrow \quad U = -F \cdot \delta = -W \tag{2.23}$$

Thus, the total potential energy of our system when external loads are applied can be calculated by deducting the work done by these loads to expression (2.19):

$$\begin{aligned} U = \frac{2}{5}\sum_{b=1}^{B}\left[K_{Tot}^{1b}(\delta_{Tot}^{1b})^{5/2} + K_{Tot}^{2b}(\delta_{Tot}^{2b})^{5/2}\right] \\ + \frac{1}{2}[\{D_{out}\}^T[K_{out}]\{D_{out}\} + \{D_{in}\}^T[K_{in}]\{D_{in}\}] \\ - F_a\delta_a - F_r\delta_r - M_t\theta_t \end{aligned} \tag{2.24}$$

The final state of the system after the application of the loads will be determined, one more time, by the configuration that minimizes the potential energy. For a certain given F_a, F_r, and M_t load combination, displacements δ_a, δ_r, and θ_t can be calculated by minimizing equation (2.24). The inverse procedure will also be possible. Note that, in any case, there are only three more unknowns than in (2.19), so the computational cost is very similar.

For the case of rigid rings, the problem can be simplified. When displacements δ_a, δ_r, and θ_t are the input data, the minimization of equation (2.24) is not needed. Once equilibrium is reached by minimizing equation (2.13) for the assembled bearing, and because the rings will not be deformed whatever the load is, the inner ring can be directly displaced from the equilibrium position, and the corresponding loads calculated from the reaction forces at the springs. Contrarily, if the inputs are the applied loads, a minimization will be required for each load combination, as it is for the case of deformable rings. Of course, since for rigid rings the deformations are null, equation (2.24) is simplified as follows:

$$U = \frac{2}{5}\sum_{b=1}^{B}\left[K_{Tot}^{1b}(\delta_{Tot}^{1b})^{5/2} + K_{Tot}^{2b}(\delta_{Tot}^{2b})^{5/2}\right] - F_a\delta_a - F_r\delta_r - M_t\theta_t \tag{2.25}$$

In this Doctoral Thesis, the rigid rings case is mainly used for comparison purposes in order to assess the effect of ring flexibility.

2.5 Final results and additional remarks

In this section, the final results for the load distribution in the measured bearing are presented and discussed. Then, some additional comments are made to finish with the chapter.

2.5.1 Load distribution results and discussion

Once the equilibrium is reached for a particular load case, not only the interferences but also normal forces and contact angles distributions among balls is obtained from the BIME model. This data can be then used as the input for the tangential problem, as illustrated in Figure 1.17. Therefore, the load distribution was obtained for the measured bearing with 67 balls, without preload and considering ring flexibility. Figure 2.13 shows the normal forces and contact angles among the balls for the unloaded case, supporting once more time the relevance of the manufacturing errors. Although the normal forces are clearly affected, in this case the contact angle is practically constant and equal to the initial value. Figure 2.14, Figure 2.15 and Figure 2.16 show the results for the cases with an axial load, a radial load and a tilting moment respectively. The applied loads are one half the static capacity of the bearing. From these plots, it can be concluded that under external loads, the effect of manufacturing errors on the load distribution is residual for every load case.

2.5.2 Additional comments

Apart from the fact that the BIME model considers manufacturing errors and ring flexibility, it offers another important advantage. When the stiffness of the ball-raceway contact is simplified by means of a beam-spring mechanism in FE calculations, as done by Smolnicki [81] or Daidié [83], the simulation of the balls is avoided, which means a big advantage in terms of computational costs. Nevertheless, this simplification has one main drawback. The simplified mechanism is thought to be in the radial plane of the bearing, but when a radial load is applied, the mechanism leaves this plane, as represented in Figure 2.17. When this happens, an unreal (and therefore not desired) radial stiffness appears due to the misalignment of the springs. Since the circumferential degree of freedom is not considered in the proposed semi-analytical procedure, as explained in the FE model description, the BIME model avoids this problem, thus offering more reliable results for load cases which involve radial displacements (Figure 2.15). Moreover, once the stiffness matrices have been calculated, the BIME model is much faster than a FE

model with any simplified mechanism. The BIME model only requires FE analysis for the calculation of the stiffness matrices, and then any load case can be solved quickly, while regular FE models require one calculation (or load step) for each load case.

Despite all the mentioned advantages of the BIME model, it has a drawback. This model needs the stiffness matrices of the rings themselves or the rings with whatever adjacent structure that is wanted to be considered. These matrices are calculated by means of FE static condensation techniques. To apply such techniques, a linear model is required. In the machines where slewing bearings are used, large bolted joints are involved, which can be a non-linearity source due to the sliding or the opening of the joint. Nonetheless, works that use FE condensation techniques for the simplification of the structures in joints involving slewing bearings [40,87] demonstrated that assuming a linear behaviour for bolted joints does not affect significantly the load distribution.

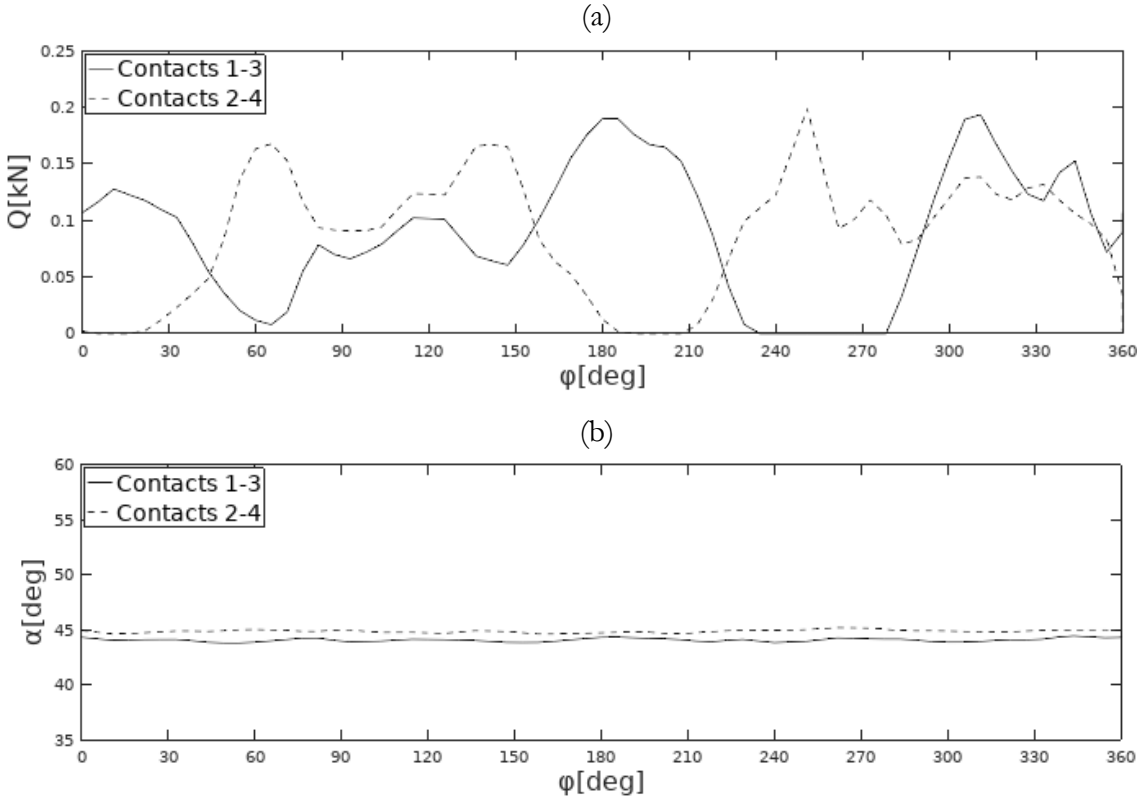

Figure 2.13. Load distribution in the measured bearing without preload and no applied loads: (a) normal forces; (b) contact angles.

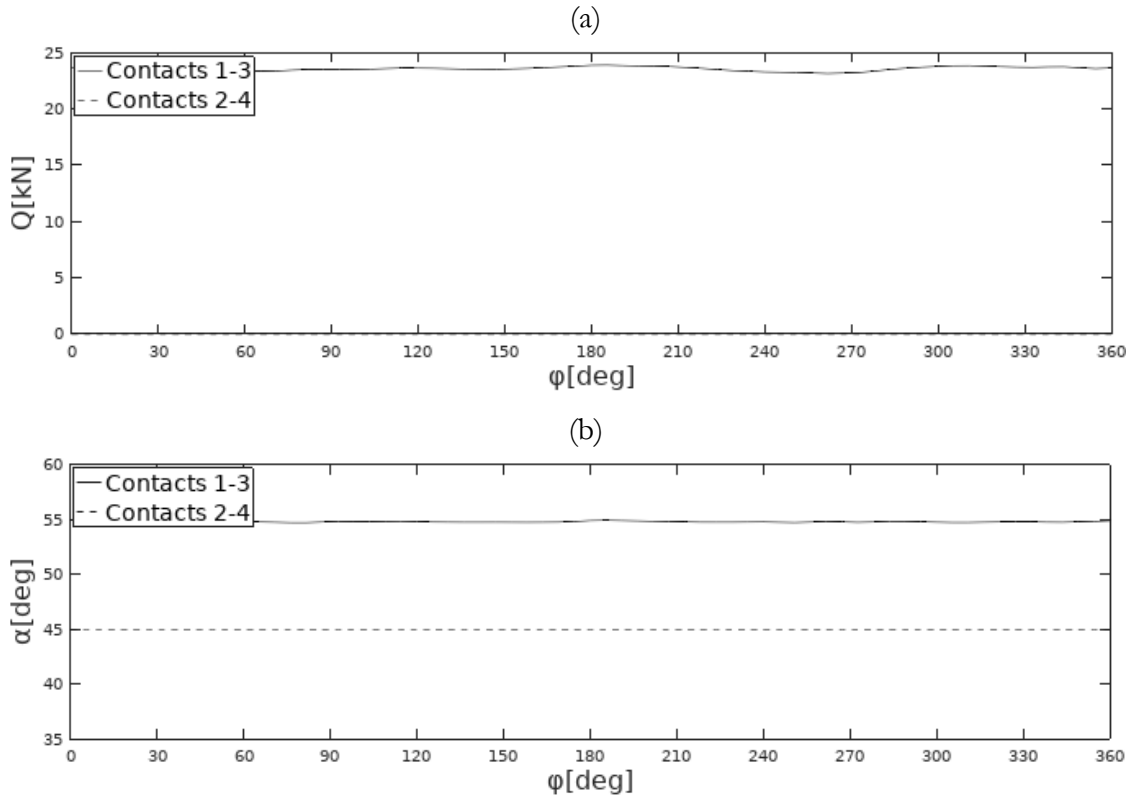

Figure 2.14. Load distribution in the measured bearing without preload and for an axial load: (a) normal forces; (b) contact angles.

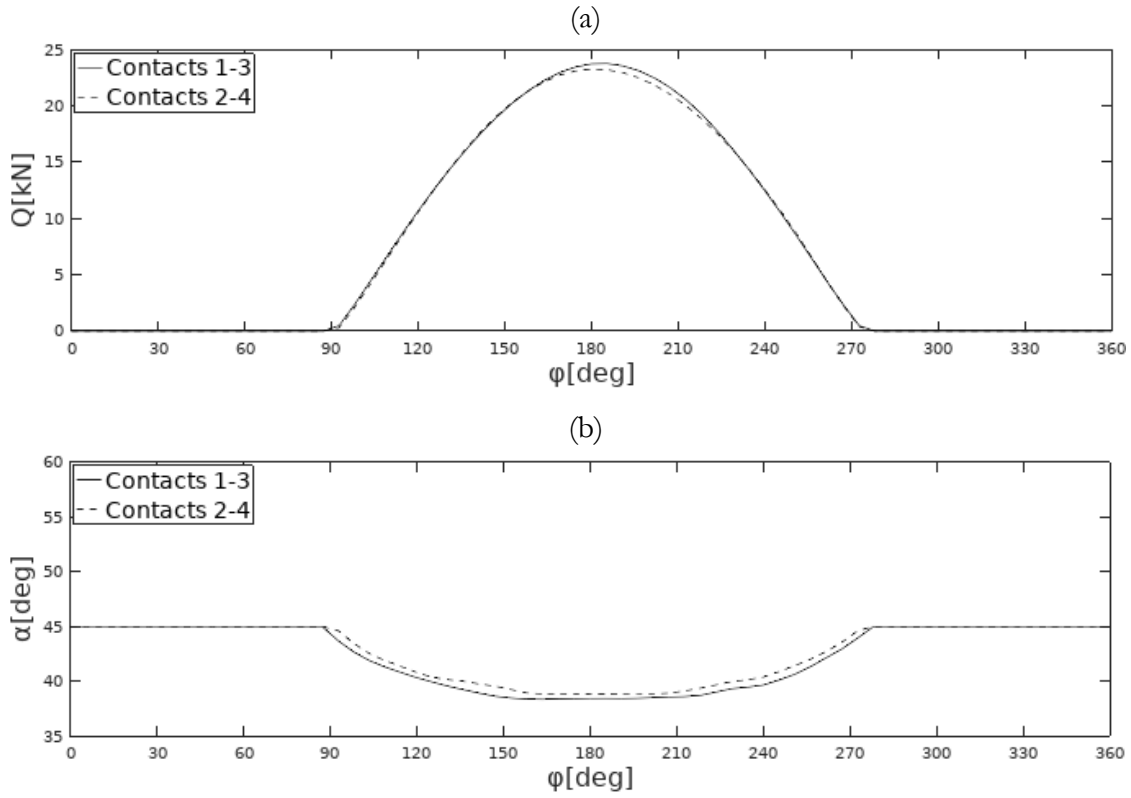

Figure 2.15. Load distribution in the measured bearing without preload and for a radial load: (a) normal forces; (b) contact angles.

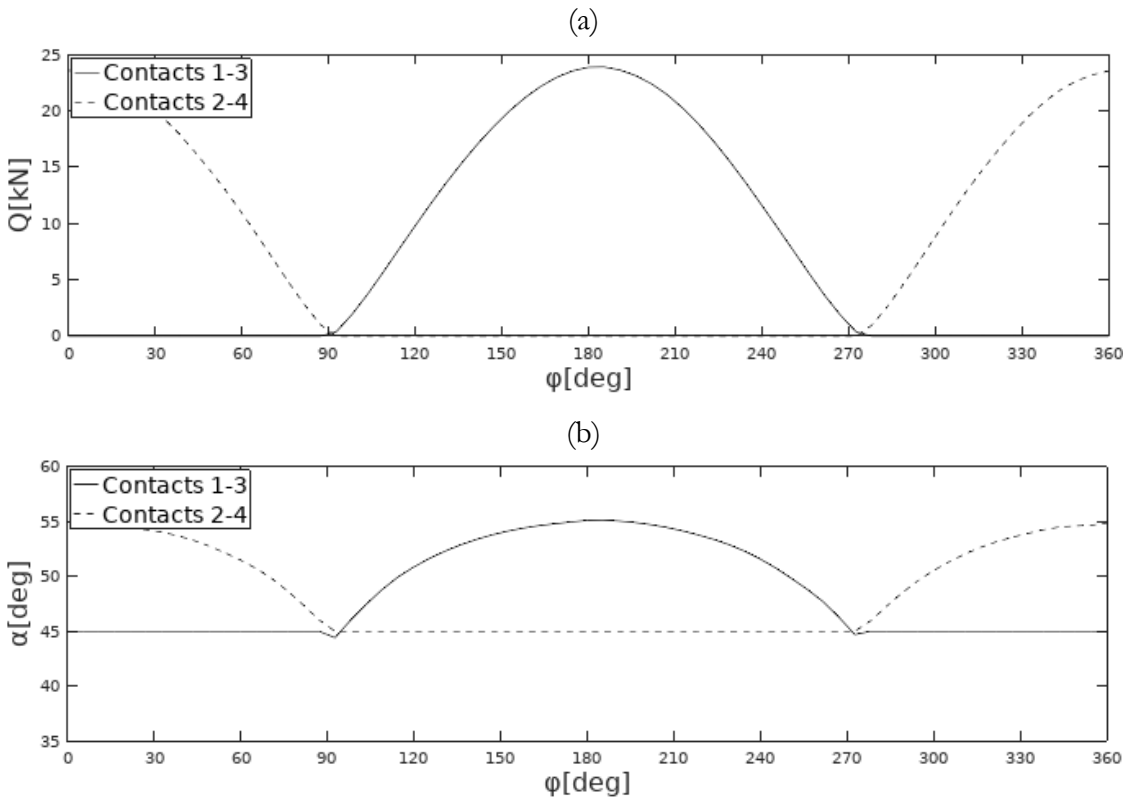

Figure 2.16. Load distribution in the measured bearing without preload and for a tilting moment: (a) normal forces; (b) contact angles.

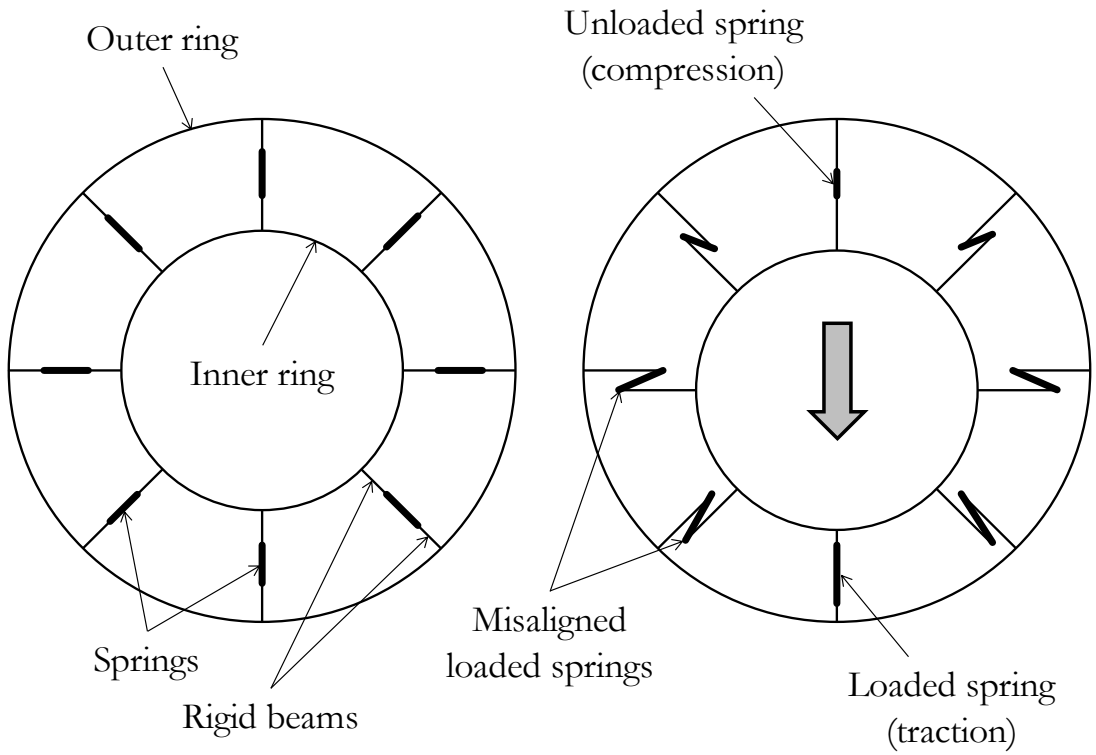

Figure 2.17. Schematic representation of the misalignment of Daidié's mechanism when a radial load is applied.

Finally, and to end this chapter, stiffness curves of the studied bearing are presented to obtain some additional conclusions about manufacturing errors and ring stiffness. Nevertheless, the bearing stiffness is thoroughly discussed in Chapter 5. Once more, the measured bearing is employed for the calculations, with 67 balls and no preload. Three load cases are considered: pure axial load, pure radial load and pure tilting moment. The curves were obtained with the BIME model and considering both rigid rings and deformable rings. From these calculations, it was demonstrated that manufacturing errors do not have a significant effect on the stiffness curves. This means that, as demonstrated before, the effect of the manufacturing errors lessens with external loads, although they are important for the idling case. Therefore, the graphs in Figure 2.18 represent the stiffness curves for the nominal geometry. The curve for rigid rings was obtained for validation purposes, and it was proven that the results are the same as the ones obtained with the analytical model proposed by Aguirrebeitia et al. [44]. With flexible rings, displacements increase drastically, making clear that ring deformations do not only affect the load distribution, but also the global stiffness of the bearing.

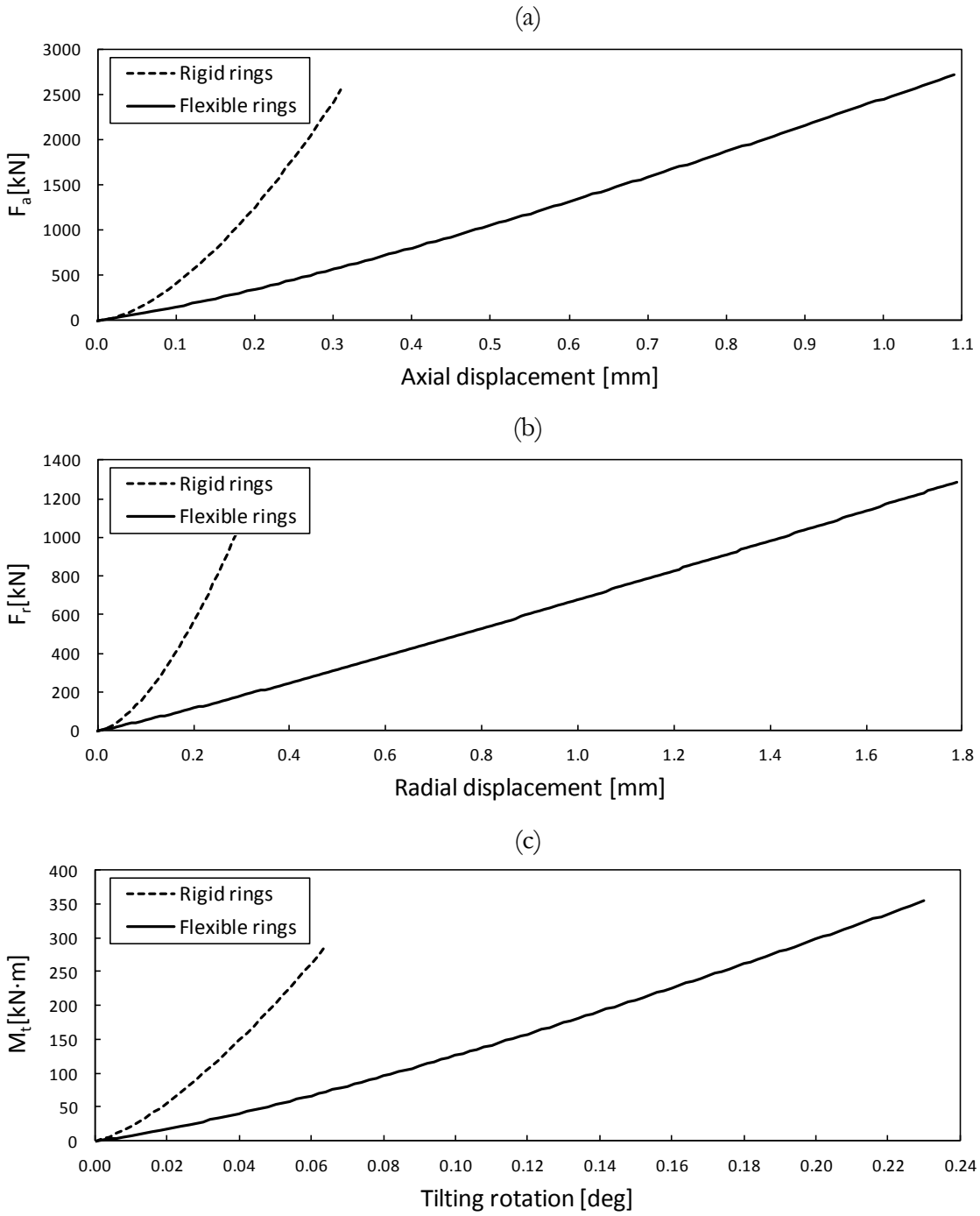

Figure 2.18. Stiffness curves for the measured bearing with 67 balls and no preload, calculated with the BIME model for rigid rings and flexible rings.

3 Study of the friction torque through the Finite Element Method

3.1 Introduction

Once ball-raceway contact loads and angles are known, the friction torque can be calculated. Friction torque is the moment that is needed to rotate one ring with respect to the other. In the machines where slewing bearings are used, an actuation system is required to apply this torque. The actuation system usually consists of one or a series of electric gear motors, but hydraulic systems are also used for high friction torques. To design and determine the size and capacity of such systems, the friction torque of the bearing is a mandatory parameter. An accurate calculation of the friction torque in the design stage allows the required capacity of the system to be determined, thus avoiding oversized actuators and resulting in cost effective machines. Therefore, a reliable methodology for the friction torque calculation would be a powerful tool to obtain efficient orientation systems.

The origin of the friction torque is in the friction forces in ball-raceway contacts. Thus, the behaviour of the contact must be somehow characterized for the friction torque calculation. State of the art models for four-point contact bearings assume that full sliding occurs at the contact [56,57,59], assumption that is also considered in angular contact bearings [54]. In these models, the kinematics are formulated and solved by imposing the equilibrium of the involved forces. As full sliding is assumed at the contact, shear stresses are directly computed as the contact pressure multiplied by the friction coefficient. Nevertheless, this assumption can have certain limitations. In four-point contact slewing bearings, there are usually only two points in contact in regular working conditions because of the large tilting moments (Figure 3.1), so balls roll in the same way as in a typical angular contact

bearing. When the ball rolls, a no-slip band exists in the contact ellipse according to the Heathcote slip [60], which divides the contact area into three different regions: the one in the centre is known as the backward slip region, whereas the other two, at both sides, are the forward slip regions. In the backward region, the ball´s relative velocities with respect to the raceway are in the opposite direction to the ball´s rigid body relative displacement, so shear stresses due to contact friction have the same direction as the relative movement. On the contrary, in the forward regions, friction forces act against this relative movement. Considering elastic micro-deformations at the contact surface, a no-slip region rather than a no-slip band will exist. Furthermore, and as later demonstrated in this chapter, the stick region is not only located between the backward and forward regions, but also along the leading edge of the contact ellipse, as illustrated in Figure 3.2. The presence of this stick region contravenes the full sliding assumption made by the state of the art analytical models. Obviously, in the stick region, shear stress will be equal or lower than the product of the pressure and the friction coefficient. Nevertheless, full sliding hypothesis does not necessarily involve an overestimation of friction torque: depending on the extension and the location (backward or forward zone) of the stick region, the value of the friction torque can be higher or lower than that calculated under a full sliding assumption, so no clear tendency can be deducted without a more thorough study.

Whatever the effect of stick regions on the friction torque is, it is clear that they will affect the shear stress field. Shear stresses are responsible for the wear of the contacting elements, and are therefore involved in damage and failure types like fretting or false brinelling (Figure 3.3), commonly present in bearings [98,99]. A model capable of accurately calculating shear stresses could be used to predict such failures. Moreover, it also would be useful for fatigue calculations.

In this chapter, different approaches are proposed for the friction torque calculation and the ball-raceway contact study through FE analysis, the results of which are presented and compared. These FE models need contact interferences and angles as input, which will be provided by the BIME model (Chapter 2) for our procedure. The objective of the proposed models is to predict the stick region of the contact ellipse and evaluate the effect it has both on the shear stress field and on the friction torque.

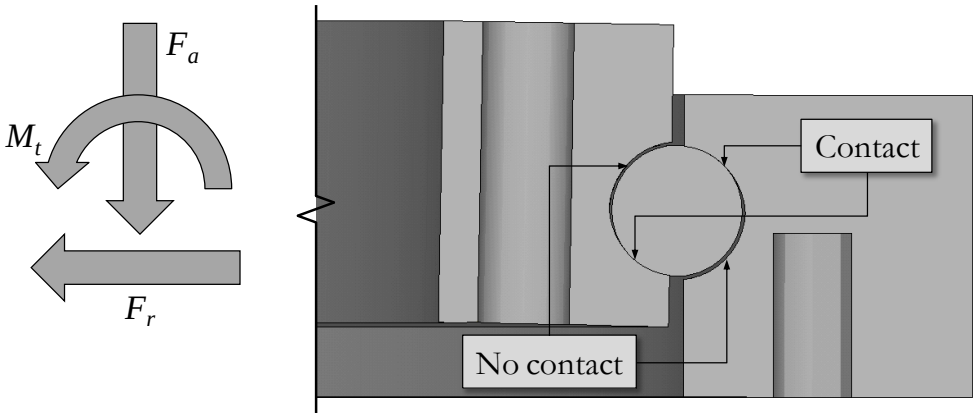

Figure 3.1. Deformed shape of a four-point contact slewing bearing under applied loads.

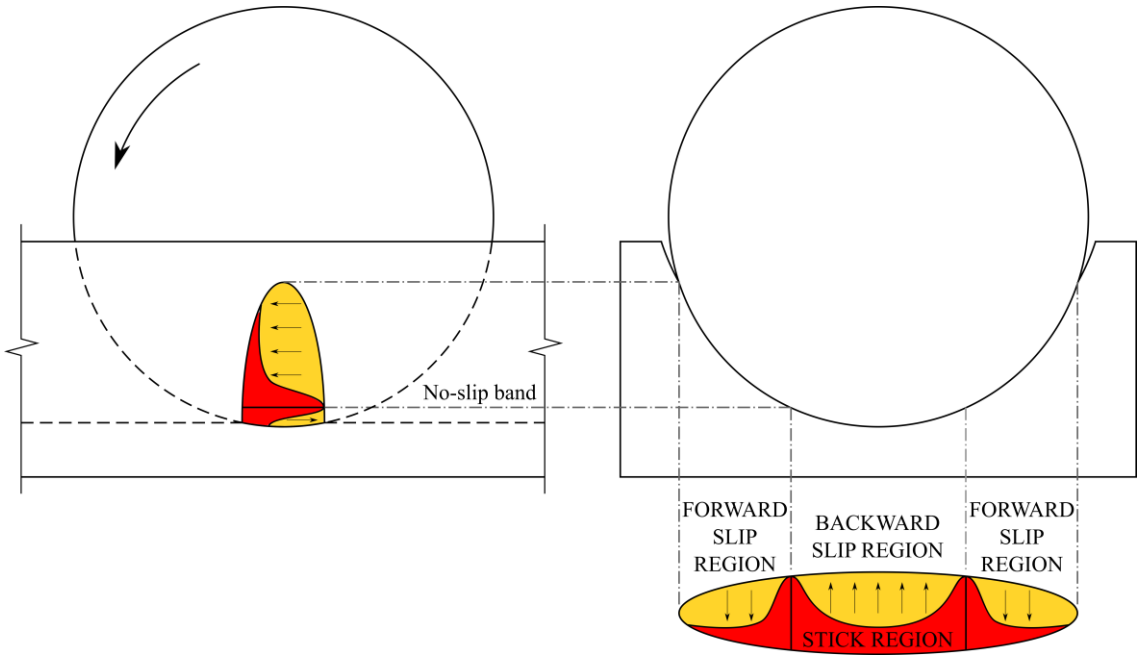

Figure 3.2. Contact ellipse regions in a ball rolling on a grooved track.

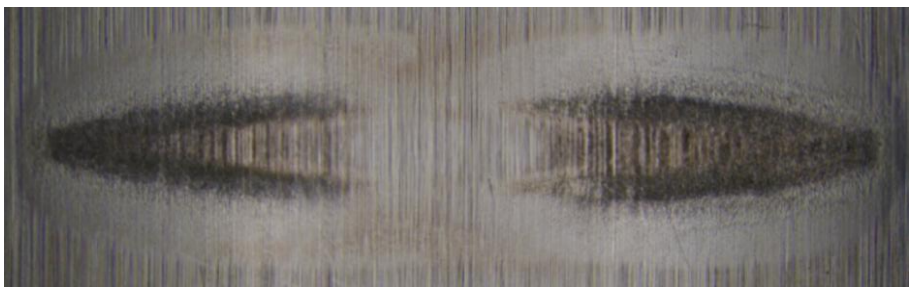

Figure 3.3. Microscopy of a false brinelling damaged bearing raceway (courtesy of Fabian Schwack).

In a first approach, an FE model was used to evaluate the extent of the stick region and its effect in the shear stress field. This first model (Rigid-FEM) assumed rigid rings, which means that they could not globally deform, but the local deformations of the contacts were considered. Later, an FE model capable of considering ring flexibility was developed (Flexible-FEM). These models were fed with contact forces and angles calculated with the BIME model for the measured bearing (Chapter 2), and the effect of manufacturing errors and ring stiffness on the friction torque was studied. Additionally, the effect of the number of balls was also analysed. For this study, rigid rings were assumed in the BIME model (Rigid-BIME). The obtained contact loads and angles where then introduced in the FE model for rigid rings on the one hand (1st way, see Table 3.1), and for flexible rings on the other hand (2nd way). Thus, the 1st way does not consider ring deformations, while the 2nd one does through the FE model. Later, an alternative method was developed to consider ring deformations. This method consists of calculating the interferences for deformable rings (Flexible-BIME), and then assuming rigid rings in the FE model (3rd way). The 2nd and 3rd ways must provide the same results, which is demonstrated, while the 3rd offers a number of advantages.

In addition to the two mentioned FE models, a submodel was also developed for the detailed study of the contact. This submodel is based on the previous mentioned models, and an extremely fine mesh is used, so the contact can be studied in more detail. The FE models, as well as mentioned developments, are explained more extensively in the following sections. For clarification purposes, Figure 3.4 represents schematically all the models used in this Doctoral Thesis.

The final goal of the study is to develop an analytical model capable of calculating the friction torque and the shear stress field at the contact, considering the stick regions (4th way, see Table 3.1). This model is presented in Chapter 4.

ID	Load distribution	Contact simulation
1	Rigid-BIME	Rigid-FEM
2	Rigid-BIME	Flexible-FEM
3	Flexible-BIME	Rigid-FEM
4	Flexible-BIME	New analytical model

Table 3.1. Different approaches for the friction torque calculation.

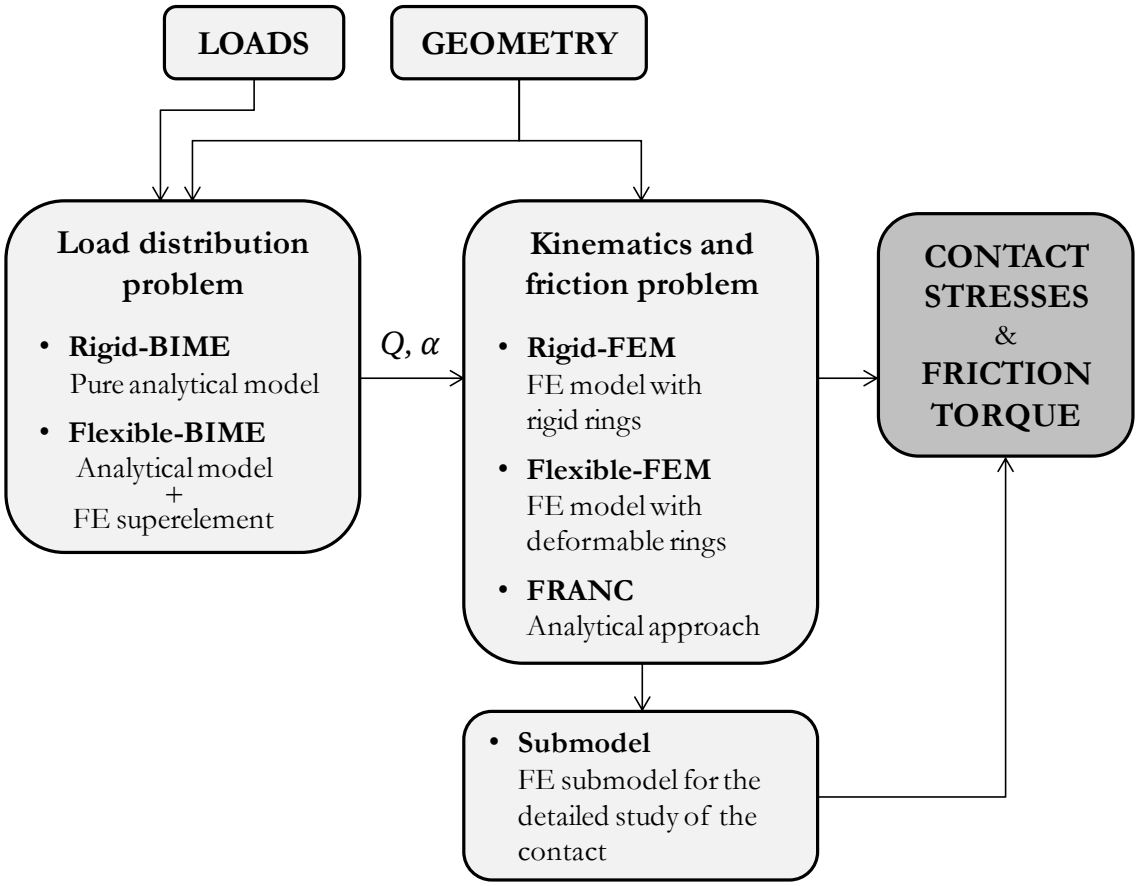

Figure 3.4. Schematic representation of the developed models.

3.2 Finite Element models for the friction torque calculation

The simulation of the friction torque through FE calculations is a very sensitive matter. In spite of being a quasi-static problem, the analysis is highly nonlinear due to the required large displacements and the sensitivity of the ball-raceway contact, which takes place in a small area and changes with the rotation of the bearing. Nonetheless, these inconveniences have been addressed and overcome successfully.

In this section, the developed FE models for friction torque calculation and contact analysis are described. Three different models have been used for this purpose: one with rigid rings, another with deformable rings, and a third that is a submodel of the contact region. The commercial software ANSYS® was used for the FE modelling, while Matlab® was also useful for better graphical representation of some results.

3.2.1 Finite Element model with rigid rings

For the friction torque calculation, only the sector corresponding to one ball is considered, since the contribution of each ball to the total friction torque can be calculated separately. This simplification supposes a great advantage over a full model, not only in terms of computational cost, but also to ensure the convergence. The inputs of the model will be contact interferences and angles, which can be calculated through the BIME model, and the outputs will be the friction torque, contact results (pressure, shear stress and contact status) and ball kinematics. To obtain these results, one of the rings must be rotated with respect to the other, which involves large displacements. During the simulation, the ball also undergoes large displacements and rotations, so it must be modelled as a solid body. Simplifications like the ones proposed by Smolniki and Rusiński [81] or Daidié et al. [83], although very practical for load distribution analysis, they are not applicable in this case.

In this first model, rigid rings will be considered, as they are in most analytical models for the load distribution [38,39,44]. Considering rigid rings involves not allowing them to have global deformations, but they must have the capability to deform within the contact vicinity. For this reason, only the parameters that affect the geometry of the ball-raceway contact will have an impact on the results. These parameters are bearing mean diameter (D_{pw}), ball diameter (D_w), osculation ratio (s) and initial contact angle (α_0), and are called contact parameters (see Figure 3.5). The rest of the parameters will not affect the results, as long as the distance from the raceways to the outer faces of the rings, where boundary conditions are imposed, is large enough so contact deformations are not influenced. These parameters are the inner diameter (D_i), the outer diameter (D_o), the clearance between rings (e), the ring height (H) and the span angle for the sector (Ψ), and are called secondary parameters. Their values have been set as a function of the contact parameters:

$$\begin{aligned} D_i &= D_{pw} - 2D_w \\ D_o &= D_{pw} + 2D_w \\ H &= 1.5D_w \\ e &= 0.1D_w \\ \Psi &= \frac{D_w}{D_{pw}/2} = 2\frac{D_w}{D_{pw}} \end{aligned} \tag{3.1}$$

Of course, the raceway radius (R_C) affects the geometry of the contact, but it is also a derived parameter, that is a function of the ball diameter (D_w) and the osculation ratio (s), as explained in the previous chapter. Furthermore, the angular span of the section (Ψ) fixes the total DoF of the FE model. Thus, the minimum angle capable of covering the contact patch area and its trajectory along the raceways is sought. It must be also taken into account that results can be affected by boundary conditions if the contact area reaches the vicinity of the limits of the raceway. In this sense, the value adopted in (3.1) for Ψ has proven to be the most cost-effective, avoiding any side effect due to imposed boundary conditions. As a result, the geometry shown in Figure 3.6 is obtained. Note that it is divided into several bodies, so different mesh sizes can be defined, with an appropriate transition.

Rings and ball are simulated as deformable bodies in order to suitably replicate contact deformations. To assume rigid rings, boundary conditions are employed, which are specified later. The material used for the simulations is steel, with an elastic modulus of 200GPa and a Poisson coefficient of 0.3. A small spherical region of the centre of the ball is simulated as rigid (Figure 3.6), so ball kinematics can be directly obtained. This rigid sphere is far from the contact areas on the surface, so it does not affect the behaviour of the system. Figure 3.6 shows 3 regions, where different mesh types are employed:

- ESIZE-1: this region is the most important, since it is the region where the contact happens (marked in black in Figure 3.6). Therefore, it is meshed with very regular elements, composed exclusively by SOLID186 second order hexahedrons (20 nodes) with a high aspect ratio. There are two layers of these elements on the contact surface. The element size is 0.02 times the diameter of the ball.
- ESIZE-2: this region is the transition between ESIZE-1 and ESIZE-3 regions. SOLID187 second order tetrahedrons (10 nodes) are employed for their adaptability, although some SOLID186 pyramids (13 nodes) are required for the elements in contact with the hexahedrons. The element size is three times that employed in ESIZE-1.
- ESIZE-3: this is the farthest region from the contact and the same elements of ESIZE-2 are used, but with a size four times greater. Since this region is far from the contact, it could have been considered as rigid. Nonetheless, the nodes in this region represent a small part of the total. Moreover, meshing this region makes easier switching from the rigid rings assumption to deformable rings.

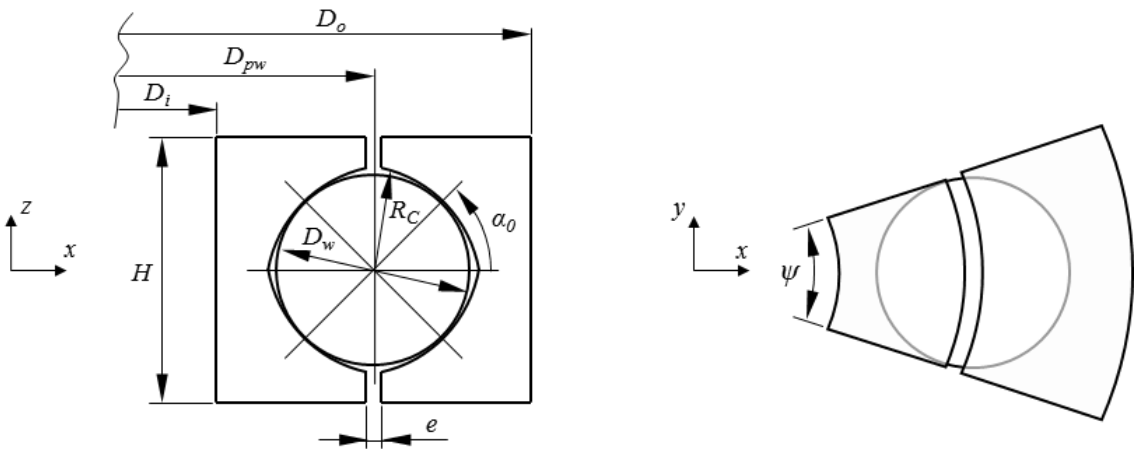

Figure 3.5. Geometrical parameters of the FE model.

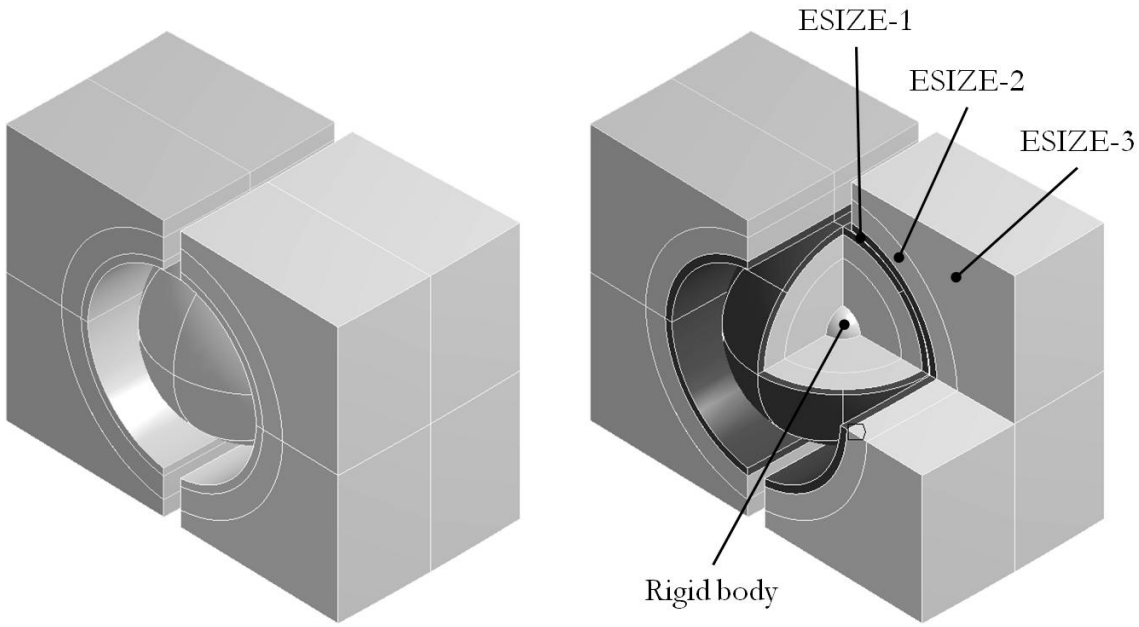

Figure 3.6. Geometry of the FE model.

Figure 3.7 and Figure 3.8a show the resulting mesh. Of course, a sensitivity analysis was performed before defining the described mesh, which studied the effect of the mesh size on the results. The computational cost is also a limiting factor, so this mesh offers a good (accuracy)/(computation cost) ratio for the friction torque calculation when many analyses are required. Nevertheless, for a detailed study of the contact, a more refined mesh is used. Figure 3.8b shows this mesh, where the element size for the contact (ESIZE-1) is 0.01 times the ball diameter. The first described mesh (Figure 3.8a) has a total of nearly 10^6 DoF, while the refined one (Figure 3.8b) has over $3.5 \cdot 10^6$ DoF. Later in this section, results are analysed for these two different mesh sizes for a particular bearing.

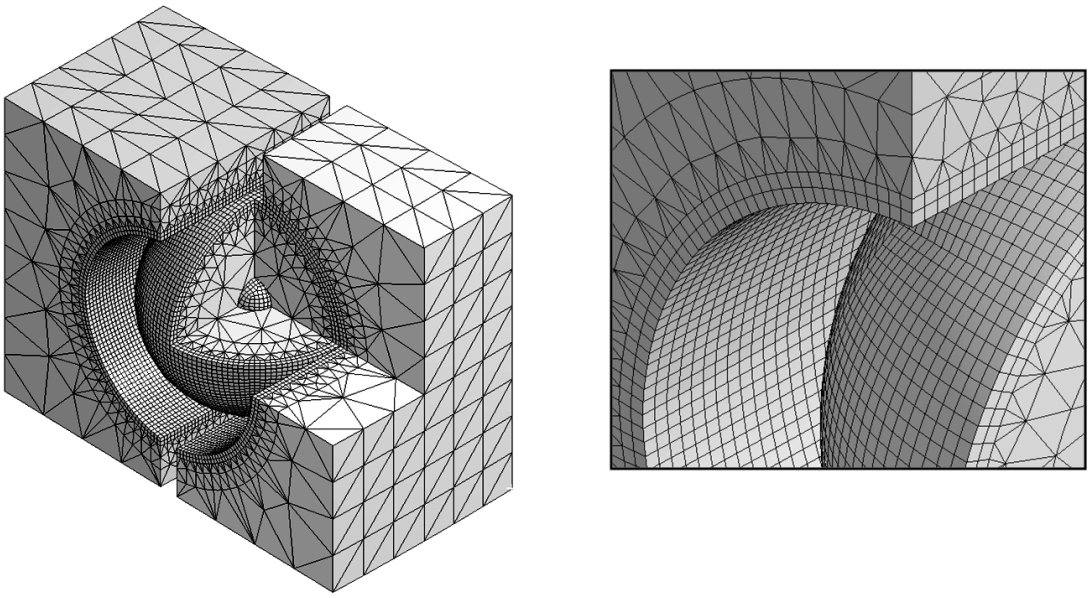

Figure 3.7. FE mesh.

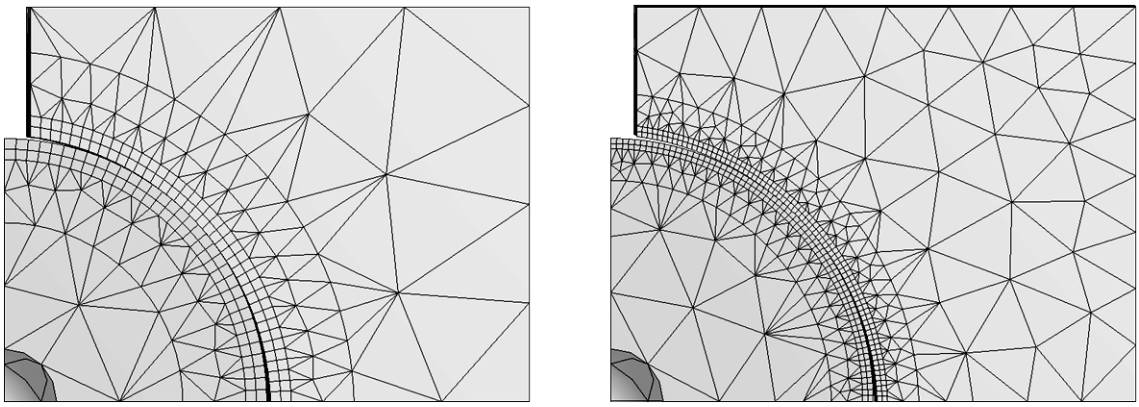

Figure 3.8. Different mesh refinements: (a) friction torque calculation; (b) detailed contact analysis.

This model requires two contact types. Defining contacts involve new elements, which are CONTA174 and TARGE170 in ANSYS®. The contacts are defined below:

- Ball-raceway contact: the study of this contact, and the friction torque derived from the shear stresses on it, is the objective of this model, so it is of crucial importance. Of course, it is a frictional contact, defined by a constant frictional coefficient. In order to make the post-process easier, each of the ball-raceway contacts is defined separately. As the surface of the ball is convex and the raceway is concave, and because the mesh size is the same in both bodies, the former is set as the contact (where new CONTA174 surface elements will be created) and the latter is the target (TARGE170 elements). It is important to set a penetration tolerance value in order to avoid mesh interferences between the ball and the raceway. A

value of 1μm is imposed, since maximum penetrations of 0.1μm are observed after the analysis, which is well below the magnitude order of the interferences due to ball preloads or manufacturing errors (as seen in Chapter 2). The normal stiffness of the contact is regulated by the criterion of the program, although better convergence behaviour is observed if the update of the stiffness is allowed for each iteration. Regarding contact formulation, Augmented Lagrange is proven to give good results, while Normal Lagrange gives the same results but with higher computational cost, so the first one is employed.

- Rigid ball - deformable ball contact: a contact is defined between the small rigid sphere in the centre of the ball and the ball itself. A typical bonded contact is defined, with pure penalty formulation. Note that, although the rigid body is not deformed, the surface must be meshed (through TARGE170 elements) for the contact definition.

To simulate rigid rings, no deformations of their outer faces are allowed. These faces are marked in black in Figure 3.9. On the one hand, the faces of the outer ring are fixed, while on the other hand, the faces of the inner ring are displaced, but not deformed. To apply the displacements, these faces are rigidly linked to a remote point, placed in the centre of the bearing. The rigid connection between the remote point and the faces is defined through constraint equations, so no additional elements are required (the lines in Figure 3.9 are only for representation purposes).

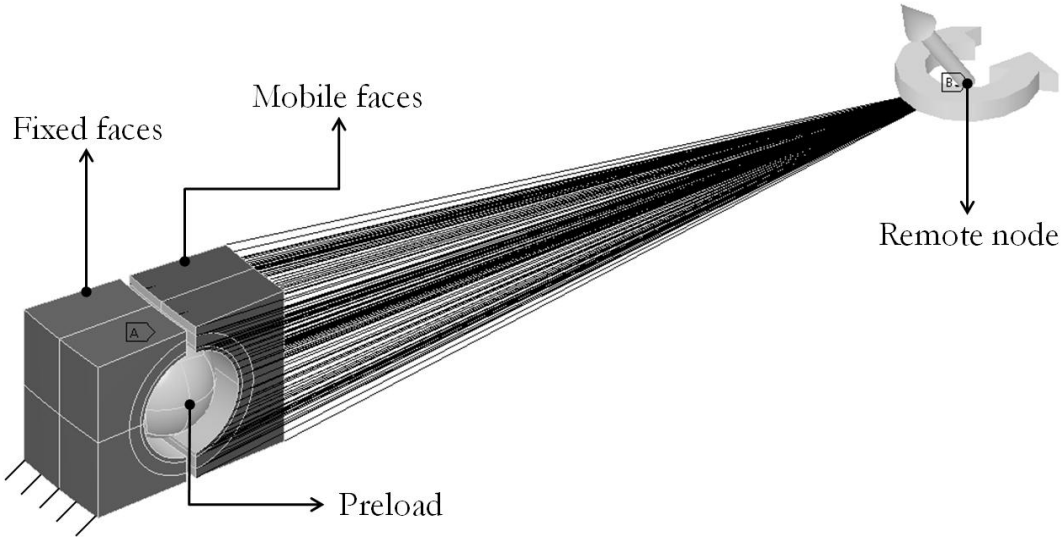

Figure 3.9. Loads and boundary conditions.

Before applying the rotation to the inner ring, loads from different sources can be applied. In the next points, the different load steps are described, while not all of them must be present in an analysis:

- 1st step: Contact interferences
  The defined ball-raceway contact allows initial interferences between contacting surfaces to be imposed. They can be the interferences calculated with the BIME model. These interferences are introduced gradually through a ramped function.
- 2nd step: Ball preload (δ_P)
  Considering an oversized ball is not a straightforward task in an FE simulation. If the real geometry is considered, initial geometrical interferences will exist between ball and raceways. This is proved to cause convergence problems in many cases, so a more robust alternative is required. Thus, the nominal ball is considered in the geometry, and in a second step, a thermal jump is introduced to the ball, according to the following formula:

$$\Delta V = 3\alpha_L \cdot \Delta T \cdot V_0 \;\rightarrow\; \Delta T = \frac{(D_w + \delta_P)^3 - D_w^3}{3\alpha_L D_w^3} \tag{3.2}$$

  Where α_L is the linear thermal expansion coefficient (not to be confused with the contact angle), the value of which is around $1.2 \cdot 10^{-5} K^{-1}$ for stainless steel. In this case, the real value of the coefficient does not matter, since the thermal expansion is a mere simulation ruse. Through the thermal expansion, the preload is gradually introduced, so the convergence is ensured.
- 3rd step: External displacements
  As a result of combined axial, radial and tilting loads, the bearing segment corresponding to each ball experiences certain axial and radial displacements. These external axial or radial displacements can be applied to the inner ring through the remote node.
- 4th step: Rotation
  Finally, the rotation is applied to the inner ring. As done with external axial and radial displacements, the rotation is applied through the remote node to the ring. When the rotation starts, the contact experiences a change and undergoes a transitory stage until it is stabilized (see Figure 3.10). Therefore, several substeps are required in order to appropriately simulate this phenomenon. Since very large displacements are involved during the

rotation, a high number of substeps will also help in achieving the convergence. After trying a different number of substeps, 50 was proved to be the lowest value that provides good convergence and reliable results.

In the research framework of this Doctoral Thesis, the 3rd step was only used for some preliminary tests. In most cases, only the 1st and 4th steps were used, since the interferences calculated by the BIME model, which are introduced in the 1st step, already consider the ball preload and the external loads or displacements. Nevertheless, the 2nd and 4th steps were applied for some analysis. In any case, the 4th step is of course mandatory, and some kind of load must be applied before, so at least there must be two steps.

According to Kalker [68], the ball needs to be displaced at least one time an entire contact ellipse in order to achieve the stabilization of the friction torque. Therefore, we have to displace the inner ring at least 4 times the minor semiaxis of the ellipse (b) (see Figure 3.11). Just to ensure the stabilization and being conservative, the inner ring is displaced 1.5 times the minimum required:

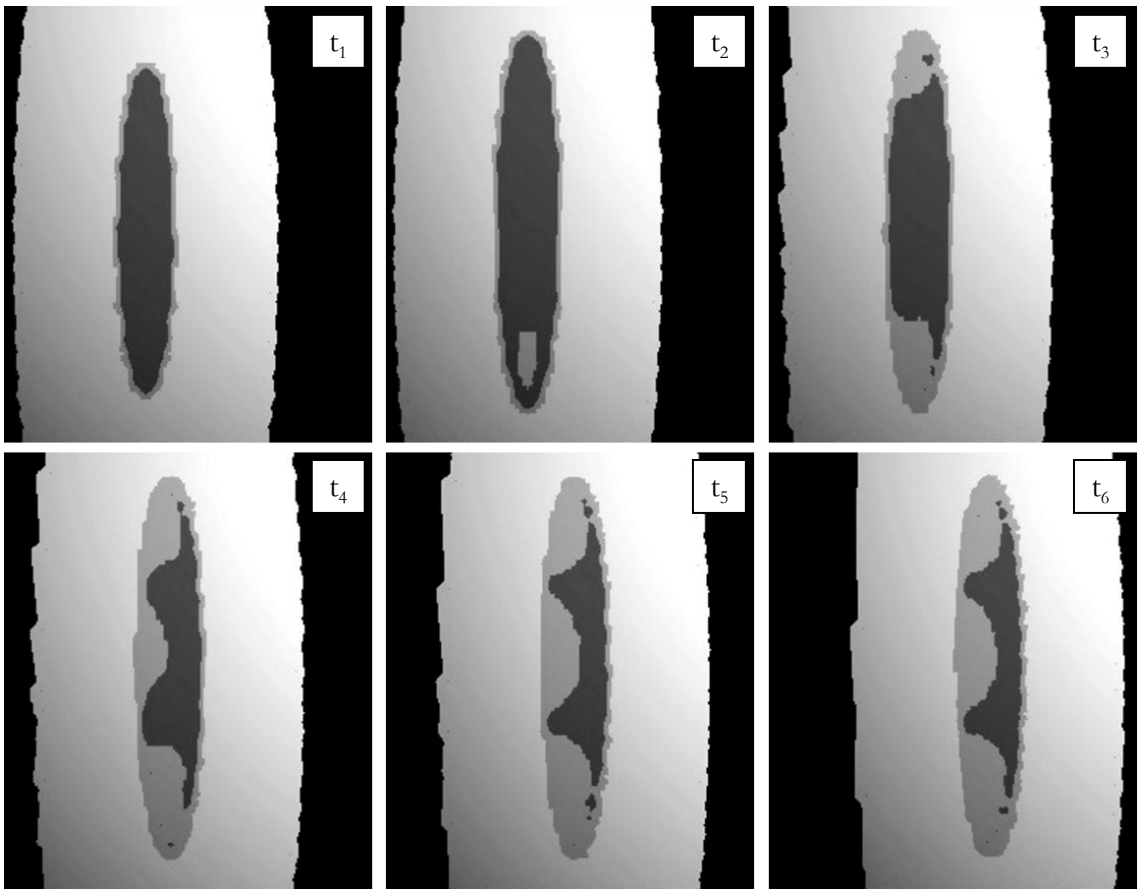

Figure 3.10. Evolution of the contact status in the contact ellipse.

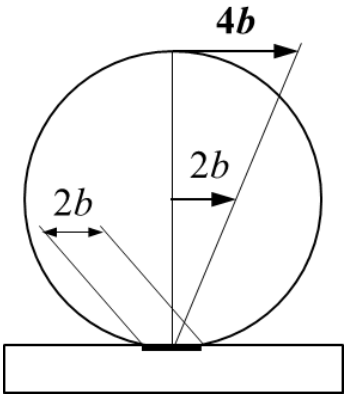

Figure 3.11. Minimum required displacement for the stabilization of the contact.

$$R_y = 1.5\frac{4b}{D_{pw}/2} = 12\frac{b}{D_{pw}} \tag{3.3}$$

To calculate major and minor semiaxes, the approximation of Houpert [30] of the exact solution [17] for osculation ratios in the range of $0.89 < s < 0.99$ is used (as done in Chapter 2 for the contact stiffness):

$$\begin{aligned} a &= 1.3085(1-s)^{-0.4091}\left(\frac{1-\nu^2}{E}\right)\left(\frac{D_w}{2}\right)^{1/3} Q^{1/3} \\ b &= 1.1687(1-s)^{0.1974}\left(\frac{1-\nu^2}{E}\right)\left(\frac{D_w}{2}\right)^{1/3} Q^{1/3} \end{aligned} \tag{3.4}$$

Which can be particularized for the case of steel (assuming typical values of $E = 2\cdot 10^5 MPa$ and $\nu = 0.3$):

$$\begin{aligned} a &= 0.01721(1-s)^{-0.4091} D_w^{1/3} Q^{1/3} \\ b &= 0.01537(1-s)^{0.1974} D_w^{1/3} Q^{1/3} \end{aligned} \tag{3.5}$$

The external faces of the rings are rigid, according to the imposed boundary conditions. These conditions can affect the results when the contact region is near the external faces, so this is an undesirable effect to be avoided. It is demonstrated that the results are never affected by imposing the next limit to the applied rotation, whatever the load or the geometry is:

$$R_y^{max} = \frac{0.5D_w}{D_{pw}/2} = \frac{D_w}{D_{pw}} \tag{3.6}$$

On the other hand, the size of the elements at contact surfaces is also determining. It is observed that friction torque results provided by FE

calculations have an oscillatory nature (as later illustrated for a particular bearing), and each oscillation corresponds to the transition of the contact from one element to the contiguous one during the rolling of the ball over the raceway. As a criterion, a minimum of 4 oscillations is established in order to obtain reliable results. Thus, the inner ring is required to displace at least 8 times the element size at ESIZE-1:

$$R_y^{min} = \frac{8 \cdot ESIZE_1}{D_{pw}/2} = \frac{8 \cdot 0.02 D_w}{D_{pw}/2} = 0.32 \frac{D_w}{D_{pw}} \tag{3.7}$$

If R_y does not reach this minimum, it means that the mesh is not fine enough for the small size of the contact area. According to the established limits, the rotation must be ensured to be within the following limits, so the results will be reliable:

$$0.32 < R_y \frac{D_{pw}}{D_w} < 1 \tag{3.8}$$

The model was done in ANSYS® Workbench, including the geometry, for which ANSYS® DesignModeler was used. Nevertheless, an APDL script was developed to apply the loads as defined, since Workbench shows certain parameterization limitations.

As discussed at the beginning of the section, the model is highly nonlinear due to the large displacements involved and the punctual and variable nature of the contacts. Nevertheless, a parametric and robust model has been achieved, which reports reliable results and does not show convergence problems for any geometry or load case. This is due to the employed mesh, contact formulation and progressive application of the loads. For the reference mesh (Figure 3.7 and Figure 3.8a), the computational time is between 2 and 8 hours, depending on the magnitude of the loads and the number of contacting points (2 or 4). For the refined model (Figure 3.8b), the computational cost is between 10 and 40 hours. These times have been obtained in a high performance work station, with an Intel® Xeon® E5-2697 v3 @ 2.6GHz processor with 14 physical cores (28 logical) and a RAM of 128GB. For the optimization of the computing time, only 4 processors were used per each calculation, allowing the parallelization of different analyses. Considering all this, the reference mesh is suitable to perform series of calculations to obtain the friction torque for a large number of geometrical

configurations under different load conditions, while the refined model is only affordable to study the contact in detail for a limited number of cases.

To show the results that the model provides and explain how they are post-processed, a particular case is going to be studied. The values of the parameters are shown in Table 3.2. In the analysis, an interference corresponding to 50% of the static capacity is introduced on one of the diagonals (δ_1), while the other remains unloaded so the ball will roll.

Figure 3.12 shows friction torque results for the model with the reference element size and for the refined one. In the figure, the aforementioned oscillatory nature is clearly appreciated. It can be observed how the period of the oscillations for the reference mesh is twice that of the refined mesh. Since the element size in the refined model is half the size of the reference, this is consistent with what was explained before. In any case, these fluctuations must be filtered, whatever the mesh is. For this purpose, the next functional approximation is used:

Parameter	**Value**
Bearing mean diameter (D_{pw})	1000.00 mm
Ball diameter (D_w)	30.00 mm
Osculation ratio (s)	0.95
Friction coefficient (μ)	0.10
Contact angle (α_1)	45°
Contact interference (δ_1)	50%

Table 3.2. Values of the parameters of the studied case.

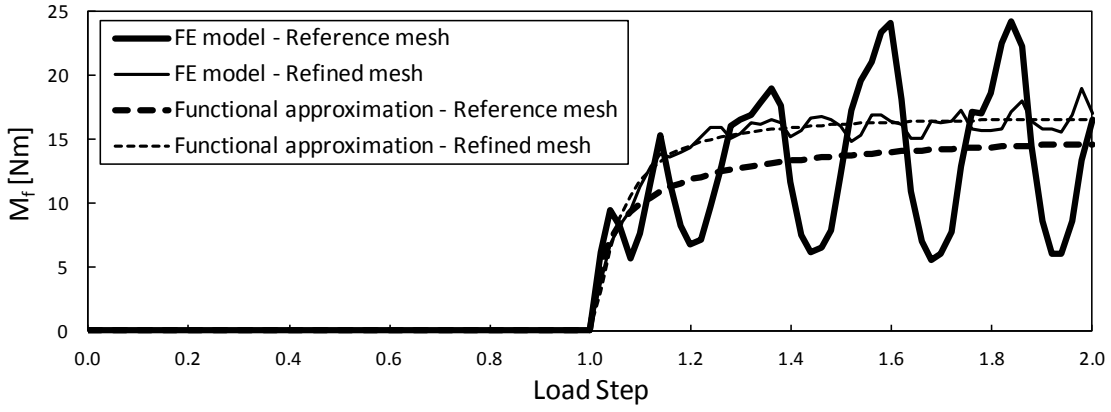

Figure 3.12. Friction torque results for different mesh sizes.

$$M_{inst}(t) = \frac{M_f(t-1)^{\eta}}{\beta + (t-1)^{\eta}} \tag{3.9}$$

Where M_{inst} is the instantaneous friction torque, M_f is the stationary friction torque (the sought value) and β and η are coefficients to be determined. The values of the coefficients will be those which minimize the quadratic error between the functional approximation and the instantaneous friction torque. According to this approximation, the stationary value of the friction torque is 16.2N·m for the reference model, and 16.9N·m for the refined one. Analyses were performed for different geometries and loads, and in every case higher values were reported for the refined model. Since the effect of the mesh size is consistent, both models are equally valid to qualitatively study the effect that different parameters can have on the friction torque. However, the fluctuations and the strong dependency of the final result on the mesh size show that the accuracy of the model is limited to a certain extent for the friction torque calculation.

Ball kinematics can be directly obtained from the model and show no fluctuations or dependence on the mesh size. For the particular case that is being studied, the results are represented in Figure 3.13. This plot has been directly obtained from the program, so no further post-process is required.

To obtain normal contact forces and angles, the process is not so straightforward. ANSYS® Workbench gives the forces for each contact (F_R and F_z in Figure 3.14), but does not distinguish between normal and tangential forces (Q and F_t). Thus, some calculations must be done. According to Figure 3.14, the contact angle can be calculated as follows:

$$\alpha = atan\left(\frac{F_z}{F_R}\right) - asin\left(\frac{F_t}{F}\right) \tag{3.10}$$

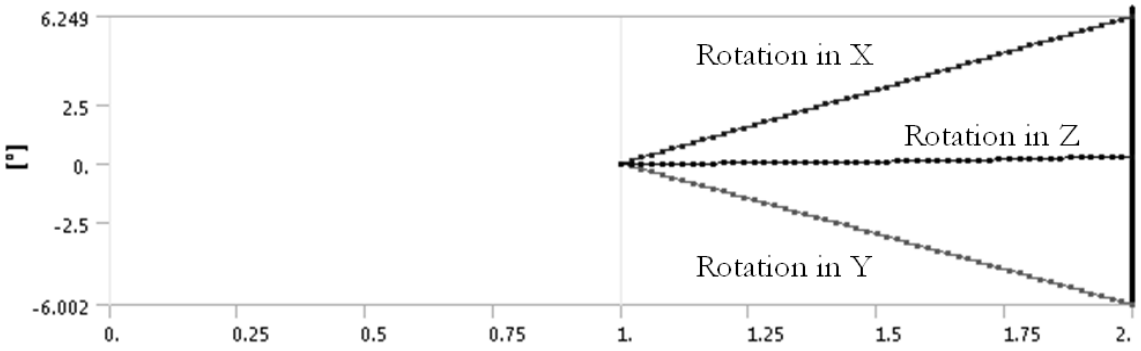

Figure 3.13. Results for ball kinematics.

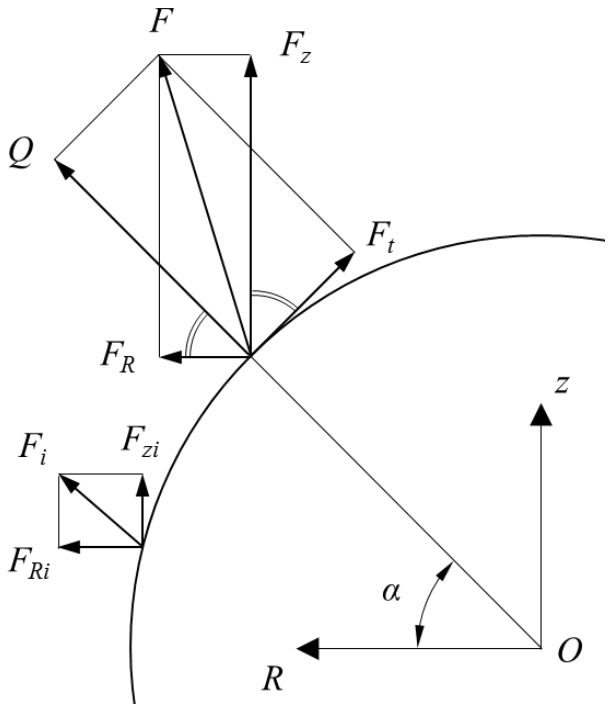

Figure 3.14. Forces in the contact.

F_R and F_z are the components of the total force F, which are known, and F_t is the tangential component of the resulting force, which is unknown. To calculate this component, the moment it generates with respect to the centre of the ball (point O, see Figure 3.14) is formulated, which will be equal to the summation of the moments generated by the contact force at each node:

$$M_O = \sum_i (-F_{Ri} z_i + F_{zi} R_i) \cong \frac{1}{2} D_w F_t \tag{3.11}$$

Where R_i and z_i are the coordinates of the node i from the centre of the ball (considering displacements and deformations) and F_{Ri} and F_{zi} are the components of the contact force. Therefore, the final contact angle can be calculated by the following expression, which is obtained from combining (3.10) and (3.11):

$$\alpha \cong atan\left(\frac{F_z}{F_R}\right) - asin\left(2\frac{\sum_i (-F_{Ri} z_i + F_{zi} R_i)}{F D_w}\right) \tag{3.12}$$

Note that calculations for contact forces and angles are done before rotating the inner ring, so the contact ellipse is centred in the Rz plane.

Contact pressure can be obtained in a direct way from the Workbench environment. The results can be compared with the pressure distribution

from the Hertz theory, confirming its suitability for these kinds of contacts. Figure 3.15 shows pressure results along the major semiaxis for the studied case. This plot shows that FE results are slightly higher than the values from the Hertz theory, as demonstrated by Pandiyarajan [29], but they are still very close. Once more, Houpert's approximation can used as well for analytical calculations [30], obtaining the next expression for the maximum pressure (P_{max}) for steel and high osculation ratios:

$$P_{max} = 1805(1-s)^{0.2117}\frac{Q^{1/3}}{D_w^{2/3}} \tag{3.13}$$

The most challenging post-processing task is to obtain shear stresses. The module can be easily plotted, but there is no option to plot the directions, neither in Workbench nor in the Classic environment. Through APDL commands, the components of the shear stress can be obtained, but in the element local coordinates. Thus, to obtain shear stresses in the same coordinate system, the following steps are carried out by a parametric APDL script for every contact element:

- Obtain shear stress components in the local coordinate system for each node (τ_{Ri} and τ_{Si}).
- Compute the element average value of each component (τ_R and τ_S).
- Obtain the coordinates of the three nodes that define the local coordinate system, in the global coordinate system.
- From the global coordinates of the nodes, calculate the components of the normalized vectors that define the local coordinate system, in the global coordinate system.

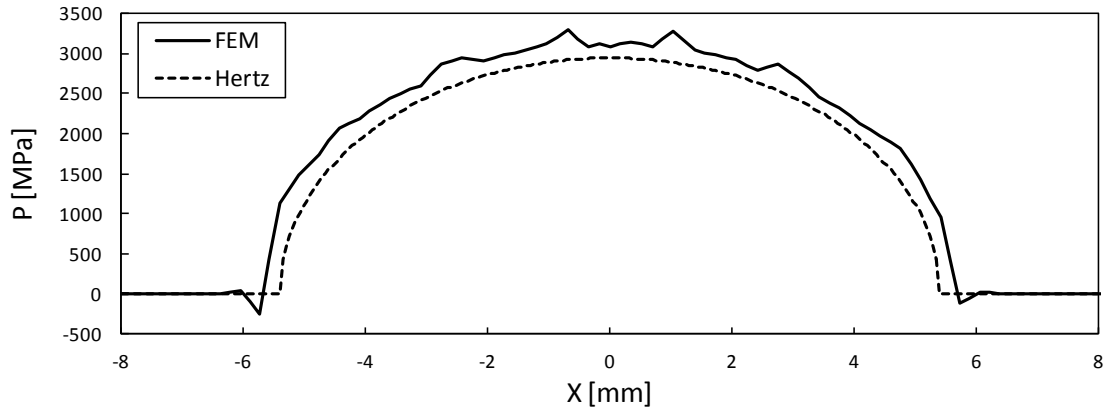

Figure 3.15. Contact pressure along the major semiaxis.

- Project each of the shear stress components in the local coordinate system (τ_R and τ_S), in the global coordinate system (τ_{Rx}, τ_{Ry}, τ_{Rz}, τ_{Sx}, τ_{Sy}, and τ_{Sz}).
- Compute the total value of the shear stress components in the global coordinate system (τ_x, τ_y and τ_z).

Once the shear stresses are obtained in the global coordinate system, they can be plotted in the Classic environment. Figure 3.16 shows the results for the resulting plots, which are not easily interpretable for the case of the vector field. For this reason, and to later compare the results in a more direct way with those obtained with the analytical model, shear stresses are exported to Matlab®. Ball kinematics are also exported to Matlab® so the shear stress field can be plotted as shown in Figure 3.17 after making the corresponding coordinate changes. The plots show the results in the contact ellipse projected in a plane (the ellipse is projected, not the value of the shear stress).

Together with the shear stress field, pressure and contact status are reported in Figure 3.17. Contact pressure is also exported to Matlab® for better representation of the results. The contact status can be directly obtained from the FE model and provide information about the extent to which full sliding friction is being contravened. Figure 3.17c shows an important stick region (in black), which is clearly affecting the shear stress field. From comparing shear stresses with contact pressure, it is evinced that the former are under the value that would be obtained by assuming full sliding. Therefore, further research in this topic is justified.

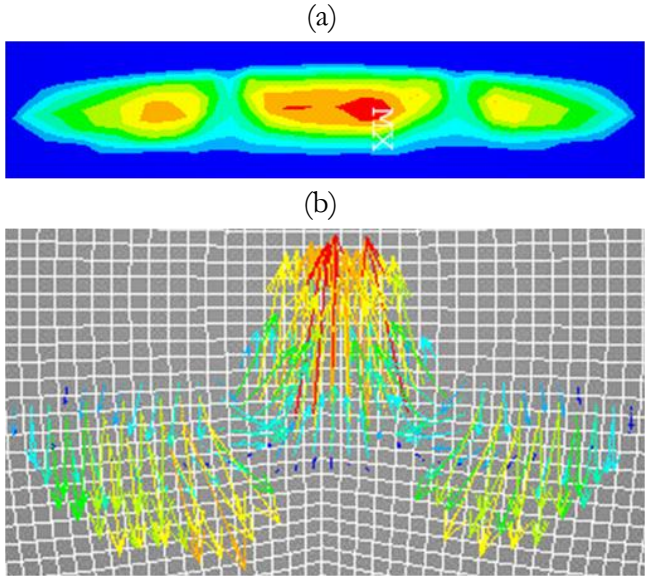

Figure 3.16. Shear stress plots in ANSYS®: (a) modulus; (b) vector field (raceway reactions).

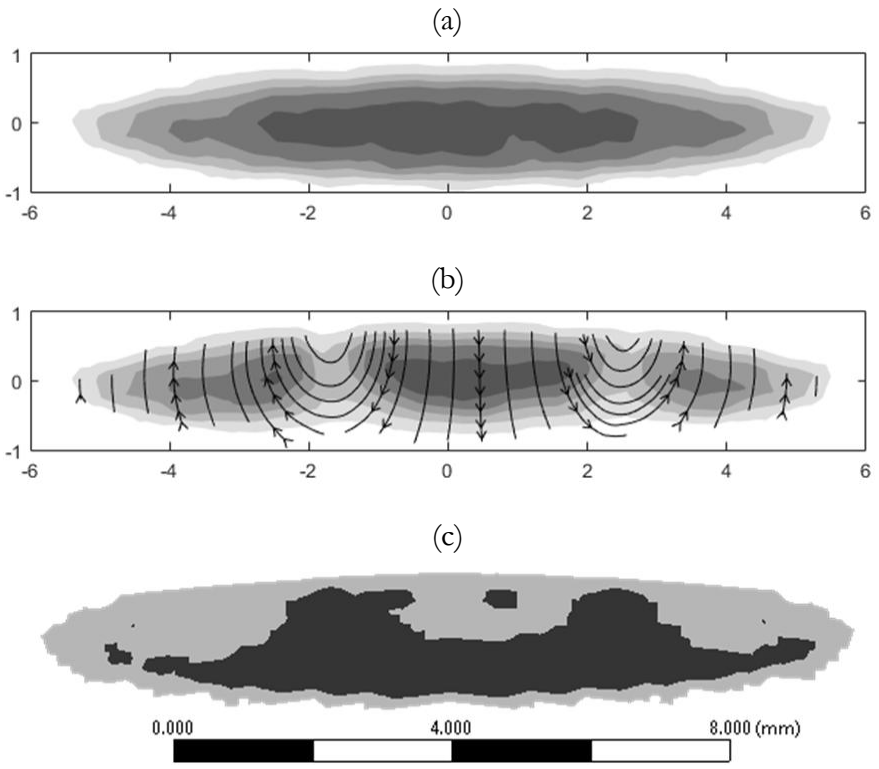

Figure 3.17. Contact results for the refined model: (a) pressure; (b) shear stress (ball reactions); (c) status.

3.2.2 Finite Element model with deformable rings

In order to allow rings deformations, two aspects of the previous model must be reconsidered: boundary conditions and geometry. On the one hand, for the case of rigid rings, no deformations were allowed to their external surfaces (thick lines in Figure 3.18a). On the other hand, with deformable rings, only the displacements in the normal direction of the lateral faces of the sector are restricted, allowing free sliding movement so that the rings can deform in the radial and axial directions (see Figure 3.18b). With these boundary conditions, an additional constraint must be imposed in order to avoid rigid body motion. For this purpose, the deformations of the nodes in the middle plane of the outer ring (parallel to the xy plane, see Figure 3.5) are restricted to this plane. Such constraints imply that rings can deform freely, replicating the conditions of an experimental idling friction torque measurement, for example. This measurement is done before assembling the bearing in the machine, so ring deformations are not restricted. Figure 3.19a shows how rings are deformed considering the described boundary conditions.

As the deformation of the system will depend on the deformability of the rings, their real geometry must be considered. Therefore, the so called

secondary parameters, namely inner diameter (D_i), outer diameter (D_o), clearance between rings (e), ring height (H) and span angle for the sector (Ψ) (Figure 3.5), will affect the results, and thus the real values must be adopted. Note that the sweep angle (Ψ) will be a function of the number of balls. Rolling bearings can be mounted with or without spacers, and the dimensions of these can be variable, so the number of balls can change, and consequently the value of the sweep angle. As will be demonstrated, this fact has a relevant effect on the behaviour of the bearing.

Slewing bearings require holes for the bolted joints, and usually have a gear either on the inner or outer ring. Nonetheless, they are demonstrated to have little effect on the ring stiffness, so they are neglected, as is done in the FE model for the calculation of the stiffness matrix (explained in the previous chapter). Figure 3.19b shows the FE model for the measured bearing, considering 32 balls. This bearing can harbour up to 67 balls without spacers, so the considered span angle is 2.1 times that in (3.1). Considering the real geometry of the rings, and especially increasing the span angle, involves a significant increment of the DoF, resulting in higher computational cost. The model in Figure 3.19b, for example, consists of nearly $2{\cdot}10^6$ DoF, twice the DoF of the reference model with rigid rings.

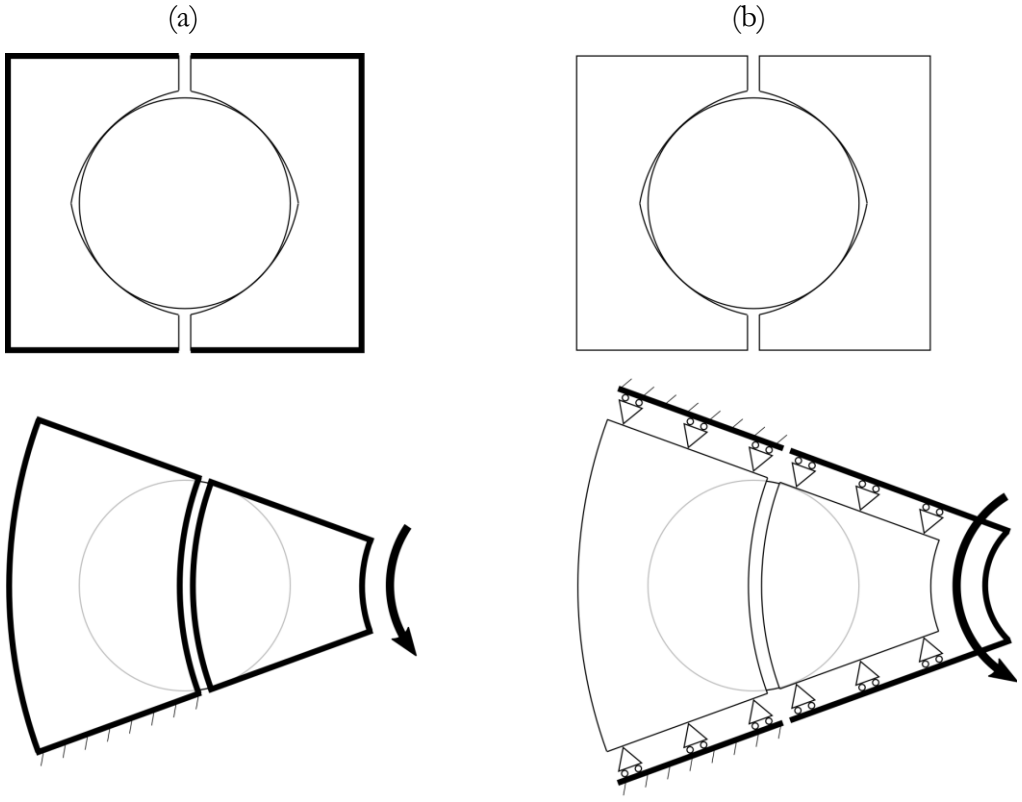

Figure 3.18. Boundary conditions of the FE model: (a) rigid rings; (b) flexible rings.

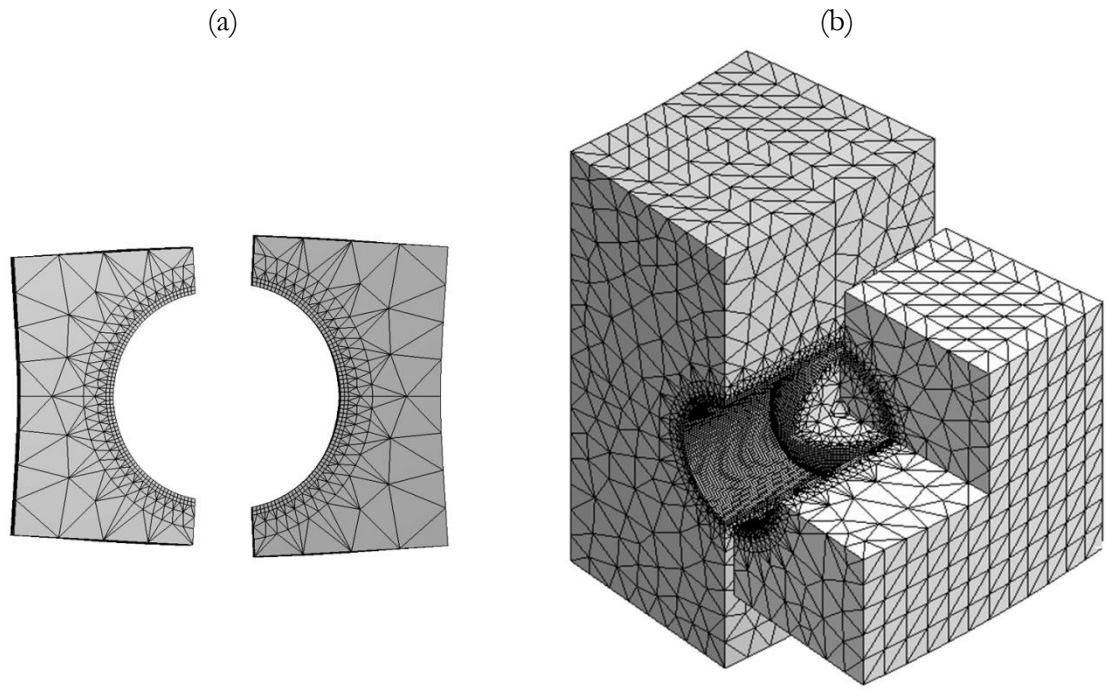

Figure 3.19. FE model for deformable rings: (a) deformed shape; (b) measured bearing.

3.2.3 Submodeling

The submodeling technique allows a detailed study of a localized region of a previously analyzed FE model [97]. This technique consists of taking the localized region to be studied apart, so it can be modelled with a finer mesh, and thus obtain more detailed and accurate results. This technique is based on Saint-Venant's Principle, which states that "[...] the difference between the effects of two different but statically equivalent loads becomes very small at sufficiently large distances from load" [100]. This implies that the displacements calculated in the original (or global) model can be imposed to the cut boundary of the submodel, where the cut boundary is formed by the areas through which the global model has been cut to obtain the geometry of the submodel. As long as the cut boundary is far enough from the studied region, the Saint-Venant's Principle will be applicable. Note that, since the mesh is not the same in the cut boundary for the global model and the submodel, the displacements from the global model must be interpolated to the nodes of the submodel.

In the sector model of the bearing, the submodeling technique is useful to study the contact region in more detail, so more accurate results can be obtained for the shear stress field and the contact status because the mesh of the submodel will be much finer. For the submodel, the superficial layer of the ball and the raceway corresponding to one contact are considered. Taking

advantage of the partitions of the geometry for the definition of the mesh, the ESIZE-1 region (Figure 3.6) corresponding to one contact is considered for the submodel. The ESIZE-1 is divided into different parts as well, so only those corresponding to one contact are selected. In Figure 3.20 the geometry and the cut boundary of the submodel (marked in black) is represented. Figure 3.21 shows the mesh of the submodel, where a progressive element size is used, thus achieving elements three times smaller than in the refined sector model in the vicinity of the contact region. The submodel has $4 \cdot 10^6$ DoF, and the computing time is around 30h.

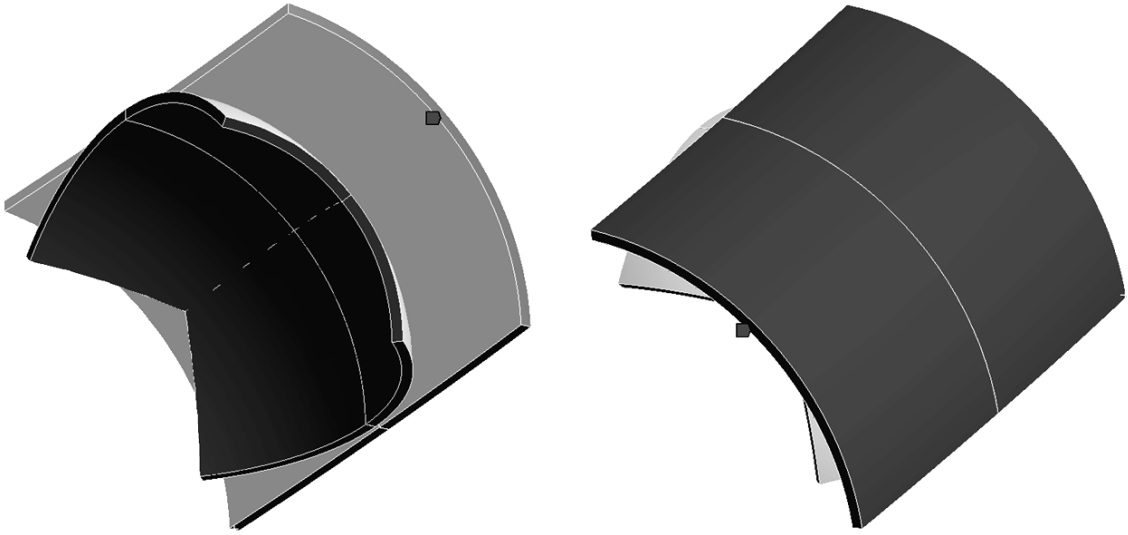

Figure 3.20. Cut boundary of the submodel.

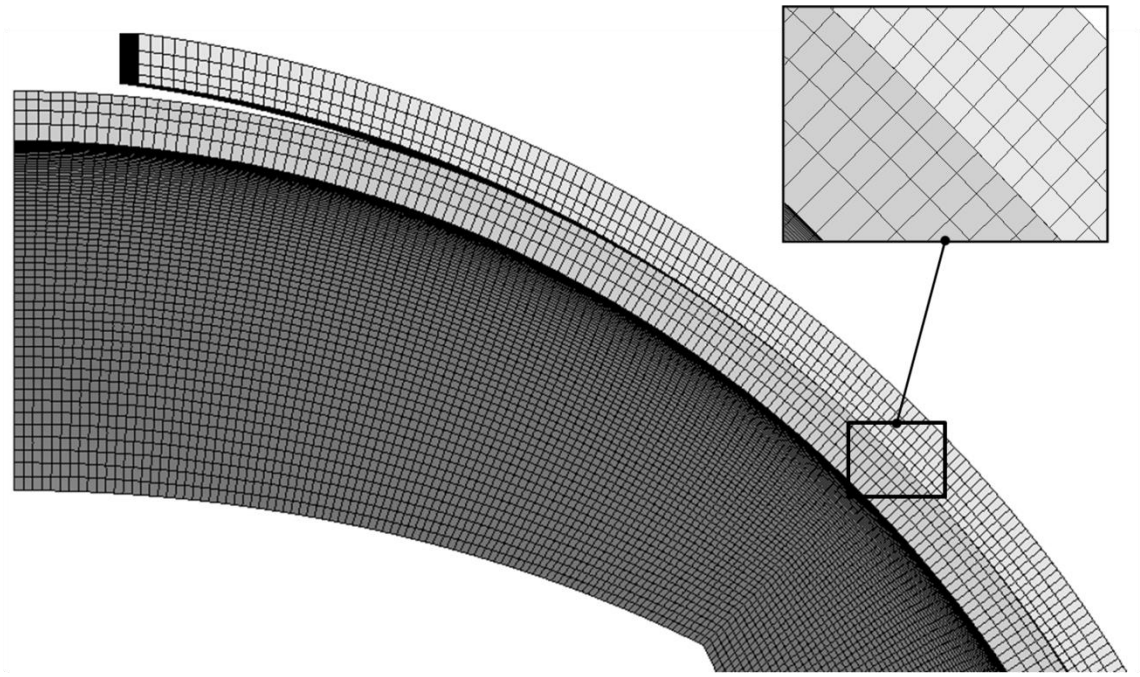

Figure 3.21. FE mesh of the submodel.

Shear stress and contact status results from the submodel are compared with those obtained from the refined model in Figure 3.22. Due to the finer discretization, the results from the submodel are more accurate than those from the global model. However, it can be used to analyse only particular cases because of its high computational cost. The submodel shows a more localized stick region, so the shear stress is affected to a lesser extent. Nevertheless, the stick region still represents an important area of the contact ellipse.

3.3 Effect of manufacturing errors, ring stiffness and ball number on the friction torque

The Rigid-BIME model was used in combination with the Rigid-FEM (1st way, according to Table 3.1) and the Flexible-FEM (2nd way) to evaluate the effect of manufacturing errors, ring stiffness and ball number on the idling friction torque (i.e. with no external loads). For this purpose, the bearing used in Chapter 2 to illustrate the relevance of manufacturing errors was employed. Because of the high number of simulations required, the FE model with the reference mesh was used.

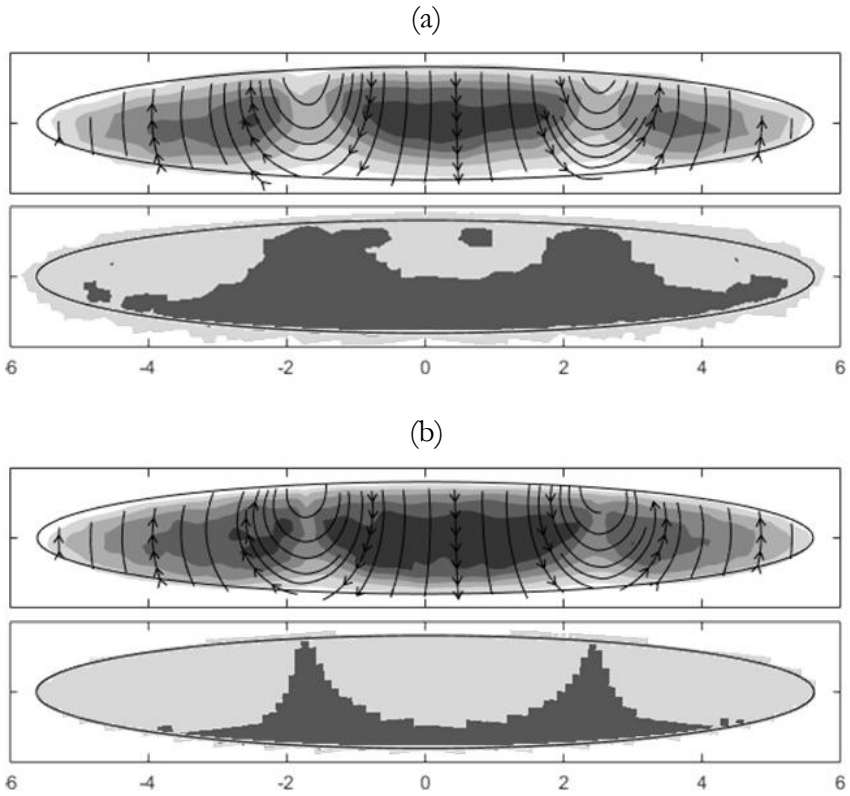

Figure 3.22. Shear stress and contact status: (a) global model; (b) submodel.

3.3.1 Functional approximation for the friction torque calculation

In order to calculate the friction torque for the whole bearing, as many calculations as balls inside the bearing are needed, introducing to each one its corresponding interference values. Since no external loads are considered, these interferences will be due to the manufacturing errors and the ball preload. For simplification purposes and to avoid high computational costs, a Design Of Experiments (DOE) was planned considering the three parameters related to the tolerances: the interferences in each contact pair (δ_1 and δ_2) and the osculation ratio (s). Note that, since manufacturing errors are being considered, the osculation ratio can change. Taking peak and valley values for the three parameters, a full factorial DOE was performed. For the osculation ratio, three levels were considered, 0.93, 0.94 and 0.95, based on the raceway radius obtained from the measurements. For the interferences, four levels were considered, with values up to 65μm. Based on Hertz's theory [17] and Houpert's formulation [30], the following functional approximation is proposed for the friction torque:

$$M_f = \begin{cases} \dfrac{C_1(\delta_1^n + \delta_2^n) + C_2(\delta_1+\delta_2)^n}{(1-s)^m} & \text{if} \quad \delta_1 \cdot \delta_2 \neq 0 \\ 0 & \text{if} \quad \delta_1 \cdot \delta_2 = 0 \end{cases} \tag{3.14}$$

The values for the coefficients are different if the ball is spinning on all contacts or if it is rolling with respect to two points and sliding with respect to the other two. To better identify the point at which this transition happens, some extra calculations were required for intermediate values of the inferences. In the cases under study, only preload (and no external load) is considered, so no case will exist with a big interference in one contact diagonal and no contact in the other. Consequently, if contact exists only at two points ($\delta_1 \cdot \delta_2 = 0$), the interference will be the order of few microns, and the friction torque will be therefore negligible. To know if a ball is spinning or rolling, the interference ratio (r_δ) is defined, which relates both interferences in each ball:

$$r_\delta = \frac{max\ (\delta_1, \delta_2)}{min\ (\delta_1, \delta_2)} \tag{3.15}$$

If this ratio is lower than the transition value (r_δ^{tr}), the ball will be spinning; if not, the ball will be rolling. The values for r_δ^{tr} were determined based on the results from the FE calculations. Table 3.3 compiles the values for the

coefficients from equation (3.14), which were obtained by the least squares fitting with the points from the DOE. Using the values of Table 3.3 and introducing δ in [mm] in (3.14), M_f is obtained in [N·m]. For the model with deformable rings, 32 balls were considered; this aspect is important because the sweep angle (Ψ) affects the response of the sector, as previously mentioned. Note that this approximation is only valid for the idling friction torque calculation of the particular bearing that is being analysed, for interferences up to 65μm and osculation ratios between 0.93 and 0.95.

Ring behaviour	r_δ^{tr}	4 points spinning				2 points rolling + 2 sliding			
		n	m	C_1	C_2	n	m	C_1	C_2
Rigid rings	7.5	2.09	0.85	531	28.2	2.09	0.85	-1344	1376
Flexible (32 balls)	3.5	1.81	0.75	291	-84	8.93	1.87	0	$3.08 \cdot 10^7$

Table 3.3. Values for the functional approximation (3.14) for the friction torque calculation.

Figure 3.23 compares the results from the 52 FE calculations of the DOE (markers) with the functional approximation (3.14) for the case with deformable rings (lines), illustrating the excellent correlation between them (similar correlation appears for the rigid ring case). Several detailed views of two regions of the plot are also shown for clarity. The jump discontinuity in the curves represents the transition related to the kinematic of the ball, from rolling ($r_\delta > r_\delta^{tr}$) to spinning ($r_\delta < r_\delta^{tr}$).

Finally, the proposed formula (3.14) was used to calculate the friction torque due to each ball, so the total torque can be calculated as the sum of all the balls in the bearing. The results are shown in the next section.

3.3.2 Effect of manufacturing errors and ring stiffness

The Rigid-BIME was used to obtain the interference values for the case of nominal ball (Figure 2.6a) and balls with 10 different preloads, ranging from -15μm to +30μm. The latter represents 13% of the static load capacity, which is a high preload value. By feeding (3.14) the interference values from the Rigid-BIME and using the coefficients in Table 3.3, the contribution of each ball to the friction torque was obtained for both rigid rings (1st way in Table 2.1) and deformable rings (2nd way).

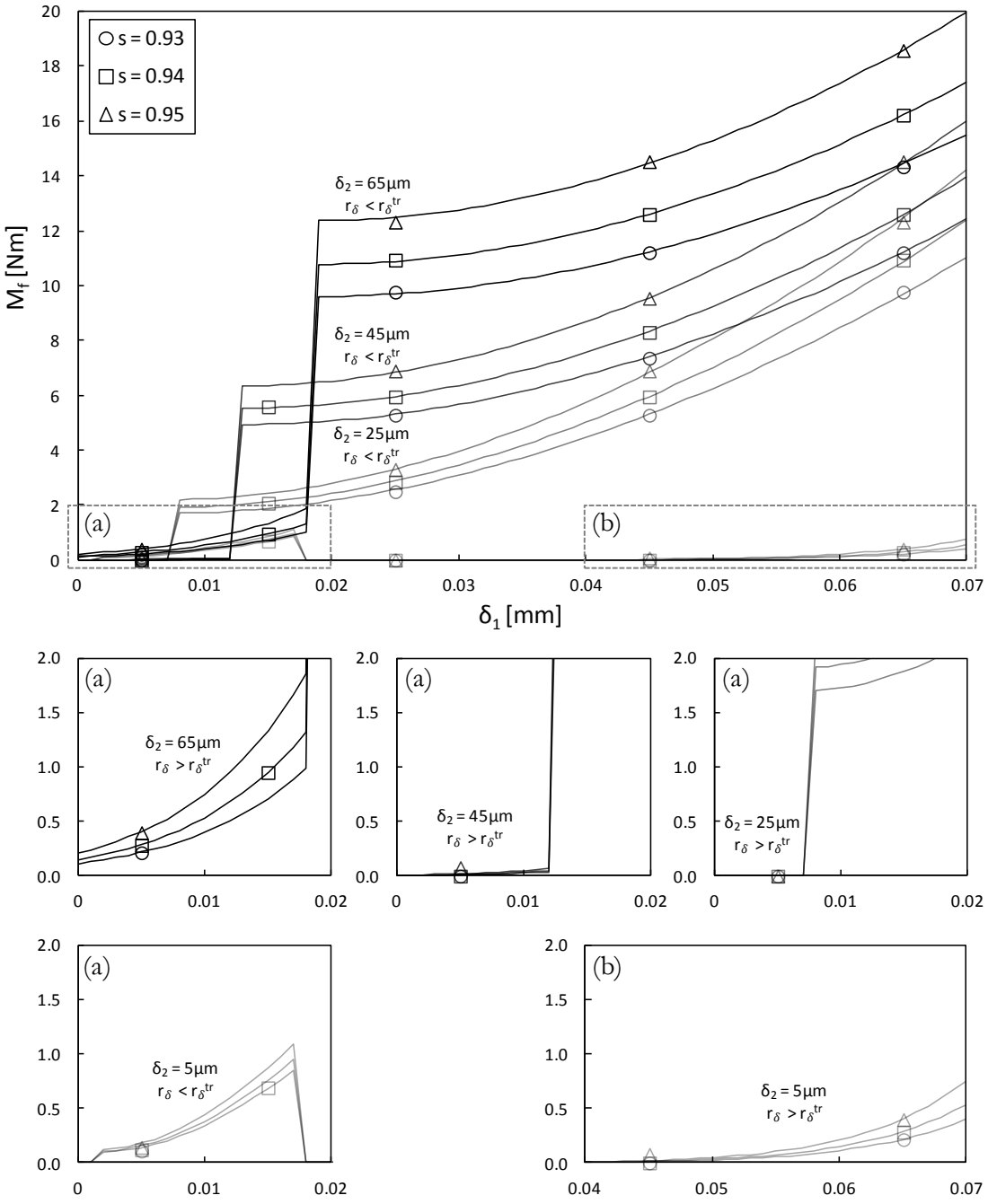

Figure 3.23. Friction torque results for the DOE (markers) and calculated functional approximation (lines) for deformable rings.

For the sake of completeness of the work, two additional aspects were considered when calculating the interferences: the relative angular position between the rings, i.e. the rotation of the inner ring in the *z* axis, and the manufacturing tolerances of the balls (not to be confused with the manufacturing errors of the raceways). The ball quality used in this bearing was grade 40, which implied a variation of 2μm in the ball diameter from the same lot [101] (this information was provided by the ball manufacturer). The

results for the total torque of the bearing, with the scatter due to these two factors, are given in Figure 3.24 for rigid and deformable rings. It is worth pointing out that the influence of the relative angular position between the rings was demonstrated residual, and consequently ball tolerances are responsible for the dispersion observed in the plots.

In order to evaluate the effect of manufacturing errors in the friction torque, FE calculations were also performed with the nominal geometry, i.e. with no manufacturing errors, for every preload case; these results are also shown in Figure 3.24. It can be observed that the effect of manufacturing errors has a great influence on the friction torque, ergo they must be considered when accurate results are required. Moreover, the high relevance of the deformability of the rings on the friction torque is also evinced. To quantify these effects, the results are compared in Table 3.4 for three preload levels. Looking at the influence of manufacturing errors, the differences are proportionally very big for small preloads, while the total discrepancy grows with the preload. Therefore, establishing a unique value to quantify the effect is not possible, although it is clear that they can largely influence the idling friction torque. The table also shows that the effect is proportionally very similar for rigid and flexible rings. On the other hand, the results for rigid and flexible rings are compared, using the values obtained for the nominal geometry (with no manufacturing errors). In this comparison, not only the total but also the relative discrepancy grows with the preload level. For the preload of 25μm (11% of the static capacity), the results for rigid rings are more than twice those for the flexible rings.

δ_P		**Effect on the idling friction torque (ΔM_f)**					
		Manufacturing errors				**Ring stiffness**	
		Rigid rings		Flexible rings			
[μm]	[%]*	[N·m]	[%]	[N·m]	[%]	[N·m]	[%]
5	2%	20.95	340%	13.60	321%	1.93	46%
15	7%	44.09	67%	22.93	62%	29.10	79%
25	11%	61.63	32%	28.76	30%	99.23	105%

* Percentage over the static load capacity.

Table 3.4. Effect of manufacturing errors and ring stiffness in the idling friction torque of the measured bearing.

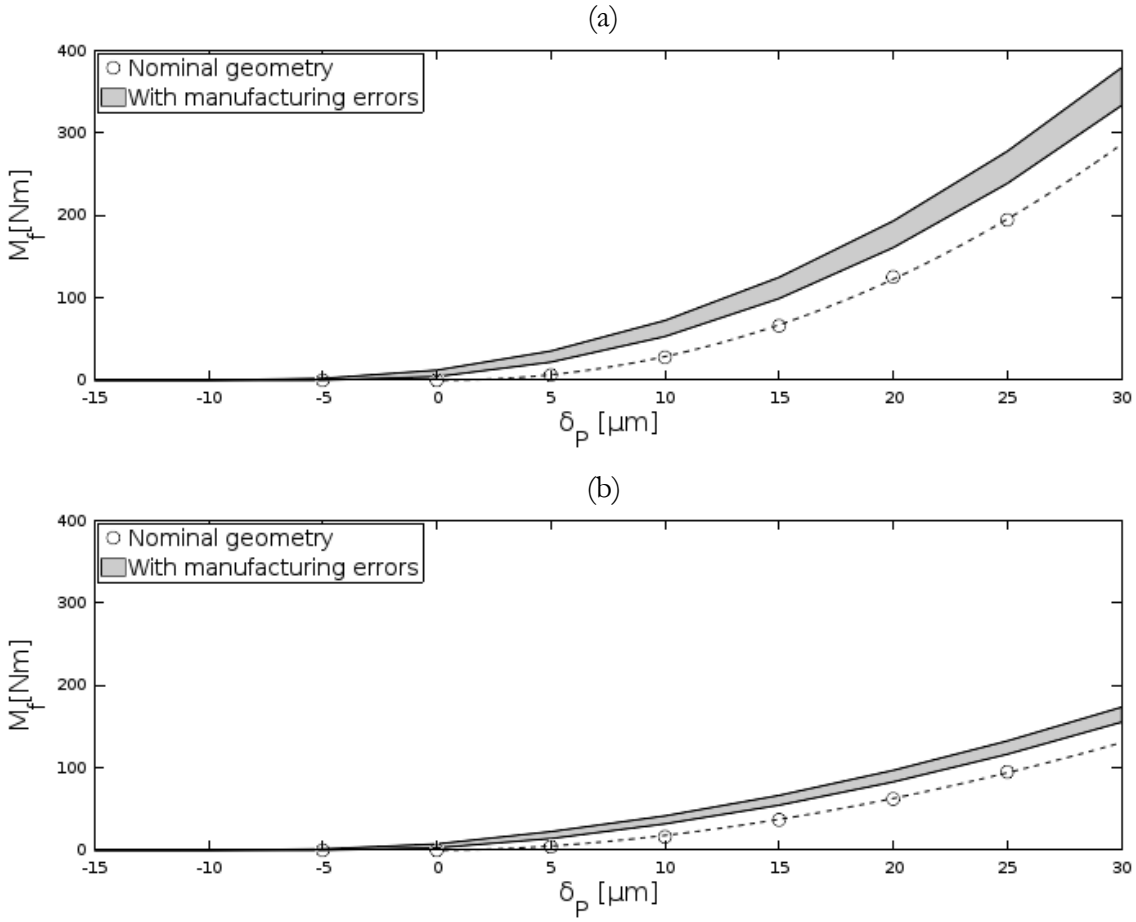

Figure 3.24. Friction torque VS Ball preload with (band) and without (dotted line) the effect of manufacturing errors: (a) rigid rings; (b) deformable rings.

3.3.3 Effect of ball number

Additionally, the effect of the number of balls on the friction torque was studied. For this purpose, and without taking into account manufacturing errors, FE calculations with deformable rings were performed, varying ball number (4 levels) and preload (5 levels). It was found that the effect of the number of balls is logarithmical, and the next functional expression proved to properly fit FE results:

$$M_f = C{\delta_P}^n \cdot ln\left(\frac{N}{N_r} + 1\right) \tag{3.16}$$

Where δ_P is the preload, N is the number of balls and n, C and N_r are coefficients to be determined for each bearing. For this particular case, the values of the coefficients that best fit the FE calculations are 1.84, 0.15 and 8 respectively, so M_f will be obtained in [N·m] if δ_P is introduced in [µm]. Thus, for the measured bearing the formula will be:

$$M_f = 0.15{\delta_P}^{1.84} \cdot ln\left(\frac{N}{8}+1\right) \tag{3.17}$$

Figure 3.25 shows the results from the FE calculations (markers) and the functional approximation in (3.17) (solid lines). Furthermore, the results for rigid rings are shown for one preload case (25μm, dotted line), illustrating that if the elasticity of the rings is not considered, the influence of the ball number is linear.

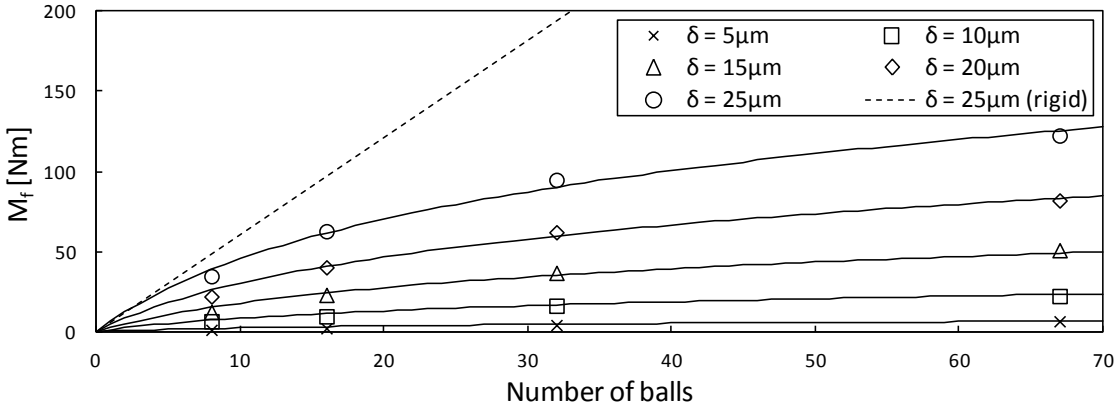

Figure 3.25. Influence of the number of balls on the friction torque.

3.4 Improvement of the BIME-FEM methodology

In the previous section, the Rigid-BIME model has been used to feed both Rigid-FEM and Flexible-FEM models, which represent the proposed 1st and 2nd ways to calculate the friction torque, according to Table 3.1. In this section, an alternative procedure to the 2nd way is presented, which also allows ring flexibility to be considered. This procedure, which is called the 3rd way, offers important advantages both in terms of accuracy and computational cost. The basis of this procedure lies in considering the ring elasticity in the BIME model instead of in the FE model. As will be reasoned and demonstrated in this section, the 2nd and 3rd ways are equivalent. However, the lower computational cost of the 3rd way allows using a much finer mesh in the FE models, which leads to more accurate results.

Apart from the advantages of the 3rd way over the 2nd, demonstrating that they offer the same results (when the same mesh is used in the FE models) allows the validation of the Flexible-BIME. This validation is required in order to later develop the 4th way. The 4th way substitutes the FE model by an analytical model, but this analytical model requires real contact forces and angles, having considered ring deformations for their calculation. This means

that the Flexible-BIME is required for the 4th way. Therefore, the validation of the Flexible-BIME is necessary to ensure that the analytical model for the friction torque calculation will be fed by reliable contact forces and angles.

3.4.1 An alternative model for the friction torque calculation

First of all, let us go over the 2nd way. The ball-raceway interferences calculated by the Rigid-BIME model are the interferences that would exist if the rings were infinitely rigid. Therefore, these interferences are the geometrical interferences, which are larger than the real ones. Up to this point, no ring flexibility is considered. Then, these geometrical interferences are introduced in the Flexible-FEM in a first load step, where the rings are deformed and the real interferences are reached. Then, once the real interferences are achieved, the inner ring is rotated in a second step to calculate the friction torque.

Let us now consider the inverse procedure. If the Flexible-BIME model is used in the first place, the calculated interferences will be directly the real ones, smaller than the geometrical interferences. These interferences must be the same as those obtained in the 2nd way after applying the fist load step to the FE model. Thus, these interferences can be introduced in the Rigid-FEM in the first step of the analysis. As ring deformations are not allowed in this FE model, the interferences after the first load step will be the same as those calculated with the Flexible-BIME, and therefore the same as those obtained in the 2nd way after ring deformations. Consequently, the interferences in the 2nd and 3rd ways will be the same before rotating the inner ring. In the second step, the rotation is applied, and since the interferences are the same, so will the friction torque.

In order to obtain the same results as in the previous section, the same mesh must be used. In the FE model for the friction torque calculation, the mesh that determines ring global deformations is the one at ESIZE-3 (Figure 3.6). Therefore, the mesh from ESIZE-3 is replicated in the FE model for the calculation of stiffness matrices of the rings. Figure 3.26 compares the mesh of the FE model for the friction torque calculation (Figure 3.26a) with that of the FE model for the stiffness matrices calculation (Figure 3.26b). Apart from the refinement at the raceways, which should not affect global deformations, the mesh is very similar.

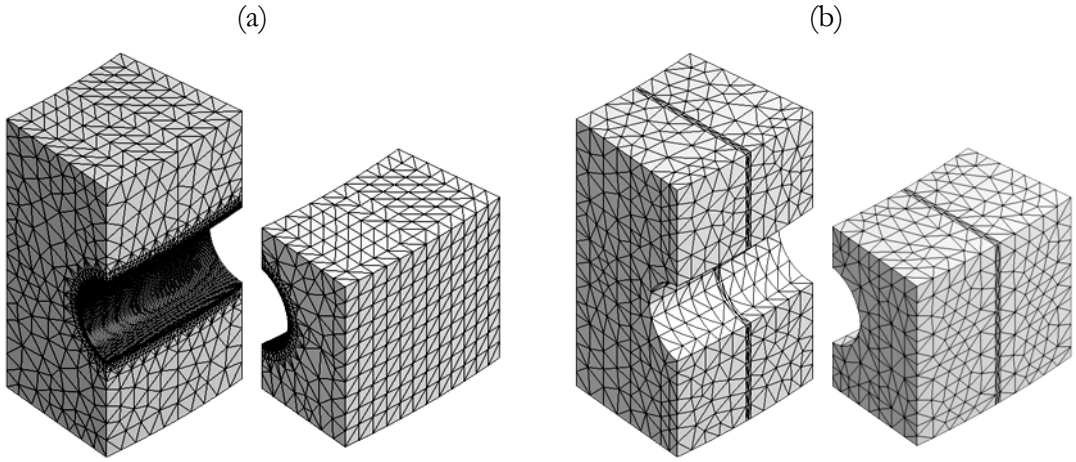

Figure 3.26. Ring mesh in different models: (a) for the friction torque calculation; (b) for the stiffness matrix calculation (only a sector is represented).

Another relevant aspect to be considered is boundary conditions. The conditions imposed on the Flexible-FEM imply assuming that every ball in the bearing is experiencing the same interferences. In other words, imposed boundary conditions simulate cyclic symmetry, so the calculated friction torque is the contribution of one ball to the total friction torque in a bearing where every ball is under the same interferences. This fact is addressed later in section 3.4.3 and demonstrated to have no effect.

The calculations for the stiffness matrices required for the 3rd way were therefore performed using the mesh in Figure 3.26b, and the results are shown in Figure 3.27. In the figure, the results from the 2nd way are also presented, so a direct comparison is allowed. Through this comparison, it is demonstrated that both ways offer very similar results. Moreover, the little differences can be due to the mesh, which is not exactly the same in both cases. As demonstrated in the following section, the mesh has a great effect on the results, so the little discrepancies of the results from both ways are justified.

3.4.2 Improvement in the accuracy

The first advantage of the 3rd way over the 2nd is that it allows a finer mesh for the simulation of the flexibility of the rings. The FE model for the friction torque calculation requires a very fine mesh at the contact, so a coarse mesh is used in the rest of the model in order to achieve reasonable computational costs. Moreover, several simulations are needed with the Flexible-FEM model for each bearing in order to obtain the coefficients of the formula (3.14). On the other hand, only one analysis is required to obtain the stiffness matrices for each bearing in the 3rd way, and no mesh refinement is needed.

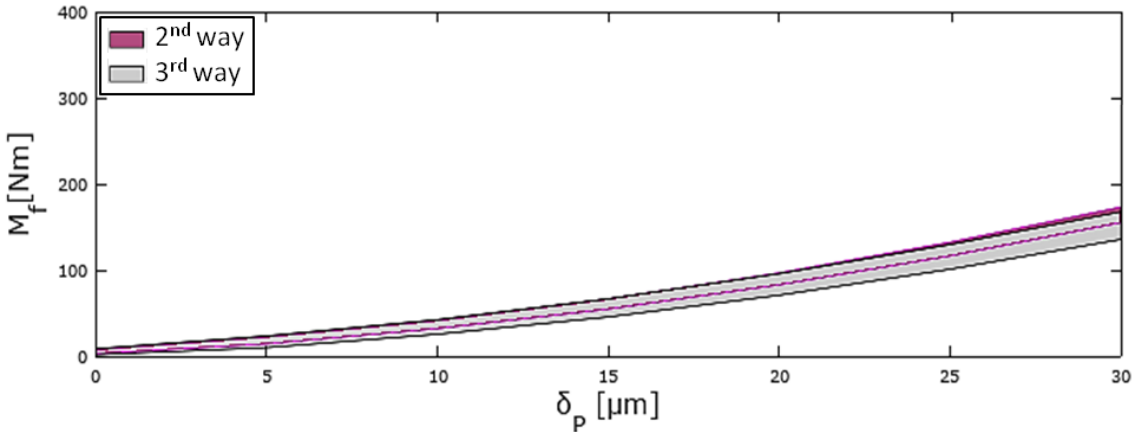

Figure 3.27. Friction torque VS Ball preload for deformable rings: comparison between the 2nd and the 3rd ways.

A sensitivity analysis was performed to evaluate the influence of the mesh size on the results. The resulting mesh is shown in Figure 3.28, the results of which are shown in Figure 3.29 and contrasted with those from the 2nd way. From the comparison, the effect of the mesh size is demonstrated to be very large. Therefore, the effect of the ring stiffness on the idling friction torque is even greater than that observed with 3.3.2.

3.4.3 Improvement in the computer time

The other advantage of the 3rd way is the computational cost savings. For reference, Table 3.5 shows the computational cost of one calculation for each model used for the performed analyses in the 2nd and 3rd ways (they can change for a different bearing). On the one hand, the 2nd way requires a new DOE when any parameter is changed. This DOE, performed with the Flexible-FEM, will last around a month (without parallelizing calculations) for a bearing like the one that is being studied. On the other hand, the 3rd way only requires a new DOE when contact parameters change. For example, the coefficients of Table 3.3 for rigid rings are valid for any bearing with a 25mm ball, a mean diameter of 541mm, an initial contact angle of 45° and osculation ratios between 0.93 and 0.95. Therefore, they are still valid for different values of inner or outer diameters or ring heights, for example. Contrarily, the coefficients for flexible rings are valid only for the specific geometry of this bearing. Moreover, the Rigid-FEM has lower computational cost, so a DOE will last around 10 days, which is three times less than the time required for flexible rings. In return, the Flexible-BIME requires more time than the Rigid-BIME. Nonetheless, the additional computational cost is widely compensated by the cost saving of the FE model.

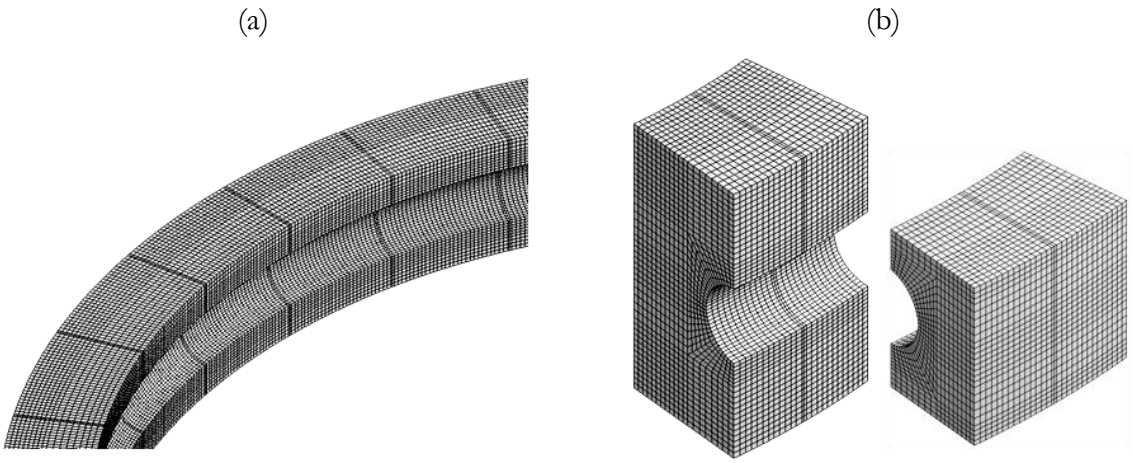

Figure 3.28. Final model for the stiffness matrix calculation: (a) global view; (b) sector corresponding to one ball (32 balls).

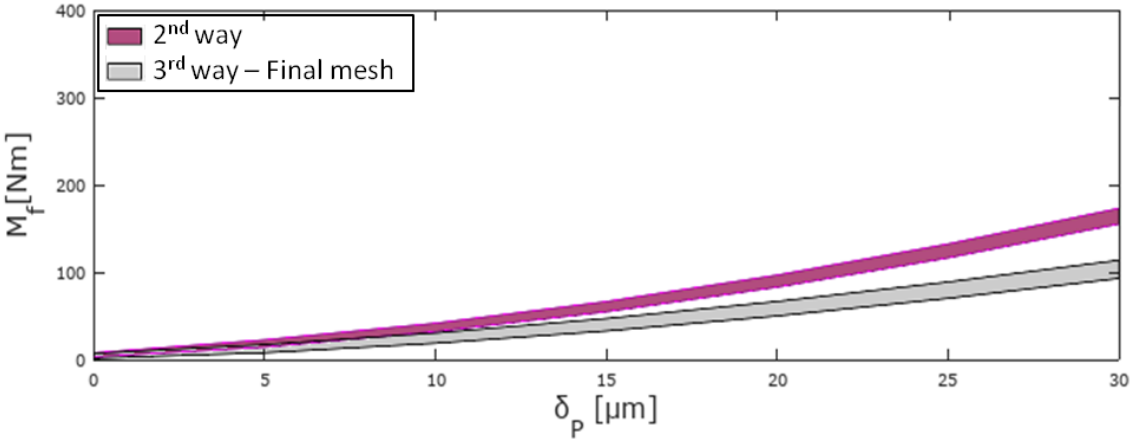

Figure 3.29. Friction torque VS Ball preload for deformable rings: comparison between the 2nd way and the 3rd way with the final mesh.

Model	Rings behaviour	Global/Sector	Computational cost
BIME	Rigid	Global	10s
	Flexible	Global	10min with sparse matrix 2min with band matrix
FE-Torque Reference mesh	Rigid	Sector	2-8h
	Flexible	Sector	5-20h
FE-Superelement Coarse mesh	Flexible	Global	20min
	Flexible	Sector	10s
FE-Superelement Final mesh	Flexible	Global	17h
	Flexible	Sector	5min

Table 3.5. Computational costs of the analyses for the different models required in the BIME-FEM procedure.

The cost of the stiffness matrices calculation must be also considered. The Flexible-BIME requires these matrices, which involve one extra calculation per ring for each new bearing. The cost of these analyses using the mesh in Figure 3.1 is 17h for each ring. Although this cost is still widely compensated by the cost saving of the friction torque simulations, a much faster model is proposed for the stiffness matrices calculation. Instead of considering the whole ring for the FE condensation, only the sector corresponding to one ball can be considered instead. By imposing the same boundary conditions as those in the Flexible-FEM, it is demonstrated that contact interferences and friction torque results are the same. By using the sector model for the stiffness matrices calculation, the computational cost for each ring dropped from 17h to 5 minutes, which is a negligible cost in comparison with the time required by each FE analysis for the torque calculation. By the way, this demonstrates that the boundary conditions used in the Flexible-FEM model are not a cause of error.

The stiffness matrices obtained from the sector model must be expanded for the entire bearing. As a result, band matrices are obtained. The calculations with the Flexible-BIME model using the band matrices are 5 times faster than with the sparse matrices obtained from the global model, as reflected in the table.

As a conclusion, the 3rd way requires much less computer time than the 2nd way and reports more accurate results due to the possibility to use a much finer mesh in the FE simulations. Depending on the number of calculations and the parameters to be considered, the cost savings will be higher or lower. Nevertheless, as it is always faster and more accurate, the 3rd way will be always preferred over the 2nd. In the following chapter, the analytical model for the tangential problem solution is presented, which finally leads to the 4th way.

4 Friction analysis model

4.1 Introduction

The FE models developed in Chapter 3 have been proved as a useful tool to adequately simulate the contact behaviour and calculate the friction torque. Nonetheless, these models show two main drawbacks: the high computational cost and the dependency of the results on the mesh size. The high computational cost limits the number of calculations that can be performed, which is a shortcoming for the design process. Optimization procedures usually require a large number of calculations, so a computationally expensive model means large calculation times or performing fewer analyses than required.

On the other hand, the dependency of the results on the mesh size compromises the accuracy of the results. FE models have been proved useful for comparative purposes. By using the same model, the effect of different parameters or conditions on the results can be evaluated. Nevertheless, the accuracy of the results for each particular case has certain limitations. Moreover, the shape of the mesh can also affect the results. Thus, models built by different analysts can offer certain discrepancies in the results. This makes unfeasible the comparison between results obtained from different FE models.

In this chapter, an analytical approach is proposed for the study of the contact and the calculation of the friction torque. The main goal of this analytical model is to address the above mentioned limitations. An analytical approach will undoubtedly entail a drastic decrease of the computational cost. Moreover, such a formulation would allow the same results to be obtained whoever performs the calculations, making them comparable with each other. For future reference, the model proposed in this section is called FRANC (FRiction ANalysis of the Contact) due to its capability to simulate the frictional behaviour of the contact.

As in the FE models, the inputs of the FRANC model will be contact forces (or interferences) and angles. Therefore, the FRANC model can directly substitute the FE model in the previously proposed BIME-FEM procedure (1st, 2nd and 3rd ways in Table 3.1), leading to the BIME-FRANC procedure (the 4th way), based exclusively on analytical approaches. The outputs of the new model will be the friction torque, contact results (pressure, shear stress and contact status) and ball kinematics, as in the FE models.

As explained in Chapter 1, Leblanc and Nelias proposed an analytical model to solve the internal kinematics in four-point contact ball bearings [56,57], a formulation which was simplified by Joshi et al. for slow speed applications [59]. Joshi et al. take advantage of the model to formulate the friction torque once the solution is found. Nonetheless, this analytical approach assumes that full sliding occurs in the ball-raceway contact. As demonstrated through the FE model, important stick regions appear when the ball is rolling at low speed, contravening this assumption. Therefore, further research is justified in order to study the limitations of this formulation and eventually propose a new approach, the FRANC model, which will be capable of considering stick regions.

The proposed analytical approach is based on the formulation of the kinematics done by Leblanc and Nelias [56,57]. Then, for the shear stress calculation, Kalker's formulations are implemented [68]. Kalker's developments are focused on the wheel-rail contact, where they have been widely used up to date. Nevertheless, they have not been applied to the study of the contacts in bearings. In this chapter, the suitability of Kalker's formulations for their application at the ball-raceway contact is studied, and the results are compared with those from the state of the art analytical models and FE calculations. By this comparison, the capabilities and limitations of both analytical approaches are determined. Finally, a procedure is proposed for the friction torque calculation, which takes advantage of the developed analytical models.

4.2 Analytical model for the friction analysis. The FRANC model

In this section, the FRANC model is presented. In a first step the kinematics are formulated. This approach is analogous to the one proposed by Leblanc and Nélias, since the kinematics formulation will be the same

whatever the assumption for the contact behaviour is. Then, a simplified approach is proposed for the kinematics, which will be useful to favour the convergence of the solution. After that, Kalker's simplified theory of contact is briefly presented and implemented in the FRANC model. This theory is what allows the new approach considering stick regions. Finally, the resulting forces are calculated and the equilibrium conditions are imposed, allowing the solution of the problem and the computation of the friction torque. For the latter, a different formulation to that used by Joshi et al. [59] is proposed.

4.2.1 Kinematics

For the analytical approach to the problem, the first step is to formulate the kinematics. The formulation presented is similar to the one developed by Leblanc and Nélias in [56], although a slightly different nomenclature is used. The global coordinate system used for the current formulas is the one used for the BIME (see Figure 2.5a), which also differs from the one adopted by Leblanc and Nélias. For the kinematical approach, only normal deformations are considered, while tangential micro-deformations are ignored. According to Kalker, and as later explained, the velocity field formulated in this way is called local rigid slip.

The approach is outlined for the contact point P_1 (see Figure 2.4), and then the formulation is given for the other points. According to Hertz theory [17], the contact radius after deformation is given by:

$$R'_{C1} = \frac{D_w}{1 - s_1} \tag{4.1}$$

Where D_w is the ball diameter and s_1 the osculation ratio of the contact point P_1. Figure 4.1 shows the geometry of the deformed contact. In this figure, the X_1Y_1 local coordinate system is defined, normal to the contact force. The X_1 axis is coincident with the major semiaxis, so the Y_1 axis is coincident with the minor semiaxis. According to Figure 4.1, the distance normal to this plane from a general (X_1Y_1) point of the contact ellipse to the centre of the ball can be calculated by the following formula:

$$r_1(X_1) = \sqrt{(R'_{C1})^2 - X_1^2} - \sqrt{(R'_{C1})^2 - a_1^2} + \sqrt{\left(\frac{D_w}{2}\right)^2 - a_1^2} \tag{4.2}$$

In Figure 4.2, the involved velocities are represented, which are the angular velocity of the ball (ω_B) and the angular velocity of the outer ring (ω_o). The direction of ω_B is defined by the β angle, which is inside the plane Rz because slow speeds are being considered. For the approach, the centre of the ball is assumed fixed. This way, the velocity in the Y_1 direction of the outer ring (o) and the ball (B) in a general (X_1, Y_1) point of the contact area can be calculated as follows:

$$V_{Y1}^{o}(X_1) = -\left(\frac{D_{pw}}{2cos\alpha_1} + r_1\right)\omega_o cos\alpha_1 + X_1\omega_o sin\alpha_1$$
$$V_{Y1}^{B}(X_1) = -r_1(\omega_z cos\alpha_1 - \omega_R sin\alpha_1) + X_1(\omega_z sin\alpha_1 + \omega_R cos\alpha_1) \quad (4.3)$$

And for the X_1 direction:

$$V_{X1}^{o}(Y_1) = -Y_1\omega_o sin\alpha_1$$
$$V_{X1}^{B}(Y_1) = -Y_1(\omega_z sin\alpha_1 + \omega_R cos\alpha_1) \quad (4.4)$$

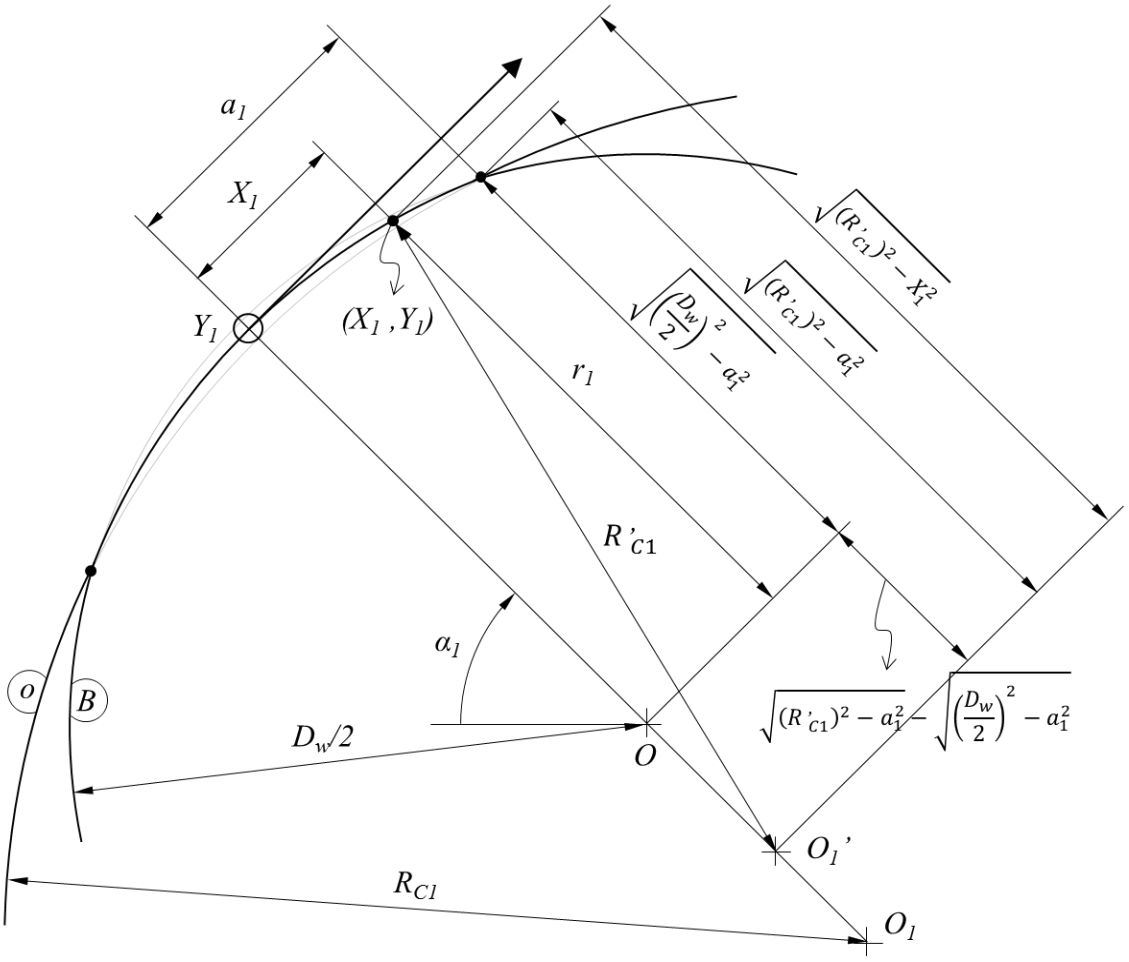

Figure 4.1. Geometry of the deformed contact.

Therefore, the relative velocity at any point of the contact ellipse will be:

$$\begin{aligned} V_{Y1}(X_1) &= V_{Y1}^{o} - V_{Y1}^{B} \\ &= -\frac{D_{pw}\omega_o}{2} \\ &+ r_1(-\omega_o cos\alpha_1 + \omega_z cos\alpha_1 - \omega_R sin\alpha_1) \\ &+ X_1(\omega_o sin\alpha_1 - \omega_z sin\alpha_1 - \omega_R cos\alpha_1) \\ V_{X1}(Y_1) &= V_{X1}^{o} - V_{X1}^{B} = -Y_1(\omega_o sin\alpha_1 - \omega_z sin\alpha_1 - \omega_R cos\alpha_1) \end{aligned} \tag{4.5}$$

If we separate rolling and spinning components as follows:

$$\begin{aligned} V_{Y1}(X_1) &= V_{Y1}^{R}(X_1) + X_1\omega_1^S \\ V_{X1}(Y_1) &= V_{X1}^{R} - Y_1\omega_1^S \end{aligned} \tag{4.6}$$

And considering the following equations (see Figure 4.2):

$$\begin{aligned} \omega_z &= \omega_B cos\beta \\ \omega_R &= \omega_B sin\beta \end{aligned} \tag{4.7}$$

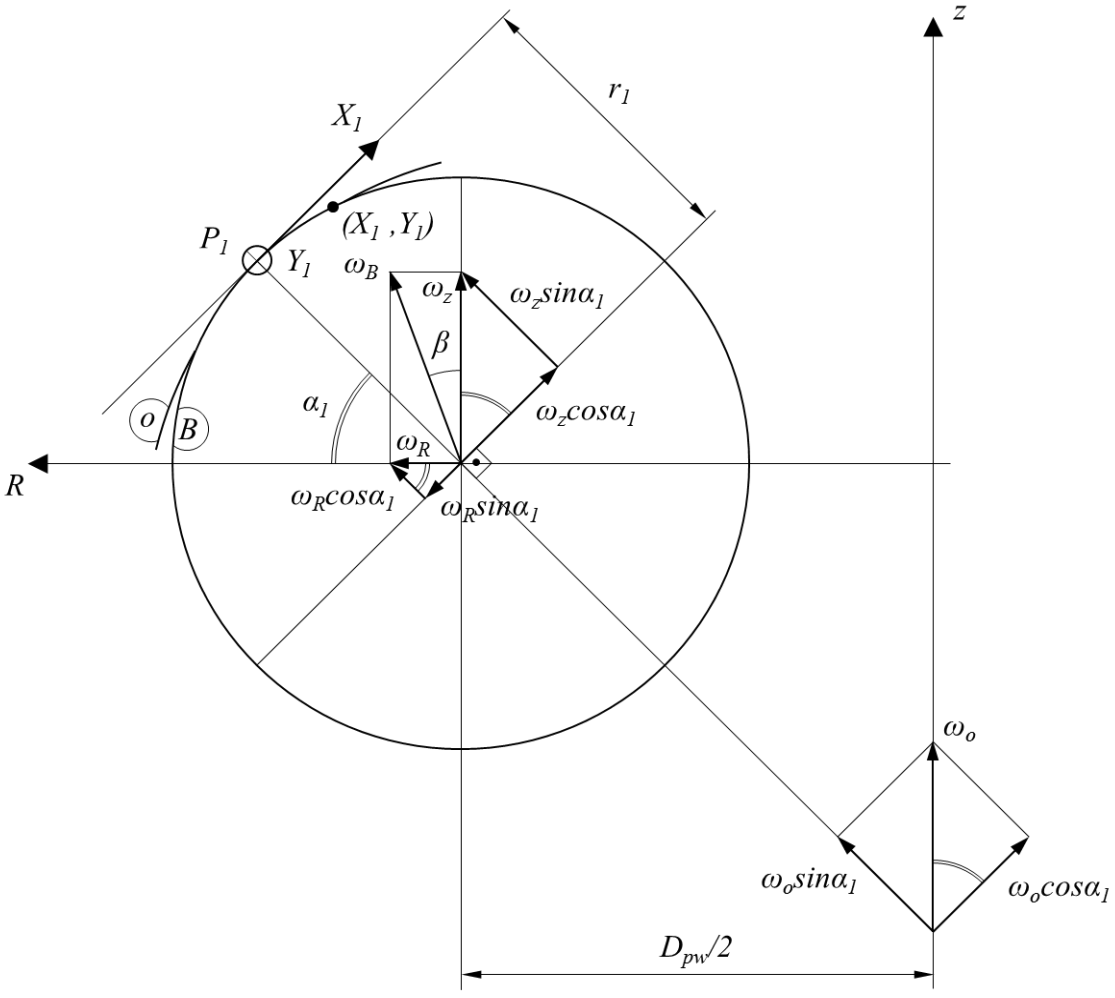

Figure 4.2. Angular velocities.

The rolling relative velocity (V_{Y1}^R) and spinning relative angular velocity (ω_1^S) from equations (4.6) are determined by the following formulas:

$$\begin{aligned} V_{Y1}^R(X_1) &= -\frac{D_{pw}\omega_o}{2} \\ &\quad + r_1[-\omega_o cos\alpha_1 + \omega_B(cos\beta cos\alpha_1 - sin\beta sin\alpha_1)] \\ \omega_1^S &= \omega_o sin\alpha_1 + \omega_B(-cos\beta sin\alpha_1 - sin\beta cos\alpha_1) \end{aligned} \tag{4.8}$$

Note that, since the rolling occurs in the Y direction, V_{X1}^R will be 0. Generalizing formula (4.6) for any i point:

$$\begin{aligned} V_{Yi}(X_i) &= V_{Yi}^R(X_1) + X_i\omega_i^S \\ V_{Xi}(Y_i) &= -Y_i\omega_i^S \end{aligned} \tag{4.9}$$

And proceeding analogously for the other contact points, the rolling relative velocity (V_{Yi}^R) and spinning relative angular velocity (ω_i^S) from equations (4.9) can be obtained for each case. Figure 4.3 defines the local coordinate system of each contact point. Accordingly, the following expressions are obtained for contact point P_2:

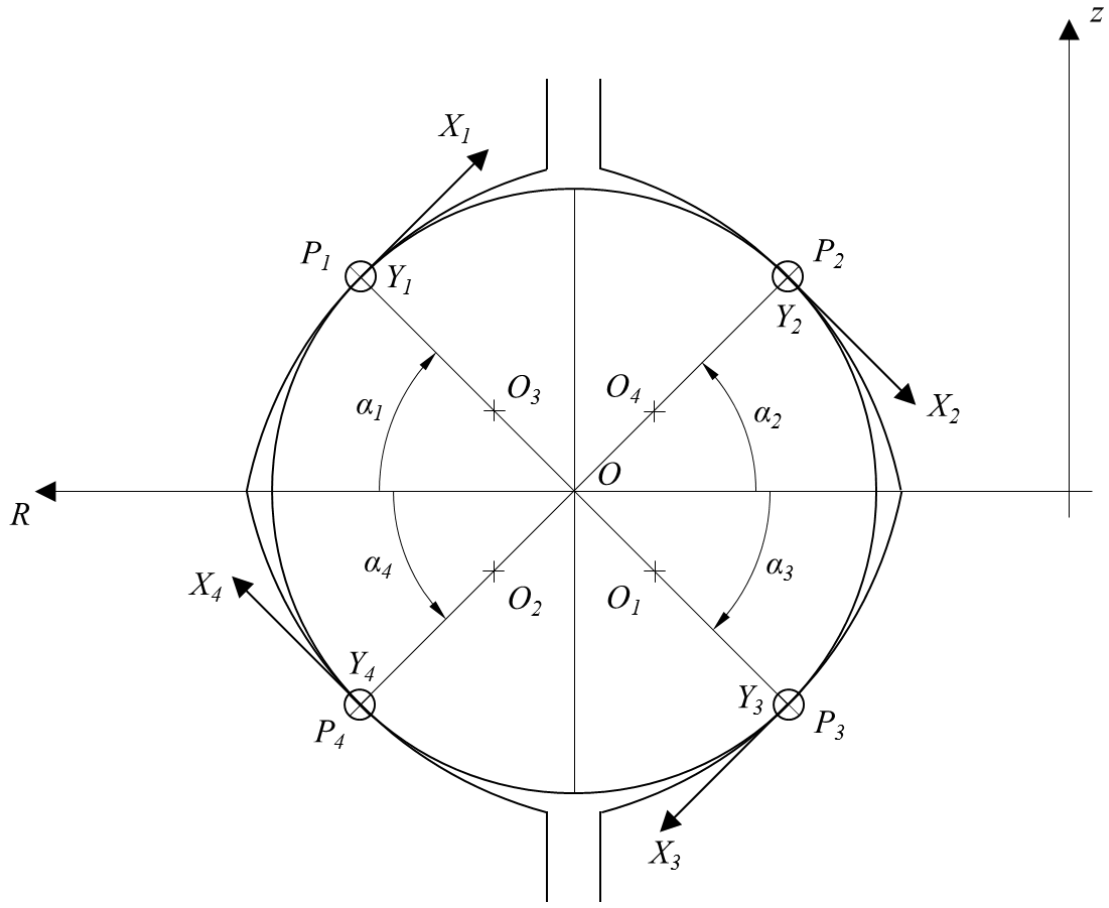

Figure 4.3. Local coordinate system for each contact.

$$V_{Y2}^{R}(X_2) = -\frac{D_{pw}\omega_i}{2} + r_2[\omega_i cos\alpha_2 + \omega_B(-cos\beta cos\alpha_2 - sin\beta sin\alpha_2)] \qquad (4.10)$$
$$\omega_2^S = \omega_i sin\alpha_2 + \omega_B(-cos\beta sin\alpha_2 + sin\beta cos\alpha_2)$$

Where ω_i is the angular velocity of the inner ring. For contact point P_3:

$$V_{Y3}^{R}(X_3) = -\frac{D_{pw}\omega_o}{2} + r_3[\omega_i cos\alpha_3 + \omega_B(-cos\beta cos\alpha_3 + sin\beta sin\alpha_3)] \qquad (4.11)$$
$$\omega_3^S = -\omega_i sin\alpha_1 + \omega_B(cos\beta sin\alpha_3 + sin\beta cos\alpha_3)$$

And for contact point P_4:

$$V_{Y4}^{R}(X_4) = -\frac{D_{pw}\omega_o}{2} + r_4[-\omega_o cos\alpha_4 + \omega_B(cos\beta cos\alpha_4 + sin\beta sin\alpha_4)] \qquad (4.12)$$
$$\omega_4^S = -\omega_o sin\alpha_4 + \omega_B(cos\beta sin\alpha_4 - sin\beta cos\alpha_4)$$

Equations (4.8) to (4.12) define the relative velocity field at the four contacts. In these equations, there are four unknowns: ω_i, ω_o, ω_B and β. Since the approach is thought for slow speeds, no inertial or centrifugal forces are involved. Therefore, contact forces and stresses are not affected by the rotation speed of the bearing, and so neither will the friction torque be. Since the purpose of the approach is to calculate the friction torque and study the contact status and shear stresses, the formulation can be normalized with respect to one of the unknowns. The angular velocity of the inner ring (ω_i) is used for this purpose, but for the sake of clarity in the formulation, an arbitrary value of 1rad/s is established instead of normalizing with respect to this parameter. Thus, this leaves only three unknowns: ω_o, ω_B and β.

4.2.2 Approximated kinematical approach

The next step is to calculate the resulting forces at the contacts and formulate equilibrium conditions to solve the problem and find the values of the three mentioned unknowns. Nevertheless, finding a solution requires a first estimation for the unknowns. In this regard, the better the estimation is, the faster the solver will find the solution. Moreover, not providing a good first shot can make the solution not converge. For this reason, an approximated approach is proposed in order to estimate the kinematics in a direct and simple way.

For the approximation, two cases are distinguished: four contact point case and two contact point case. The four contact point case is addressed in the first place. For this approach, it is assumed that the contact takes place at a point instead of in an area, and that no sliding occurs at this punctual contact. It is known that the latter assumption only can be fulfilled for certain contact angles, but it is assumed anyway for a first approximation in the following formulation. Thus, the velocity of P_1 is formulated for the outer ring (o) and the ball (B):

$$\begin{aligned} V_{Y1}^{o} &= -\left(\frac{D_{pw}}{2} + \frac{D_w}{2} cos\alpha_1\right)\omega_o \\ V_{Y1}^{B} &= -\frac{D_w}{2} sin\left(\frac{\pi}{2} - \beta - \alpha_1\right)\omega_B = -\frac{D_w}{2} cos(\beta + \alpha_1)\omega_B \end{aligned} \tag{4.13}$$

As no sliding is assumed, these velocities are the same. Equating both formulas, the following expression is obtained:

$$\omega_B = \frac{\frac{D_{pw}}{D_w} + cos\alpha_1}{cos(\beta + \alpha_1)}\omega_o \tag{4.14}$$

In the same way, the velocity of contact point P_2 is formulated for the ring (i) and the ball (B):

$$\begin{aligned} V_{Y2}^{i} &= -\left(\frac{D_{pw}}{2} - \frac{D_w}{2} cos\alpha_2\right)\omega_i \\ V_{Y2}^{B} &= \frac{D_w}{2} sin\left(\frac{\pi}{2} + \beta - \alpha_2\right)\omega_B = \frac{D_w}{2} cos(\beta - \alpha_2)\omega_B \end{aligned} \tag{4.15}$$

And then both formulas are equated, obtaining the following expression:

$$\omega_B = -\frac{\frac{D_{pw}}{D_w} - cos\alpha_2}{cos(\beta - \alpha_2)}\omega_i \tag{4.16}$$

The same can be done for point P_3:

$$\begin{aligned} V_{Y3}^{i} &= -\left(\frac{D_{pw}}{2} - \frac{D_w}{2} cos\alpha_3\right)\omega_i \\ V_{Y3}^{B} &= \frac{D_w}{2} sin\left(\frac{\pi}{2} - \beta - \alpha_3\right)\omega_B = \frac{D_w}{2} cos(\beta + \alpha_3)\omega_B \end{aligned} \tag{4.17}$$

Equating the formulas:

$$\omega_B = -\frac{\frac{D_{pw}}{D_w} - cos\alpha_3}{cos(\beta + \alpha_3)}\omega_i \tag{4.18}$$

And finally, for point P_4:

$$\begin{aligned} V_{Y4}^o &= -\left(\frac{D_{pw}}{2} + \frac{D_w}{2}cos\alpha_4\right)\omega_o \\ V_{Y4}^B &= -\frac{D_w}{2}sin\left(\frac{\pi}{2} + \beta - \alpha_4\right)\omega_B = -\frac{D_w}{2}cos(\beta - \alpha_4)\omega_B \end{aligned} \tag{4.19}$$

And equating:

$$\omega_B = \frac{\frac{D_{pw}}{D_w} + cos\alpha_4}{cos(\beta - \alpha_4)}\omega_o \tag{4.20}$$

The slow speed assumption implies that $\alpha_3 = \alpha_1$ and $\alpha_4 = \alpha_2$, so equations (4.18) and (4.20) can be rewritten as follows:

$$\omega_B = -\frac{\frac{D_{pw}}{D_w} - cos\alpha_1}{cos(\beta + \alpha_1)}\omega_i \tag{4.21}$$

$$\omega_B = \frac{\frac{D_{pw}}{D_w} + cos\alpha_2}{cos(\beta - \alpha_2)}\omega_o \tag{4.22}$$

According to this approach four equations have been defined, (4.14), (4.16), (4.21) and (4.22), where only three parameters are unknown, namely ω_o, ω_B and β, since ω_i is known. By equating equations (4.14) and (4.22), unknowns ω_o and ω_B disappear and the following formula is obtained, where the only unknown is the β angle:

$$\left(\frac{D_{pw}}{D_w} + cos\alpha_1\right)cos(\beta - \alpha_2) = \left(\frac{D_{pw}}{D_w} + cos\alpha_2\right)cos(\beta + \alpha_1) \tag{4.23}$$

Doing the same with equations (4.16) and (4.21), unknowns ω_i and ω_B disappear and a similar expression is achieved:

$$\left(\frac{D_{pw}}{D_w} - cos\alpha_1\right)cos(\beta - \alpha_2) = \left(\frac{D_{pw}}{D_w} - cos\alpha_2\right)cos(\beta + \alpha_1) \tag{4.24}$$

For the case of $\alpha_1 = \alpha_2$, both (4.23) and (4.24) are fulfilled for $\beta = \pi$. If $\alpha_1 \neq \alpha_2$, then (4.23) and (4.24) are fulfilled for different values of β, which

means that sliding must occur at the contacting points. Nevertheless, it is demonstrated that, for different values of α_1 and α_2, the β values that fulfil (4.23) and (4.24) are very near to each other. Moreover, the average of both values is equal to the following value:

$$\beta = \pi + \frac{\alpha_2 - \alpha_1}{2} \tag{4.25}$$

This β value coincides with the bisector of the angle formed by contact diagonal 1 ($\overline{P_1P_3}$) and 2 ($\overline{P_2P_4}$), as illustrated in Figure 4.4. Taking this value means assuming that the sliding is equally divided among the contacts of the inner and the outer ring, which will be close to the real solution for slewing bearings, where $D_{pw} \gg D_w$.

To obtain the expression for the outer ring angular velocity as a function of the angular velocity of the inner ring, formulas (4.14) and (4.21) are equated and the following expression is obtained:

$$\omega_o = -\frac{\frac{D_{pw}}{D_w} - cos\alpha_1}{\frac{D_{pw}}{D_w} + cos\alpha_1}\omega_i \tag{4.26}$$

Doing the same with equations (4.16) and (4.22):

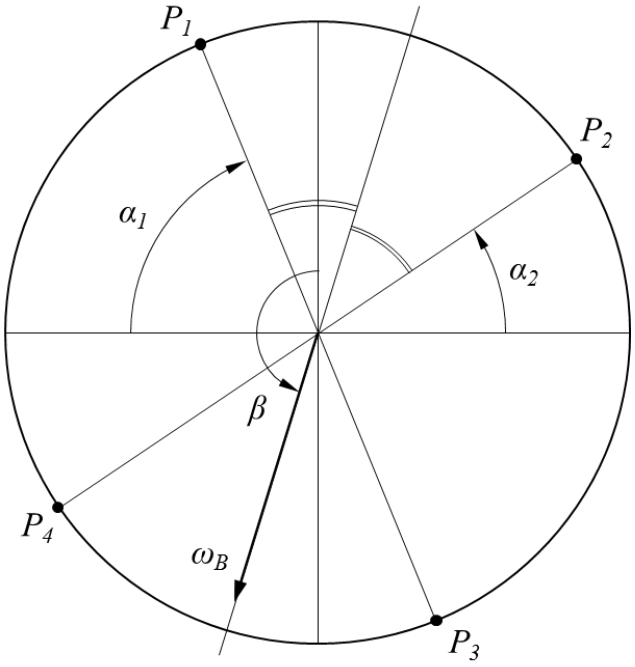

Figure 4.4. Approximated direction of the β angle for four contact point case.

$$\omega_o = -\frac{\frac{D_{pw}}{D_w} - cos\alpha_2}{\frac{D_{pw}}{D_w} + cos\alpha_2}\omega_i \tag{4.27}$$

As happened with the β angle, equations (4.26) and (4.27) will only be equal for $\alpha_1 = \alpha_2$. For the case of $\alpha_1 \neq \alpha_2$, the following expression is adopted in order to achieve an approximated result:

$$\omega_o = -\frac{\frac{D_{pw}}{D_w} - cos\left(\frac{\alpha_1 + \alpha_2}{2}\right)}{\frac{D_{pw}}{D_w} + cos\left(\frac{\alpha_1 + \alpha_2}{2}\right)}\omega_i \tag{4.28}$$

Note that this expression is not the average of (4.26) and (4.27). Of course, ω_o has the contrary sign to ω_i (opposite direction) and it has a slightly lower value (bigger diameter).

Finally, the expression of ω_B as a function of ω_i will be obtained. For this purpose, equations (4.16) and (4.21) will be used. Considering the adopted value for the β angle in (4.25), the following can be written:

$$cos(\beta + \alpha_1) = cos\left(\pi + \frac{\alpha_2 - \alpha_1}{2} + \alpha_1\right) = -cos\left(\frac{\alpha_1 + \alpha_2}{2}\right) \tag{4.29}$$

$$cos(\beta - \alpha_2) = cos\left(\pi + \frac{\alpha_2 - \alpha_1}{2} - \alpha_2\right) = -cos\left(\frac{\alpha_1 + \alpha_2}{2}\right) \tag{4.30}$$

Substituting (4.29) in (4.21):

$$\omega_B = \frac{\frac{D_{pw}}{D_w} - cos\alpha_1}{cos\left(\frac{\alpha_1 + \alpha_2}{2}\right)}\omega_i \tag{4.31}$$

And substituting (4.30) in (4.16):

$$\omega_B = \frac{\frac{D_{pw}}{D_w} - cos\alpha_2}{cos\left(\frac{\alpha_1 + \alpha_2}{2}\right)}\omega_i \tag{4.32}$$

Once again, equations (4.31) and (4.32) will only provide the same results for $\alpha_1 = \alpha_2$. Similarly to what has been done for ω_o, the following expression is adopted:

$$\omega_B = \frac{\frac{D_{pw}}{D_w} - cos\left(\frac{\alpha_1 + \alpha_2}{2}\right)}{cos\left(\frac{\alpha_1 + \alpha_2}{2}\right)} \omega_i \tag{4.33}$$

Thus, equations (4.25), (4.28) and (4.33) offer an initial estimation for the kinematics in the case of four contact points.

For the case of two contact points, only two equations can be defined. Suppose points P_1 and P_3 are in contact, while no forces exist at P_2 and P_4. Thus, equations (4.14) and (4.21) will continue to be fulfilled according to the proposed assumptions, but not (4.16) and (4.22). From these equations, expression (4.26) is obtained for the ω_o, but an additional assumption is required in order to calculate ω_B and β as a function of ω_i. For this purpose, relative angular velocities will be analysed. Being ω_{Bo} the relative angular velocity of the ball with respect to the outer raceway, and ω_{Bi} the relative angular velocity of the ball with respect to the inner raceway, the following relationships are satisfied:

$$\begin{aligned} \vec{\omega}_{Bo} &= \vec{\omega}_B - \vec{\omega}_o \\ \vec{\omega}_{Bi} &= \vec{\omega}_B - \vec{\omega}_i \end{aligned} \tag{4.34}$$

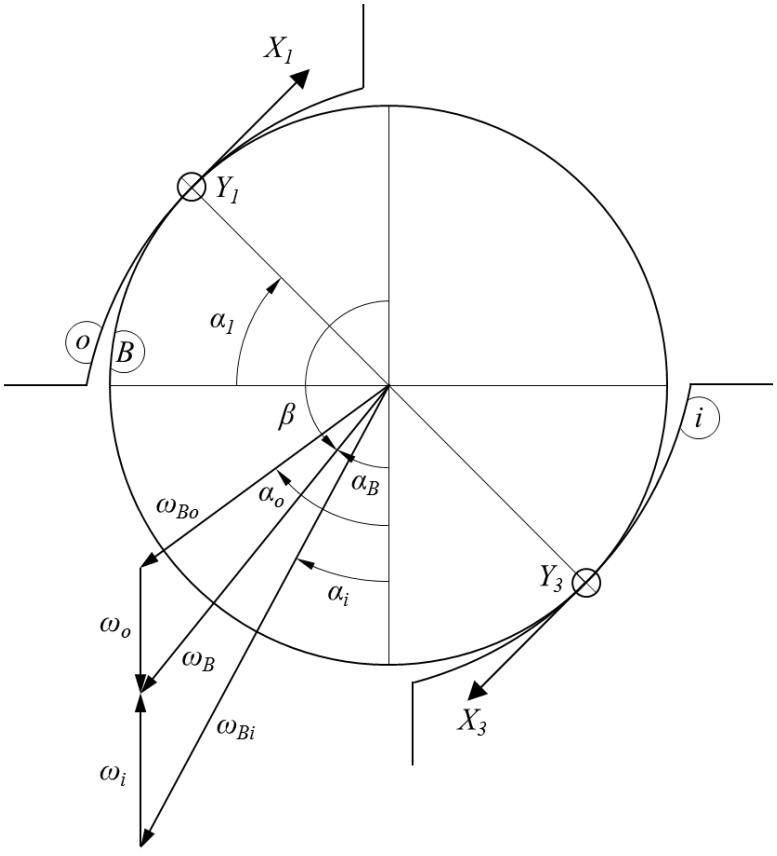

Figure 4.5. Relative angular velocities in the ball.

These vectors are schematically represented in Figure 4.5. In this figure, angle α_B is defined as the supplementary angle of β:

$$\beta = \pi - \alpha_B \tag{4.35}$$

To define the α_B angle (and therefore β), an assumption about the spinning of the ball must be adopted. Taking into account that the osculation ratio in the circumferential direction (in φ according to Figure 2.5) is bigger for the outer ring than for the inner , the inner raceway will offer less opposition to the spinning. Thus, assuming that pure rolling exists in the outer ring (point P_1), ω_{Bo} will be parallel to X_1, which means that $\alpha_o = \alpha_1$, so $\alpha_B < \alpha_1$, and therefore $\beta > \pi - \alpha_1$. On the other hand, if it is assumed that pure rolling occurs, ω_{Bi} will be parallel to X_1, which means that $\alpha_i = \alpha_1$, so $\alpha_B > \alpha_1$, and therefore $\beta < \pi - \alpha_1$. In slewing bearings, where $D_{pw} \gg D_w$, the differences in the osculation ratio of inner and outer rings are far less important than in small bearings, and spinning will be at both points. Moreover, it will happen that $\omega_B \gg \omega_o$ and $\omega_B \gg \omega_i$, so $\alpha_B \cong \alpha_1$. Consequently, the next value can be assumed, which will provide a quite accurate approximation:

$$\beta = \pi - \alpha_1 \tag{4.36}$$

Substituting this expression in (4.21):

$$\omega_B = \left(\frac{D_{pw}}{D_w} - cos\alpha_1\right)\omega_i \tag{4.37}$$

Therefore, equations (4.26), (4.36) and (4.37) provide an initial estimation for the kinematics when contact exists at points P_1 and P_3. If the contact exists at points P_2 and P_4 instead of at points P_1 and P_3, and proceeding in the same way, the β angle will be defined as follows:

$$\beta = \pi + \alpha_2 \tag{4.38}$$

Which can be substituted in expression (4.16):

$$\omega_B = \left(\frac{D_{pw}}{D_w} - cos\alpha_2\right)\omega_i \tag{4.39}$$

So equations (4.27), (4.38) and (4.39) offer an initial estimation for the kinematics when contact exists at points P_2 and P_4. The formulation for the three cases can be summarized by the following formulas:

$$\beta = \pi + \frac{\alpha_2' - \alpha_1'}{2}$$
$$\omega_o = -\frac{\frac{D_{pw}}{D_w} - cos\left(\frac{\alpha_1' + \alpha_2'}{2}\right)}{\frac{D_{pw}}{D_w} + cos\left(\frac{\alpha_1' + \alpha_2'}{2}\right)}\omega_i \tag{4.40}$$
$$\omega_B = \frac{\frac{D_{pw}}{D_w} - cos\left(\frac{\alpha_1' + \alpha_2'}{2}\right)}{cos\left(\gamma\frac{\alpha_1' + \alpha_2'}{2}\right)}\omega_i$$

The values of α_1', α_2' and γ are different for each case and are given in Table 4.1. Although in this approximated approach only three cases are considered, intermediate kinematical situations can take place. In those cases where there are four contact points but the normal load in one of the diagonals is much greater than in the other, it is not possible to establish beforehand if the ball is spinning with respect to the four points (K3) or if it is rolling with respect to the most loaded points (K1 or K2). For this reason an iterative algorithm is required, which is defined later in section 4.2.5. Nevertheless, from the FE calculations performed in Chapter 3, it is known that the transition between K1 or K2 to K3 is abrupt, so there is little room for intermediate cases.

Kinematical case	Contact points	Contact diagonal	α_1'	α_2'	γ
K1	P_1 and P_3	1	$2\alpha_1$	0	0
K2	P_2 and P_4	2	0	$2\alpha_2$	0
K3	P_1, P_2, P_3 and P_4	1 and 2	α_1	α_2	1

Table 4.1. Values of the parameters for the generalized formulation of the approximated kinematical approach.

4.2.3 Tangential problem

Before calculating the forces acting on the ball, it must be determined how the tangential problem is going to be addressed. State of the art analytical models for four-point contact slewing bearings assume that full sliding occurs between the ball and the raceway [56,57,59]. This assumption leads to the simplest approach possible for the contact simulation. This way, the normal problem is solved through Hertz theory, and then the shear stresses can be directly computed as the pressure multiplied by the friction coefficient. As demonstrated through FE calculations (Figure 3.10, Figure 3.17 and Figure

3.22), important stick regions can exist in the contact ellipse, affecting the shear stress field. Therefore, the full sliding assumption will provide overestimated shear stresses in the stick regions, which can affect the friction torque.

There exist a number of different ways to solve the contact problem. The approach proposed in this research work is based on the one developed by Kalker for his FASTSIM algorithm. Kalker developed a simplified theory for the solution of the tangential problem [66], which was later implemented in the mentioned algorithm [67]. This algorithm offers a simple and powerful tool for the solution of the tangential problem, allowing fast simulations. The FASTSIM has been, and still is, broadly used for the analysis of the rail-wheel contact, and has been demonstrated to give reliable results for this application with very low computational costs. For these reasons, this formulation has been adopted for the ball-raceway contact. Nevertheless, the ball-raceway contact differs significantly from the rail-wheel contact, so the suitability of Kalker's formulation for this type of contact is to be demonstrated.

To apply Kalker's simplified theory, the following hypotheses are assumed:

- Quasi-static movement: no effects forces are taken into account.
- Steady state rolling: as shown in Figure 3.10, the contact status undergoes a transient state before stabilising. This transient state is not considered, so the studied contact is assumed invariant with time.
- Non-conformal contact: like Hertz theory, Kalker's simplified theory assumes non-conformal contact. This allows it to be considered that contacting bodies behave like half spaces.
- Thin elastic layer: each contacting surface is assumed to have a thin elastic layer underneath, attached over a flat rigid base. The layer is loaded in a region which is large with respect to its thickness.
- Same material in both contacting bodies: contacting bodies are assumed to have the same elastic properties.

These hypotheses considerably simplify the stress-deformation relationship at the contact, allowing normal and tangential problems to be decoupled. It is expected that the assumption of non-conformal contact can lead to a certain lack of accuracy in the results. Although the contact is non-conformal in the circumferential direction, it is conformal in the radial plane. Nevertheless, Hertz theory also assumes non-conformal contact, and it is typically used for the simulation of ball-raceway contacts, offering reliable results [29]. The goal

of implementing Kalker's formulation in the analytical approach of the ball-raceway contact is to obtain more accurate results than with the full sliding assumption and to test its suitability for these type of contact.

Assuming the above hypotheses and considering a body rolling with a V velocity in the x_1 direction according to Figure 4.6a, the relationship between the velocity field and contact deformations is given by [68]:

$$\vec{s}(\vec{x}) = \vec{w}(\vec{x}) - V\frac{\partial \vec{u}(\vec{x})}{\partial x_1} \tag{4.41}$$

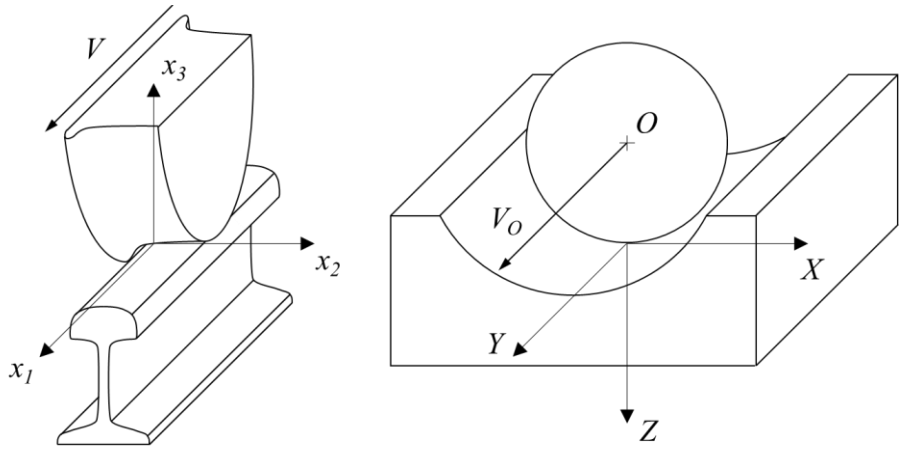

Figure 4.6. Contact coordinate systems: (a) for rail-wheel contact; (b) for the current approach.

Where $\vec{s}$ is the relative velocity of the point $\vec{x}$ of the contact area considering elastic deformations at the contact, or local slip according to Kalker's nomenclature; $\vec{w}$ is the relative velocity considering rigid bodies, or local rigid slip; and $\vec{u}$ is the elastic deformation. Note that the coordinate system defined in Figure 4.6a is mobile, so it is displaced with the contact. In the case of the ball, and for considered local coordinate system (Figure 4.6b), the movement takes place in the Y direction, and the rolling velocity is the velocity of the centre of the ball (point O):

$$\vec{s}(X,Y) = \vec{w}(X,Y) - V_O\frac{\partial \vec{u}(X,Y)}{\partial Y} \tag{4.42}$$

Dividing this expression by V_O:

$$\vec{s}_r(X,Y) = \vec{w}_r(X,Y) - \frac{\partial \vec{u}(X,Y)}{\partial Y} \tag{4.43}$$

Kinematics in section 4.2.1 were formulated ignoring tangential deformations. Therefore, the obtained velocity field is the local rigid slip ($\vec{w}$).

Expressions (4.8) to (4.12) formulate the relative velocity of the raceways with respect to the ball. Therefore, the local rigid slip for the ball is equal but with the opposite direction. From (4.9):

$$\vec{w}_r(X,Y) = -\frac{1}{V_O}\begin{Bmatrix} V_Y(X) \\ V_X(Y) \end{Bmatrix} = \frac{1}{V_O}\begin{Bmatrix} -V_Y^R(X) - X\omega^S \\ Y\omega^S \end{Bmatrix} \tag{4.44}$$

Using the creepage parameters defined by Kalker:

$$\begin{aligned} \xi(X) &= -\frac{V_Y^R(X)}{V_O} \\ \Phi &= -\frac{\omega^S}{V_O} \end{aligned} \tag{4.45}$$

The local rigid slip is defined as:

$$\vec{w}_r(X,Y) = \begin{Bmatrix} \xi(X) + X\Phi \\ -Y\Phi \end{Bmatrix} \tag{4.46}$$

Where ξ is the longitudinal creepage and Φ is the spin. The lateral creepage η is 0 in the studied case. Note that if this expression is compared with the one at [68], the terms for the spinning in (4.46) have the contrary sign. This is because the Z axis of the coordinate system of this approach has the opposite direction to that of the x_3 axis of the coordinate system used by Kalker, as represented in Figure 4.6.

For the formulation of the deformations, Kalker proposed a simplified theory [66], which is based on the thin elastic layer theory. According to the simplified theory, the deformations at a point of the contact ellipse can be formulated as a function of the shear stresses at the same point through the flexibility parameter L:

$$\vec{u}(X,Y) = L\vec{\tau}(X,Y) \tag{4.47}$$

The FASTSIM algorithm developed by Kalker for the rolling contact simulation [67] is based on this simplification. Substituting (4.47) in (4.43):

$$\vec{s}_r(X,Y) = \vec{w}_r(X,Y) - L\frac{\partial\vec{\tau}(X,Y)}{\partial Y} \tag{4.48}$$

In the stick region of the contact, the local slip ($\vec{s}$) will be 0:

$$\vec{s}_r(X,Y) = 0 \;\rightarrow\; \partial\vec{\tau}^A(X,Y) = \vec{w}_r(X,Y)\partial Y \tag{4.49}$$

Assuming that the leading edge will be in adhesion, the previous formula can be integrated from this edge (Y_0) to any Y:

$$\vec{\tau}^A(X,Y) = \frac{1}{L}\int_{Y_0}^{Y}\begin{Bmatrix}\xi(X)+X\Phi\\-Y\Phi\end{Bmatrix}\partial Y = \frac{1}{L}\begin{Bmatrix}\xi(X)+X\Phi\\-\frac{1}{2}(Y+Y_0)\Phi\end{Bmatrix}(Y-Y_0) \qquad (4.50)$$

Where:

$$Y_0 = \sqrt{b^2\left(1-\frac{X}{a}\right)^2} \qquad (4.51)$$

Of course, the shear stress is 0 at the limits of the contact ellipse, so $\vec{\tau}^A(X,Y_0)=0$. To obtain the value of the flexibility parameter (L), the linear theory is used. The linear theory was developed by Kalker before the simplified theory [65], and it solved the problem for the case of full adhesion contact. The full adhesion takes place when the local rigid slip is very small. Particularizing the simplified theory for the full adhesion case and equating with the results from the linear theory, it is demonstrated that different flexibility parameters are required to match the results [68]:

$$\vec{\tau}^A(X,Y) = \begin{Bmatrix}\frac{\xi(X)}{L_1}+\frac{X\Phi}{L_3}\\-\frac{(Y+Y_0)\Phi}{2L_3}\end{Bmatrix}(Y-Y_0) \qquad (4.52)$$

The flexibility parameter L_2 is for the lateral creepage (η), which is 0 in the studied case. Putting components separately and substituting (4.45) in (4.52):

$$\begin{aligned}\tau_Y^A(X,Y) &= \frac{1}{V_O}\left(\frac{V_Y^R(X)}{L_1}+\frac{X\omega^S}{L_3}\right)(Y_0-Y)\\ \tau_X^A(X,Y) &= -\frac{\omega^S}{2V_O L_3}(Y_0^2-Y^2)\end{aligned} \qquad (4.53)$$

The flexibility parameters are a function of the creepage coefficients C_{ij}:

$$\begin{aligned}L_1 &= \frac{8b}{3C_{11}G}\\ L_3 &= \frac{\pi b^{3/2}}{4a^{1/2}C_{23}G}\end{aligned} \qquad (4.54)$$

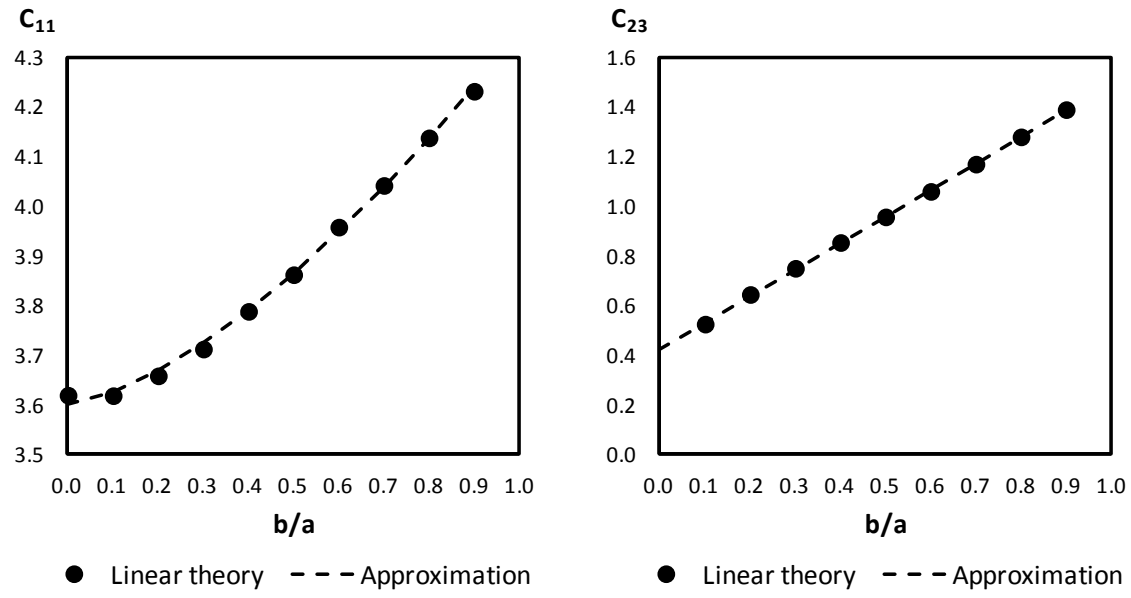

Figure 4.7. Approximated functions for creepage coefficients for $\nu = 0.3$.

The values of the creepage coefficients for the exact theory can be found in [65] or in [68]. These values are tabulated for different a/b ratios and Poisson coefficients (ν) of 0, 0.25 and 0.5. As the material typically used in slewing bearings is steel, the values for $\nu = 0.3$ were obtained by linear interpolation, and calculated values were approximated by the following formulas, which are represented in Figure 4.7:

$$C_{11} = 3.6 + 0.75\left(\frac{b}{a}\right)^{1.5}$$
$$C_{23} = 0.42 + 1.07\frac{b}{a} \tag{4.55}$$

The creepage coefficients (C_{ij}) were approximated instead of directly approximating flexibility parameters (L_i) because they were found more suitable to fit through simple functional forms like those in (4.55).

The value of the V_o velocity is still to be formulated. This is the velocity of the centre of the ball with respect to the contact, so it will be different for each one. Equations (4.13), (4.15), (4.17) and (4.19) calculate the velocities of the contacting points considering the centre of the ball is fixed. Therefore, the velocity of the ball with respect to the contacting points, considering the corresponding raceway fixed in each case, will be the same but with the contrary sign:

$$
\begin{aligned}
V_{O1} &= \left(\frac{D_{pw}}{2} + \frac{D_w}{2} cos\alpha_1\right)\omega_o \\
V_{O2} &= \left(\frac{D_{pw}}{2} - \frac{D_w}{2} cos\alpha_2\right)\omega_i \\
V_{O3} &= \left(\frac{D_{pw}}{2} - \frac{D_w}{2} cos\alpha_1\right)\omega_i \\
V_{O4} &= \left(\frac{D_{pw}}{2} + \frac{D_w}{2} cos\alpha_2\right)\omega_o
\end{aligned}
\tag{4.56}
$$

Equations (4.53) calculate the shear stress in the stick regions. On the other hand, if a certain point of the contact ellipse is slipping, the shear stress will be calculated as follows, according to the Amontons-Coulomb laws of dry friction:

$$\tau^S(X,Y) = \mu P(X,Y) \tag{4.57}$$

Where μ is the friction coefficient. According to Hertz theory [17], the contact pressure is calculated by:

$$P(X,Y) = \frac{3Q}{2\pi ab}\sqrt{1 - \frac{X^2}{a^2} - \frac{Y^2}{b^2}} \tag{4.58}$$

Defining γ according to the formulation of Jones [54] and Leblanc and Nélias [56] (see Figure 4.8) and formulating each component of the shear stress separately:

$$
\begin{aligned}
\tau_Y^S(X,Y) &= \mu P cos\gamma = \mu P \frac{V_Y}{V} \\
\tau_X^S(X,Y) &= -\mu P sin\gamma = \mu P \frac{V_X}{V}
\end{aligned}
\tag{4.59}
$$

Where V is the modulus of the local rigid slip:

$$V(X,Y) = \sqrt{V_Y^2 + V_X^2} \tag{4.60}$$

Unlike in [54,56], in the proposed approach, both τ_Y and τ_X are defined according the same local coordinate system as the velocities (in [54,56], τ_X is considered positive in the $-X$ direction). Note that the shear stresses in the ball (τ) have the same direction as the relative velocities of the raceways with respect to the ball (V) in the slip region, as represented in Figure 4.8.

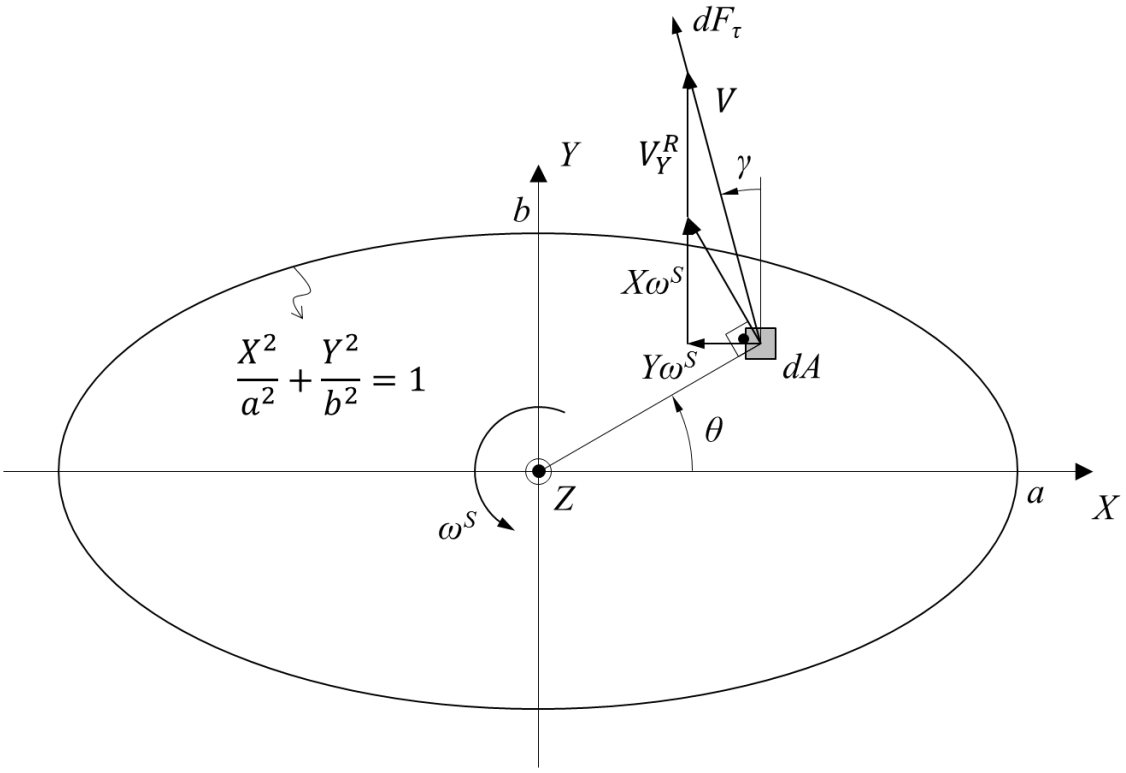

Figure 4.8. Velocities and tangential forces in the slip region.

Summarizing, equations (4.53) and (4.59) calculate shear stresses in stick and slip regions, respectively. To know if a point from the contact ellipse is in the stick or the slip region, the moduli of the stresses according to each assumption are calculated:

$$\begin{aligned}\tau^A(X,Y) &= \sqrt{[\tau_Y^A(X,Y)]^2+[\tau_X^A(X,Y)]^2}\\ \tau^S(X,Y) &= \sqrt{[\tau_Y^S(X,Y)]^2+[\tau_X^S(X,Y)]^2}\end{aligned} \tag{4.61}$$

Then, the lowest value determines the contact status, as represented in Figure 4.9. In this way:

$$\begin{aligned}&\left.\begin{aligned}\tau_Y(X,Y)&=\tau_Y^A(X,Y)\\ \tau_X(X,Y)&=\tau_X^A(X,Y)\end{aligned}\right\} \quad \text{if} \quad \tau^A(X,Y)<\tau^S(X,Y)\\ &\left.\begin{aligned}\tau_Y(X,Y)&=\tau_Y^S(X,Y)\\ \tau_X(X,Y)&=\tau_X^S(X,Y)\end{aligned}\right\} \quad \text{if} \quad \tau^A(X,Y)>\tau^S(X,Y)\end{aligned} \tag{4.62}$$

It must be pointed out that the proposed approach differs slightly from the one proposed by Kalker. For the calculation of the components of the shear stresses in the slip region, Kalker proposes the next formulation, which is not the same as the one stated in (4.59):

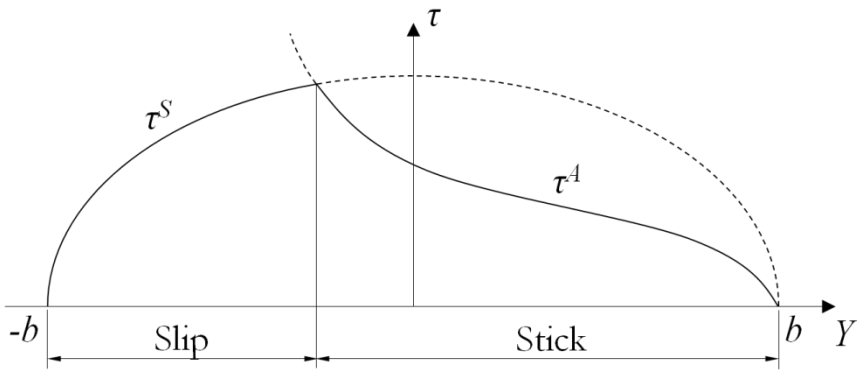

Figure 4.9. Stick and slip regions in the contact.

$$\tau_Y^S(X,Y) = \mu P \frac{\tau_Y^A}{\tau^A} \neq \mu P \frac{V_Y}{V}$$
$$\tau_X^S(X,Y) = \mu P \frac{\tau_X^A}{\tau^A} \neq \mu P \frac{V_X}{V} \quad (4.63)$$

With this formulation, Kalker assumes that the direction of the shear stress is defined by $\vec{\tau}^A$, whatever the studied point is in the stick or the slip region. On the other hand, in (4.59) it is assumed that the direction of the shear stresses in the slip region are determined by the local rigid slip ($\vec{V}$), as done by Jones [54] and Leblanc and Nélias [56]. It is difficult to establish which of the assumptions is more correct beforehand. For this reason, in the next section results from both assumptions are compared. From the comparison, it is concluded that although the results are very similar, (4.59) offers a slightly better match with FE results.

4.2.4 Force equilibrium

Once the shear stresses have been formulated, tangential forces and moments can be calculated. In a differential area $dA = dXdY$, these forces and moments can be expressed as follows:

$$dF_Y = \tau_Y(X,Y)dXdY$$
$$dF_X = \tau_X(X,Y)dXdY$$
$$dM_S = \sqrt{X^2+Y^2}\,\tau(X,Y)cos(\gamma-\theta)dXdY \quad (4.64)$$
$$dM_R = r(X)dF_Y = r(X)\tau_Y(X,Y)dXdY$$

Where:

$$\gamma = atan\left(\frac{\tau_X}{\tau_Y}\right) \quad (4.65)$$

So:

$$\gamma = \begin{cases} atan\left(\frac{\tau_X^A}{\tau_Y^A}\right) \neq atan\left(\frac{V_X}{V_Y}\right) & \text{if} \quad \tau^A(X,Y) < \tau^S(X,Y) \\ atan\left(\frac{\tau_X^S}{\tau_Y^S}\right) = atan\left(\frac{V_X}{V_Y}\right) & \text{if} \quad \tau^A(X,Y) > \tau^S(X,Y) \end{cases} \tag{4.66}$$

To compute total forces and moments, equations (4.64) are integrated in the contact ellipse:

$$\begin{aligned} F_Y &= \int_{-a}^{a} \int_{-\frac{b}{a}\sqrt{a^2-X^2}}^{\frac{b}{a}\sqrt{a^2-X^2}} \tau_Y(X,Y) dY dX \\ F_X &= \int_{-a}^{a} \int_{-\frac{b}{a}\sqrt{a^2-X^2}}^{\frac{b}{a}\sqrt{a^2-X^2}} \tau_X(X,Y) dY dX \\ M_S &= \int_{-a}^{a} \int_{-\frac{b}{a}\sqrt{a^2-X^2}}^{\frac{b}{a}\sqrt{a^2-X^2}} \sqrt{X^2+Y^2}\, \tau(X,Y) cos(\gamma-\theta) dY dX \\ M_R &= \int_{-a}^{a} \int_{-\frac{b}{a}\sqrt{a^2-X^2}}^{\frac{b}{a}\sqrt{a^2-X^2}} r(X) \tau_Y(X,Y) dY dX \end{aligned} \tag{4.67}$$

To simplify these expressions, the next coordinate change is used:

$$\begin{aligned} X &= a\rho cos\theta \\ Y &= b\rho sin\theta \end{aligned} \tag{4.68}$$

This coordinate change allows a discretization of the contact ellipse that is adjusted to its boundaries. This way, formulas (4.67) are rewritten as follows:

$$\begin{aligned} F_Y &= ab \int_0^{2\pi} \int_0^1 \rho \tau_Y(\rho,\theta) d\rho d\theta \\ F_X &= ab \int_0^{2\pi} \int_0^1 \rho \tau_X(\rho,\theta) d\rho d\theta \\ M_S &= ab \int_0^{2\pi} \int_0^1 \rho^2 \sqrt{a^2 cos^2\theta + b^2 sin^2\theta}\, \tau(\rho,\theta) cos(\gamma-\theta) d\rho d\theta \\ M_R &= ab \int_0^{2\pi} \int_0^1 \rho r(\rho,\theta) \tau_Y(\rho,\theta) d\rho d\theta \end{aligned} \tag{4.69}$$

If the kinematics are known, these expressions allow the calculation of forces and moments at the four contact points (see Figure 4.10). Nevertheless, the problem has three unknowns, which are ω_o, ω_B and β (see section 3.5.1). To solve the problem, forces and moments equilibrium is formulated:

$$\begin{aligned}
&F_{Y1} + F_{Y2} + F_{Y3} + F_{Y4} = 0 \\
&M_{S1}cos\alpha_1 + M_{R1}sin\alpha_1 - M_{S2}cos\alpha_2 + M_{R2}sin\alpha_2 - \\
&-M_{S3}cos\alpha_3 - M_{R3}sin\alpha_3 + M_{S4}cos\alpha_4 - M_{R4}sin\alpha_4 = 0 \\
&M_{S1}sin\alpha_1 - M_{R1}cos\alpha_1 - M_{S2}sin\alpha_2 - M_{R2}cos\alpha_2 + \\
&+M_{S3}sin\alpha_3 + M_{R3}cos\alpha_3 - M_{S4}sin\alpha_4 + M_{R4}cos\alpha_4 = 0
\end{aligned} \tag{4.70}$$

The kinematics that fulfil the equilibrium as stated in (4.70) will be the solution of the problem.

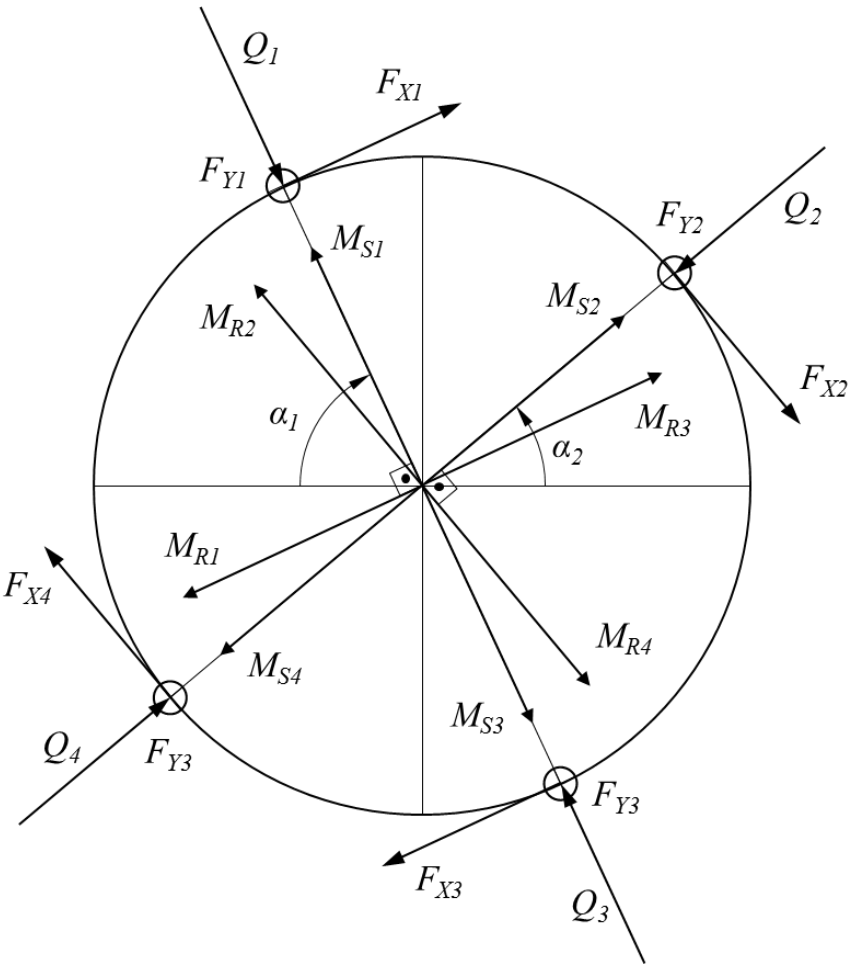

Figure 4.10. Forces and moments acting on the ball.

4.2.5 Solution of the problem

To solve equation (4.70), the proposed formulation was implemented in Matlab®. The trust-region-dogleg algorithm was demonstrated to be effective in finding a solution for this problem as well as cost efficient, being faster than the trust-region-reflective algorithm and showing a better convergence behaviour than the Levenberg-Marquardt method. These are the algorithms that are available in Matlab®. However, in some cases there may exist convergence problems, which can be tackled as explained in the following lines.

The input of the program is the solution of the load distribution problem, that is, contact forces (Q) and angles (α). Nevertheless, some additional parameters are defined, which are described below:

- To automatically calculate the starting point for the solver: K, K_r and K_r^{lim}. In section 4.2.2, an approximated kinematical approach was proposed in order to provide a starting point to the solver. This approach distinguishes between three different kinematical cases (K1, K2 and K3 in Table 4.1). In order to set the kinematical case, the K parameter is used, which will adopt values from 1 to 3. To automatically set the value of K, parameter K_r is defined as the ratio between contact forces in diagonals 1 and 2. If the value of K_r is above a defined limit K_r^{lim} ($K_r > K_r^{lim}$), it will be considered that the ball is rolling with respect to contact points P_1 and P_3 ($K = 1$). Contrarily, if the inverse of K_r is above this limit ($1/K_r > K_r^{lim}$), it will be assumed that the ball is rolling with respect to contact points P_2 and P_4 ($K = 2$). If none of these conditions is fulfilled, it means that $1/K_r^{lim} < K_r < K_r^{lim}$, and therefore it will be considered that the ball is spinning with respect to the four contact points ($K = 3$). An approximated value of $K_r^{lim} = 20$ is adopted based in the results obtained for different cases, although there is not a unique value which is valid for every geometry. Therefore, an iterative procedure is required to find the appropriate value of K, because the model does not to converge if the provided initial point is not close enough to the solution. This iterative procedure is programmed through the Soubroutine-1 (see Figure 4.11), which is later explained.
- To set a different starting point: Ini and ω_{ini}.
  The model is programmed in such a way that a different initial point can be provided to the solver. The parameter Ini sets if a manual entry is

wanted ($Ini = 1$ for manual entry, $Ini = 0$ for automatic calculation), and ω_{ini} sets the values for the initial point (used if $Ini = 1$). This way, if the kinematics have been solved beforehand using a different approach (the model of Leblanc and Nélias or FE calculations, for example), they can be directly introduced as an input.

- To consider stick regions or assume full sliding: FS.
  It has been estimated appropriate to include the option to consider the full sliding hypothesis. Thus, for $FS = 1$, full sliding will be assumed, while stick regions will be considered for $FS = 0$. For the simulation assuming full sliding, the program sets very low values for the flexibility parameters. Note that, since formulas (4.59) are used for the slip region instead of (4.63), considering full sliding will provide the same results as the model of Leblanc and Nélias. This fact allows easy and direct comparisons between the results provided by this model and the one proposed in the current Doctoral Thesis.

Therefore, the inputs for the basic program are: contact forces (Q) and angles (α), K, Ini, ω_{ini} and FS. This basic program can be used to analyse particular cases, but the next two subroutines are proposed for automation purposes. These subroutines avoid manually selecting parameters K, Ini and ω_{ini} and also solve possible convergence problems:

- Soubroutine-1:
  Figure 4.11 shows the flux diagram of the Subroutine-1. As can be seen, K is not among the input parameters. In the first place, this subroutine selects the appropriate initial value for this parameter according to the defined K_r^{lim}. The problem is solved for this K value, and the convergence is evaluated through parameter $info$, which is greater than 0 for converged solutions. If the solution does not converge, the subroutine will try solving the problem for different values of K. If rolling is supposed in the first iteration ($K = 1$ or $K = 2$) and the solution does not converge, only one additional calculation is performed assuming spinning ($K = 3$). Contrarily, if spinning movement is supposed in the first iteration ($K = 3$) and the solution does not converge, then two additional calculations can be done for $K = 1$ and $K = 2$.

- Soubroutine-2:
  It may happen that, when stick regions are considered, a converged solution is not found (1st iteration). For these cases, Soubroutine-2 will solve the problem for full sliding in a first place (2nd iteration), and then the obtained kinematics will be used as an input for the program, considering now the stick regions (3rd iteration). This has been proved to be an effective procedure to solve convergence problems, since the model is more robust for the full sliding assumption. The flow diagram for this subroutine is shown in Figure 4.12, which only requires three inputs: Q, α and FS. Note that, according to the flow diagram, if full sliding is wanted to be assumed ($FS = 1$ as input of the subroutine) and a converged solution is not reached, the program will make an extra attempt considering stick regions in order to obtain a good first shot for the kinematics. Nevertheless, since the full sliding assumption offers better convergence behaviour, if a solution is not reached for $FS = 1$, it will not be very likely that the problem will converge for $FS = 0$.

To set the number of elements in which the contact ellipse is discretized for the calculations, a sensitivity analysis was performed. It was proved that the finer the mesh, the lower the value of the friction torque, similar to what happens with the FE model. Nevertheless, the analytical approach is much less sensitive to the discretization. Moreover, it allows a much larger amount of elements to be used. The value of the friction torque is stabilized for 18000 elements. With this discretization, equation (4.70) can be evaluated 100 times per second. The solver used requires typically between 50 and 250 iterations to find a solution to the problem, while the algorithm does not converge if 500 iterations are exceeded. Thus, a limit of 500 iterations is set for the solver, which means that the basic program requires a maximum of 5s to know if a solution can be found. According to the proposed calculation procedure, a maximum of 9 runs of the basic program could be required, which means a maximum of 45s. Therefore, the computational cost for one ball is between 0.5s and 45s. It goes without saying that this value is nowhere near the computational costs required by FE simulations.

Additionally, calculations were performed for different speeds, setting different values for the inner ring angular velocity (ω_i). The results showed that, effectively, the model is insensitive to the rotation speed.

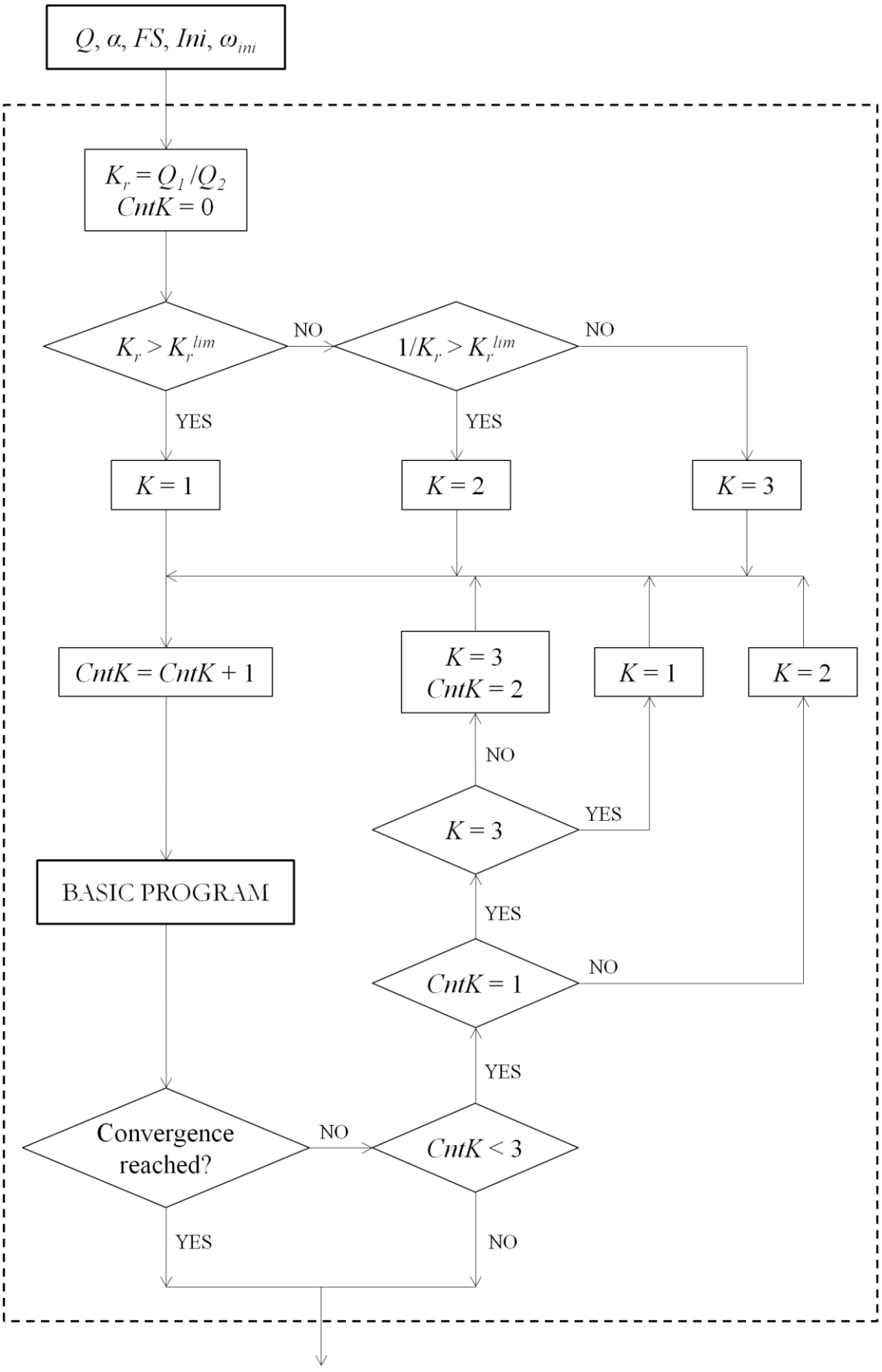

Figure 4.11. Flow diagram of Subroutine-1.

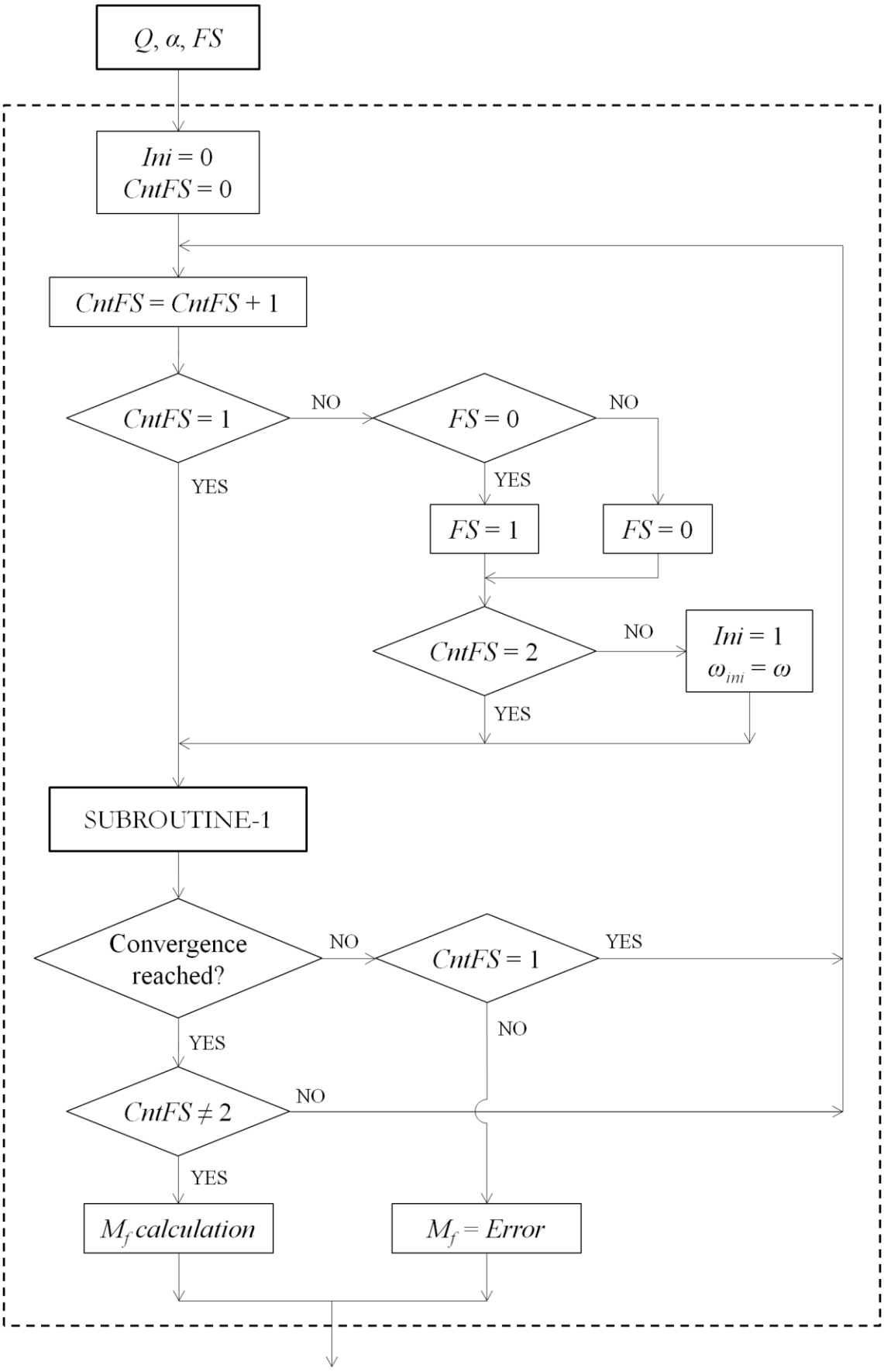

Figure 4.12. Flow diagram of Subroutine-2.

4.2.6 Friction torque calculation

Once the kinematics are known, contact stresses and forces can be calculated, as well as the friction torque. For the calculation of the friction torque, a different approach from the one by Joshi et al. is proposed. While in [59] the friction torque was computed from the resultant forces and moments applied in the effective rolling radii, in the proposed model it is computed directly by integrating the circumferential component of the friction force (F_Y) multiplied by the corresponding distance to the centre of the bearing in the contact ellipse. Thus, the contribution of the friction force in a differential area to the torque is:

$$dM_f(X,Y) = -r^{ap}(X)dF_Y(X,Y) \tag{4.71}$$

Where r^{ap} is the distance from the axis of the bearing to the point where dF_Y is applied, which can be calculated as follows (see Figure 4.1):

$$r^{ap} = \frac{D_{pw}}{2} \pm (r^2 + X^2)^{1/2} cos\left[\alpha \pm atan\left(\frac{X}{r}\right)\right] \tag{4.72}$$

The sign of the second term in equation (4.72) must be positive for the outer ring (P_1 and P_4), and negative for the inner ring (P_2 and P_3), while the sign inside the cosine will be positive for the contact diagonal 1(P_1 and P_3), and negative for the contact diagonal 2 (P_2 and P_4). Integrating (4.71) in the contact ellipse, the contribution of the contact i to the friction torque is obtained:

$$M_{fi} = ab \int_0^{2\pi} \int_0^1 \rho r_i^{ap} \tau_Y(\rho,\theta) d\rho d\theta \tag{4.73}$$

Therefore, the total friction torque for the outer and the inner rings will be:

$$\begin{aligned} M_{fo} &= M_{f1} + M_{f4} \\ M_{fi} &= M_{f2} + M_{f3} \end{aligned} \tag{4.74}$$

As the system is in equilibrium, these values are the same.

4.3 Analytical model *VS* FE model

In this section, the results of the proposed analytical model (the FRANC model) are presented for different cases. The FRANC model is compared

with the analytical approach proposed by Leblanc and Nélias and with FE results. The objective of this comparison is to study the applicability and limitations of each approach.

As a first step, and before comparing analytical and FE models, a sensitivity analysis was performed with the FE model in order to evaluate the effect the different parameters of the problem have on the stick region of the contact ellipse. For this purpose, the refined model was used (Figure 3.8b), since detailed contact results are required. After this analysis, the cases to be studied are defined, the results of which are shown and compared for the different approaches.

4.3.1 Sensitivity analysis

The objective of this preliminary study is to set out the cases for the FE-analytical comparison. The variables to be considered in the sensitivity analysis are the contact parameters, namely ball diameter (D_w), bearing mean diameter (D_{pw}), contact angles (α), osculation ratio (s), friction coefficient (μ) and ball-raceway interferences (δ). First, a nominal design point using typical values of the parameters was defined (see Table 4.2); afterwards, each of the parameters was independently varied so that their influence could be evaluated. The analyses were performed in an automated way taking advantage of the parameterization of the FE model. Table 4.2 summarizes the maximum and minimum values for each parameter, where the interferences are expressed as a percentage over the static load-carrying capacity of the bearing for each case. The capacity was calculated by formulas (4.58) and (2.10), knowing that the maximum allowable pressure is 4200MPa [8] (for a linear elastic calculation) and that it takes place in the centre of the contact ellipse.

Case study	D_w	D_{pw}	α	s	μ	δ_1	δ_2
	[mm]	[mm]	[deg]	[-]	[-]	[%]	[%]
Nominal	30	1000	45	0.95	0.100	50%	0%
Minimum	20	500	45	0.92	0.005	25%	0%
Maximum	40	2500	45	0.98	0.300	75%	0%

Table 4.2. Design space of the sensitivity analysis.

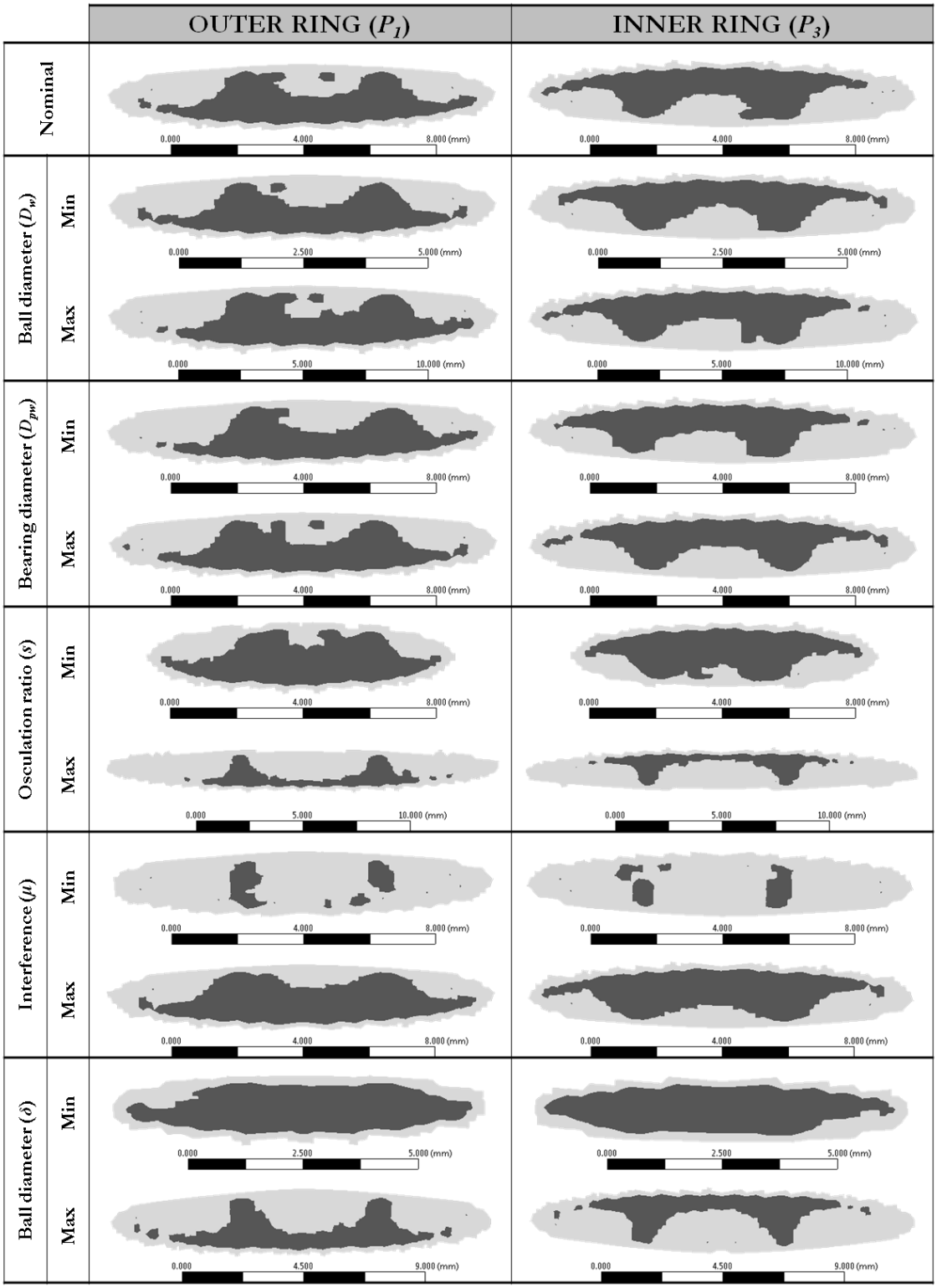

Figure 4.13. Stick region for studied cases.

Stick regions only exist when the ball rolls, so the parametric study was carried out for the case of two contact points, i.e. one of the diagonals is unloaded in every case ($\delta_2 = 0$). The contact angle will affect the location of the contact ellipse (and thus the kinematics of the ball and the friction torque) but not the contact regions themselves. Consequently, a typical value of 45º was taken, as pointed out in Table 4.2, ensuring that no truncation of the ellipse will take place in any case. Although the truncation can be simulated through FE calculations [12], this effect is not considered in the analytical model; therefore, it has been avoided to allow a direct comparison between the models. Figure 4.13 shows the FE results of the contact status for all of the design points of the sensitivity analysis, where stick regions are represented in black. From these results, the next conclusions arise:

- Ball diameter (D_w) and mean bearing diameter (D_{pw}) have no effect on the stick region in the studied design space. Thus, in slewing bearings, where the dimensions of the section are significantly smaller than the mean diameter ($D_w \ll D_{pw}$), none of these parameters will affect the stick region.
- The lower the osculation ratio (s) is, the more relevant the stick region will be. This effect is justified, because the contact ellipse grows with the conformity, moving away from the ideal condition of point contact with null relative velocity, and therefore making ball-raceway adhesion more unlikely.
- As was predictable, sliding increases as the friction coefficient (μ) decreases.
- Similarly to what happens with the conformity, ball-raceway adhesion becomes more unlikely when the interference (δ) is increased due to the growth of the contact ellipse.

From the conclusions of the sensitivity analysis, two different case studies are proposed for comparison: Case A, where the values selected for parameters s, μ and δ favour sliding; and Case B, where the maximum area for the stick region is sought. For Case A, similar results are expected for the three approaches (Leblanc and Nélias [56], FRANC and FE). On the contrary, important discrepancies should be reported for Case B, since full sliding is assumed in the model of Leblanc and Nélias.

In order to extend the conclusions of the study to every load condition, three different subcases have been considered for both cases A and B: the first with two contact points (allowing ball rolling) as in the sensitivity analysis;

the second for four equally loaded contact points, forcing ball spinning at all of the contacts; and finally the third, which will be an intermediate case where four contact points will exist but one contact diagonal will be predominant over the other. Table 4.3 summarizes the parameters used for each analysis. Note that peak and valley values for conformity and friction coefficient do not match those in Table 4.2. This is because the values in Table 4.3 correspond to typical values found in catalogues or obtained from experimental measurements [59,102], while in the sensitivity analysis of Table 4.2, the design space was extended to evince the effect of each parameter.

Case study		Kinematical case	D_w	D_{pw}	α	s	μ	δ_1	δ_2
			[mm]	[mm]	[deg]	[-]	[-]	[%]	[%]
Nominal		K1	30	1000	45	0.95	0.10	50%	0%
Case A Sliding favoured	A1	K1	30	1000	45	0.96	0.09	75%	0%
	A2	K3	30	1000	45	0.96	0.09	75%	75%
	A3	K1 or K3	30	1000	45	0.96	0.09	75%	5%
Case B Sticking favoured	B1	K1	30	1000	45	0.94	0.13	25%	0%
	B2	K3	30	1000	45	0.94	0.13	25%	75%
	B3	K1 or K3	30	1000	45	0.94	0.13	25%	5%

Table 4.3. Studied cases for contact results comparison.

4.3.2 Results comparison

First, the cases in Table 4.3 were analyzed through the FE refined model. Then, contact forces and angles were obtained from this model as explained in section 3.2.1 and introduced as input in the analytical models. This way, the capability of each model for the simulation of the tangential problem can be evaluated through a direct comparison of the results, avoiding possible differences due to the load distribution calculation.

The objective of the comparison between the different approaches is to highlight the capabilities and limitations of each one. On the one hand, the model of Leblanc and Nélias is thought for applications where full sliding can be assumed at the ball-raceway contact. Therefore, it will have some limitations when computing shear stresses at the contact when the ball is rolling, which happens for two contact point cases (load case 1). The error will presumably be slight for limited stick regions (case A1), while a greater error is

expected when the stick region prevails in the contact ellipse (case B1). Contrarily, in those cases where spinning occurs at the contacts (cases A2 and B2), the model of Leblanc and Nélias is predicted to provide accurate results. On the other hand, the FE model considers stick regions, so it will allow the limitations to be assessed of the Leblanc and Nélias model. Nevertheless, it should be recalled that the FE model's accuracy is very dependent on the mesh size at the contact region. Consequently, the FE model is useful for a qualitative comparison, while numerical results must be carefully interpreted. Finally, the FRANC model is expected to report more accurate contact results than the model of Leblanc and Nélias when the ball is rolling. As regards friction torque, it is not possible to foresee if the results of the FRANC model will be higher or lower than assuming full sliding. As explained in the introduction of Chapter 3 (see Figure 3.2), this will depend on how the stick region affects the forward or the backward region.

In the following lines, the results for the kinematics (Table 4.4 and Table 4.5), friction torque (Table 4.6 and Table 4.7) and contact behaviour (Figure 4.14 to Figure 4.25) are compared. Succinctly, the differences are very slight for the kinematics, while important disagreements are detected in the shear stresses when the ball is rolling, which affects the friction torque but to a lesser extent. Contrarily, when the ball is spinning with respect to the four contact points, a good match is observed between the different models.

Case study		**Kinematical case**	**Approx.**	**Leblanc &Nélias**	**FRANC**	**FE**	**FRANC VS FE**
			[rad/s]	[rad/s]	[rad/s]	[rad/s]	[%]
Nominal		K1	32.63	32.96	32.97	32.83	0.4%
Case A Sliding favoured	A1	K1	32.63	33.27	33.27	33.12	0.4%
	A2	K3	46.30	43.39	43.39	42.79	1.4%
	A3	K1	32.63	33.27	33.26	33.10	0.5%
Case B Sticking favoured	B1	K1	32.63	32.76	32.77	32.63	0.4%
	B2	K3	46.16	45.50	45.50	45.06	1.0%
	B3	K3	46.15	43.91	43.91	42.80	2.6%

Table 4.4. Results for the angular velocity of the ball (ω_B).

Case study		Kinematical case	Approx.	Leblanc &Nélias	FRANC	FE	FRANC VS FE
			[deg]	[deg]	[deg]	[deg]	[deg]
Nominal		K1	134.9	134.9	134.9	133.8	1.1
Case A Sliding favoured	A1	K1	134.8	134.8	134.8	133.9	0.9
	A2	K3	180.0	180.0	180.0	180	0.0
	A3	K1	134.8	136.3	136.0	135.9	0.1
Case B Sticking favoured	B1	K1	135.0	135.0	135.0	133.8	1.2
	B2	K3	180.0	180.0	180.0	180	0.0
	B3	K3	180.0	176.9	176.9	175.8	1.1

Table 4.5. Results for the angle of the angular velocity of the ball (β).

The kinematics are going to be studied first. Table 4.4 shows the results for the angular velocity of the ball (ω_B) for an angular velocity of 1rad/s for the inner ring (ω_i), while Table 4.5 compiles the values of the β angle. The tables show that the kinematics are almost the same for both analytical models in any case. FE results are also very close, with a maximum relative error of 2.6% for ω_B and 1.1º for β. In both tables, it is demonstrated that the approximated approach proposed in the subsection 4.2.2 provides a good estimation for the kinematics (Approx. in Table 4.4 and Table 4.5). Regarding the intermediate cases A3 and B3, it was found that the ball rolls with respect to diagonal 1 (points P_1 and P_3) and slides on diagonal 2 (points P_2 and P_4) in A3 (K1 case), while spinning occurs at the four points in B3 (K3 case). For the sake of clarity, the kinematical case (Table 4.1) is also given in the results tables.

Let us now compare friction torque results in Table 4.6. In those cases where spinning occurs (K3 case), both analytical models achieve exactly the same results, since no stick regions exist at the contacts. Contrarily, when rolling occurs (K1 case), FRANC offers slightly smaller values. The discrepancy is scant in the A1 and A3 cases, while a difference of 8% takes place in the B1 case. This makes sense, since the sliding is favoured in the A cases and sticking in the B cases, and the model of Leblanc and Nélias does not consider stick regions. Moreover, the friction torque calculated by the FRANC model is always smaller, which means that both forward and backward regions are being equally affected by the stick region. Looking at the FE results, they are close to the analytical models when spinning occurs, with

a maximum difference of 5%, and always give slightly greater values. Contrarily, when rolling occurs, important differences are detected. In cases A1 and A3, the results from the FRANC model are 12-13% lower than those provided by the FE model, while in case B1 it is 59% higher. However, in the nominal case the results are practically the same. To better understand these facts, shear stresses must be analysed.

Case study		Kinematical case	Leblanc &Nélias	FRANC	FE	L&N VS FRANC	FRANC VS FE
			[N·m]	[N·m]	[N·m]	[%]	[%]
Nominal		K1	17.1	16.8	16.9	2%	0%
Case A Sliding favoured	A1	K1	64.7	64.2	73.4	1%	-12%
	A2	K3	1165.4	1165.4	1228.9	0%	-5%
	A3	K1	138.9	138.4	158.3	0%	-13%
Case B Sticking favoured	B1	K1	2.9	2.7	1.7	8%	59%
	B2	K3	117.2	117.2	121.0	0%	-3%
	B3	K3	57.5	57.5	59.4	0%	-3%

Table 4.6. Friction torque results comparison.

Before looking at the stresses, the friction torque results will be studied in more detail. For this purpose, the friction torque is divided into two components: the friction torque due to the forces in the forward region, opposed to the rotation, and the friction torque due to the forces in the backward region, in the contrary direction. The total torque is the subtraction of both components. These components were obtained for the different studied cases using the FRANC model, and they are listed in Table 4.7. This table shows that forward and backward components are of the same order of the total friction torque when spinning occurs, but they are 1 or 2 magnitude orders higher when rolling. This means that the problem is very sensitive in the latter case. To illustrate this fact, the nominal case is used. In this case, the forward component is 674.6N·m, and the backward 657.8N·m, so the total friction torque is 16.8N·m. As demonstrated before, the kinematics are almost the same for both analytical models. Nevertheless, if the kinematics obtained from the model of Leblanc and Nélias are introduced in the FRANC model, changing ω_B from 32.9650rad/s to 32.9609rad/s (-0.01%), the total friction torque is largely affected. This small change in the kinematics very slightly

affects each component, incrementing the forward by 0.7% and decreasing the backward by 0.9%. Nonetheless, this small effect on each component has a great impact on the subtraction of both values, achieving a total friction torque 61.9% greater. This means that, to obtain accurate results, a very restrictive convergence criterion is required.

Case study		Kinematical case	Forward	Backward	Total
			[N·m]	[N·m]	[N·m]
Nominal		K1	674.6	657.8	16.8
Nominal with kinematics from the model of Leblanc and Nélias		K1	679.0 (+0.7%)	651.8 (-0.9%)	27.2 (+61.9%)
Case A Sliding favoured	A1	K1	1346.3	1282.0	64.2
	A2	K3	3284.6	2119.2	1165.4
	A3	K1	1419.4	1281.0	138.4
Case B Sticking favoured	B1	K1	241.7	239.0	2.7
	B2	K3	634.8	517.6	117.2
	B3	K3	339.7	282.2	57.5

Table 4.7. Detailed friction torque results for FRANC model.

Contact results are going to be studied now. Figure 4.14 to Figure 4.19 shows shear stresses and contact status for the cases where the ball is rolling. Since stick regions exist in these cases, one of the contacts (P_1) was studied in more detail through the submodel, in order to obtain more accurate FE results. Therefore, these figures show contact results for both analytical approaches and both FE models, allowing a direct comparison. Looking at the contact status, the dependency of the FE model on the element size is once more evinced. Moreover, the stick region is always smaller in the submodel, obtaining results very similar to the ones offered by the FRANC model. In other words, the more accurate the FE results, the more similar they are to the results from the FRANC model. Looking at the shear stresses, it can be seen how they are evidently affected by the stick regions. Nevertheless, the FRANC model shows a high gradient in the stick regions, which is not reproduced in the FE model. This is because in the latter, the shear stresses are computed for each element, and there are not enough elements in the adhesion band to show these kinds of stress gradients.

As expected, the stick region in cases A1 (Figure 4.15) and A2 (Figure 4.16 to Figure 4.18) is less significant than in the nominal case (Figure 4.14). Note how the adhesion bands in A2 are displaced in the $-X$ direction with respect to A1, both in the FRANC model and FE models. Looking at the vector field superposed on the module plot, it can be noticed how in A2, the spinning component is more noticeable at point P_3 (Figure 4.17) than at point P_1 (Figure 4.16) according to both analytical models. This is consistent with the fact that the contact is less conformal in the circumferential direction in the inner ring, thus offering less opposition to the spinning movement. As the ball is rolling in A2 but there are four points in contact, the ball slides with respect to the raceway in the less loaded diagonal (see Figure 4.18).

On the other hand, the stick region in B1 is very relevant (Figure 4.19). In this case, the global model shows a contact that is in adhesion in almost the entire ellipse (Figure 4.19c). Therefore, shear stresses are largely affected both in the backward region and in the forward region, so the difference is also very small. This is why this model offers such a low value for the friction torque in B1 in Table 4.6 for the FE model. In the submodel, the stick region is more restricted and tends to the results provided by the FRANC model. Note that, as the element size in the FE submodel is the same for every case, and since the contact area is very small in B1, this contact is represented by fewer elements than in the other cases. This is why the submodel differs more from the FRANC model than in other cases, although the tendency is clearly convergent towards the analytical approach. This case is the one that represents more clearly the limitations of the FE models and the approach of Leblanc and Nélias in comparison with the FRANC model.

Looking at the vector plots, two vortexes can be noticed on the rear edge of the contact ellipse in FE calculations when the ball rolls. In the FRANC model, one of the vertexes is also placed on the rear edge, but the other one is near the leading edge. Although FE results can lack accuracy, qualitatively they are expected to represent better contact deformations, so this fact represents a limitation of the analytical approach. This leaves the door open for future research and improvement of the FRANC model.

Figure 4.20 to Figure 4.23 show the results for those cases where the ball is spinning at the contacts. In this case, the results are the same for both analytical models, and show a good match with FE calculations. The stick regions according to FE analyses are located in the vortexes of the vector field, where the relative velocity is null. In the B2 and B3 cases, a small stick

region is obtained on the leading edge (Figure 4.21 and Figure 4.22), but it must be noted that in these cases the contact has not enough elements in order to adequately represent the stick regions (as in Figure 4.19c).

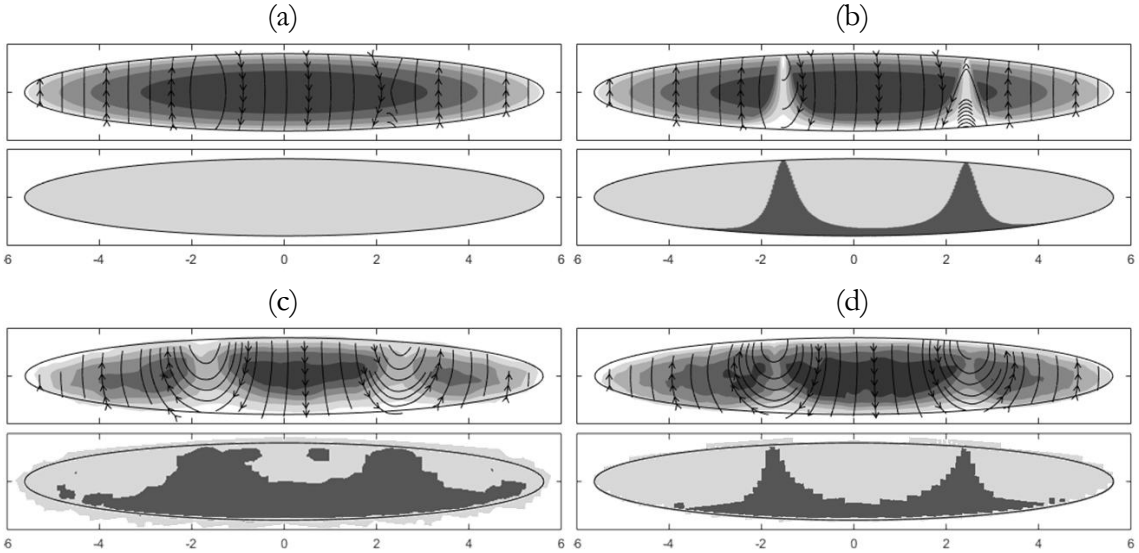

Figure 4.14. Shear stress and contact status for point P1 of the nominal case: (a) Leblanc and Nélias' model; (b) FRANC model; (c) FE global model; (d) FE submodel.

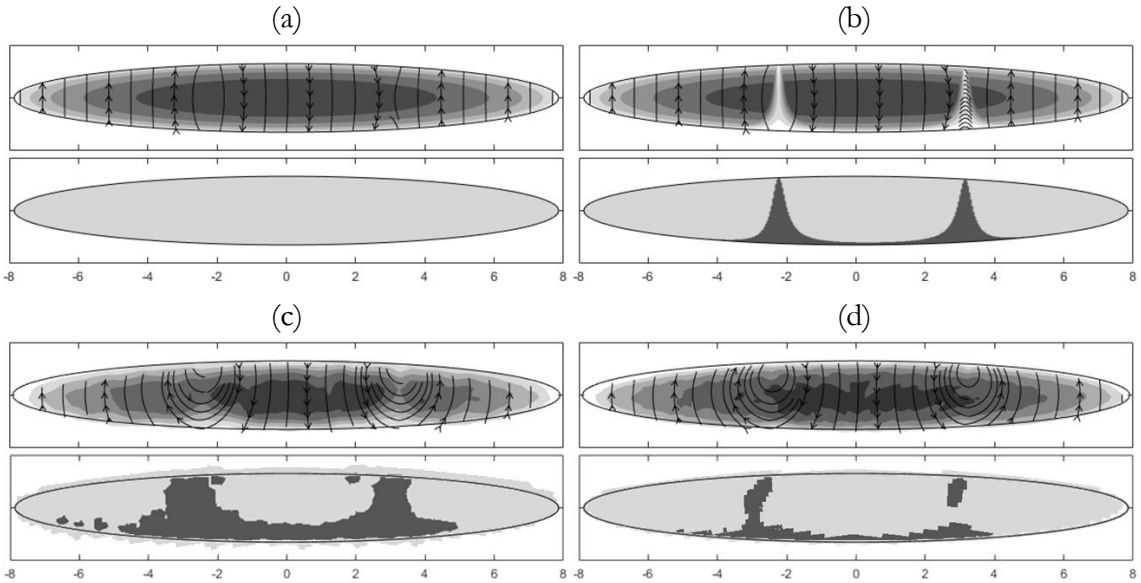

Figure 4.15. Shear stress and contact status for point P1 of the A1 case: (a) Leblanc and Nélias' model; (b) FRANC model; (c) FE global model; (d) FE submodel.

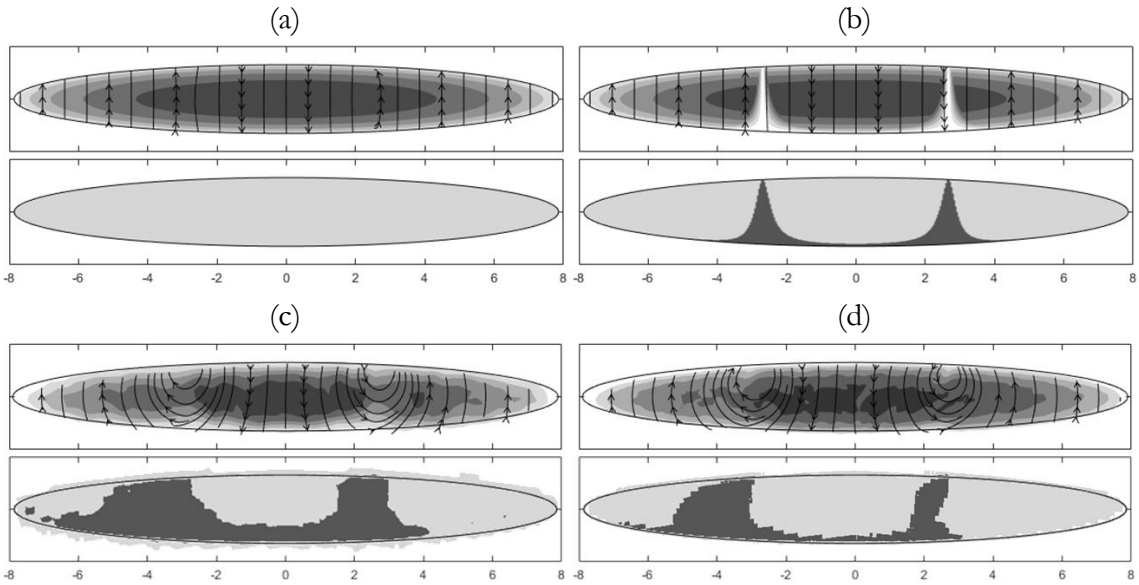

Figure 4.16. Shear stress and contact status for point P1 of the A3 case: (a) Leblanc and Nélias' model; (b) FRANC model; (c) FE global model; (d) FE submodel.

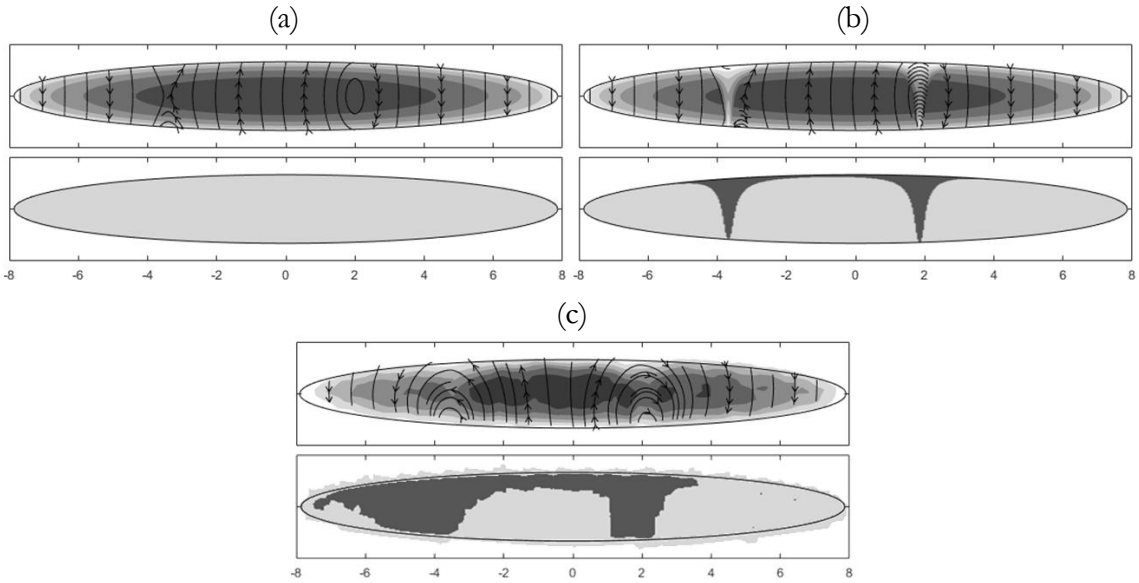

Figure 4.17. Shear stress and contact status for point P3 of the A3 case: (a) Leblanc and Nélias' model; (b) FRANC model; (c) FE global model.

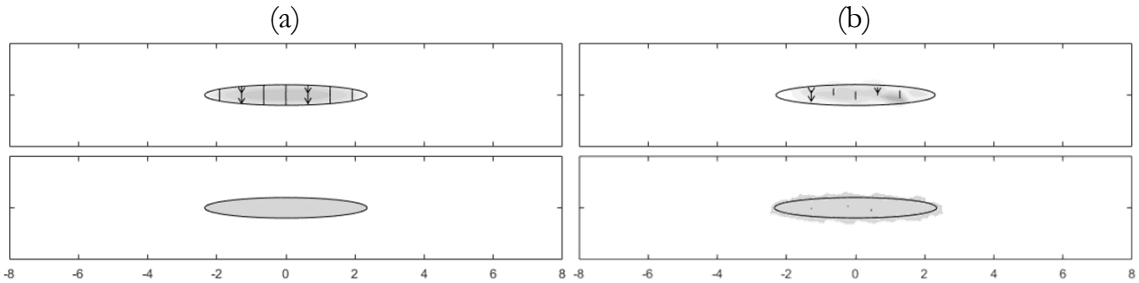

Figure 4.18. Shear stress and contact status for point P2 of the A3 case: (a) analytical models (Leblanc and Nélias' model or FRANC model); (b) FE global model.

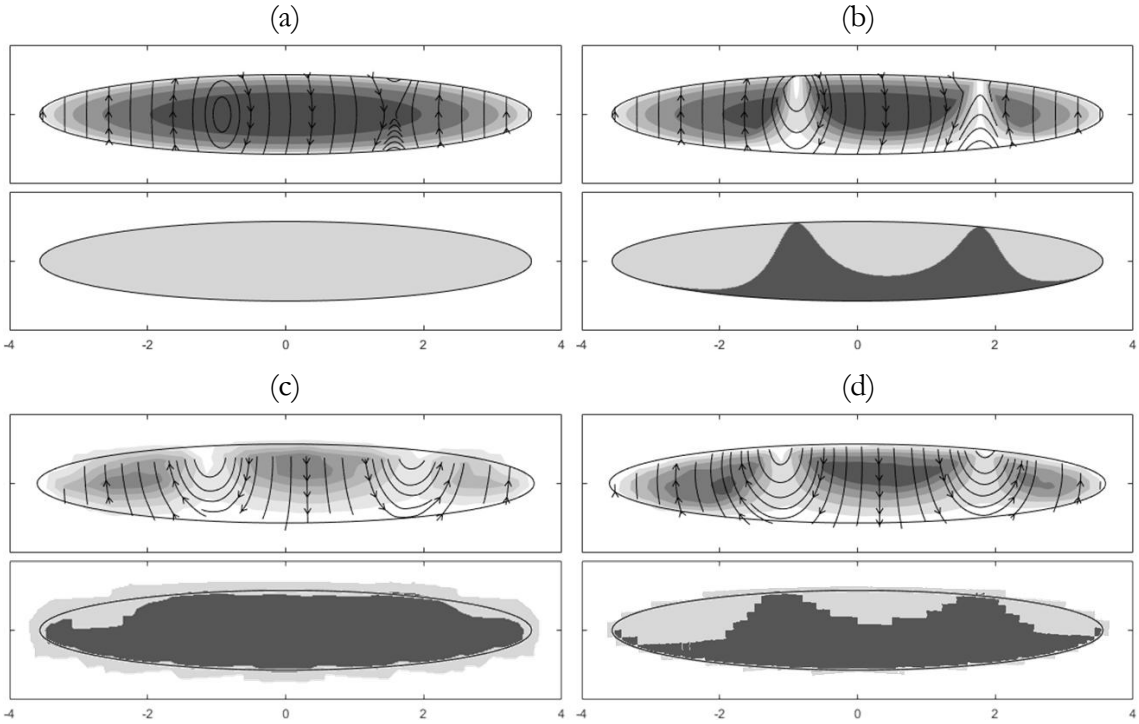

Figure 4.19. Shear stress and contact status for point P1 of the B1 case: (a) Leblanc and Nélias' model; (b) FRANC model; (c) FE global model; (d) FE submodel.

Finally, Figure 4.24 and Figure 4.25 show the results for the nominal case (rolling) and B2 case (spinning) considering that the shear stresses in the slip region are given by equation (4.63) instead of (4.59). This means that the directions of the shear stresses in the slip region are calculated from the components τ_Y^A and τ_X^A instead of τ_Y^S and τ_X^S , as proposed by Kalker for the plane contact. By this assumption, the friction torque does not vary for the nominal case, and decreases from 117.2N·m to 105.9N·m for B2. Looking at the shear stress vector field, it is very similar when rolling, but it changes slightly when the ball is spinning. In the latter case, the FRANC model is more similar to the FE results, except for the location of the vortex of the vector field. Figure 4.25b shows how, assuming (4.63), this vortex is displaced towards the rear edge, which is consistent with what is observed in the FE model. Therefore, further research can be done to find the values of the flexibility parameters (L) that, assuming Kalker's formulation for the directions of the shear stresses in the slip regions, would fit the directions observed in the FE results.

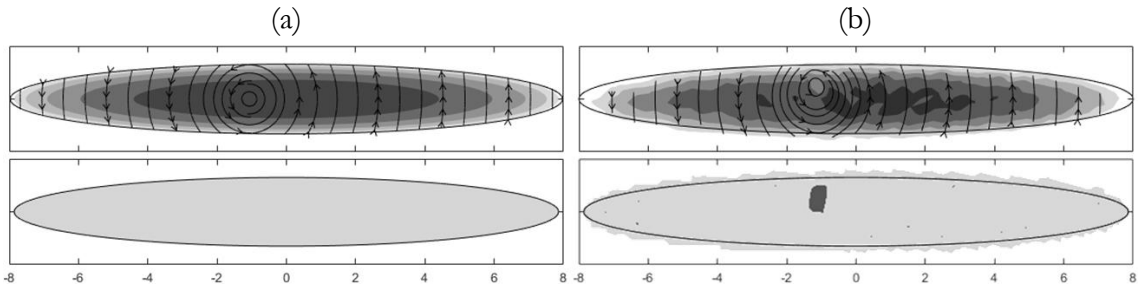

Figure 4.20. Shear stress and contact status for point P1 of the A2 case: (a) analytical models (Leblanc and Nélias' model or FRANC model); (b) FE global model.

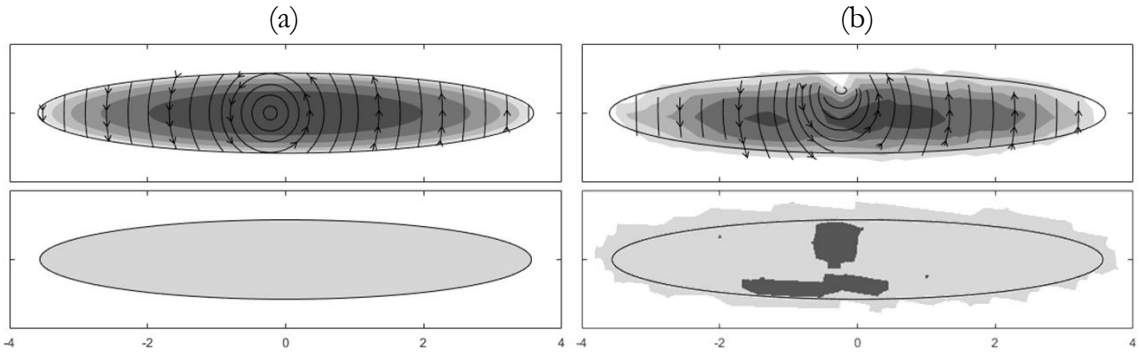

Figure 4.21. Shear stress and contact status for point P1 of the B2 case: (a) analytical models (Leblanc and Nélias' model or FRANC model); (b) FE global model.

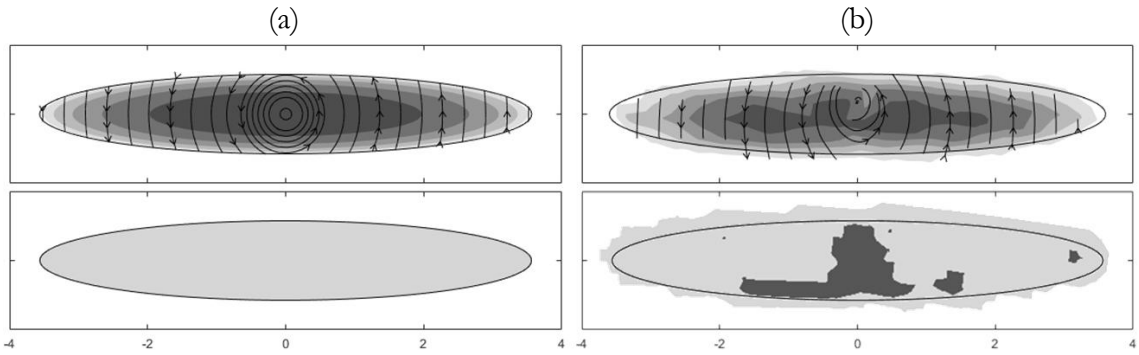

Figure 4.22. Shear stress and contact status for point P1 of the B3 case: (a) analytical models (Leblanc and Nélias' model or FRANC model); (b) FE global model.

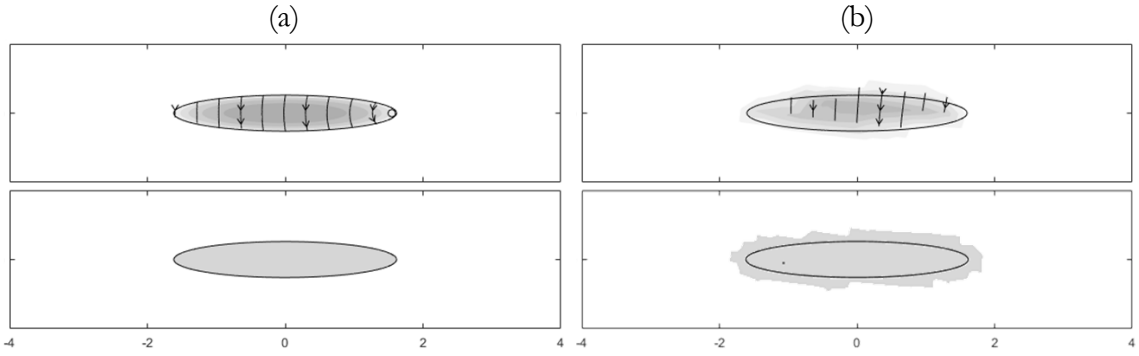

Figure 4.23. Shear stress and contact status for point P2 of the B3 case: (a) analytical models (Leblanc and Nélias' model or FRANC model); (b) FE global model.

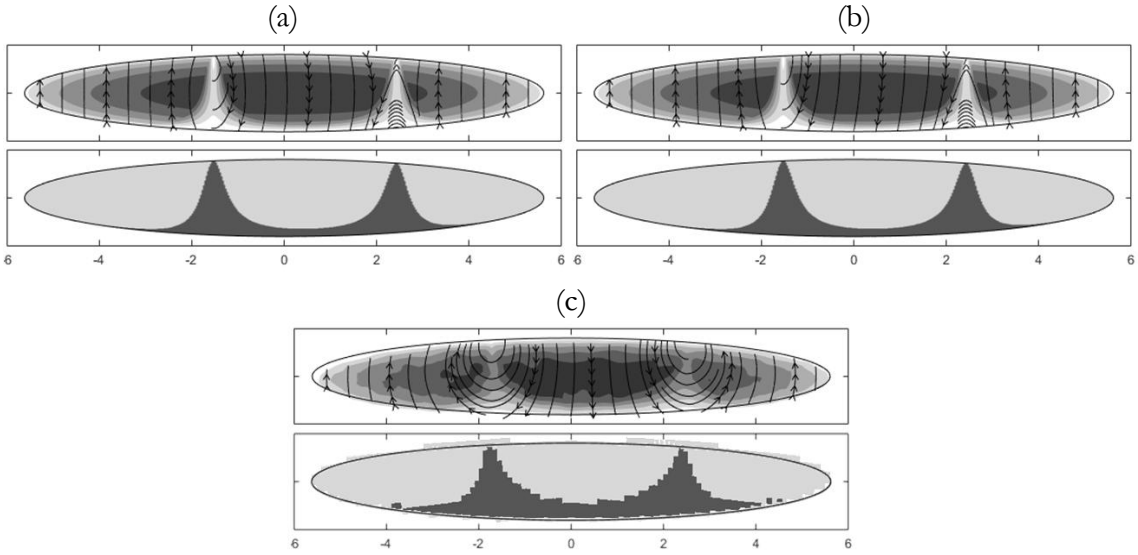

Figure 4.24. Shear stress and contact status for point P1 of the nominal case: (a) FRANC model; (b) Kalker's formulation; (c) FE submodel.

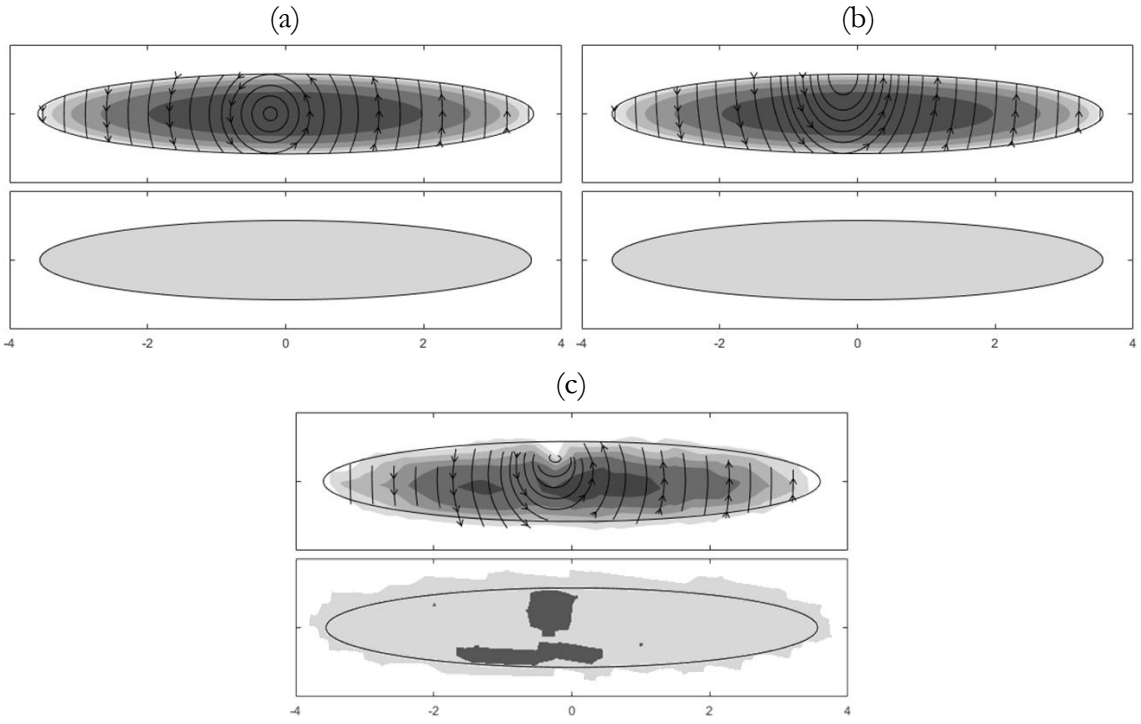

Figure 4.25. Shear stress and contact status for point P1 of the B2 case: (a) FRANC model; (b) Kalker's formulation; (c) FE global model.

As a conclusion, the FRANC model was proved to give more realistic results for shear stresses than the approach of Leblanc and Nélias when the ball rolls. Taking into account that in slewing bearings balls mainly work with two contact points because of the large tilting moments, the FRANC model is more suitable to estimate the shear stress field in such components. Nonetheless, the model of Leblanc and Nélias has been demonstrated to give good results when the ball is spinning. It is also appropriate to predict kinematics and for friction torque calculations in any load condition.

In comparison with the FE models, the FRANC model offers two main advantages. On the one hand, the FE model requires a very fine mesh to reproduce results similar to the ones obtained with the FRANC model. This involves very high computational costs, while the FRANC model only requires a few seconds. On the other hand, and due to the sensitivity of the problem when the ball is rolling, a very restrictive criterion is required for the convergence of the calculations. In this aspect, the FRANC model can be easily controlled by imposing small tolerances on the kinematical variables and the imposed equilibrium equations in the solver. Contrarily, the convergence criterion of the FE model is only based on the reaction forces. This criterion is usually automatically controlled by the FE program, and fixing a different one would require further research. Moreover, FE results depend strongly on other aspects like the discretization or the contact formulation. Therefore, the results obtained by different analysts can vary, making direct comparisons difficult between results obtained from different models.

4.4 Friction torque calculation procedure

The FRANC model was linked to the BIME model in Matlab®, forming a unique program capable of calculating load distribution, friction torque and contact stresses, considering manufacturing errors, ring stiffness and stick regions at the contact. This program constitutes a new and powerful tool for the design of four-point contact slewing bearings, which allows accurate simulations with a low computational cost to be performed. The models were programmed to offer the option to perform calculations for the nominal geometry (with no manufacturing errors), considering rigid rings or assuming full sliding at the contact. This way, comparisons can be made quickly, and the effect of each assumption evaluated.

At least, the program requires the following inputs: bearing mean diameter (D_{pw}), ball diameter (D_w), osculation ratio (s), initial contact angle (α_0), number of balls (N), ball preload (δ_P) and applied forces (F_a, F_r and M_t) or displacements (δ_a, δ_r and θ_t). To take advantage of all the capabilities of the BIME and FRANC models, it also requires raceway measurements and the ring's stiffness matrices. Having all this information, calculating the friction torque for any bearing and load case is straightforward and will require some seconds or minutes, depending on the number of balls.

Nevertheless, measuring the raceways is a time consuming task and requires having a coordinate measuring machine. For this reason, an alternative procedure to calculate the friction torque calculation is proposed in Chapter 6. According to this procedure, the idling friction torque is required to be experimentally obtained instead of raceways geometry. With this information, the friction torque can be calculated for any applied load, and manufacturing errors estimated.

5 Bearing global stiffness

5.1 Introduction

The global stiffness tells us how much a bearing is deformed when a certain load is applied. While the stiffness matrix calculated for the load distribution in Chapter 2 establishes the structural relationship between the different points of the bearing, the global stiffness is a more extensive parameter that is used to determine how the bearing behaves in a machine with respect to the other components. In this sense, this parameter allows the designers to calculate global deformations, and consequently predict possible interferences between adjacent components or unacceptably large displacements. For this reason, the global stiffness is not only a parameter to be known in the design process when bearings are used in a machine, but it can also be subjected to certain specifications or criteria, since high values of the stiffness are required to minimise large displacements.

But the global stiffness is not only useful for such rough calculations. Moreover, it allows detailed simulations to be performed that predict the static or dynamic behaviour of the entire machine. As was explained in Chapter 1, slewing bearings are used in many machines. These machines constitute complex multibody systems, and the behaviour of their components must be somehow characterized for numerical simulations. For this purpose, the FE Method is a very useful tool. Nevertheless, an FE model for the simulation of a machine composed of several components, including rolling bearings, will be computationally unapproachable if they are not simplified by some means. A typical way to simplify the modelling of rolling bearings is to substitute them with the global stiffness matrix, and also with the corresponding mass matrix in the case of a dynamic simulation. This way, the global stiffness allows these calculations to be carried out with affordable computational costs.

Being such an important parameter, it is usually required by bearing customers in order to perform their calculations before selecting the most suitable bearing for their particular application (Figure 5.1). This information, although it rarely appears in catalogues, is usually provided by manufacturers to their clients. Nevertheless, the way they calculate it is undisclosed, for it is part of their know-how. Therefore, a simple and direct way of calculating it would be a very powerful tool for buyers. Such a tool would allow designers to select the appropriate bearing by themselves, and then make direct comparisons between the solutions offered by different bearing manufacturers.

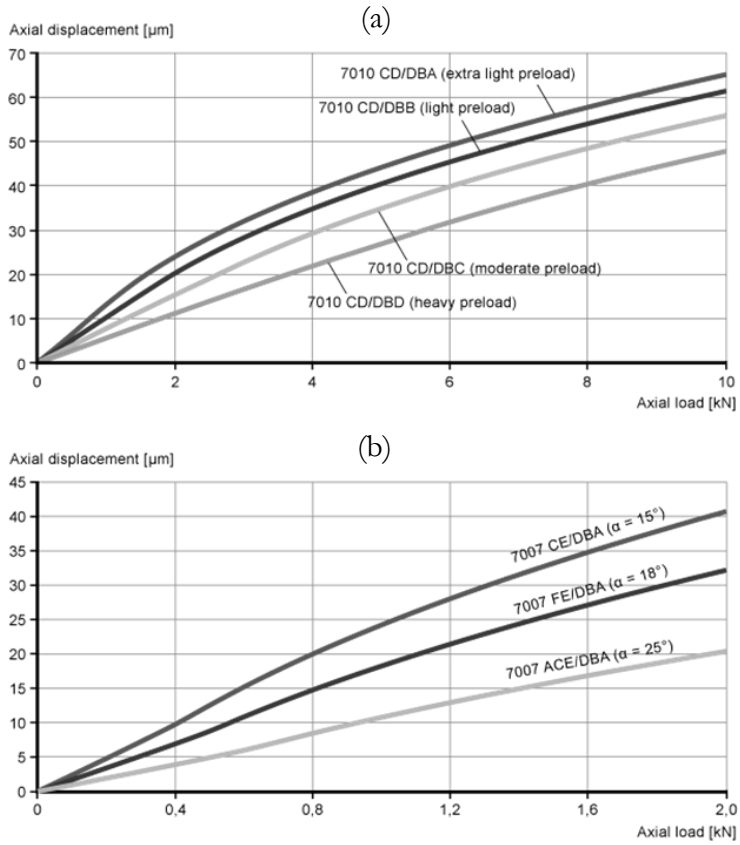

Figure 5.1. Axial stiffness plots from SKF [103]: (a) for different preloads; (b) for different contact angles.

Apart from the restricted information given by the manufacturers, neither was a methodology found in the literature for a direct calculation of the global stiffness. In Chapter 1, many load distribution models were presented, from which load-deformation curves can be built. On the one hand we have the analytical models that consider rigid rings [38,39,44], which are very practical but inaccurate, since in slewing bearings the ring flexibility is highly important (as demonstrated in [44] and also later in this chapter). On the other hand, there are both semi-analytical [40] and numerical [77,81,83] models that can

deal with the ring flexibility issue, but they need FE calculations, either for the stiffness matrix calculation or to directly perform the load distribution simulation. In any case, they can calculate the stiffness considering the ring flexibility, but only for one particular design and through complex and computationally expensive FE models. Neither is any formulation nor methodology for the stiffness estimation in any bearing standard [8,9] or recognized design guideline like NREL [19].

What it is proposed in this chapter is to obtain a direct and simple way of calculating the global stiffness in four-point contact slewing bearings, considering ring flexibility. For this purpose a methodology is proposed, which is developed in the following sections, and which can be later replicated for other types of slewing bearings (crossed roller, three row roller, etc). As a result, a simple formulation is obtained, which is demonstrated to replicate the effect of main geometrical parameters and contact variables.

The proposed methodology to achieve the desired formulation is based on the fact that slewing bearings fulfill certain geometrical relationships. In this sense, and as later demonstrated, the geometry of four-point slewing bearings is mainly defined by the bearing mean diameter (D_{pw}), which gives the global size, and the ball diameter (D_w), which determines the dimensions of the radial section. These parameters are called main parameters. The first step is to study the design space, namely, to ascertain the typical values of the main parameters, and so delimit the scope of the study. Then, the standard design must be defined. The standard design is defined only by the main parameters, and fulfills the geometrical relationships mentioned before. For these two first steps, the catalogues of the main slewing bearing manufacturers [6,7,20,25,104] were used, to ensure that the standard design is representative for every commercial bearing.

Once the standard design is defined, a Design Of Experiments (DOE) is proposed; in other words, a series of calculations are planned, covering the delimited design space by considering different values of the main parameters. As a result of the DOE, the load-deformation curves are obtained for each Design Point (DP) of the DOE and each load case, namely, axial and radial forces and tilting moment. The calculations to obtain these curves must be as accurate as possible, taking into consideration not only the ring-flexibility, but also other phenomena like flange-ring contact nonlinearities or bolt preload. Therefore, semi-analytical models like the one proposed in Chapter 2 do not fulfill the desired accuracy, despite the fact that they consider ring flexibility.

For this reason, the FE method is used. Although FE calculations are highly time consuming, the goal of the methodology is not to have to use them again in the future for the stiffness calculation. Finally, the results are analyzed and a formulation proposed. The aim of the results analysis is to reach a formula for each load case, which will be a function of the main parameters, capable of reproducing the load-deformation curves obtained from all FE calculations. In other words, the goal is to obtain simple mathematical expressions to calculate the stiffness of any bearing. Additionally, the formulation is extended to also consider contact parameters.

It is worth pointing out that the load cases to be considered are axial and radial forces and tilting moment. Consequently, three formulas are obtained from the application of the described methodology. Each formula will give the stiffness curve for each load, but not the interactions between them. Slewing bearings are designed to face a combination of such loads, so simplifying their stiffness behavior by a diagonal matrix is an approximation. Nevertheless, it must not be forgotten the wide-range application field of the proposed approach, which also reproduces the nonlinearity of the load-deformation curves. A non-zero out-of-diagonal terms matrix can be calculated by FE calculations for a specific bearing and certain load range, but to obtain such a matrix for a general purpose is beyond the scope of this research. Moreover, this data is commonly not offered by bearing manufacturers, since it is rarely required by customers.

5.2 Standard design definition

As explained in the introduction, the geometry of slewing bearings mainly depends on two parameters: the bearing mean diameter (D_{pw}) and the ball diameter (D_w). These parameters are called main parameters, and the standard design is a bearing that is defined only by them. Therefore, the dimensions of the radial section of the bearing, the number of balls (N_b), the number of holes (N_h) and the bolt metric (M) of the standard design will be a function of D_{pw} and D_w.

Conversely, there are other parameters that are not a function of the main parameters. These are contact parameters, namely conformity ratio (s), initial contact angle (α), filing ratio (R_{fill}, which is defined later) and ball preload (δ_P), and bolt preload. Although the last two are not geometrical parameters, they must be defined, since they affect the structural behaviour of the bearing.

In this section, a standard design capable of representing every bearing in the catalogues of the main manufacturers is defined. Nonetheless, a prior study is presented, where the design space to be considered is defined.

5.2.1 Study of the design space

For the study of the design space, the catalogues from Iraundi [25], SKF [7], Rothe Erde [6], Schaefler [20] and Lyc [104] were studied. Some other manufacturers, like Rollix, do not include the dimensions of the ball in their catalogues [23], while others, like Laulagun, do not have a catalogue because they offer particular solutions for each application [26]. The values of the main parameters for every four-point contact slewing bearing were compiled and represented in the plot in Figure 5.2. In the plot, over 200 bearings are represented, including regular and light series (see Chapter 1). Based on this point-cloud, the design space is defined, which is delimited by the curves on the same plot, representing upper and lower limits. Therefore, the scope of the study covers every slewing bearing from the main manufacturers, embracing bearings with balls between 15mm and 55mm, and with a mean diameter up to 3500mm.

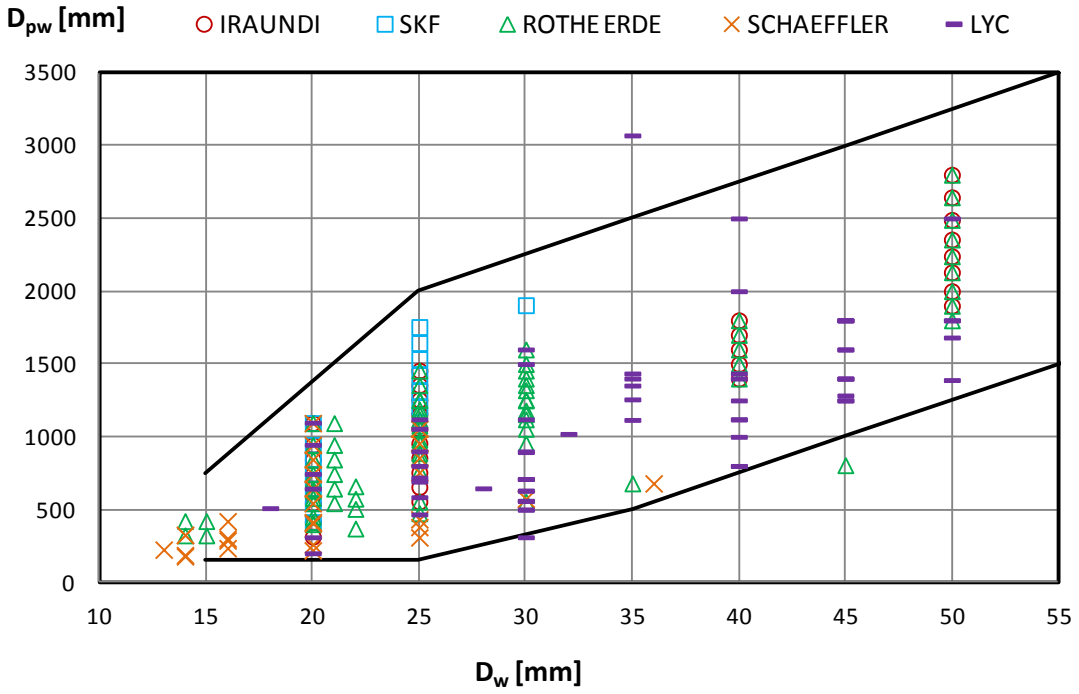

Figure 5.2. Values of the main parameters for slewing bearings from the main manufacturers.

It is remarkable the homogeneity in the dimensions noticed through the different catalogues. For the 20mm ball, for example, Iraundi, SKF, Rothe

Erde and Schaefler offer bearings with a mean diameter of 414mm, 544mm, 644mm, 744mm, 844mm, 944mm and 1094mm, exactly the same values in all the catalogues.

Based on the design space defined in Figure 5.2, the DOE in Figure 5.3 is proposed, which consists of 14 design points. In the figure, the number of each DP is shown for further referencing. Note that three FE calculations correspond to each design point, one for each load case, so a total of 42 calculations are proposed.

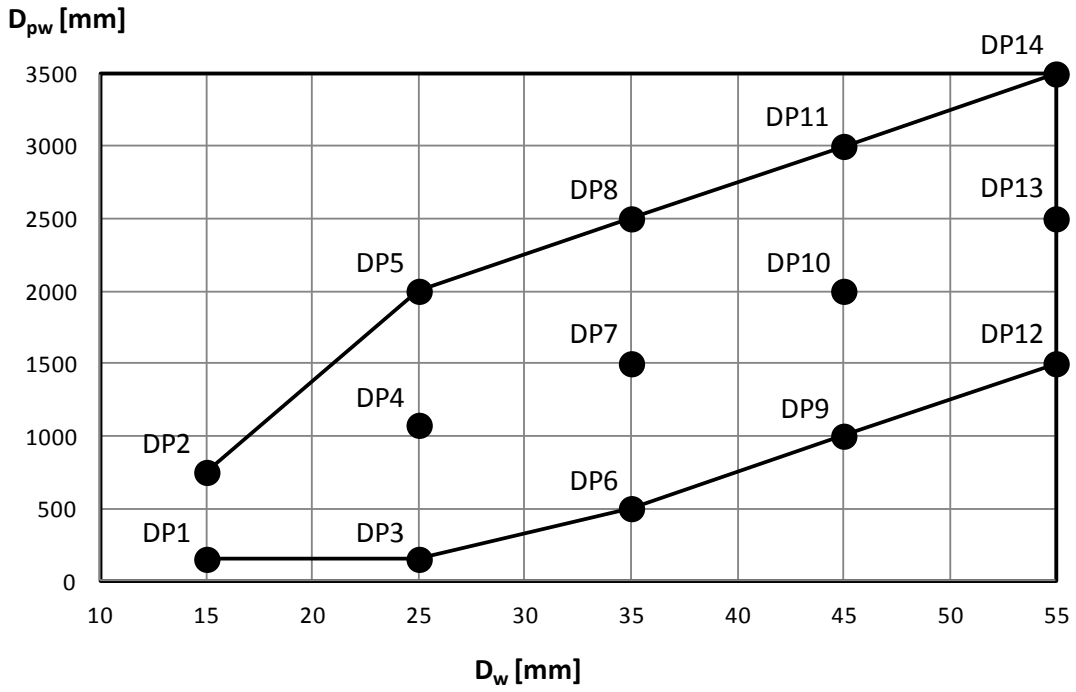

Figure 5.3. Proposed DOE for the design space study.

5.2.2 Study of the parameters

For the standard design definition, the bearings from the catalogues of Iraundi and SKF were used in a first approach. For this study, only standard series were considered with internal, external or no gear. Overall, the parameters of 90 bearings were considered. After defining the standard design, it was validated by contrasting it with bearings from the catalogues of the other mentioned manufacturers.

For the standard design, the following considerations were assumed in order to simplify its definition and minimise the number of involved parameters. Such simplifications were demonstrated not to affect the results.

- Anti-symmetric section: the radial section is assumed anti-symmetric.

- No geared rings: no gear is considered in the standard design. Nevertheless, the dimensions of the geared bearings in the catalogues were taken into account for the standard design dimensioning. In such cases, the primitive diameter was considered.
- No threaded through holes: in real bearings, holes can be through or blind, threaded or not threaded. For simplifying purposes, no threaded through holes are considered.
- Same number of holes: under a certain tilting moment, inner bolts are more stressed than outer ones. For this reason, sometimes more bolts are placed in the inner ring. However, the difference between inner and outer bolt numbers is small, especially for big diameters. For this reason, the same number of holes is considered in both inner and outer rings.

Figure 5.4 shows the sketch of the section of the standard design. According to the mentioned assumptions, the section is defined by eight parameters apart from the main ones, five of which are a function of the ball diameter (D_w) through R_H, R_L, R_{Lg}, R_{Lt} and R_{Dt} ratios. The other three are the height H_g and contact parameters s and α. Non-contact parameters were addressed first. Thus, the values of the mentioned ratios and H_g were calculated and compiled for the 90 bearings. By analysing them, it was found that they were very similar for every case, so average values were adopted. Table 5.1 shows these values.

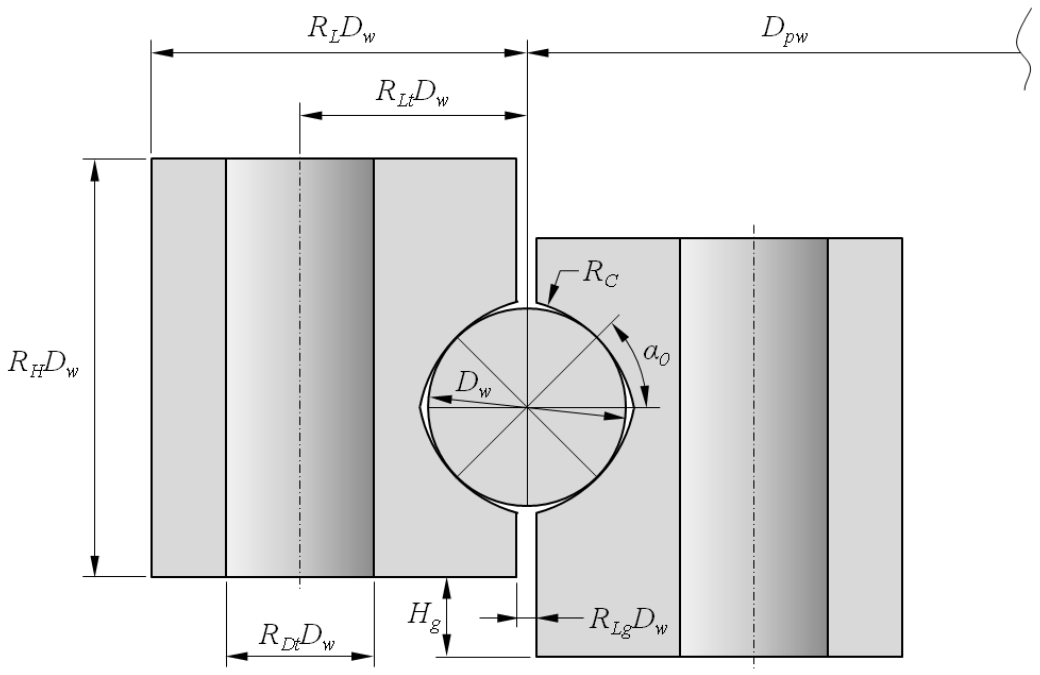

Figure 5.4. Sketch of the standard section.

R_H	H_g	R_L	R_{Lg}	R_{Lt}	R_{Dt}	R_{Nh}
2.15	10mm	1.9	0.1	1.15	0.75	1

Table 5.1. Dimensional values for the standard design.

Table 5.1 also shows the value for another coefficient, R_{Nh}, which relates the number of holes (N_h) with the main parameters through the following expression:

$$N_h = R_{Nh}\frac{D_{pw}}{D_w} = \frac{D_{pw}}{D_w} \tag{5.1}$$

Figure 5.5 compares the values of the dimensions of the bearings from the catalogues (dots) with the standard design for the adopted values. Subscripts a and i correspond to outer and inner rings respectively, according to the nomenclature of Iraundi. On the other hand, Figure 5.6 shows the same comparison but only for the number of holes, which is a function of both main parameters. These plots make clear that the proposed standard design satisfactorily fits the commercial designs of Iraundi and SKF. Additionally, and for validation purposes, the standard design was compared with bearings in the catalogues from the other mentioned manufacturers, also achieving a good match (see Figure 5.7). Therefore, the standard design is demonstrated as a simple way to represent regular slewing bearings. Figure 5.8 shows two examples of the standard design for different configurations.

There are still other variables to be set. For contact parameters s and α, typical values of 0.943 and 45° are assumed. It should be recalled that the ball number (N_b) is a function of the main parameters and R_{fill}, which represents the ball filling ratio:

$$N_b = round\left[R_{fill}\cdot trunc\left(\pi\frac{D_{pw}}{D_w}\right)\right] \tag{5.2}$$

According to information given by Iraundi, parameter R_{fill} goes from 80% to 100%, where this last value corresponds to the case with no ball separators. For the first approach and before including contact parameters in the study, a value of 90% is assumed. As no contact parameters are to be included for the moment, no ball preload is considered.

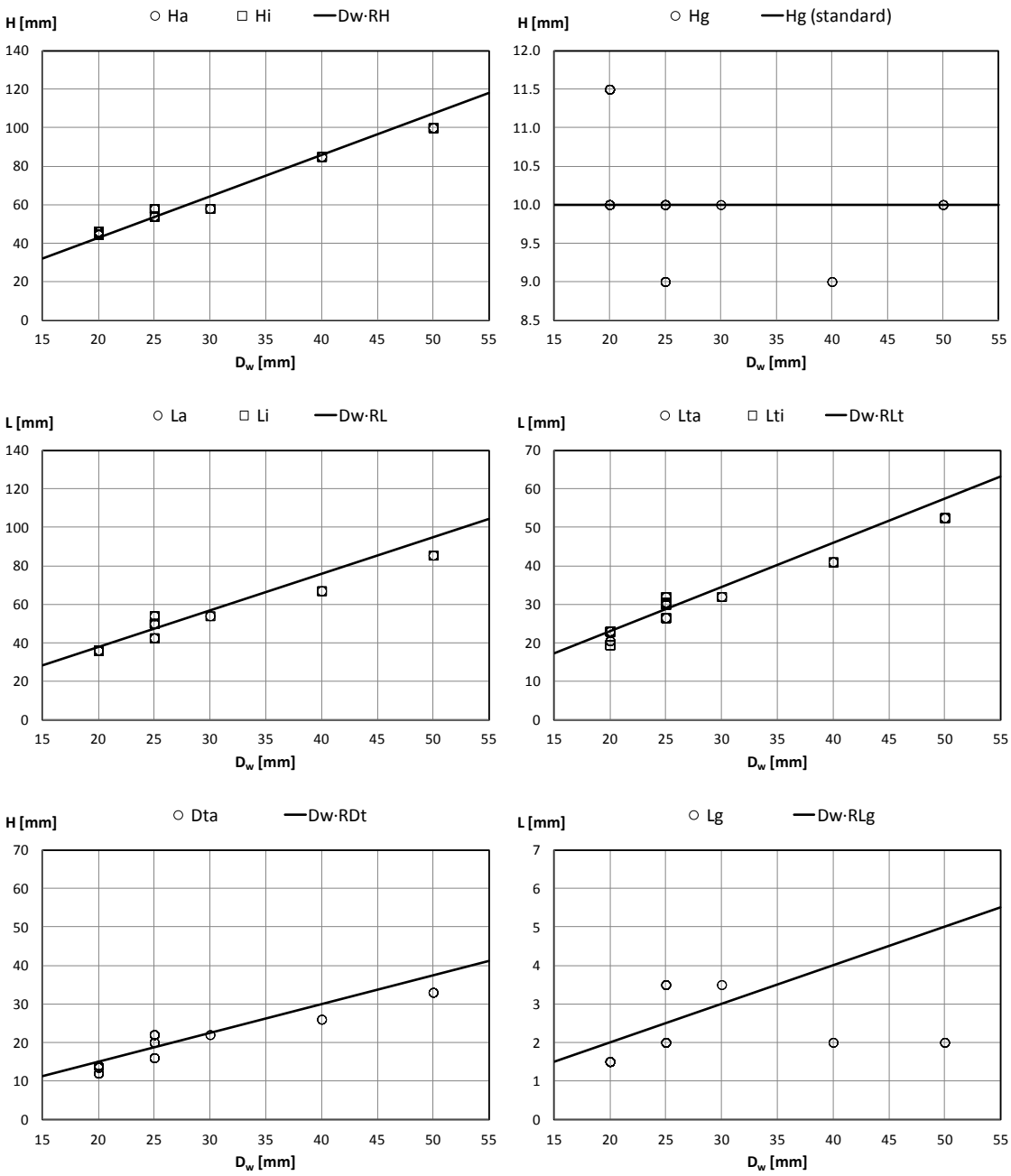

Figure 5.5. Standard section (lines) VS Catalogues (dots).

Finally, the bolted joint must be defined. Bolt preload is defined as a percentage of its elastic capacity, and in slewing bearings values from 70% to 90% are commonly used. For the standard design, a typical value of 75% is adopted. For the bolt metric, the following formula is considered, which is consistent with the bolts used according to the catalogues.

$$M = 2 \cdot trunc\left(\frac{D_t - 1.5}{2}\right) \tag{5.3}$$

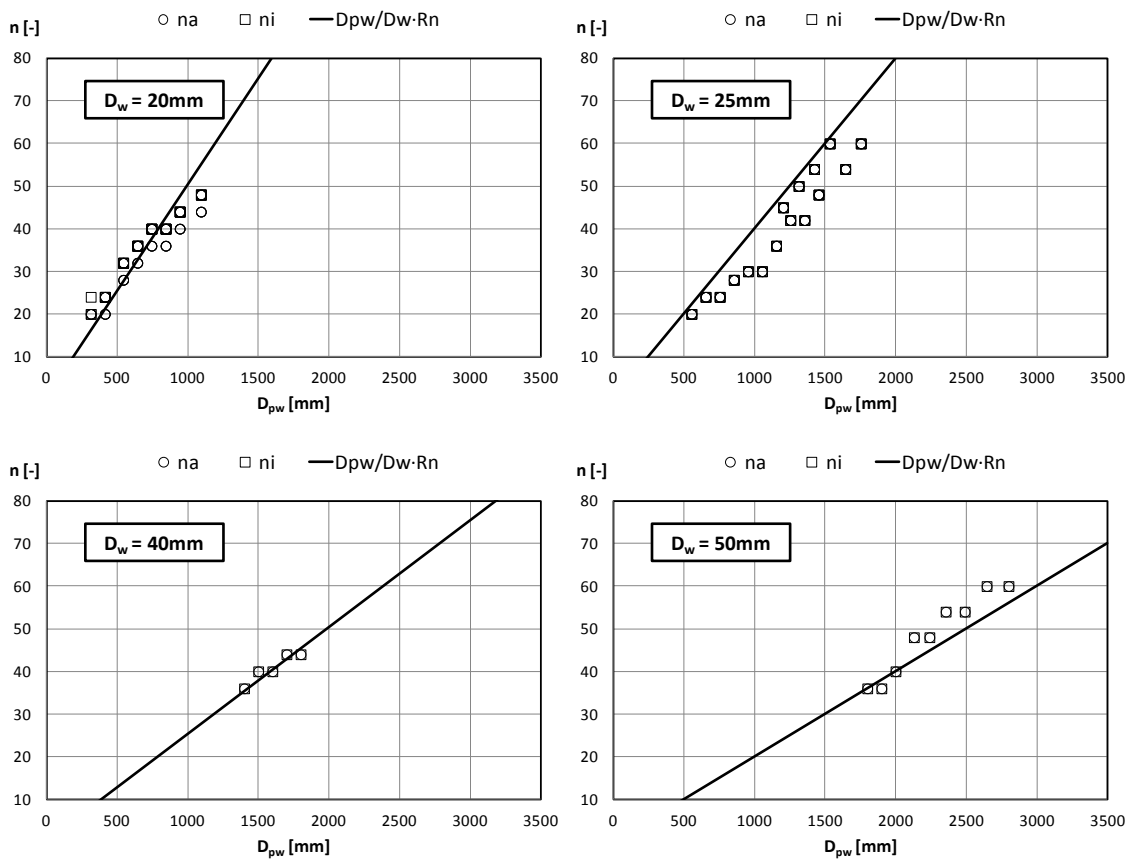

Figure 5.6. Number of holes: Standard design (lines) VS Catalogues (dots).

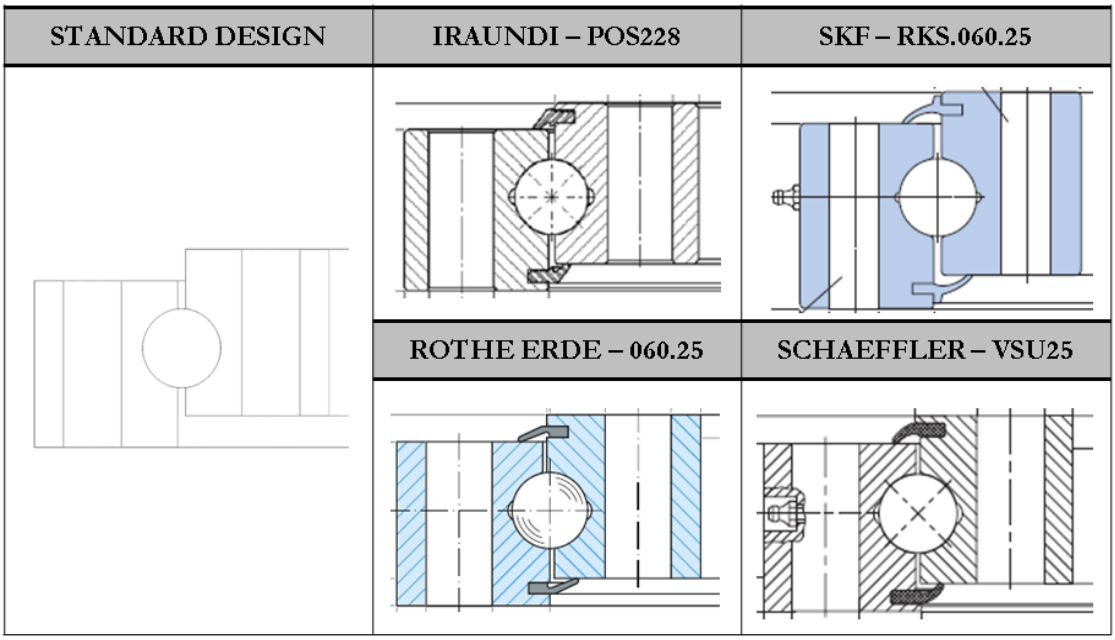

Figure 5.7. Comparison between the section of the standard design and bearings of the main slewing bearing manufacturers for D_w=25mm.

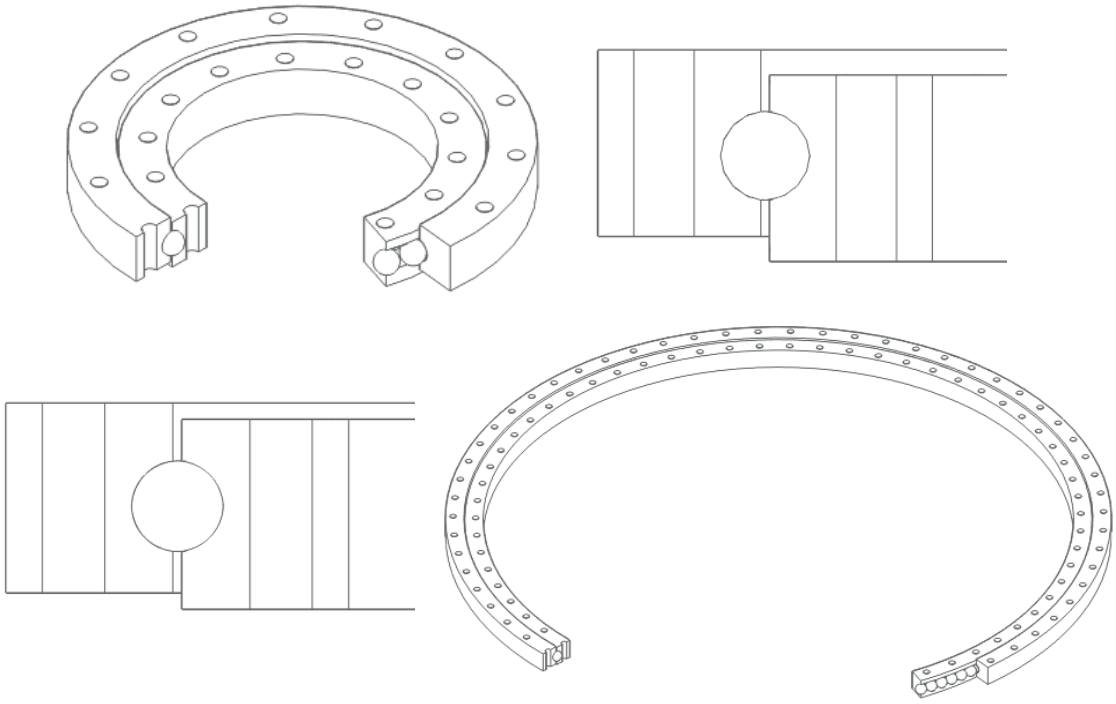

Figure 5.8. Examples of the standard design for two different configurations (DP6 and DP14).

It should be mentioned that the considered material for every component is steel, with an elastic modulus of 200GPa.

5.3 Finite Element model

The objective of the FE model is to simulate the stiffness behaviour of the bearing in the most realistic possible way. Moreover, a fully parametric and robust model is wanted in order to perform a series of calculations in an automated way, considering any geometry or load condition. For this purpose, the commercial software ANSYS® was used. Specifically, the ANSYS Workbench package was used for its parametrization capabilities, even though APDL scripts were required to address some limitations of the Workbench environment.

The geometry was done in ANSYS Design Modeller. It is a 3D geometry, where all the components are considered except for the bolts, which are introduced into the model through an APDL script, as explained later. Due to the symmetry of the geometry and the loads (see Chapter 1), only half the bearing is considered, which saves computational cost. The geometry is fully parametric, so any bearing can be obtained in a straightforward way. It is not only valid for the standard design, but any section (from regular or light series), type of hole (through or blind) or shape in general can be reproduced.

There exist simulation techniques for the simplification of the balls [81,83], which involve mechanisms formed by rigid beams and springs with the stiffness of the contacts. These techniques save computational cost and provide good results for axial load and tilting moment. Nevertheless, they have limitations for radial load. When a radial load is applied, the mentioned mechanisms are displaced in the circumferential direction and springs, which are thought to be in the radial plane, leave it and thus introduce an additional and unreal radial stiffness. As explained in Chapter 2, this residual radial stiffness can be eliminated by the proposed semi-analytical model for the load distribution calculation, but not in a FE model. For this reason, and to achieve the most accurate results possible, solid balls are used.

Apart from the bearing itself, flanges are also considered in the model. They are part of the model to simulate the joint between the rings and the adjacent structures, which involves preloaded bolts and non-linear contacts. Flanges and bolts prevent rings from deforming freely, and therefore allow a more realistic simulation. Nevertheless, the stiffness of the adjacent structures is not considered in this study, since it can change considerably with the application. Moreover, what is wanted is to calculate the stiffness of the bearing, without introducing the effect of the surrounding components. For this reason, and to obtain a wide-range formulation applicable to any case, rigid flanges are considered. Therefore, the thickness of these components is not relevant. It is worth pointing out that assuming rigid rings is not a limitation of this work, since the deformability of the surrounding structures could be considered in further calculations, where the bearing would be simplified by means of the formulas derived from the current study.

The FE simulation of a 3D bearing with solid balls involves a high computational cost. For this reason, special attention was paid to the meshing process. The geometry was divided into sweepeable bodies in order to make it easier for the mesher and achieve elements with high aspect ratios and avoid irregular residual elements. A fine mesh is only used in the contact zone, favouring the convergence of the analysis. Element size is also parametrized and it is a function of ball diameter. Figure 5.9 shows the mesh for a particular bearing from the catalogue of Iraundi, and the different colours represent different parts, so the mesh is not shared among them. In the figure, some bodies have been removed to show the internal mesh. The number of the degrees of freedom varies depending on the dimensions of the bearing, but for the standard design, it goes from around $2.6 \cdot 10^5$ for low D_{pw}/D_w ratios to

$3.6 \cdot 10^6$ for high D_{pw}/D_w ratios. The mesh used in each part is detailed in the following points:

- Rings: they are meshed with SOLID185 3D elements, with a linear displacement behaviour, mainly through hexahedrons (8 nodes), although some wedges (6 nodes) are also required in located areas. The element size is one-fourth the diameter of the ball.
- Flanges: despite wanting to simulate these as rigid bodies, this formulation showed numerical singularities and convergence problems. For this reason, the same mesh for the rings is applied to the flanges, and the rigidity is imposed by means of boundary conditions (later explained).
- Balls and contact region of the rings: due to the punctual and variable nature of the ball-raceway contact, a fine mesh of high order elements is required in the region. Consequently, SOLID186 elements are used in balls and in the rings within the raceways' vicinity, mainly through hexahedrons (20 nodes), though some wedges (15 nodes), pyramids (13 nodes) and tetrahedrons (SOLID187, 10 nodes) are also occasionally used. In the rings, the mesh from the refined part does not share nodes with the rest in order to avoid elements with a poor aspect ratio in the transition (see Figure 5.9). This is later solved by means of contact formulations.

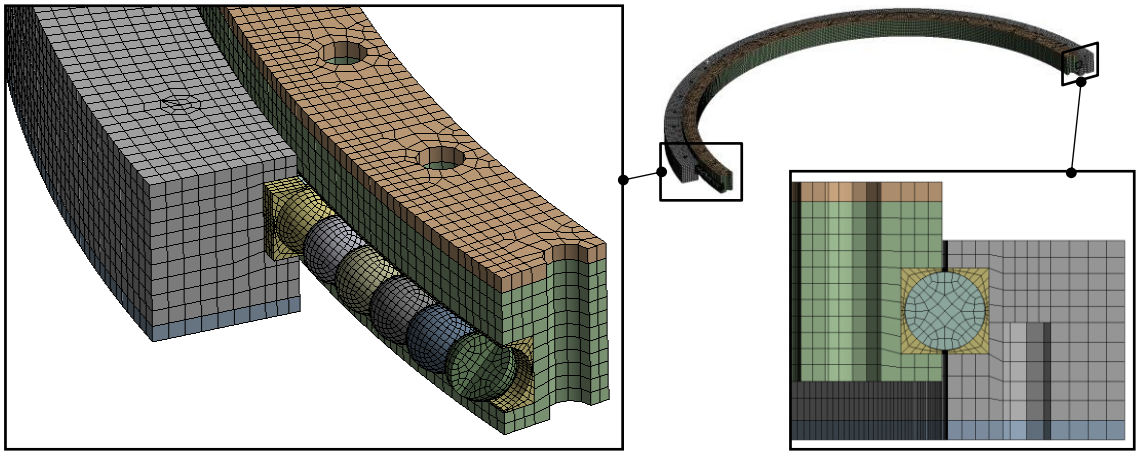

Figure 5.9. FE mesh for the Iraundi POS214-8 bearing [25].

- Bolts: bolts are considered in the model to simulate the nonlinearity of the ring-flange joint and the preload in the structural behaviour of the bearing, but the objective of the analysis is not to study them. Therefore, a linear element based on the Timoshenko beam theory, such as BEAM188, is sufficiently accurate for the aim of the study. Additionally, PRETS179 elements are used to apply the corresponding bolt preload. As mentioned

before, these elements are directly inserted in the model through a parametric APDL script.

To establish the relationship between the different parts of the model, contacts are defined. The definition of the contacts involves additional elements, but no extra nodes. These elements are CONTA174 and TARGE170, and MPC184 for bolt-housing contacts. In the following points each contact is described separately:

- Ball-raceway: a frictional contact is required in this case. A typical friction coefficient of 0.1 is adopted [59,102], though it will have little effect on the stiffness. Note that, to ease the convergence in the first step, the nodes from balls and raceways have been matched on the contact point (matched but not merged).
- Ring-flange: it is a frictional contact too, allowing the sliding or the opening of the joint. In this case, the friction coefficient is the typical one for a steel-steel contact, which is 0.3.
- Raceway-ring: this contact is defined to join the refined part of the rings to them. A bonded contact is set, with a pure-penalty formulation.
- Bolt-housing: bolts must be tied to rings and flanges. This union is made through the previously mentioned APDL script that creates the bolts, and is made through infinitely rigid MPC184 beams (see Figure 5.10).

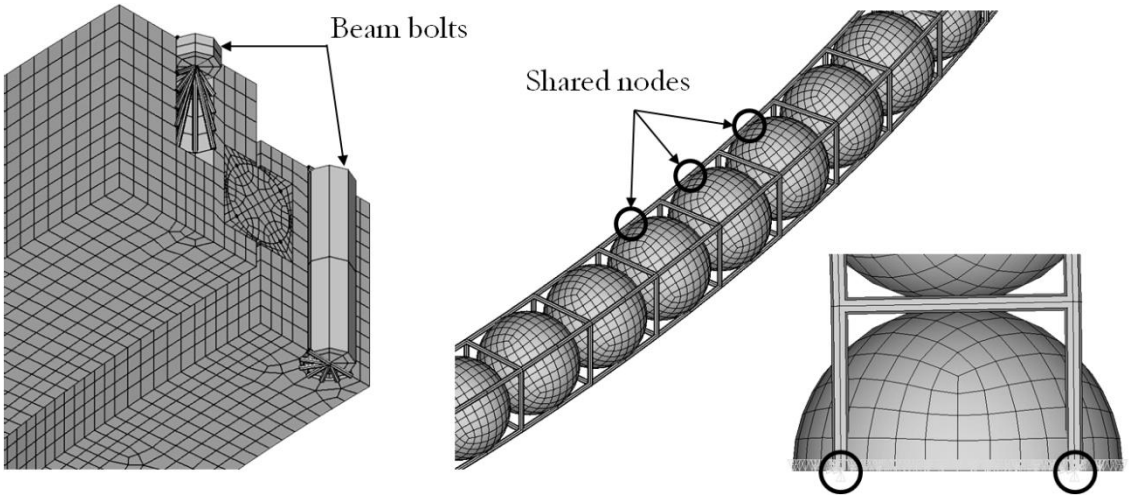

Figure 5.10. FE model details in the classic environment.

To simulate the symmetry of the model, frictionless boundary conditions are imposed on the faces on the symmetry plane, involving rings, flanges, balls and bolts. The bearing is held by the outer flange, so its nodes are fixed; by fixing all the nodes, a rigid flange is being considered. The displacements are

applied to the inner flange through a remote node placed in the centre of the bearing and at the height of the interface between the flange and the ring. The remote node is connected by MPC184 rigid beams to every node of the inner flange, so it can not be deformed. The preload of the bolts is gradually applied in a first step, while the displacements of the inner ring are introduced in 10 substeps in the second step in order to reproduce the load-deformation nonlinear behaviour.

In the simulation, large displacements are involved and they must be taken into account, especially because the variation of the ball-raceway contact angle significantly affects the stiffness of the bearing. This fact, together with the ball-raceway and ring-flange frictional contacts, makes the model highly nonlinear. More specifically, the model shows important convergence problems due to the ball-raceway contacts, which are very sensitive in the first load steps. When the preload is applied, and also in the first substeps of the second step, some balls lose the contact and therefore they are unconstrained. This problem is especially notable when a pure radial load is applied, when half the balls lose the contact. This is a typical problem in ball bearing simulations, but no method was found in the literature to deal with it. Therefore, to avoid this problem and ensure the convergence of the model, many different tests were performed, but only the two most successful ones are going to be discussed. The first option was to tie balls through weak springs and introduce a slight preload, ensuring the contact between them and the inner ring. In other words, it was like making an elastic necklace with the balls. This option showed good convergence behaviour with some models; nonetheless, it requires high preloads in the springs in certain cases, while in others the convergence was not reached. Therefore, a second option was finally implemented, which involves a cage formed by thin beams like the one shown in Figure 5.10. This weak structure is more restrictive than the first one and ensures the convergence for every design and load case. It was checked that both options offer exactly the same results, so the additional stiffness due to the cage is proved to be negligible. Thus, this innovative method solves a typical problem of ball bearing FE simulations, ensuring the convergence for any calculation and offering reliable results.

A robust fully parametric and realistic FE model is therefore achieved, capable of addressing any kind of load. The computational cost of each calculation varies from 1 hour for low D_{pw}/D_w ratios to 1 day for high D_{pw}/D_w ratios. For the calculations, a high performance work station was

used, with an Intel® Xeon® E5-2697 v3 @ 2.6GHz processor with 14 physical cores (28 logical) and a RAM of 128GB.

5.4 Formulation for the main parameters

5.4.1 Finite Element results

In this section, the results from the FE model will be analyzed. Nevertheless, some issues should be addressed first.

As we know from the Hertz theory [17], the ball-raceway contact obeyed the following relationship between the normal load (Q) and the local deformation (δ):

$$Q = K\delta^{3/2} \tag{5.4}$$

Based on this expression, the following formulas can be proposed for a first approximation to the results given by the FE model, establishing a relationship between the applied loads (F_a, F_r and M_t) and the corresponding displacements (δ_a, δ_r and θ_t):

$$\begin{aligned} F_a &= K_a\delta_a^{n_a} \\ F_r &= K_r\delta_r^{n_r} \\ M_t &= K_t\theta_t^{n_t} \end{aligned} \tag{5.5}$$

Where subscript a is for axial, r for radial and t for tilting. In this case, the values of the exponentials will not have the same value as they had in the normal problem (1.5), not only because the flexibility of the rings is involved, but also due to the change of the contact angle with the load. For the axial load case, for example, the greater the axial load is, the larger the contact angle will be, and therefore the more aligned the normal load (Q) will be with the applied force (F_a); due to this effect, the exponent (n_a) is expected to be greater than 1.5, at least when only local contact deformations are assumed. An analogous reasoning is applicable to radial load or tilting moment. Besides, if we consider the deformations of the rings, the problem is more complex, and therefore the values of the exponentials are more difficult to predict.

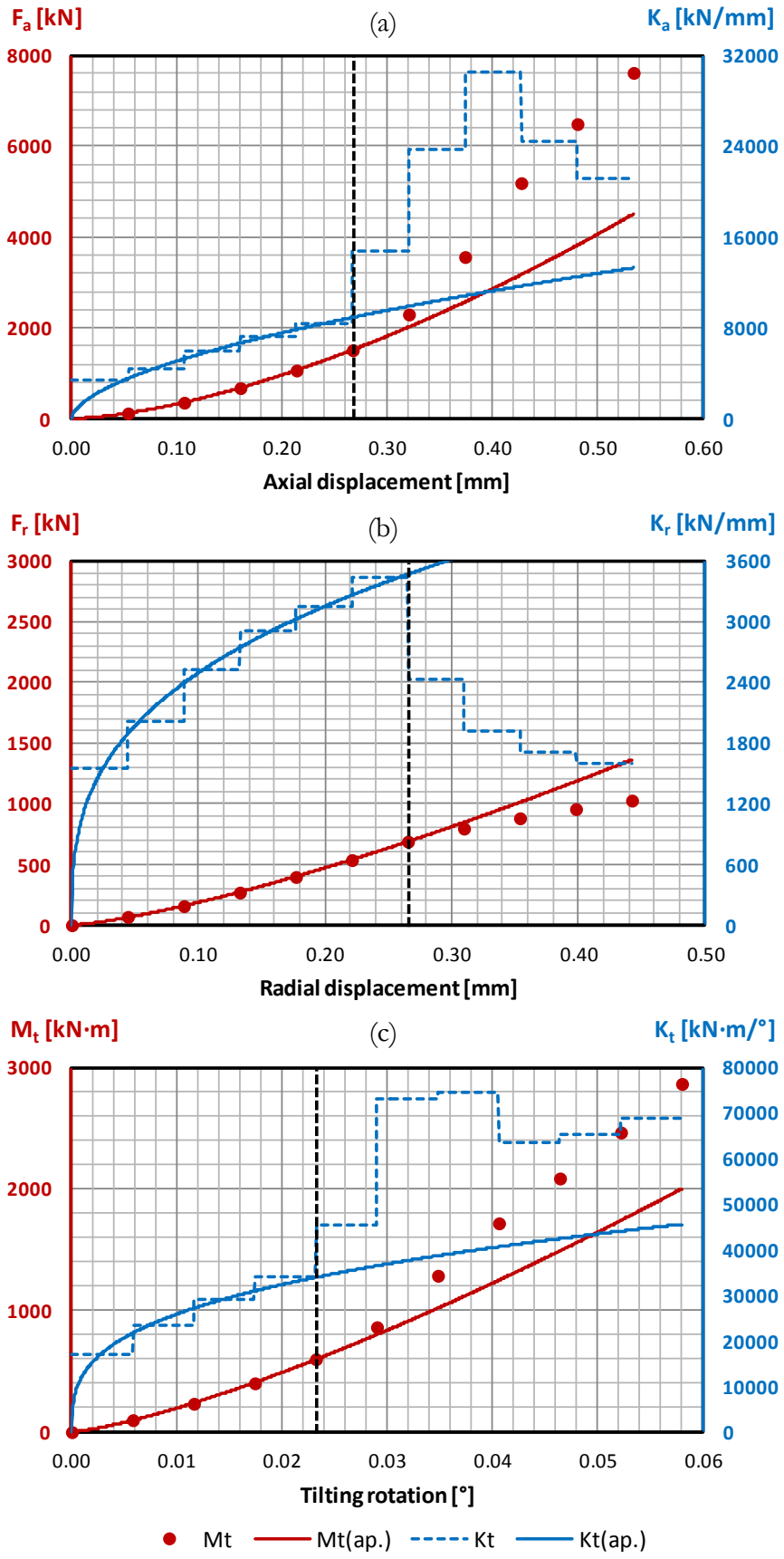

Figure 5.11. FE results for displacements (red dots), stiffness (dashed blue curve) and their approximations (continuous curves) for DP7: (a) for axial load; (b) radial load; (b) tilting moment.

Having explained this, the obtained results will be analyzed. From this point on, only a particular case, the DP7 (see Figure 5.3), will be analyzed. Nevertheless, all comments and observations, as well as derived conclusions, are applicable to every case from the DOE.

Hence Figure 5.11 shows, in red dots, the axial and radial forces, as well as the tilting moment, for the increasing values of the applied displacements for a particular case (DP7). In the same plots, the stiffness for each load step is plotted with dashed blue lines. These lines evince the discontinuity in the tendency of the resistant behaviour of the bearing. In each load case, a clear jump in the stiffness can be seen, pointing to the load from which this behaviour changes. Contrasting these curves with the deformations and the contact results (pressure and contact status) in the flange-ring joints, it is identified that this change in the tendency is due to the nonlinearity of these contacts. Figure 5.12 shows how flanges start either sliding (for axial or radial load) or opening (under tilting moment) after a certain applied displacement. The effect of this contact nonlinearity has been placed outside the scope of the study in order to achieve generally applicable conclusions and results. The point where the sliding or the opening starts will depend on the stiffness of the structures to which the rings are bolted and the bolt preload level. Although the latter is usually around the established value for the standard design (75%), the stiffness of the adjacent structures can vary considerably, depending on the application. Moreover, in the FE model, the flanges are infinitely rigid, favouring a premature opening.

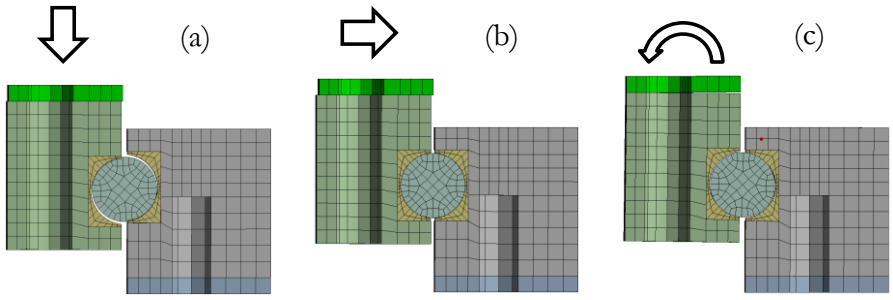

Figure 5.12. Nonlinear behaviour of the bolted joint (enlarged displacements): (a) with axial load; (b) radial load; (c) tilting moment.

In order to neglect the effect of the flange-ring contact nonlinearity, the functional form proposed in (5.5) was used. The values of the coefficients K and n were calculated for each DP considering only the points prior to the contact nonlinearity, and the resulting curves are shown in Figure 5.11 by continuous curves. These curves allow the large effect of the sliding or the opening of the joint to be observed, which makes the structural behaviour of

the bearing quite unpredictable. The functional approximation shown in these plots was used only in this first post-processing of the results in order to catch the tendencies, evaluate the effect of the flange-ring contact nonlinearity and, in general, to make the analysis of the data easier, but it has nothing to do with the formulation presented in the following section. It is remarkable that the values of the exponential coefficient (n) are quite stable for each load case, being between 1.5 and 1.6 for the axial load, between 1.3 and 1.4 for the radial load and between 1.2 and 1.4 for the tilting moment.

To evaluate the effect of the flexibility of the rings on the stiffness, and therefore justify the current research, Figure 5.13 compares the results for the cases with rigid and deformable rings. The results for the case of rigid rings were obtained through the analytical model developed by Aguirrebeitia et al. [44]. Remember that, as explained in Chapter 2, this model provides the same results as the Rigid-BIME for the nominal geometry (with no manufacturing errors). From the figure, it can be concluded that not considering the deformability of the rings will largely overestimate the stiffness of the bearing. Of course, the effect is lower for smaller bearings and larger for bigger ones, but in every case the effect is highly significant. For the case of the 35mm ball, for example, the displacements due to ring flexibility account for approximately one third of the total (36%) for the smallest bearing (DP6), while they account for nearly one half the total displacements (47%) for the medium-sized bearing (DP7), and slightly more (52%) for the largest (DP8).

It is worth mentioning that the stiffness curves from the analytical model (Figure 5.13) can also be approximated by (5.5). In this case, the exponential for every load case and DP is 1.6, which is greater than the value of 1.5 from formula (5.4), which is consistent with the reasoning at the beginning of the section.

5.4.2 Functional approximation

The proposed approach to the bearing global stiffness estimation considering the ring elasticity lies in separately calculating the displacements due to contact deformations and those due to the flexibility of the rings. Thus, the problem is decoupled so that each contribution can be calculated separately. Hence, the total displacements are formulated as follows:

$$\delta = \delta_{contact} + \delta_{rings} \tag{5.6}$$

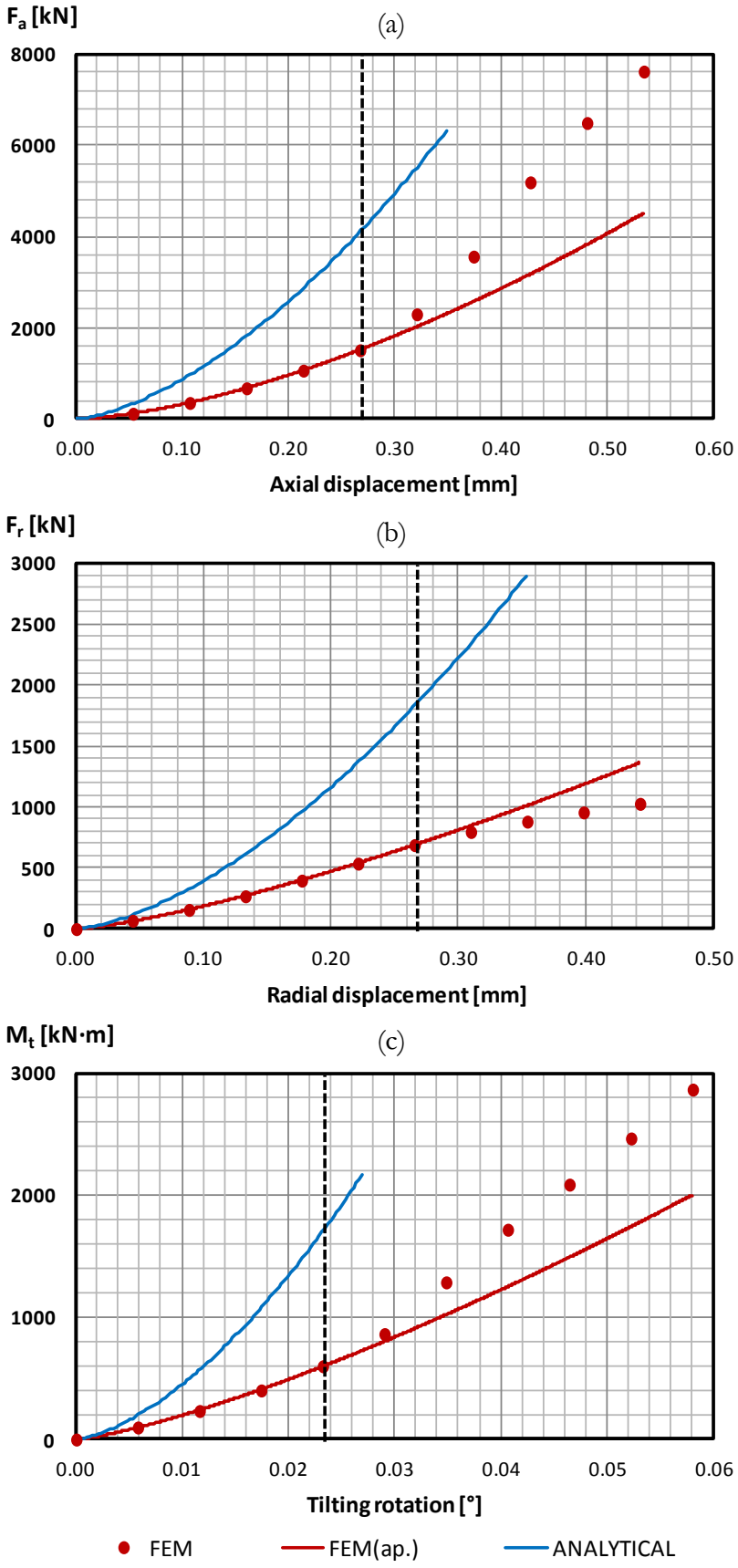

Figure 5.13. FE results (red dots), exponential approximation (red curve) and analytical model results (blue curve) for DP7: (a) for axial load; (b) radial load; (b) tilting moment.

Consequently, $\delta_{contact}$ can be calculated through the analytical model, and the challenge resides in finding a way to compute δ_{rings}. The aim of decoupling the problem is to consider separately the effect of the different parameters on the stiffness. By doing this, contact parameters such as preload or conformity ratio, will only affect $\delta_{contact}$ because the analytical model already has the capability to consider them. On the other hand, δ_{rings} is affected by the rest of the geometrical parameters, where the main ones are D_w and D_{pw}.

For the formulation of δ_{rings}, a functional approximation is proposed, based on the results from the DOE. The proposed formulation is, once again, the one at (5.5), but in this case the coefficient K will be a function of the main parameters (D_w and D_{pw}):

$$F = K\delta_{rings}^{n} = K\left(D_w, D_{pw}\right)\delta_{rings}^{n} \tag{5.7}$$

Where F represents the applied load in each case (being F_a, F_r or M_t) and δ the corresponding displacement (δ_a, δ_r or θ_t). The idea is to find the $K\left(D_w, D_{pw}\right)$ function that will fit all the results from the DOE. For this purpose, the results from the analytical model are deducted from the FE results, obtaining the curves for δ_{rings}. Then, the function (5.7) was approximated for each DP independently, obtaining the values of the coefficients K and n in each case. In this first approach, it was identified how the coefficient n is very similar for every DP (under the same load case).

In a second step, the value of coefficient n was fixed and then every K coefficient recalculated to fit the curve. The obtained values are plotted in Figure 5.14. From these plots it can be concluded that the effect of D_{pw} in the coefficient K is exponential. However, no such clear tendency can be directly deducted for D_w. In Figure 5.14 it can be seen that the effect of D_{pw} is dominant, so the same plots for D_w do not show such clear information.

Before achieving the most suitable functional form for K, different options were tested, but finally the following was proved to provide the best fit, with the minimum possible number of coefficients:

$$K\left(D_w, D_{pw}\right) = C_w D_w^{n_w} + C_{pw} D_{pw}^{n_{pw}} \tag{5.8}$$

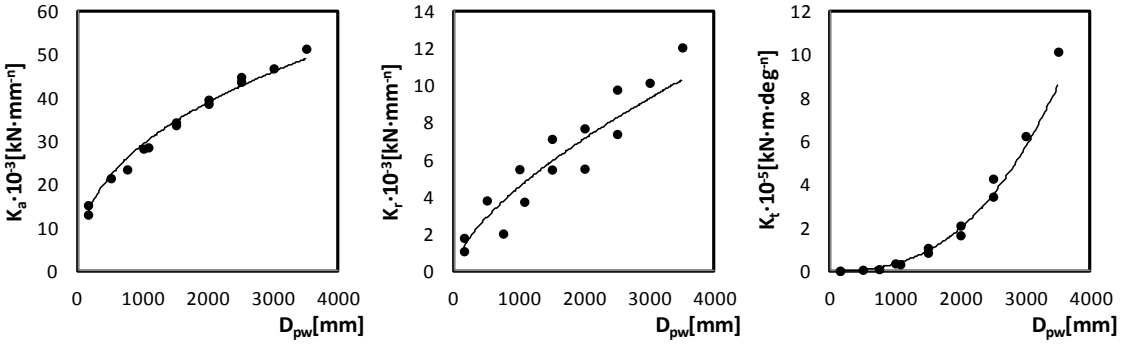

Figure 5.14. Tendencies of *K* coefficients with bearing mean diameter.

From (5.7) and (5.8), the expression for δ_{rings} is obtained:

$$\delta_{rings} = \left[\frac{F}{K\left(D_w, D_{pw}\right)}\right]^{\frac{1}{n}} = \left[\frac{F}{C_w D_w^{n_w} + C_{pw} D_{pw}^{n_{pw}}}\right]^{\frac{1}{n}} \tag{5.9}$$

The last step is to find the values of the 5 coefficients (n, C_w, n_w, C_{pw} and n_{pw}) that will fit the curves for every DP. To this end, the Mean Weighted Relative Square Error ($MWRSE$) was defined:

$$MWRSE = \frac{1}{N}\sum_{i=1}^{N}\left[\frac{1}{M_i}\sum_{j=1}^{M_i}\left[\frac{\left[\delta_{FE}^{ij} - \left(\delta_{contact}^{ij} + \delta_{rings}^{ij}\right)\right]^2}{\left(\delta_{FE}^{ij}\right)^2}\right]\right] \tag{5.10}$$

Where N is the number of DPs (14 in our case) and M_i is the number of points from the FE results for DP i before the nonlinearity of the joint occurs. By minimizing this error through the Newton-Raphson method, the values of the coefficients were obtained. Although a quadratic error was used for the minimization to favour the convergence, the Weighted Absolute Relative Error ($WARE_i$) gives a more intuitive idea of the error for each DP:

$$WARE_i = \frac{1}{M_i}\sum_{j=1}^{M_i}\left|\frac{\delta_{FE}^{ij} - \left(\delta_{contact}^{ij} + \delta_{rings}^{ij}\right)}{\delta_{FE}^{ij}}\right| \tag{5.11}$$

Table 5.2 shows the final values of the coefficients for each load case together with the mean value of the $WARE_i$ ($MWARE$). The units for C_w (and analogously for C_{pw}) are $\left[kN \cdot mm^{-(n-n_w)}\right]$ for axial and radial loads, and $[kN\,m \cdot mm^{-n_w}]$ for tilting moment. As can be seen in the table, the error is less than the 5% in any case.

	n	C_w	n_w	C_{pw}	n_{pw}	$MWARE$
Axial load	1.6	0	1	3300	0.35	1.5%
Radial load	1.0	45	1.2	0.15	1.3	3.5%
Tilting moment	1.1	$5.3 \cdot 10^{-4}$	4.5	10^{-5}	3.1	4.9%

Table 5.2. Values for the coefficients of the functional approximation for δ_{rings} and the relative error (*MWARE*).

Substituting the values from Table 5.2 in (5.8), the final formulas for the contribution of the rings to the total displacements are obtained:

$$\delta_a|_{rings} = \left[\frac{F_a}{3300 D_{pw}^{0.35}}\right]^{\frac{1}{1.6}}$$
$$\delta_r|_{rings} = \frac{F_r}{45 D_w^{1.2} + 0.15 D_{pw}^{1.3}} \tag{5.12}$$
$$\theta_t|_{rings} = \left[\frac{M_t}{53 D_w^{4.5} + D_{pw}^{3.1}} 10^5\right]^{\frac{1}{1.1}}$$

Figure 5.15 compares FE results (red dots) with the curves for $\delta_{contact}$ (from the analytical model), δ_{rings} (from the proposed formulation) and the summation of both for DP7 (for the other design points, see Appendix A). For this DP, the $WARE_i$ is 0.36%, 2.29% and 4.44% for axial, radial and tilting cases respectively, so it is a representative DP considering the mean values of the errors in Table 5.2.

5.5 Extension of the formulation for secondary parameters

As explained in the previous section, the aim of separately considering the displacements due to the contact deformations and those due to the ring flexibility is to be able to reproduce the effects of the contact parameters in the global stiffness of the bearing without making any change in the proposed formulation. Contact parameters are supposed to influence only the deformations in the ball-raceway contacts, without affecting the ring stiffness. To prove this assumption, additional FE calculations were performed, and the results compared with the ones from the proposed formulation.

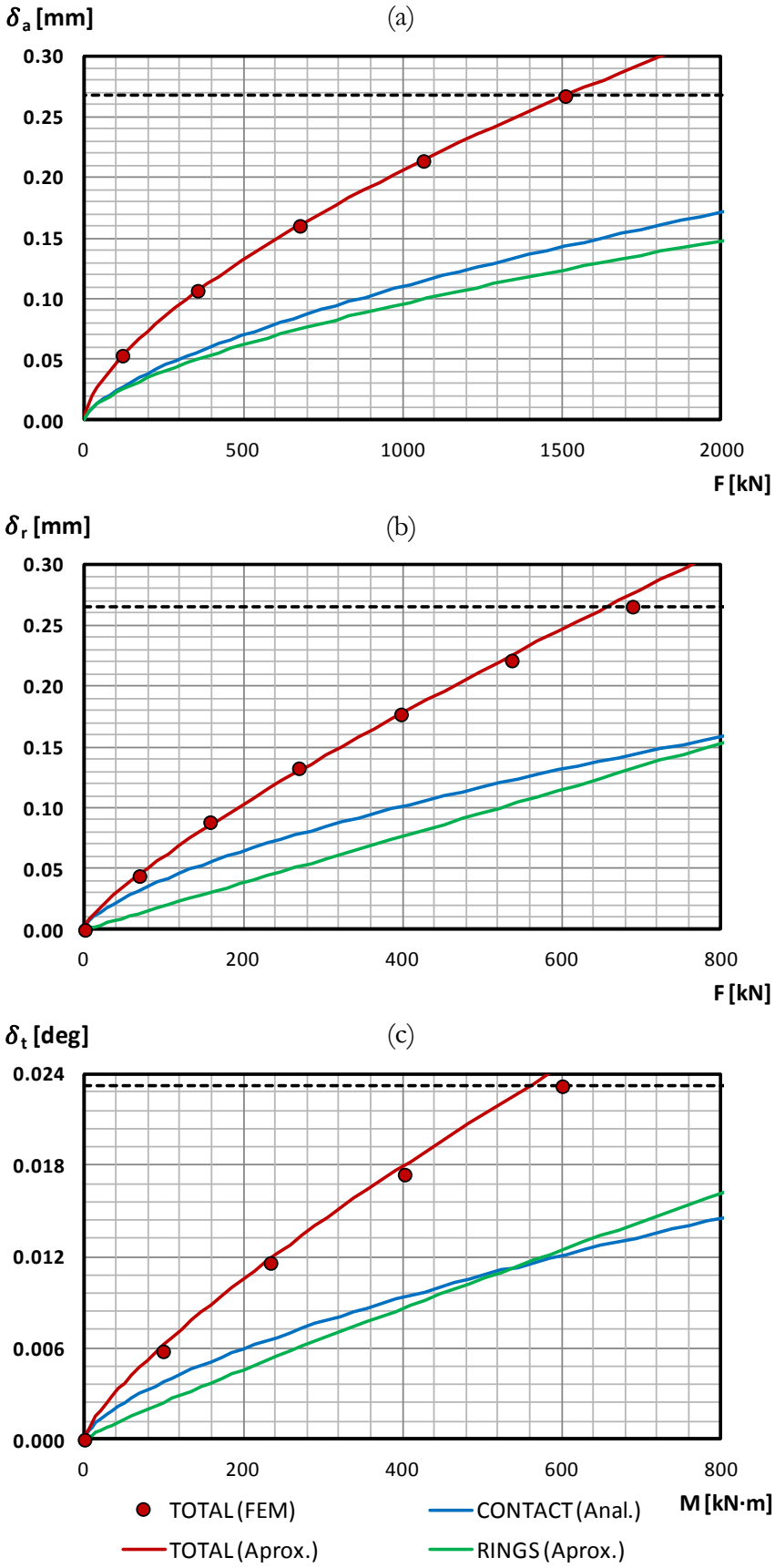

Figure 5.15. Analytical model results (blue curve), functional approximation for rings deformation (green curve), the summation of both curves (red curve) and FE results (red dots) for DP7: (a) for axial load; (b) radial load; (b) tilting moment.

The parameters related to the contact deformations are preload (δ_P), ball number (N_b), conformity ratio (s) and initial contact angle (α). Although the ball number cannot be considered as a contact parameter, it affects the deformations of the contacts because the more balls there are, the more contacts there will be. Of course, all these parameters are considered in the analytical model.

To verify that the mentioned parameters only affect $\delta_{contact}$ but not δ_{rings}, different FE calculations were carried out varying their values. For the verification a reference bearing, the DP7, was adopted, and then the effect of each parameter was studied separately.

For the case of the preload, four different values were considered up to 10% of the static load capacity, which happens at 30μm. Figure 5.16 shows the results for the reference case and the three preloads. It can be seen that the curves from the proposed methodology are near FE results, although they have certain limitations for high loads. Nevertheless, the errors are near those for the nominal case (see Table 5.3).

	δ_P	N	s	α
Axial load	1.7%	3.3%	6.8%	7.4%
Radial load	3.2%	3.3%	5.6%	3.7%
Tilting moment	5.5%	5.2%	7.5%	5.6%

Table 5.3. Relative error (*MWARE*) for the different contact parameters.

Regarding the ball number, the parameter considered is the filling ratio (R_{fill}) from formula (5.2). As explained before, the values for this ratio vary from 80% to 100%, so these two aditional cases were analysed. The results are shown in Figure 5.17 and the numerical errors are presented in Table 5.3. As with the preload, the proposed methodology lacks accuracy as the load increases, but the values of the errors are still satisfactory.

For the conformity ratio, values from 0.92 to 0.96 were analysed. In this case, the formulation catches the tendency adequately (see Figure 5.18), but the errors are bigger than for the other parameters (Table 5.3).

Finally, the effect of the contact angle was studied. For this purpose, angles from 35° to 55° were considered. If the proposed formulation is applied without introducing any correction (see dashed curves in Figure 5.19), the

curves are far from the FE results, even though the tendency is correct. Nevertheless, a correction can be easily made using the γ factor. This factor comes from the unprojection of contact forces in the vertical for axial and tilting cases, and in the horizontal for the radial case:

$$F = \gamma \cdot K\left(D_w, D_{pw}\right)\delta_{rings}^{n} \quad \text{where} \begin{cases} \gamma_{a/t} = \frac{sin\alpha}{sin45^\circ} = \sqrt{2}\, sin\alpha \\ \gamma_r = \frac{cos\alpha}{cos45^\circ} = \sqrt{2}\, cos\alpha \end{cases} \tag{5.13}$$

The corrected curves are represented in Figure 4.17, showing a good correlation with FE results.

To sum up, it can be concluded that the proposed formulation provides accurate results for every bearing. It was demonstrated that not only does it fit FE results for every combination of the main parameters (D_p, D_{pw}), but also correctly reproduces the effects of preload, ball number, conformity ratio and initial contact angle. Thus, the calculation procedure that involves both the analytical model and formulas (5.12) and (5.13) constitute a fast, reliable and powerful tool for bearing manufacturers and buyers.

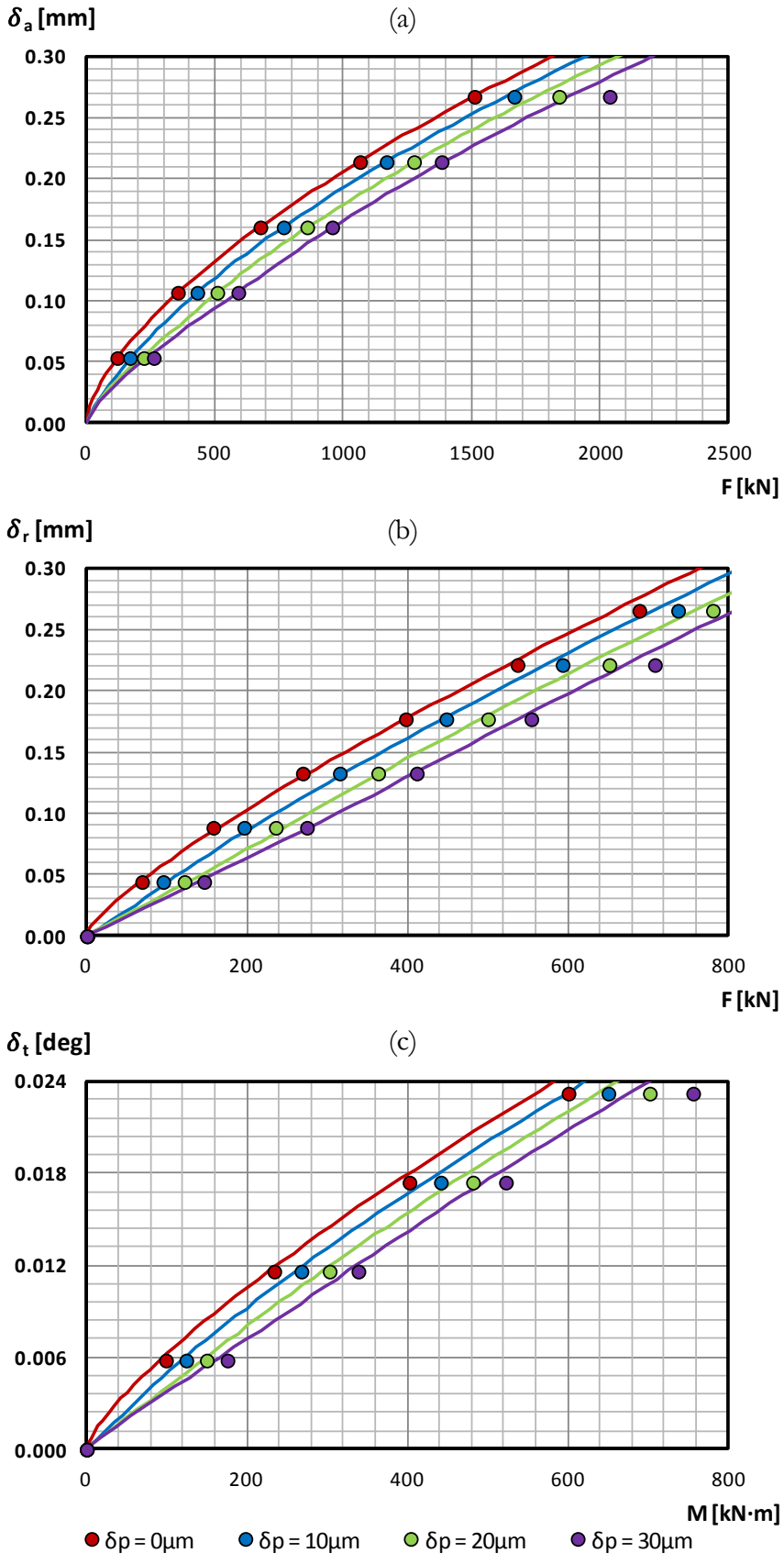

Figure 5.16. Effect of the preload according to the proposed formulation (curves) and FE results (dots) for DP7: (a) under axial load; (b) radial load; (b) tilting moment.

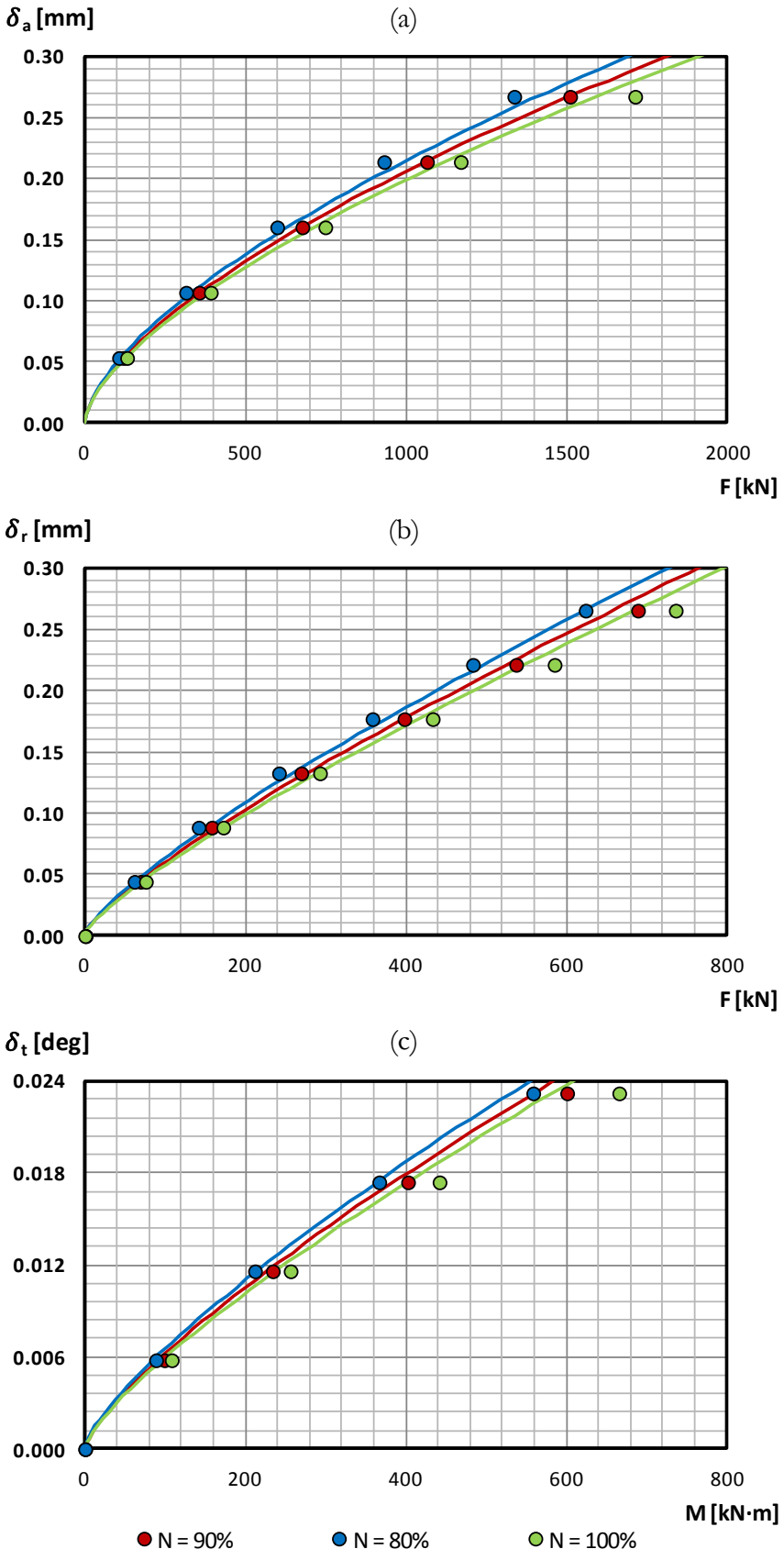

Figure 5.17. Effect of the ball number according to the proposed formulation (curves) and FE results (dots) for DP7: (a) under axial load; (b) radial load; (b) tilting moment.

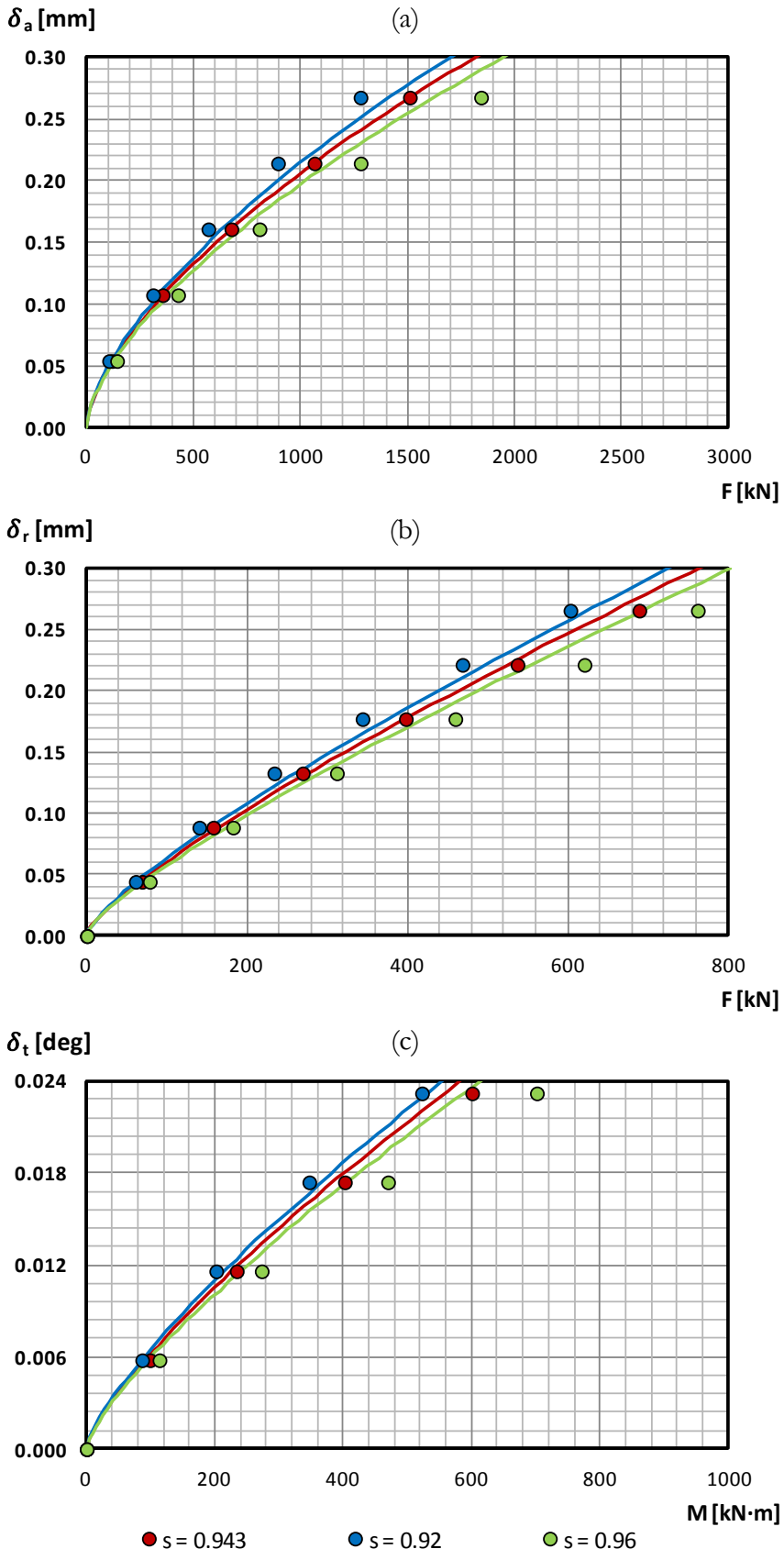

Figure 5.18. Effect of the conformity ratio according to the proposed formulation (curves) and FE results (dots) for DP7: (a) under axial load; (b) radial load; (b) tilting moment.

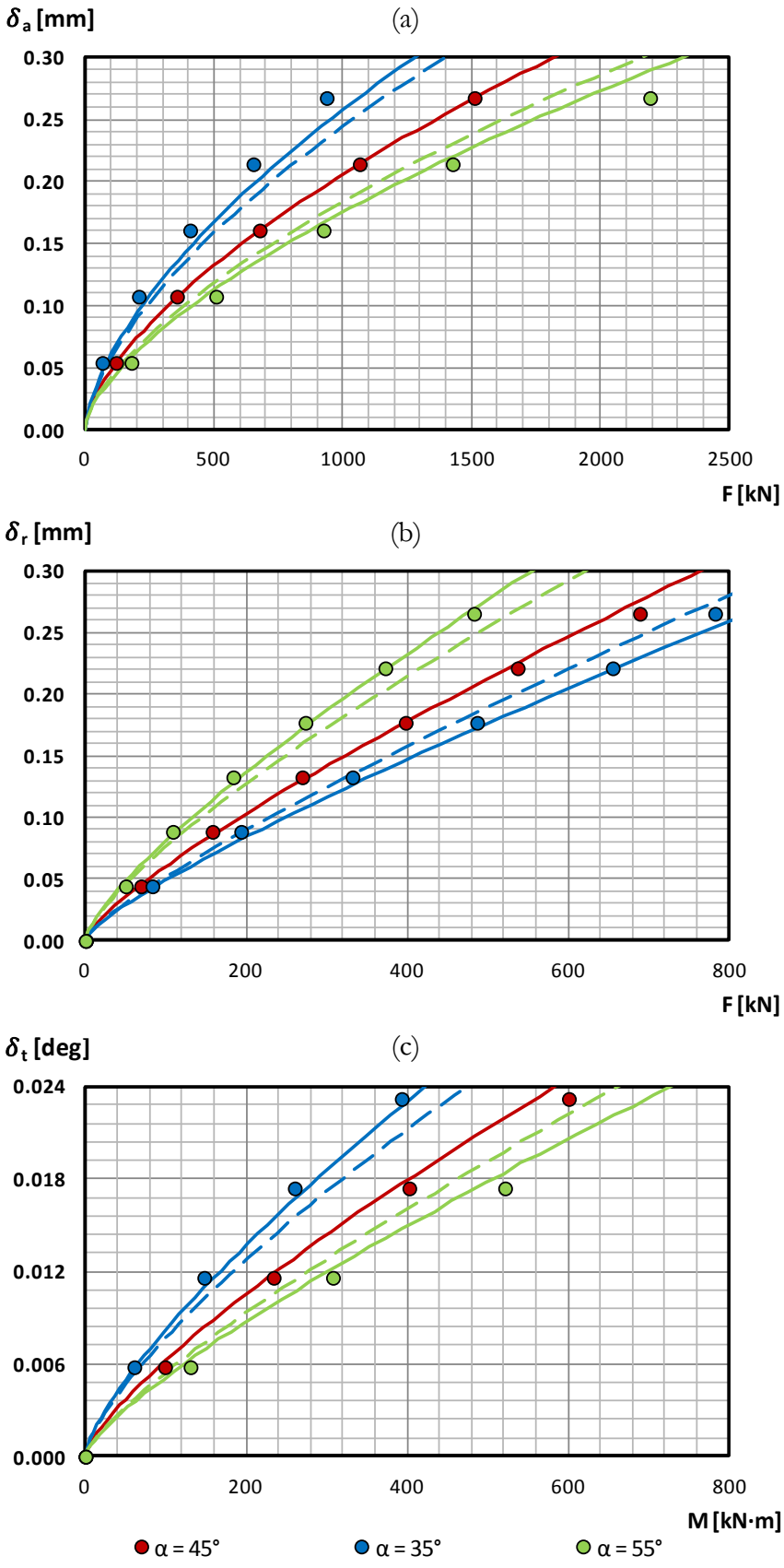

Figure 5.19. Effect of initial contact angle according to the proposed formulation without the correction (dashed curves), corrected (continuous curves) and FE results (dots) for DP7: (a) under axial load; (b) radial load; (b) tilting moment.

6 Experimental tests

6.1 Introduction

This chapter presents some preliminary tests performed to experimentally measure the friction torque. The objective of these tests is to assess the capabilities and limitations of the proposed analytical models (BIME and FRANC) for the friction torque calculation.

Previously to this Doctoral Thesis, and as explained in Chapter 1, Joshi et al. not only particularized the model of Leblanc and Nélias [56,57] for slow speed applications, but also performed some experimental tests [59]. In these tests, Joshi et al. measured the friction torque of a four-point contact bearing under different magnitudes of axial load. The cases of two contact points and four contact points were studied separately by using two different ball sizes. The results from the tests showed a good correlation with the analytical approach.

In preloaded bearings, there are four contact points for light loads, but the status switches to two contact points from certain load onwards. Nevertheless, this transition from four contact points to two contact points was not studied by Joshi et al. [59]. In the preliminary tests presented in this chapter, this issue is addressed. Moreover, Joshi et al. considered rigid rings for the load distribution [39,59]. This can be acceptable for bearings where the mean diameter (D_{pw}) is not much larger than the ball diameter (D_w). In the case of the bearing tested by Joshi et al., the D_{pw}/D_w ratio was 4, so rigid rings assumption is justified. Nonetheless, in slewing bearings the mean diameter is much larger than the ball diameter ($D_{pw} \gg D_w$), so this assumption can lead to inaccurate results. In the preliminary tests presented in this chapter three bearings were tested, where osculation ratios and contact angles are different. These bearings do not have large dimensions ($D_{pw} = 222mmm$), but they meet the geometrical proportions of standard slewing bearings ($D_{pw}/D_w = 28$ in tested bearings). Therefore, in the analytical calculations for the

experimental correlation presented in following sections, the Flexible-BIME was used.

In this chapter, an alternative procedure for the friction torque calculation is presented in a first place. This procedure takes advantage of the analytical models developed in the previous chapters, but proposes a different way to estimate manufacturing errors and their effect in the friction torque without having to measure the raceways. Then, the friction coefficient is experimentally obtained for two different greases typically used in slewing bearings. The performed preliminary tests for the friction torque measurement are presented in the last section, from which some conclusions are obtained. In these tests, only one of the greases is used. Finally, the future work to be done regarding experimental testing is outlined.

6.2 Alternative procedure for the friction torque calculation

In this section, an alternative procedure is proposed to calculate the friction torque considering the effect of manufacturing errors, as well as to approximately estimate their magnitude, without measuring the raceways. In this procedure, the idling friction torque must be experimentally obtained, which is much easier and faster than measuring the raceways. If the idling friction torque is 0, it means that no interferences exist, and therefore it is not possible to obtain information on the manufacturing errors. In this case, the calculations would be performed by considering the nominal geometry. Nevertheless, a preload is always sought. Thus, if the idling friction torque is not 0, it means that certain interferences exist at the contact. As the real geometry is unknown, it is not possible to take advantage of the developed model to calculate the real interferences for each ball. Nevertheless, it is possible to perform calculations considering the nominal geometry, using the ball preload as variable in the model. This way, there will be a value of preload that will make the developed model fit the measured idling torque. This value will be named the effective ball preload (δ_E) and will be different from the real ball preload (δ_P), which must be known if the manufacturing errors are to be estimated. Using the effective preload in the analytical model, the resulting interferences will be an intermediate value of the real interferences. Thus, once the effective preload is known, the friction torque can be calculated for any load case, using this preload instead of the ball preload.

Of course, the effective preload will be different if it is calculated considering rigid rings or flexible rings. If the objective is to estimate the manufacturing errors, the effective preload must be calculated with the flexible rings. Thus, the average geometrical interferences due to these errors (δ_{ME}) can be calculated as the difference between the effective preload and the ball preload:

$$\delta_{ME} = \delta_E - \delta_P \tag{6.1}$$

Contrarily, if the objective is to estimate the friction torque but no information about manufacturing errors is wanted, calculations could be done by assuming rigid rings, without significant errors. The example in Figure 6.1 will be used to better explain the procedure. This figure represents the results of the friction torque for a bearing under different axial loads. The axial capacity of this bearing is 857.5kN, which corresponds to an interference of 117.5μm. The solid line in Figure 6.1a was obtained for the nominal geometry, with no ball preload and assuming rigid rings. Suppose that the idling friction torque is experimentally measured for this bearing and a value of 52N·m is obtained for a ball preload (δ_P) of 4μm. Then, calculations are performed with the analytical model for different ball preloads and with no applied loads. As a result, it is obtained that a ball preload of 10μm is required to obtain a value of 52N·m for the idling friction torque. Therefore, the effective preload for rigid rings (δ_E) is 10μm, which means an interference of 10μm in the ball-raceway contact. Then, using this effective preload in the model, the dotted line in Figure 6.1a is obtained. This line shows an initial part that differs from the case with no interferences because there are four points in contact. As the axial load increases, one of the contact diagonals becomes more loaded and the other less loaded. This way, there is a load from which the ball starts to roll, and then a transition happens from four contact points to two contact points. In this transition, the friction torque decreases drastically, and from 50kN onwards, both curves are practically the same.

If the effective preload is calculated considering flexible rings, it will be greater than the value of 10μm obtained for rigid rings. To obtain the measured idling friction torque, an interference of 10μm is required, and to reach such an interference, a larger ball preload is needed if the rings are deformed. Thus, the value of the effective preload is calculated for flexible rings and a value of 24μm is obtained. This means that if the raceways were perfect, this is the ball preload that would be needed in order to obtain an

idling friction torque of 52N·m (i.e. the measured value). This value of the effective preload includes the geometrical interferences due to the actual ball preload and to the manufacturing errors. Note that these geometrical interferences are bigger than the interferences after ring deformations. Consequently, by subtracting the ball preload (i.e. 4μm in the example) from the effective preload calculated for flexible rings, the average value of the geometrical interferences due to the manufacturing errors is obtained, and thus it provides an estimation of these errors. For the example:

$$\delta_{ME} = \delta_E - \delta_P = (24 - 4)\mu m = 20\mu m \tag{6.2}$$

Then, if the entire M_f-F_a curve is obtained for flexible rings considering the effective preload of 24μm, it is demonstrated to be very close to that for rigid rings considering the effective preload of 10μm (see Figure 6.1b). For the same axial load, and considering the corresponding effective preload in each case, the load distribution among the balls will be very similar in both cases. For flexible rings, contact angles will be slightly higher, which means lower loads and therefore a lower friction torque, but very similar nevertheless.

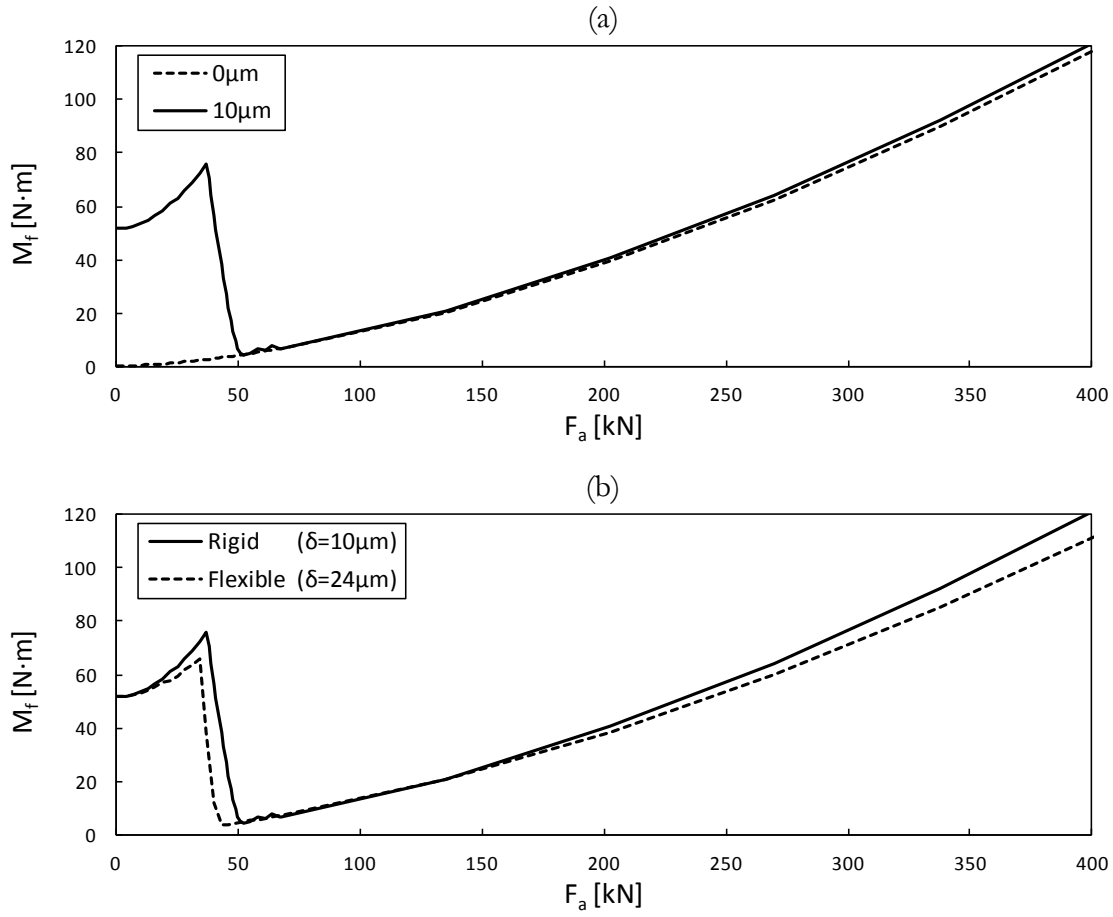

Figure 6.1. Friction torque VS axial load: (a) rigid rings with and without preload; (b) with preload for rigid and deformable rings.

To sum up, if no measurements of the raceways are available and the friction torque is wanted to be estimated for low loads, the proposed alternative procedure can be used considering rigid rings. Additionally, if an estimation of the manufacturing errors is desired, flexible rings must be considered to calculate the effective preload.

6.3 Friction coefficient measurement

The friction coefficient is a mandatory parameter for the analytical characterization of the contact. To obtain this parameter, experimental tests were performed. In these tests, two greases typically used in four-point contact bearings were studied (Grease-1 and Grease-2). In the next points, the followed experimental procedure is described. The results are then processed and a value is set for each grease.

6.3.1 Test bench setup

For the determination of the friction coefficient, the Linear Reciprocating Tribometer (LRT) in Figure 6.2 was employed. The experimental tests were performed in IK4-Tekniker research centre. These types of tests consist of holding a ball so that it can not move, and rubbing it against a test specimen that simulates the raceway. The rubbing movement is linear and reciprocating, so both static and dynamic friction coefficients can be measured.

To reproduce slewing bearings working conditions, two material properties are of vital importance: surface appearance and hardness. For the surface appearance, the same machining procedure used for the raceways was employed for the specimen. However, the hardness was more difficult to reproduce, because the raceways are induction hardened, while the specimens have to be heat-treated in a furnace. 42CrMo4 steel had to be used for this purpose, which after hardening and tempering in the furnace, it achieved the hardness of 56-60HRc, typical in bearing raceways. Contrarily, the ball was made of 100CrMo4, commonly employed material for the rolling elements.

Table 6.1 shows the details of the tests. four different loads were used to study its effect on the measurements. A maximum of 800N was applied according to the limitations of the LRT. The tests were performed twice for each load in order to check the repeatability. A low frequency was set to replicate the slow speed conditions in slewing bearings.

Figure 6.2. Linear Reciprocating Tribometer at IK4-Tekniker.

Parameter	Value
Applied forces	1N, 10N, 100N, 800N
Reciprocating movement amplitude	21mm
Frequency	0.5Hz
Test duration	2min
Ball diameter	10mm
Specimen thickness	5mm
Initial grease layer	2mm

Table 6.1. Friction coefficient measurement tests data.

6.3.2 Results

As a result, the evolution of the friction torque with time was obtained from each test. Figure 6.3 shows the results of one of the tests performed for Grease-1 and a load of 800N. The figure evinced that the friction coefficient decrease with the time during the first seconds, but it rapidly stabilizes. This higher value in the beginning is due to the viscous effects of the grease layer. After a few cycles (around 5), the grease is moved away and only a thin layer remains. After several cycles (15 in the case of the figure), all the grease is removed from the contact path, and then dry friction takes place. In order to filter the initial viscous effects and the dry friction at the end of the tests, the next functional expression was used:

$$\mu_i(t) = \mu_{fi} \frac{\mu_{0i} - \mu_{fi}}{e^{nt}} \tag{6.3}$$

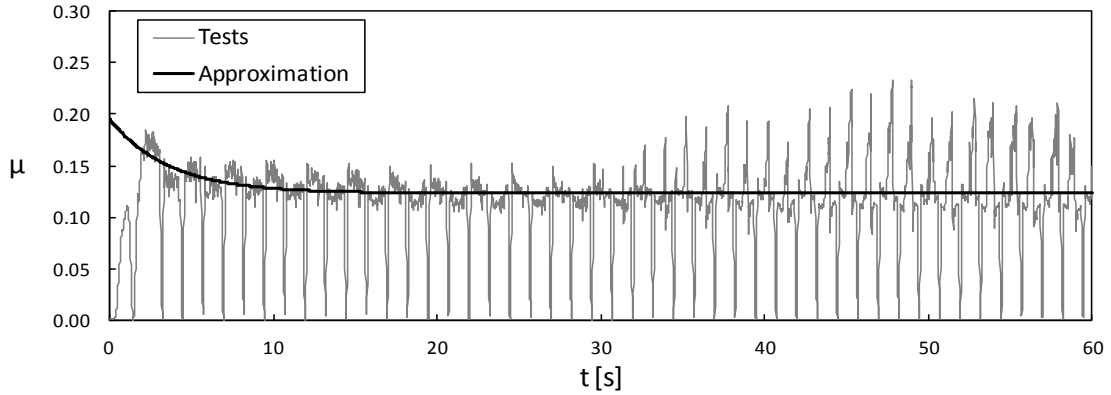

Figure 6.3. Evolution of the friction coefficient with time.

The final values of coefficients μ_{fi}, μ_{0i} and n are those which minimize the quadratic error between the functional approximation and the measured instantaneous friction coefficient before dry friction occurs. More specifically, μ_{fi} is the value of the stabilized friction coefficient for each test. Figure 6.4 represents all these μ_{fi} values for both greases and every test. From the graphics, it is concluded that the friction torque decreases with the load, but rapidly reaches a constant value, even for very low loads. Therefore, a similar expression to (6.3) is used in order to calculate a unique value for the friction coefficient for each grease:

$$\mu(F) = \mu_f \frac{\mu_0 - \mu_f}{e^{nF}} \tag{6.4}$$

Where μ_f is the sought constant value. Table 6.2 compiles the average values of μ_{fi} for each load and grease, and gives the final μ_f to be adopted in the calculations for each grease.

F [N]	μ_{fi}	
	Grease-1	**Grease-2**
1	0.23	0.27
10	0.19	0.18
100	0.15	0.15
800	0.12	0.14
μ_f	**0.12**	**0.14**

Table 6.2. Average friction coefficient for different loads and greases.

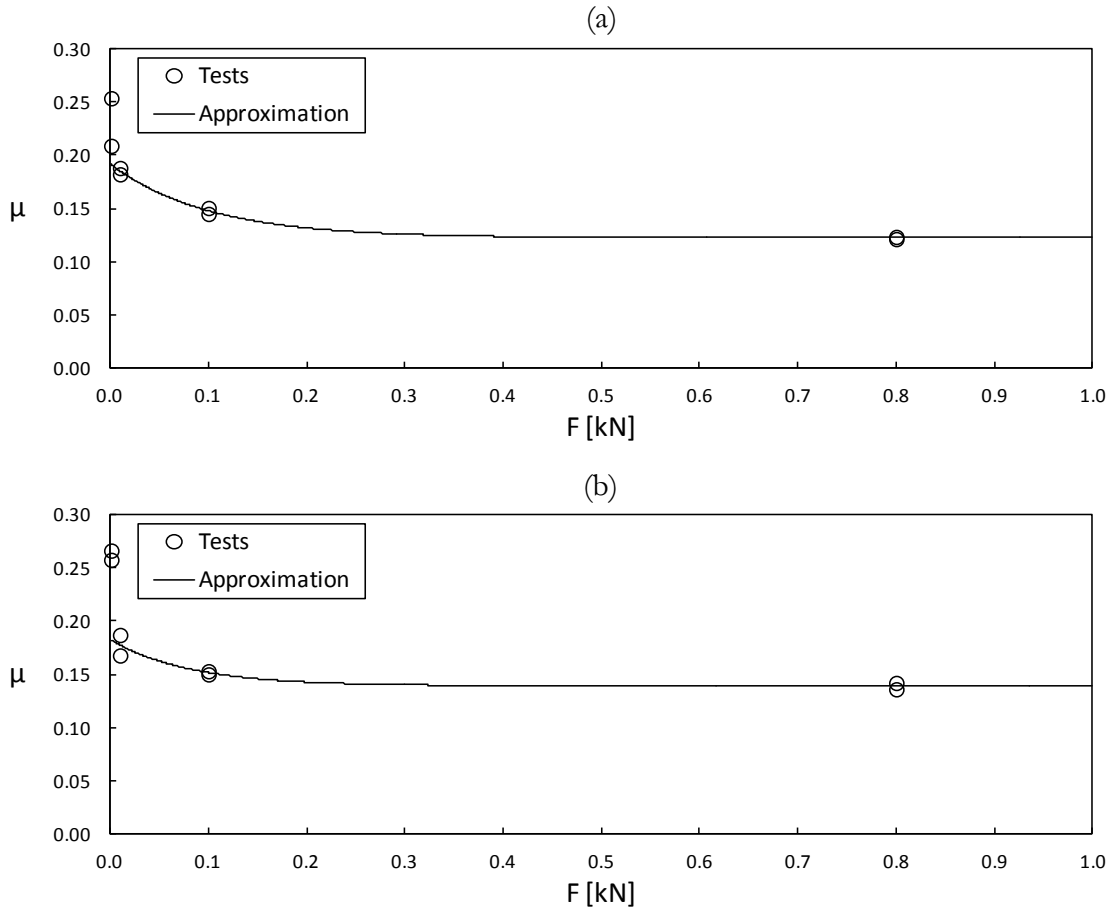

Figure 6.4. Friction coefficient VS applied force: (a) for Grease-1; (b) for Grease-2.

6.4 Friction torque measurement

In this section, the performed experimental tests for the friction torque measurement are described. Then, the results are compared with the analytical simulations carried out with the BIME and FRANC models, following the alternative calculation procedure proposed in section 6.2.

6.4.1 Test bench setup

For the experimental measurements of the friction torque, a test bench available in the facilities of the INSA-Lyon was used (Figure 6.5). The test bench is called Rhéos and is part of the equipment of the Laboratoire de Mécanique des Contacts et des Structures (LaMCoS) [105]. The Rhéos is designed to apply large compression loads and then rotate and measure the friction torque. For the data acquisition two load sensors are available, which measure both axial load and friction torque: the first one measures values up to 750kN and ±2000N·m (Sensor-1), while the second one bears maximum loads of 60kN and ±50N·m (Sensor-2). The axial load and the rotation are applied by a hydraulic cylinder and a brushless electric motor respectively. The first one is driven by a PID controller (Proportional Integral Derivative), which allows setting an objective applied load, but not a specific axial position. However, the position can be measured by a LVDT (Linear Variable Differential Transformer). The motor is controlled by a software which allows setting variables like rotation angle or speed. Considering that the current research is focused in low speed applications, an angular speed of 0.5rpm was set for the tests. In order to check possible misalignments of the bearings, two full rotations were applied to the bearings for each load case.

It is important to point out that the distance between the columns of the test bench is 430mm (Figure 6.5), so there is no room for the bearing measured in Chapter 2. For this reason, Iraundi S.A. provided three smaller bearings with an outer diameter of 254mm (Figure 6.6). The bearings are equal to each other except for the osculation ratio and the initial contact angle. The main geometrical parameters are given in Table 2.1. In the table are also included the axial static load capacity and the axial load for which the ellipse truncature takes place. These values were calculated with the BIME model considering ring flexibility. In the assembly of the bearing, no spacers were used. Nevertheless, bearings were not completely filled with balls, letting a gap between them. This was done in order to avoid ball-spacer or ball-ball

interactions, which are not considered in the analytical model. These interactions are supposed to be negligible in comparison with the forces in the ball-raceway contacts, but for these preliminary tests they were avoided in order to obtain the best correlation possible with the analytical simulations. Besides, no seals were mounted. Therefore, possible effects of ball-spacer or ball-ball interactions or seal-ring contacts are beyond the scope of these preliminary tests. Moreover, only a thin layer of grease was manually applied (see Figure 6.6) instead of filling the cavity with grease. This way, possible viscous effects are minimized.

To assembly the bearings in the test bench, two additional tools were designed and manufactured. These tools are two plates (upper and lower plates), which act as the interface between the test bench and the bearing to be tested. For the assembly, the first step is to place the new lower plate over the original lower plate of the test bench (Figure 6.7a and Figure 6.7b). The new plate is centred by means of an undercut machined in the new piece with the diameter of the original plate. The rotation is blocked by a key. Then, the bearing is placed over the new plate (Figure 6.7c), which is centred thanks to some pins (Figure 6.7b). Finally, the new upper plate is put over the bearing and is also centred by means of pins (detailed view of Figure 6.6). In the last case, spring pins were used, so they can not leave their holes in the upper disk. Once the tools and the bearing are assembled in the test bench, they are pushed upwards by the hydraulic cylinder until they meet the upper plate of the test bench (Figure 6.7d). The new plates were made large and rigid enough so they can be used in the future to test bearings with a mean diameter up to 390mm. To place a new bearing, it would be enough with drilling new holes in the plates (Figure 6.7b) to place the pins for the centring. The planes of the new tools are presented in Appendix B.

6.4.2 Results

Bearing-1 was assembled with a ball preload of 4μm. Considering that the axial load capacity of Bearing-1 against ellipse truncature is 110kN, Sensor-1 was used for the first tests. Nevertheless, a signal noise of 15-20N·m was observed for the measured friction torque while using this sensor, which is a high value considering that expected torques for this bearing do not exceed the value of 20N·m for loads below 100kN. Therefore, two tests were performed for high loads (Test-1 and Test-2), ranging from 70kN to 100kN, and then the sensor was changed, looking for a higher accuracy. With Sensor-

2, the observed signal noise was less than 1N·m, which is a value much more appropriate for the ranges of the friction torque of tested bearings. two more tests were performed with this sensor (Test-3 and Test-4) with loads up to 60kN (upper limit of Sensor-2), including the measurement of the idling friction torque, required for the calculation of the effective preload according to the alternative procedure described in section 6.2.

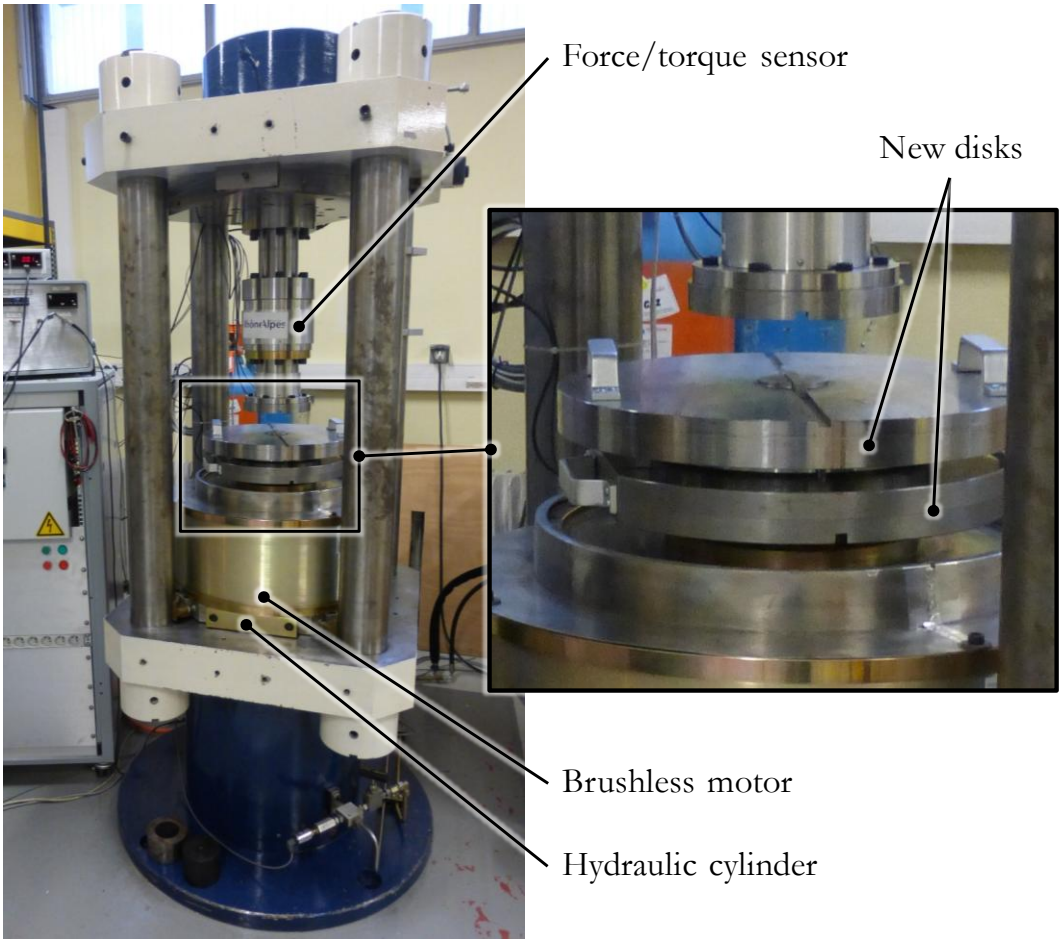

Figure 6.5. Rhéos test bench at LaMCoS.

Bearing ID	Bearing mean diameter (D_{pw})	Ball diameter (D_w)	Raceway radius (R_C)	Initial contact angle (α_0)	Axial static capacity (C_{a0})	Truncation axial load (C_{at})
1	222.00mm	7.94mm (5/16")	4.21mm (s=0.943)	45°	200kN	110kN
2	222.00mm	7.94mm (5/16")	4.12mm (s=0.963)	45°	278kN	65kN
3	222.00mm	7.94mm (5/16")	4.12mm (s=0.963)	55°	284kN	40kN

Table 6.3. Nominal dimensions and capacities of the tested bearings.

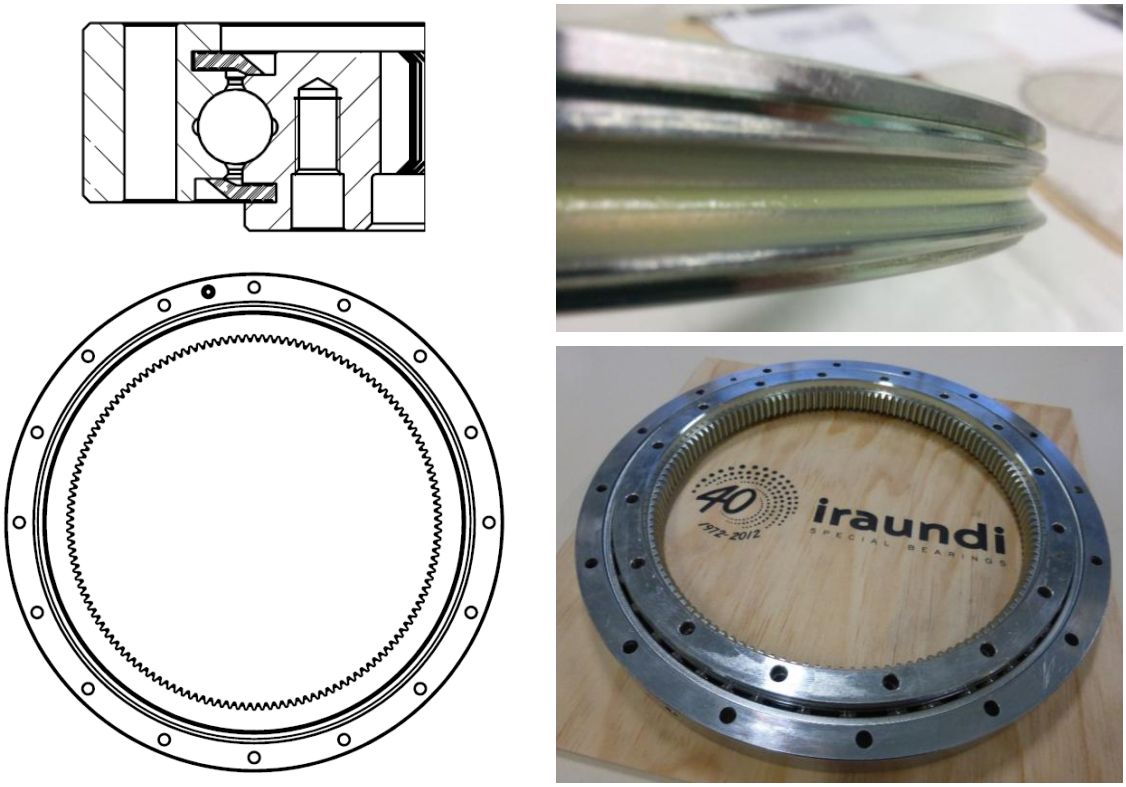

Figure 6.6. Tested bearing.

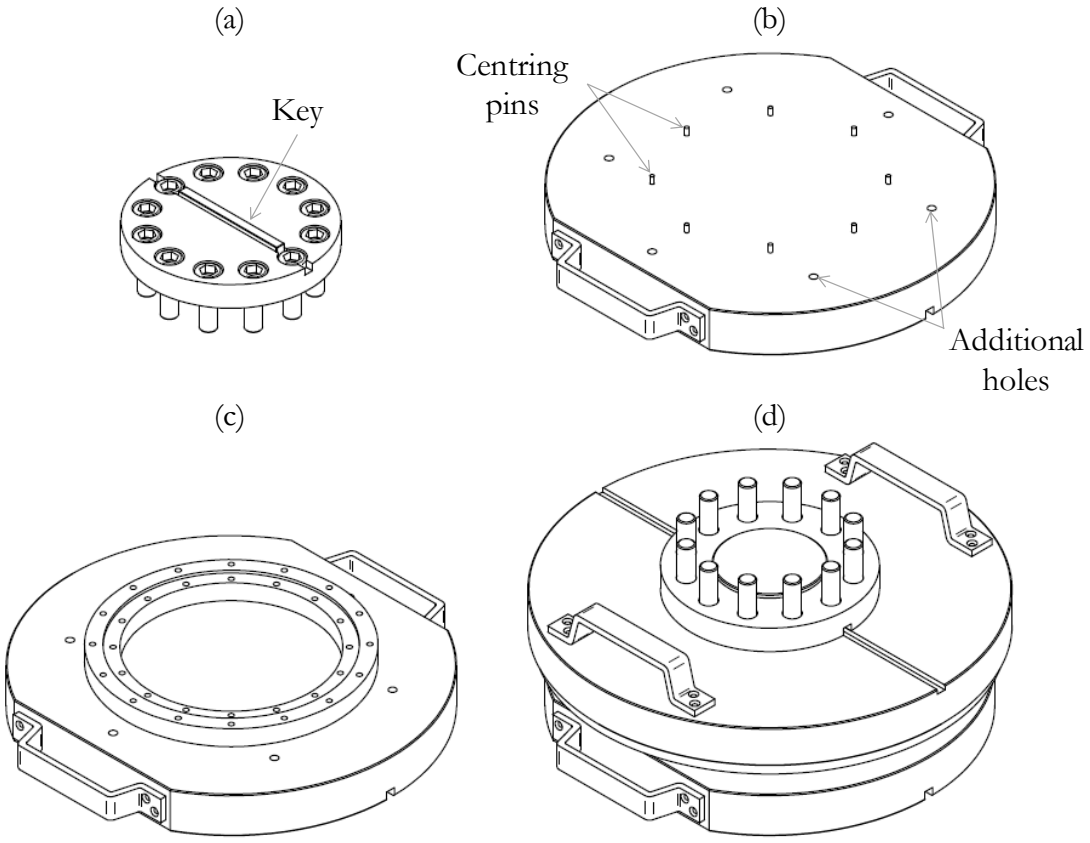

Figure 6.7. Test bench setup: (a) lower plate of the test bench; (b) new lower plate; (c) new lower plate with the bearing; (d) final setup with upper plates.

Figure 6.8 shows the results of Test-3, where vertical lines indicate where the rotation starts and ends. In this figure, significant fluctuations of the friction torque can be observed. It can be seen how the friction torque starts from a minimum, and then experiences two cycles, with two other minimums, one after each entire rotation (remember that two full rotations were applied for each axial load). This can be justified by the misalignment between the bearing and the test bench. This misalignment is possible due to the gaps between the centring pins on the plates and the holes in the rings. Therefore, the bearing is not forced initially when it is assembled in the test bench, but when the rotation starts, the moving ring is misaligned respect to the fixed one. Consequently, an undesired radial load appears, which has its maximum after half turn. This radial load introduces additional forces in the balls, which leads to higher friction torques. Accordingly, the friction torque corresponding to a pure axial load is the observed minimum value during the rotation, which takes place after each full turn.

Figure 6.9 compares the results of Test-3 and Test-4. It is worth mentioning that the bearing was disassembled and assembled again in the test bench before performing each test. A good repeatability is observed and, although Test-4 shows higher maximums, the minimum values are very similar. Additionally, one more test was performed (Test-5) for low loads up to 10kN. The results from Test-1 to Test-5 are represented in Figure 6.10. Remember that measurements up to 60kN were obtained by Sensor-2, while Sensor-1 was used for higher loads. In the figure, the results from the analytical simulations are also showed. All the calculations presented in the following graphs (Figure 6.10, Figure 6.11 and Figure 6.12) were obtained by the Flexible-BIME model. The dotted line is for the case with no preload, while the solid line was calculated by applying the alternative procedure described at the beginning of this chapter. The most significant conclusion that arises from a first comparison is that the higher the load is, the better correlation is observed.

To better understand what happens with light loads, let us go back to Figure 6.8. For the first two applied loads (8kN and 16kN), the amplitude of the friction torque fluctuations is similar. In next steps, this amplitude increases progressively with the axial load. This happens because in the equilibrium position, there are four contacting points for loads up to 16kN, while for higher loads, there are only two. Therefore, in this last case, when the bearing rotates and the radial load increases, the contact status of some balls changes

from two contact points to four contact points, which implies an important increase of the friction torque. Accordingly, these fluctuations help us to determine where the transition from four contact points to two contact points starts. In Figure 6.10, this point is marked with a vertical dotted line at 16kN. The experimental points before the transition starts show a growing tendency, but it differs from the exponential trend showed by the analytical model. After the transition, experimental results for loads above 40kN show a good correlation with analytical simulations. In the transition between 16kN and 40kN, the experimental results get progressively closer to the analytical curve.

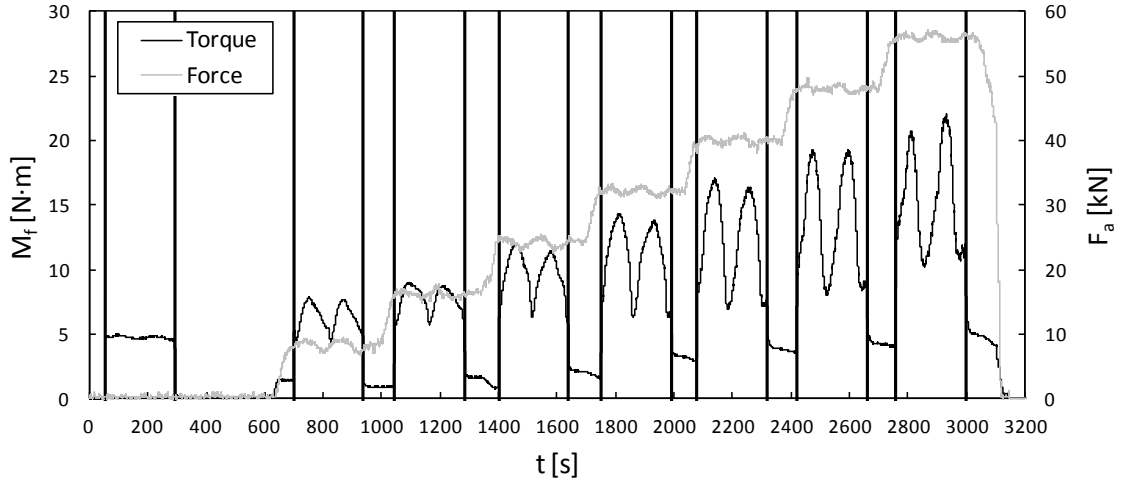

Figure 6.8. Results from the friction torque measurement for one case.

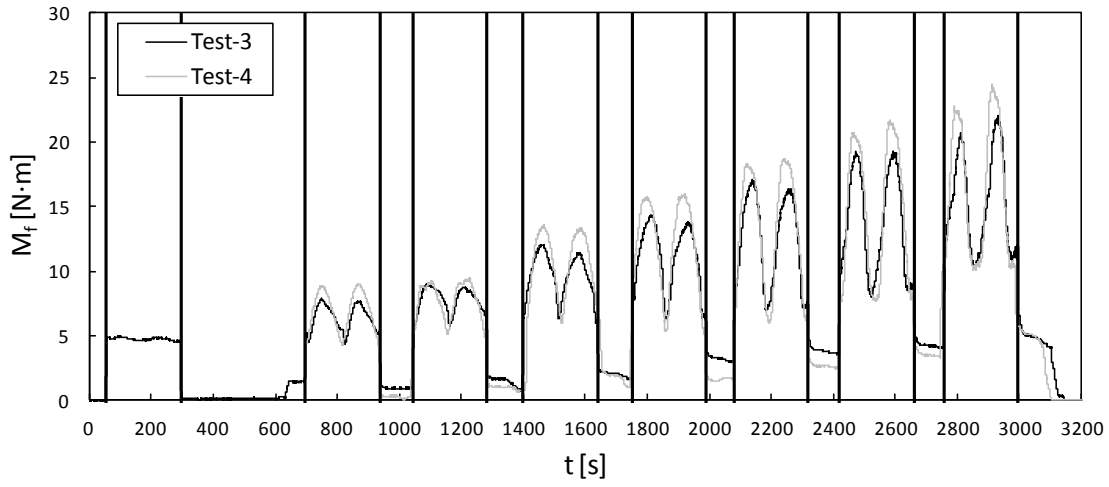

Figure 6.9. Measured friction torque comparison between two tests performed with the same bearing.

It is observed that the experimental transition takes place later than in the analytical model. Moreover, this transition is smooth, while in analytical calculations is abrupt. This behaviour can be explained by two facts. On the one hand, manufacturing errors are not known, and only an average preload

(effective preload) is being considered, assuming that all the balls are subjected to the same loads. However, for light loads and due to real manufacturing errors, there will be some balls with four contact points, but others with two. This fact will affect significantly the results, since the contribution to the friction torque of a ball with two contact points is far less than with four contact points. This also explains the difference in the tendency for the points before the transition. On the other hand, in the analytical model a ball drastically changes from having four contact points to two contact points. In practice, a thin grease layer exists. Therefore, when the ball-raceway contact is lost in a certain point, there will still be a ball-grease-raceway interaction before losing entirely the contact. This ball-grease-raceway interplay involves certain viscous effects that can be significant for light loads, but they are not considered in the analytical approach.

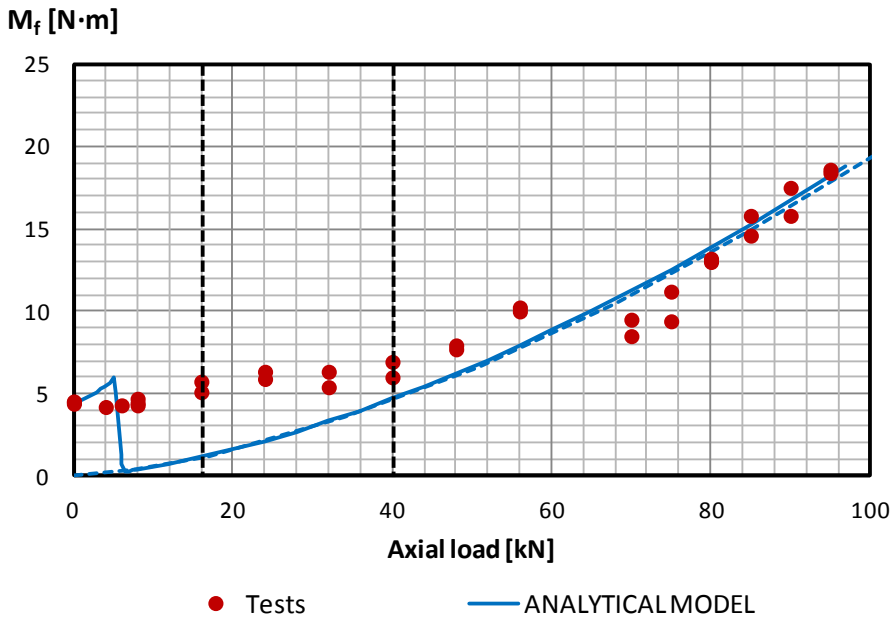

Figure 6.10. Tests VS analytical simulations for Bearing-1.

To study a case with no preload, Bearing-2 was assembled with an undersized ball ($\delta_P = -2\mu m$). Without knowing the real geometry of the raceways, this ball preload allegedly leaves a gap between balls and raceways. In this case, two tests were performed (Test-6 and Test-7) with Sensor-2. The results for the experimental tests and analytical simulations for this bearing are given in Figure 6.11. In this case, since no preload exists, two contact points take place for every load case. Nevertheless, a similar transition than the observed for Bearing-1 happens, so a discrepancy exists for light loads. For compression forces above 40kN, the trend of both experimental tests and analytical model show a similar behaviour.

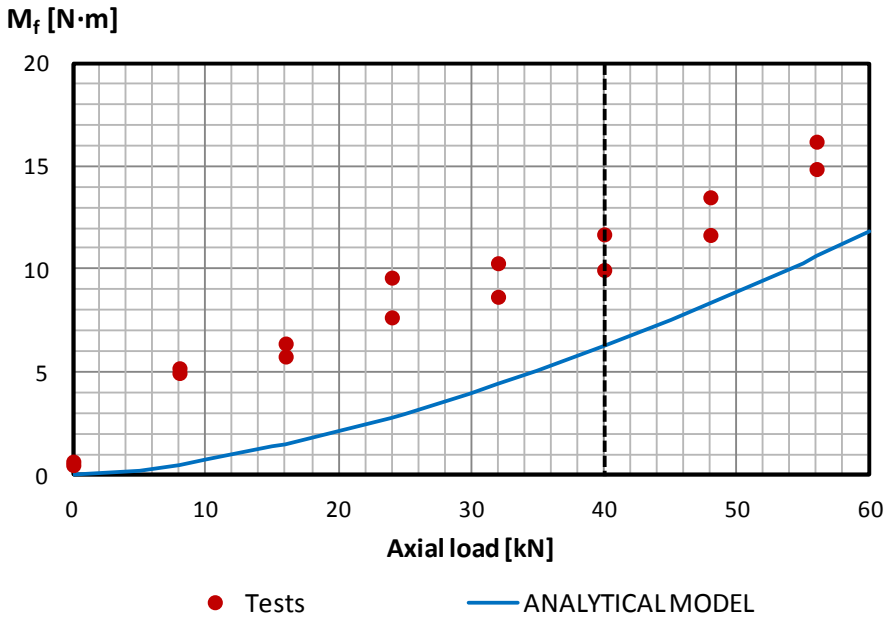

Figure 6.11. Tests VS analytical simulations for Bearing-2.

Finally, Bearing-3 was assembled with a ball preload of 6μm, which is slightly higher than the one used in Bearing-1. In this case, loads up to 40kN where considered to avoid ellipse truncature (see Table 2.1). Like with other bearings, two tests were performed (Test-8 and Test-9), and the results are showed in Figure 6.12 together with analytical calculations. In this case, the transition starts for 20kN, but as it was not possible to consider high loads, neither was to establish where the transition finishes. Nevertheless, the results for loads above 20kN show a tendency towards the analytical curve.

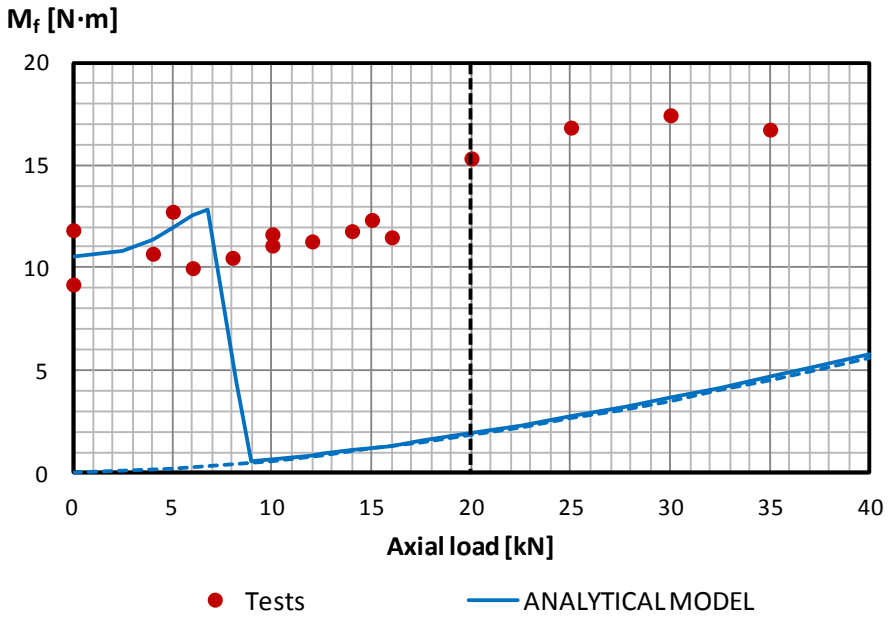

Figure 6.12. Tests VS analytical simulations for Bearing-3.

Table 6.4 compiles the values of the effective preload and the estimation of the manufacturing errors for the three bearings. Of course, since Bearing-2 was assembled with no preload, it is not possible to estimate the manufacturing errors. For Bearing-1 and Bearing-3 this estimation is of 5.1μm and 3.1μm respectively, so once more it is demonstrated that these errors are the order of the ball preloads, and they must be therefore taken into account in order to calculate the desired real preload level. Further, it can be also concluded that the proposed alternative procedure has limitations for light loads, but satisfactory results of the friction torque can be achieved for high loads. Therefore, to obtain better results, the raceways must be measured. Moreover, in future works, more tests with different preloads and greases will be required to obtain further conclusions. Besides, it would be interesting to also study the relevance of phenomena like grease viscosity, ball-ball or ball-spacer interactions or sealing. The preliminary tests presented in this chapter are only a first step of a further and more comprehensive test campaign, thought to improve and validate analytical models.

Bearing ID	**Ball preload (δ_P)**	**Effective preload (δ_E)**	**Estimated manufacturing errors (δ_P)**
1	4μm	9.1μm	5.1μm
2	-2μm	0μm	-
3	6μm	9.1μm	3.1μm

Table 6.4. Estimation of manufacturing errors in tested bearings.

7 Conclusions and future work

7.1 Conclusions

In this section the main conclusions that arise from the research work developed throughout the Doctoral Thesis are presented. For a consistent exposition, these conclusions are listed according to the order followed in the previous chapters.

- An innovative analytical approach was developed for the calculation of the load distribution among the balls, capable of considering manufacturing errors. To do so, this model requires experimental measurements of the raceways. The stiffness of the rings can also be implemented by their stiffness matrices. These matrices can be easily calculated by means of a parametric Finite Element model developed for such purpose. It was demonstrated that only a sector corresponding to one ball is required to be considered in this model. The analytical model provides as a result the normal contact forces or interferences and angles after the assembly of the bearing or for a particular external load combination in a fast way. Moreover, this approach solves the limitations of state of the art Finite Element simulation techniques to simplify the ball-raceway contact when radial displacements are involved.
- A Finite Element model for the friction torque calculation and contact simulation was developed. This model provides consistent results, although it has certain limitations due to the discretization. The submodeling technique was probed to be an effective way to provide accurate contact results. The Finite Element model evinced the relevance of the stick regions in the contact ellipse when the ball is rolling.
- The ball-raceway interferences due to manufacturing errors were found to be of the order of typical preloads, so they are a matter of concern as relevant as the preload itself. Consequently, manufacturing errors significantly affect the idling friction torque and must be therefore

considered in order to select the balls to be used to reach the sought preload level.

- Ring flexibility was demonstrated to have a great effect on ball-raceway interferences after the bearing assembly. When interferences exist due to ball preloads or manufacturing errors, the rings are deformed, and these interferences are significantly reduced. Moreover, ring deformations were evinced to have a great effect on the global stiffness of the bearing as well. Consequently, ring flexibility has to be considered when estimating the stiffness of the bearing and the idling friction torque.
- It was found that the effect of the number of balls on the idling friction torque is logarithmical, and not linear, when ring flexibility is considered.
- A novel analytical approach was developed for the friction torque calculation and contact analysis. In comparison with the model by Leblanc and Nélias, this model gives more realistic results for shear stresses in the contact ellipse for slow speed applications. Nevertheless, both approaches offer very similar friction torque values, being the results of the new model slightly lower. As regards computational costs, both approaches are equally fast. On the other hand, compared with the Finite Element model, the proposed analytical formulation offers a number of advantages. Firstly, computational costs are evidently much lower, so the discretization is not a limitation. Moreover, progressive mesh refinements in the Finite Element model showed that shear stress results converged towards the results of the analytical model. Secondly, the convergence criteria can be easily controlled, which is critical considering the sensitivity of the frictional problem. And finally, the results do not depend on the analyst that performs the calculations.
- It was proved that it is possible to consider separately the global displacements due to contact deformations and those due to the flexibility of the rings. Based on this fact, an engineering formulation was achieved to easily implement ring deformations in the analytical calculation of the stiffness curves. The procedure to reach such expressions can be applied to other slewing bearing types. Additionally, the Finite Element model developed for this procedure offers a practical solution to cope with typical convergence problems in such analysis.
- The preliminary experimental tests showed a good correlation with analytical simulations for high loads. Nevertheless, raceways must be measured before drawing conclusions for light loads

7.2 Future work

In the following points, possible future works derived from this Doctoral Thesis are proposed:

- Develop an engineering formulation for the calculation of the friction torque in four-point contact slewing bearings. The objective would be to obtain a simple formula similar to that proposed by the NREL, but considering the effect of nonlinearities, preload, contact angle and ring stiffness, among others.
- Apply the exact contact theory to solve the tangential contact problem and evaluate its suitability for slewing bearings in comparison with the approach proposed in this Doctoral Thesis.
- Study the subsurface stress when the bearing is rotating and its implications for the fatigue life of the bearing.
- Apply the procedure for the implementation of ring deformations in the analytical load distribution model for the calculation of the global stiffness to other slewing bearings, such as crossed roller bearings or two row ball bearings. Additionally, Finite Element calculations of real blade-hub or tower-nacelle assemblies can be performed to evaluate the capabilities and limitations of the simplification of the bearing by a nonlinear diagonal stiffness matrix.
- Obtain an engineering formulation for the full calculation of the stiffness curves, avoiding the need for the load distribution analytical model. This would imply more complex mathematical expressions, including contact parameters.
- Measure the raceways of the bearings used in the preliminary tests. Moreover, a more comprehensive test campaign would be needed considering different preloads and greases in order to obtain further conclusions. The relevance of other phenomena like grease viscosity, ball-ball or ball-spacer interactions or sealing can also be studied.

7.3 Research work dissemination

Part of the research work presented in this Doctoral Thesis was published in high impact factor scientific journals through the following manuscripts:

- I. Heras, J. Aguirrebeitia, M. Abasolo, Friction torque in four contact point slewing bearings: Effect of manufacturing errors and ring stiffness, Mech. Mach. Theory. 112 (2017) 145–154.
  DOI: 10.1016/j.mechmachtheory.2017.02.009
- I. Heras, J. Aguirrebeitia, M. Abasolo, J. Plaza, Friction torque in four-point contact slewing bearings: Applicability and limitations of current analytical formulations, Tribol. Int. 115 (2017) 59–69.
  DOI: 10.1016/j.triboint.2017.05.011

Furthermore, the different progresses made in the field of slewing-bearing structural characterization were presented in national and international congresses:

- J. Aguirrebeitia, M. Abasolo, J. Plaza, I. Heras, FEM model for friction moment calculations in ball-raceway contacts for applications in four contact point slewing bearings, in: 14th World Congr. Mech. Mach. Sci. 25-30 Oct., Taipei, Taiwan, 2015.
  DOI: 10.6567/IFToMM.14TH.WC.OS18.018
- I. Heras, J. Aguirrebeitia, M. Abasolo, Calculation of the Ball Raceway Interferences Due to Manufacturing Errors and Their Influence on the Friction Moment in Four-Contact-Point Slewing Bearings, in: 6th Eur. Conf. Mech. Sci. 20-23 Sept., Nantes, France, 2016.
  Best student paper award.
  DOI: 10.1007/978-3-319-44156-6_1
- I. Heras, J. Aguirrebeitia, M. Abasolo, Par de fricción en rodamientos de vuelco de cuatro puntos de contacto: estudio de las limitaciones de las formulaciones actuales mediante elementos finitos, in: XXI Congr. Nac. Ing. Mecánica. 9-11 Nov., Elche, Spain, 2016.
- I. Heras, J. Aguirrebeitia, M. Abasolo, J. Albizuri, Simplification of four contact point slewing bearings for multibody simulations, in: EUROMECH Colloq. 578. Roll. Contact Mech. Multibody Syst. Dyn. 10-13 April, Funchal, Madeira, 2017.

References

[1] The European Wind Energy Association (EWEA), 2015 European Statistics, 2016.

[2] Wind Europe, 2016 European Statistics, 2017. doi:10.1007/s10854-007-9177-9.

[3] J. Aguirrebeitia, R. Avilés, I. Fernández de Bustos, M. Abasolo, Calculation of General Static Load-Carrying Capacity for the Design of Four-Contact-Point Slewing Bearings, J. Mech. Des. 132 (2010) 64501-1–6. doi:10.1115/1.4001600.

[4] S. Kang, D. Tesar, An analytical comparison between ball and crossed roller bearings for utilization in actuator modules for precision modular robots, in: ASME 2003 Des. Eng. Tech. Conf. Comput. Inf. Eng. Conf. Sept. 2-6, Chicago, Illinois, USA, 2003: pp. 1221–1230. doi:10.1115/DETC2003/DAC-48834.

[5] Kaydon, Catalog 390, (2011).

[6] Rothe Erde, Product catalogue, (2016).

[7] SKF, Slewing bearings catalogue, (2015).

[8] ISO 76:2006. Rolling bearings - Static load ratings, 2006.

[9] ISO/TR 10657:1991. Explanatory notes on ISO 76, 1991.

[10] J. Lai, P. Ovize, H. Kuijpers, A. Bacchettto, S. Ioannides, J. Beswick, S.W. Dean, Case Depth and Static Capacity of Surface Induction-Hardened Rings, J. ASTM Int. 6 (2009) 102630. doi:10.1520/JAI102630.

[11] P. Göncz, M. Ulbin, S. Glodež, Computational assessment of the allowable static contact loading of a roller-slewing bearing′ s case-hardened raceway, Int. J. Mech. Sci. 94–95 (2015) 174–184. doi:10.1016/j.ijmecsci.2015.03.006.

[12] F. Schwack, H. Flory, G. Poll, M. Stammler, Free Contact Angles in Pitch Bearings and their Impact on Contact and Stress Conditions, in: Wind Eur. SUMMIT 2016, 27-29 Sept., Hamburg, Germany, 2016.

[13] ISO 281: 2007. Rolling bearings - Dynamic load ratings and rating life, 2007.

[14] ISO/TR 1281-1:2008. Rolling bearings - Explanatory notes on ISO 281. Part 1: Basic dynamic load rating and basic rating life, 2008.

[15] ISO/TR 1281-2:2008. Rolling bearings - Explanatory notes on ISO 281. Part 2: Modified rating life calculation, based on a systems approach to fatigue stresses, 2008.

[16] ISO/TS 16281:2008. Rolling bearings - Methods for calculating the modified reference rating life for universally loaded bearings, 2008.

[17] T.A. Harris, M.N. Kotzalas, Essential Concepts of Bearing Technology, 2006.

[18] T.A. Harris, M.N. Kotzalas, Advanced Concepts of Bearing Technology,: Rolling Bearing Analysis, CRC Press, 2006.

[19] T.A. Harris, J.H. Rumbarger, C.P. Butterfield, Wind Turbine Design Guideline DG03: Yaw and Pitch Rolling Bearing Life. NREL/TP-500-42362, 2009.

[20] Schaefler, Catalogue 404, (2012).

[21] IMO, Official website, http://www.goimo.eu.

[22] Timken, Official website, https://www.timken.com.

[23] Rollix, Official website, http://www.rollix.com.

[24] NSK, Official website, http://www.nsk.com.

[25] Iraundi S.A., Slewing bearings catalogue, (2016).

[26] Laulagun Bearings, Official website, http://www.laulagun.com.

[27] H. Hertz, On the Contact of Elastic Solids, Misc. Pap. (1896) 146–162.

[28] H. Hertz, On the Contact of Rigid Elastic Solids and on Hardness, Micellaneous Pap. (1896) 163–183.

[29] R. Pandiyarajan, M.S. Starvin, K.C. Ganesh, Contact Stress Distribution of Large Diameter Ball Bearing Using Hertzian Elliptical Contact Theory, Procedia Eng. 38 (2012) 264–269. doi:10.1016/j.proeng.2012.06.034.

[30] L. Houpert, An Engineering Approach to Hertzian Contact Elasticity — Part I, Trans. ASME. 123 (2001). doi:10.1115/1.1308043.

[31] L. Houpert, An Engineering Approach to Non-Hertzian Contact Elasticity — Part II, Trans. ASME. 123 (2001) 589–594. doi:10.1115/1.1308042.

[32] R. Stribeck, Kugellager für beliebige belastungen, Zeitschrift Des Vereines Dtsch. Ingenieure. (1901) 45(3): 73–9 (pt I) & 45(4): 118–125 (pt II).

[33] R. Stribeck, Die wesentlischen eigenschaften der gleit- un rollenlager, Zeitschrift Des Vereines Dtsch. Ingenieure. (1902) 46(37):1341–1348 (pt I) & 46(38): 1432–1438 (pt II.

[34] R. Stribeck, Ball bearings for various loads, Trans. ASME. 29 (1907) 420–463.

[35] H. Sjoväll, The load distribution within ball and roller bearings under given external radial and axial load, Tek. Tidskr. Mek. (1933) h.9.

[36] J. Rumbarger, Thrust bearing with eccentric loads, Mach. Des. (1962).

[37] A.B. Jones, Analysis of stresses and deflections., New Depart. Eng. Data. 2 (1946).

[38] S. Zupan, I. Prebil, Carrying angle and carrying capacity of a large single row ball

bearing as a function of geometry parameters of the rolling contact and the supporting structure stiffness, Mech. Mach. Theory. 36 (2001) 1087–1103. doi:10.1016/S0094-114X(01)00044-1.

[39] J.I. Amasorrain, X. Sagartzazu, J. Damián, Load distribution in a four contact-point slewing bearing, Mech. Mach. Theory. 38 (2003) 479–496. doi:10.1016/S0094-114X(03)00003-X.

[40] M. Olave, X. Sagartzazu, J. Damian, A. Serna, Design of Four Contact-Point Slewing Bearing With a New Load Distribution Procedure to Account for Structural Stiffness, J. Mech. Des. 132 (2010) 21006. doi:10.1115/1.4000834.

[41] J. Aguirrebeitia, M. Abasolo, R. Aviles, I. Fernández de Bustos, General Static Load Capacity in Slewing Bearings. Unified Theoretical Approach for Crossed Roller Bearings and Four Contact Point Angular Ball Bearings ., in: 13th World Congr. Mech. Mach. Sci. 19-25 June, Guanajuato, México, 2011.

[42] J. Aguirrebeitia, M. Abasolo, R. Avilés, I. Fernández de Bustos, Theoretical calculation of general static load-carrying capacity for the design and selection of three row roller slewing bearings, Mech. Mach. Theory. 48 (2012) 52–61. doi:10.1016/j.mechmachtheory.2011.09.003.

[43] J. Aguirrebeitia, J. Plaza, M. Abasolo, J. Vallejo, General static load-carrying capacity of four-contact-point slewing bearings for wind turbine generator actuation systems, Wind Energy. 16 (2013) 759–774. doi:10.1002/we.1530.

[44] J. Aguirrebeitia, J. Plaza, M. Abasolo, J. Vallejo, Effect of the preload in the general static load-carrying capacity of four-contact-point slewing bearings for wind turbine generators: theoretical model and finite element calculations, Wind Energy. 17 (2014) 1605–1621. doi:10.1002/we.1656.

[45] S. M S, M. K, The effect of manufacturing tolerances on the load carrying capacity of large diameter bearings, Sādhanā. 40 (2015) 1899–1911. doi:10.1007/s12046-015-0427-x.

[46] S. Aithal, N. Siva Prasad, M. Shunmugam, P. Chellapandi, Effect of manufacturing errors on load distribution in large diameter slewing bearings of fast breeder reactor rotatable plugs, Proc. Inst. Mech. Eng. Part C J. Mech. Eng. Sci. 0 (2015) 1–12. doi:10.1177/0954406215579947.

[47] M.J. Todd, K.L. Johnson, A model for coulomb torque hysteresis in ball bearings, Int. J. Mech. Sci. 29 (1987) 339–354.

[48] L. Houpert, P. Leenders, A theoretical and experimental investigation into Rolling Bearing Friction, in: Proc. Eurotrib Conf., Lyon, 1985.

[49] L. Houpert, Numerical and analytical calculations in ball bearings, 8th Eur. Sp. Mech. Tribol. Symp. (1999).

[50] L. Houpert, Ball bearing and tapered roller bearing torque: Analytical , numerical and experimental results, Tribol. Trans. (2002).

[51] D. Olaru, G.C. Puiu, L.C. Balan, V. Puiu, A new model to estimate friction torque in a ball screw system, Prod. Eng. Eco-Design, Technol. Green Energy. (2004) 333–346. doi:10.1007/1-4020-2933-0_20.

[52] M.R.D. Bălan, V.C. Stamate, L. Houpert, D.N. Olaru, The influence of the lubricant viscosity on the rolling friction torque, Tribol. Int. 72 (2013) 1–12. doi:10.1016/j.triboint.2013.11.017.

[53] M.R.D. Bălan, L. Houpert, A. Tufescu, D.N. Olaru, Rolling Friction Torque in Ball-Race Contacts Operating in Mixed Lubrication Conditions, Lubricants. 3 (2015) 222–243. doi:10.3390/lubricants3020222.

[54] A.B. Jones, Ball Motion and Sliding Friction in Ball Bearings, J. Basic Eng. 81 (1959) 1–12.

[55] B.J. Hamrock, Ball motion and sliding friction in an arched outer-race ball bearing, 1974.

[56] A. Leblanc, D. Nelias, Ball Motion and Sliding Friction in a Four-Contact-Point Ball Bearing, J. Tribol. 129 (2007) 801–808. doi:10.1115/1.2768079.

[57] A. Leblanc, D. Nelias, Analysis of Ball Bearings with 2, 3 or 4 Contact Points, Tribol. Trans. 51 (2008) 372–380. doi:10.1080/10402000801888887.

[58] S. Lacroix, D. Nelias, A. Leblanc, Four-Point Contact Ball Bearing Model With Deformable Rings, J. Tribol. 135 (2013) 1–8. doi:10.1115/1.4024103.

[59] A. Joshi, B. Kachhia, H. Kikkari, M. Sridhar, D. Nelias, Running Torque of Slow Speed Two-Point and Four-Point Contact Bearings, Lubricants. 3 (2015) 181–196. doi:10.3390/lubricants3020181.

[60] B. Bhushan, Friction, in: Princ. Appl. Tribol., John Wiley & Sons, Ltd, 2013: pp. 321–401. doi:10.1002/9781118403020.ch6.

[61] F.W. Carter, On the action of a locomotive driving wheel, Proc. R. Soc. London. Ser. A. 112 (1926) 151–157. doi:10.1098/rspa.1926.0100.

[62] H. Fromm, Berechnung des Schlupfes beim Rollen deformierbarer Scheiben, ZAMM - J. Appl. Math. Mech. / Zeitschrift Für Angew. Math. Und Mech. 7 (1927) 27–58. doi:10.1002/zamm.19270070106.

[63] K.L. Johnson, The effect of a tangential contact force upon the rolling motion of an elastic sphere on a plane, J. Aplied Mech. 25 (1958) 339–346.

[64] P.J. Vermeulen, K.L. Johnson, Contact of Nonspherical Elastic Bodies Transmitting Tangential Forces, J. Appl. Mech. 31 (1964) 338–340. http://dx.doi.org/10.1115/1.3629610.

[65] J.J. Kalker, On the rolling contact of two elastic bodies in presence of dry friction, Technische Universiteit Delft, Nederland, 1967.

[66] J.J. Kalker, Simplified theory of rolling contact, Delft Prog. Report, Ser. C Mech. Aeronaut. Eng. Shipbuild. 1 (1973) 1–10.

[67] J.J. Kalker, A Fast Algorithm for the Simplified Theory of Rolling Contact, Veh. Syst. Dyn. 11 (1982) 1–13. doi:10.1080/00423118208968684.

[68] J.J. Kalker, Three-Dimensional Elastic Bodies in Rolling Contact, Springer Netherlands, 1990. doi:10.1007/978-94-015-7889-9.

[69] L. Baeza, Desarrollo de modelos para el estudio de la dinámica de vehículos ferroviarios, Universidad Politécnica de Valencia, 1999.

[70] F. Al-Bender, K. De Moerlooze, A model of the transient behavior of tractive rolling contacts, Adv. Tribol. 2008 (2008). doi:10.1155/2008/214894.

[71] J. Blanco-Lorenzo, J. Santamaria, E.G. Vadillo, N. Correa, On the influence of conformity on wheel-rail rolling contact mechanics, Tribol. Int. 103 (2016) 647–667. doi:10.1016/j.triboint.2016.07.017.

[72] L. Houpert, A Uniform Analytical Approach for Ball and Roller Bearings Calculations.pdf, J. Tribol. (1997).

[73] T. Lim, R. Singh, Vibration transmission through rolling element bearings, part I: Bearing stiffness formulation, J. Sound Vib. 139 (1990) 179–199.

[74] X. Hernot, M. Sartor, J. Guillot, Calculation of the Stiffness Matrix of Angular Contact Ball Bearings by Using the Analytical Approach, J. Mech. Des. 122 (2000) 83–90.

[75] H.-V. Liew, T. Lim, Analysis of time-varying rolling element bearing characteristics, J. Sound Vib. - J SOUND VIB. 283 (2005) 1163–1179.

[76] D. Noel, S. Le Loch, M. Ritou, B. Furet, Complete Analytical Expression of the Stiffness Matrix of Angular Contact Ball Bearings, J. Tribol. 135 (2013) 1–8.

[77] Y. Guo, R. Parker, Stiffness matrix calculation of rolling element bearings using a finite element/contact mechanics model, Mech. Mach. Theory. 51 (2012) 32–45.

[78] A.B. Jones, T.A. Harris, Analysis of a Rolling-Element Idler Gear Bearing Having a Deformable Outer-Race Structure, J. Basic Eng. 85 (1963) 273–278. http://dx.doi.org/10.1115/1.3656576.

[79] T.A. Harris, J.L. Broschard, Analysis of an Improved Planetary Gear-Transmission Bearing, J. Basic Eng. 86 (1964) 457–461. http://dx.doi.org/10.1115/1.3653139.

[80] L. Mignot, L. Bonnard, V. Abousleiman, Analysis of Load Distribution in Planet-Gear Bearings, AGMA Tech. Pap. 10FTM16. (2010).

[81] T. Smolnicki, E. Rusiński, Superelement-Based Modeling of Load Distribution in Large-Size Slewing Bearings, J. Mech. Des. 129 (2007) 459. doi:10.1115/1.2437784.

[82] T. Smolnicki, D. Derlukiewicz, M. Stańco, Evaluation of load distribution in the superstructure rotation joint of single-bucket caterpillar excavators, Autom. Constr. 17 (2008) 218–223. doi:10.1016/j.autcon.2007.05.003.

[83] A. Daidié, Z. Chaib, A. Ghosn, 3D Simplified Finite Elements Analysis of Load and Contact Angle in a Slewing Ball Bearing, J. Mech. Des. 130 (2008) 82601. doi:10.1115/1.2918915.

[84] J. Aguirrebeitia, M. Abasolo, R. Avilés, I. Fernández de Bustos, General static load-carrying capacity for the design and selection of four contact point slewing bearings: Finite element calculations and theoretical model validation, Finite Elem. Anal. Des. 55 (2012) 23–30. doi:10.1016/j.finel.2012.02.002.

[85] S. Śpiewak, Methodology for calculating the complete static carrying capacity of twin slewing bearing, Mech. Mach. Theory. 101 (2016) 181–194. doi:10.1016/j.mechmachtheory.2016.03.017.

[86] T. Yao, Y. Chi, Y. Huang, Research on flexibility of bearing rings for multibody contact dynamics of rolling bearings, Procedia Eng. 31 (2012) 586–594. doi:10.1016/j.proeng.2012.01.1071.

[87] J. Plaza, M. Abasolo, I. Coria, J. Aguirrebeitia, I. Fernández de Bustos, A new finite element approach for the analysis of slewing bearings in wind turbine generators using superelement techniques, Meccanica. 50 (2015) 1623–1633. doi:10.1007/s11012-015-0110-7.

[88] D. Gunia, T. Smolnicki, The Influence of the Geometrical Parameters for Stress Distribution in Wire Raceway Slewing Bearing, Arch. Mech. Eng. 64 (2017). doi:10.1515/meceng-2017-0019.

[89] J.T. Sawicki, S. a. Johansson, J.H. Rumbarger, R.B. Sharpless, Fatigue Life Prediction for Large-Diameter Elastically Constrained Ball Bearings, J. Eng. Gas Turbines Power. 130 (2008) 22506. doi:10.1115/1.2772632.

[90] R. Potočnik, P. Göncz, J. Flašker, S. Glodež, Fatigue life of double row slewing ball bearing with irregular geometry, Procedia Eng. 2 (2010) 1877–1886. doi:10.1016/j.proeng.2010.03.202.

[91] P. Göncz, S. Glodež, Rolling Contact Fatigue Life Assessment of Induction Hardened Raceway, Procedia Eng. 74 (2014) 392–396. doi:10.1016/j.proeng.2014.06.286.

[92] N.D. Londhe, N.K. Arakere, G. Subhash, Extended Hertz Theory of Contact Mechanics for Case-Hardened Steels With Implications for Bearing Fatigue Life, J. Tribol. 140 (2017) 21401. doi:10.1115/1.4037359.

[93] M. Žvokelj, S. Zupan, I. Prebil, EEMD-based multiscale ICA method for slewing bearing fault detection and diagnosis, J. Sound Vib. 370 (2016) 394–423. doi:10.1016/j.jsv.2016.01.046.

[94] I. Portugal, M. Olave, A. Zurutuza, A. López, M. Muñiz-Calvente, A. Fernández-Canteli, Methodology to evaluate fatigue damage under multiaxial random loading, Eng. Fract. Mech. (2017). doi:10.1016/j.engfracmech.2017.04.012.

[95] F. Schwack, M. Stammler, G. Poll, A. Reuter, Comparison of Life Calculations for Oscillating Bearings Considering Individual Pitch Control in Wind Turbines, in: J. Phys. Conf. Ser., 2016. doi:10.1088/1742-6596/753/11/112013.

[96] M. Stammler, F. Schwack, N. Bader, A. Reuter, G. Poll, Friction torque of wind-turbine pitch bearings – comparison of experimental results with available models, Wind Energy Sci. Discuss. 2017 (2017) 1–16. doi:10.5194/wes-2017-20.

[97] R. Avilés, Métodos de análisis para diseño mecánico. Volumen II, Universidad del Pais Vasco. Escuela Superior de Ingenieros, Bilbao, Spain, 2003.

[98] F. Schwack, A. Byckov, N. Bader, G. Poll, Time-dependent analyses of wear in oscillating bearing applications, in: 72nd Soc. Tribol. Lubr. Eng. Annu. Meet. Exhib. 21-25 May, Atlanta, 2017.

[99] F. Schwack, F. Prigge, G. Poll, Frictional Work in Oscillating Bearings - Simulation of an Angular Contact Ball Bearing under Dry Conditions and Small Amplitudes, in: World Tribol. Congr. 17-22 Sept., Beijing, 2017.

[100] A.E.H. Love, A treatise on the mathematical theory of elasticity, Cambridge University Press, 1927.

[101] ISO 3290-1:2014. Rolling bearings - Balls - Part 1: Steel balls, 2014.

[102] D. Gonçalves, S. Pinho, B. Graça, A. V. Campos, J.H.O. Seabra, Friction torque in thrust ball bearings lubricated with polymer greases of different thickener content, Tribol. Int. 96 (2016) 87–96. doi:10.1016/j.triboint.2015.12.017.

[103] SKF, Official website, www.skf.com.

[104] LYC, Products catalogue, (2010).

[105] LaMCoS, Official website, http://lamcos.insa-lyon.fr/.

Appendix A: stiffness curves

This appendix compiles the stiffness curves for the proposed formulation and the results from the FE model. Remember that the proposed functional approximation is given in formulas (5.12) and (5.13). In Chapter 4 only results for DP7 were presented through Figure 5.15, while in this appendix the results are shown for every studied DP. The dashed horizontal black curve delimits where the contact nonlinearity starts.

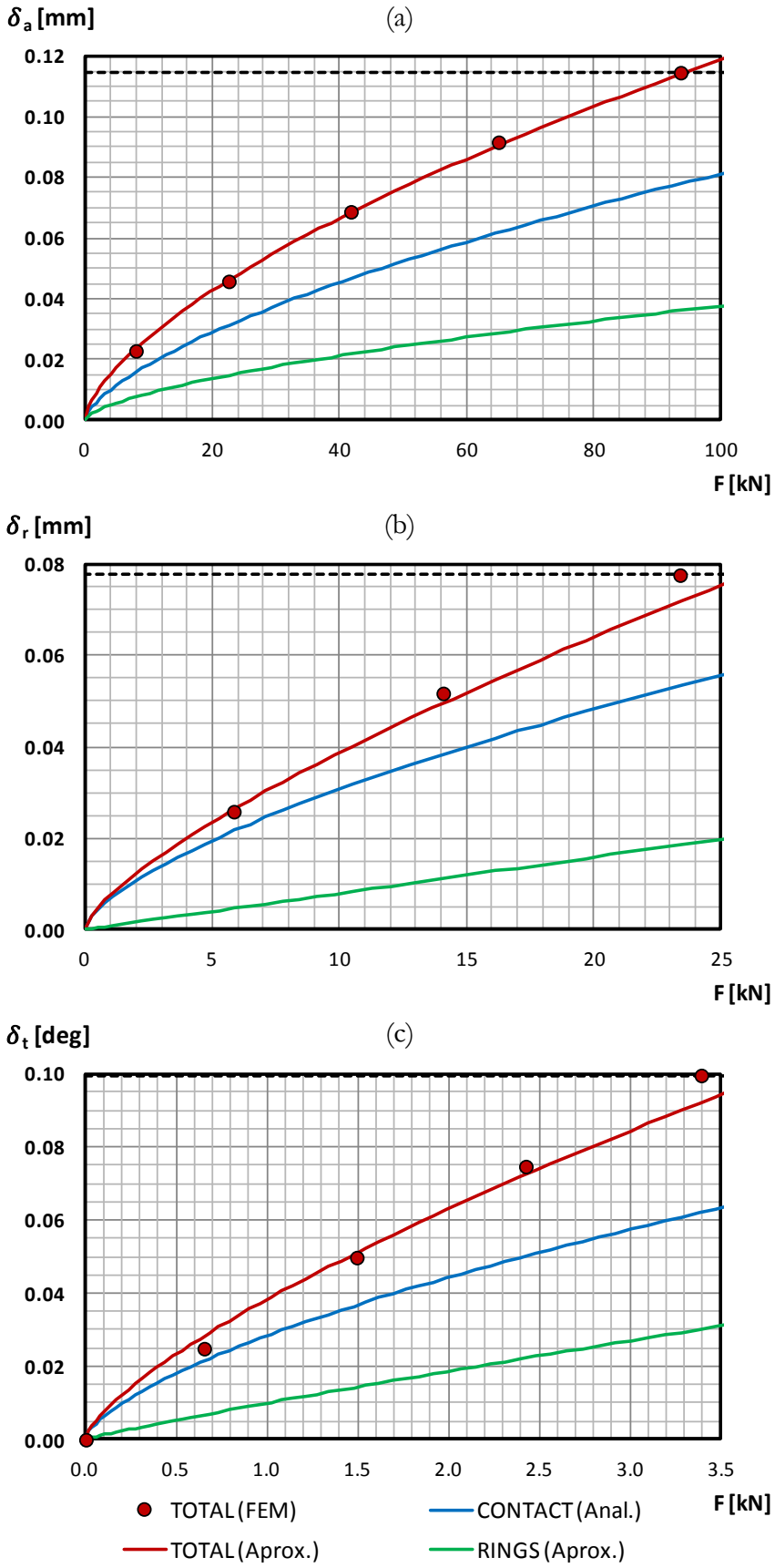

Figure A.1. Analytical model results (blue curve), functional approximation for rings deformation (green curve), the summation of both curves (red curve) and FE results (red dots) for DP1: (a) for axial load; (b) radial load; (b) tilting moment.

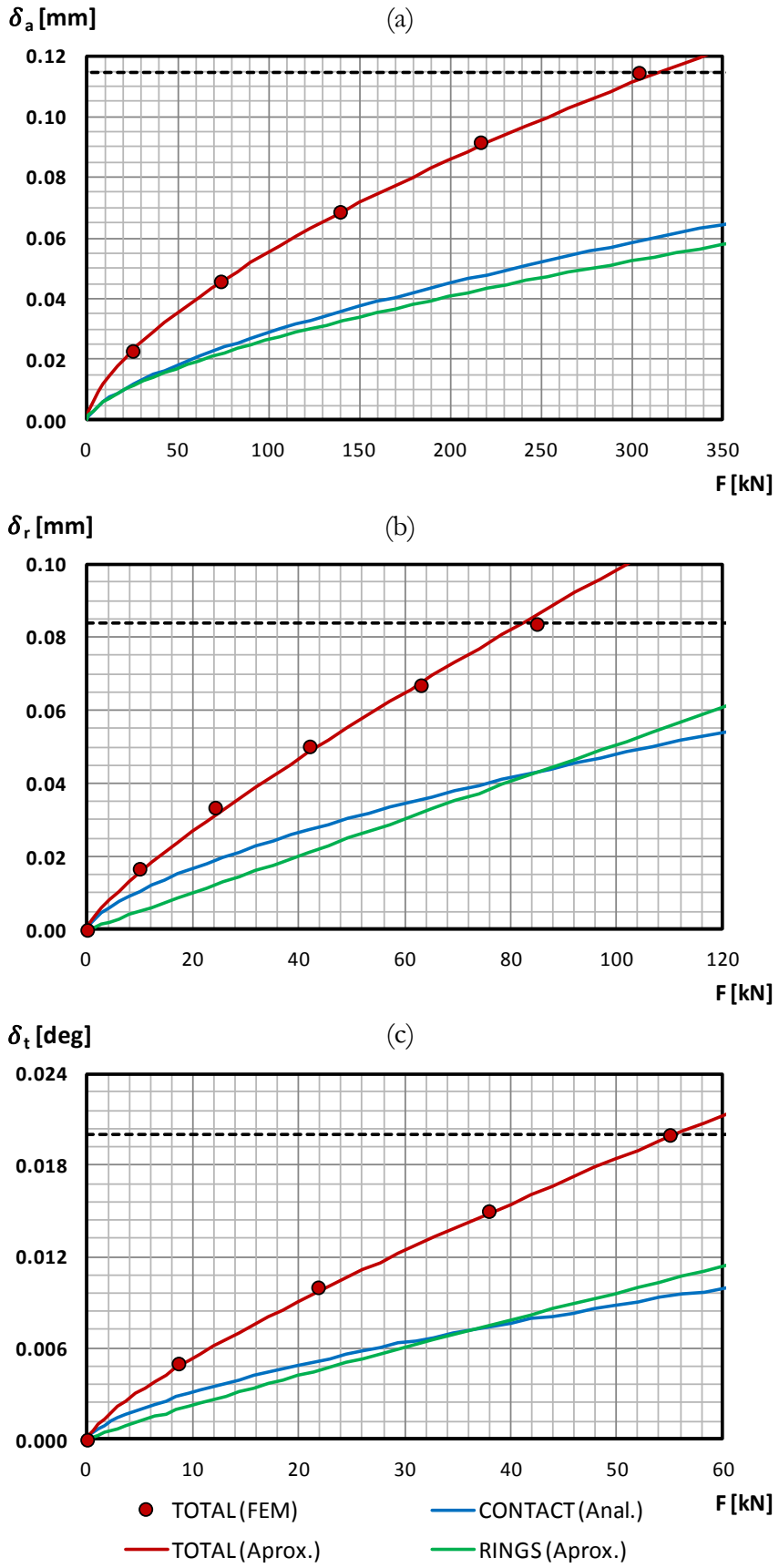

Figure A.2. Analytical model results (blue curve), functional approximation for rings deformation (green curve), the summation of both curves (red curve) and FE results (red dots) for DP2: (a) for axial load; (b) radial load; (b) tilting moment.

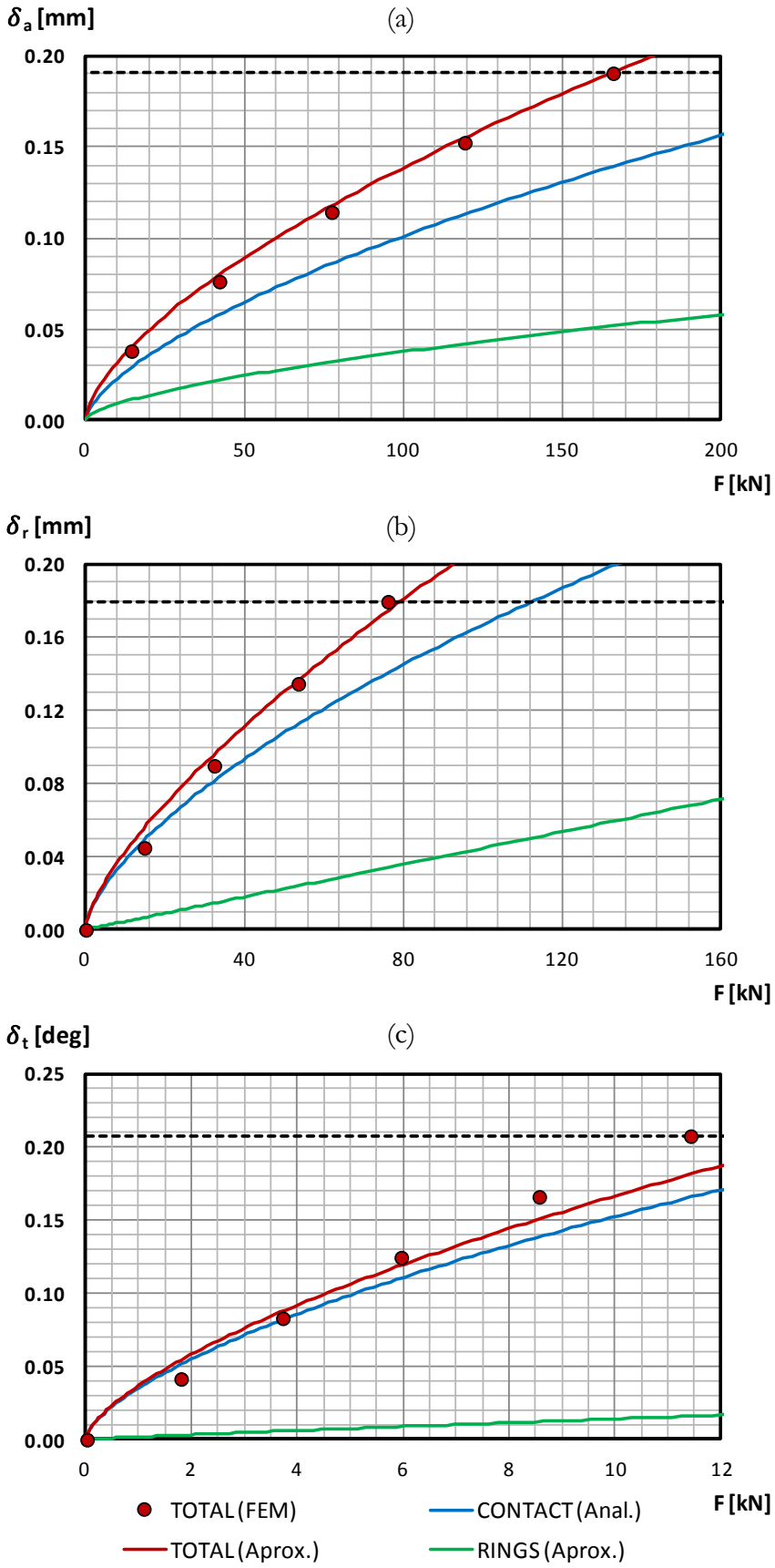

Figure A.3. Analytical model results (blue curve), functional approximation for rings deformation (green curve), the summation of both curves (red curve) and FE results (red dots) for DP3: (a) for axial load; (b) radial load; (b) tilting moment.

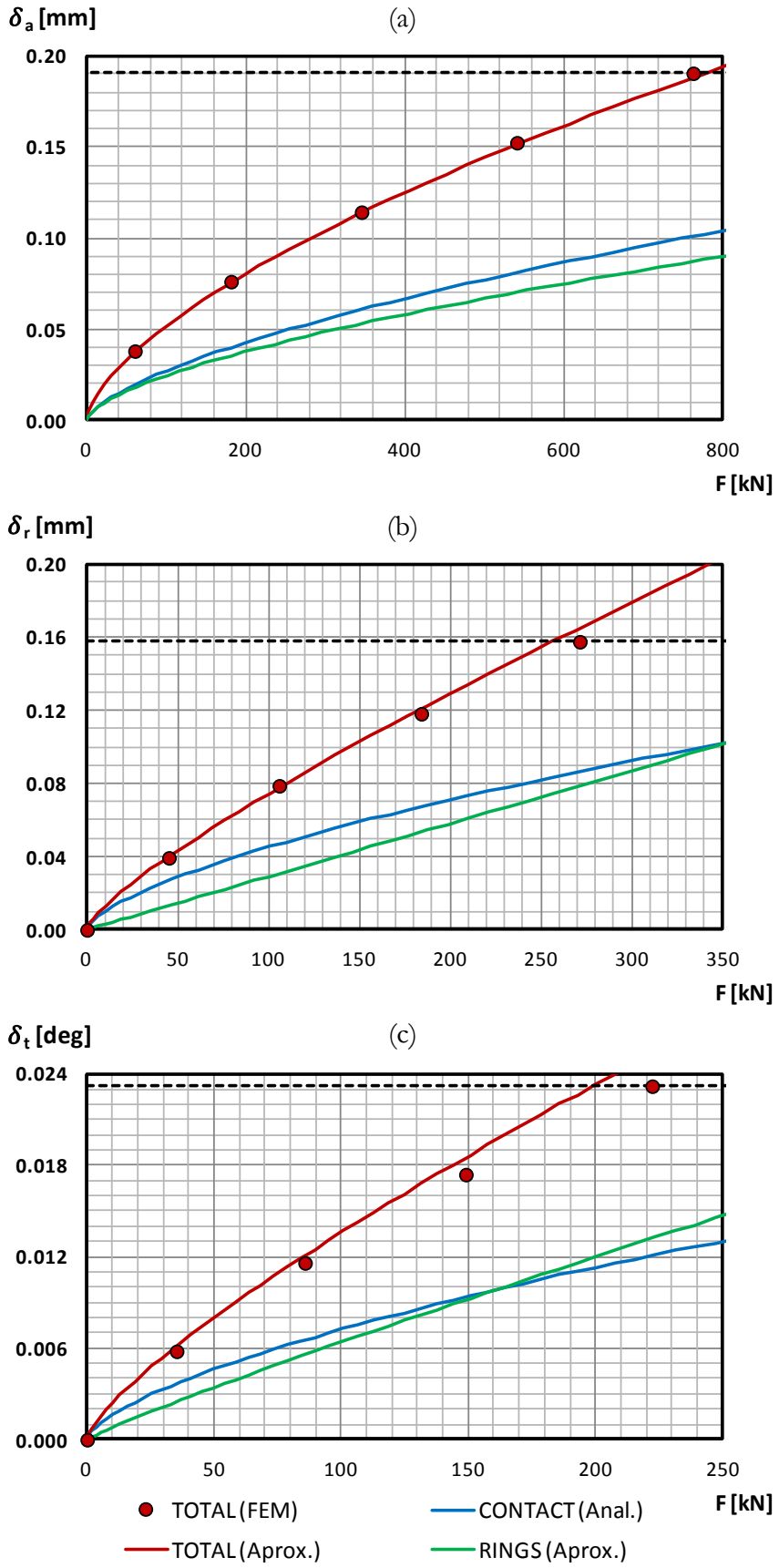

Figure A.4. Analytical model results (blue curve), functional approximation for rings deformation (green curve), the summation of both curves (red curve) and FE results (red dots) for DP4: (a) for axial load; (b) radial load; (b) tilting moment.

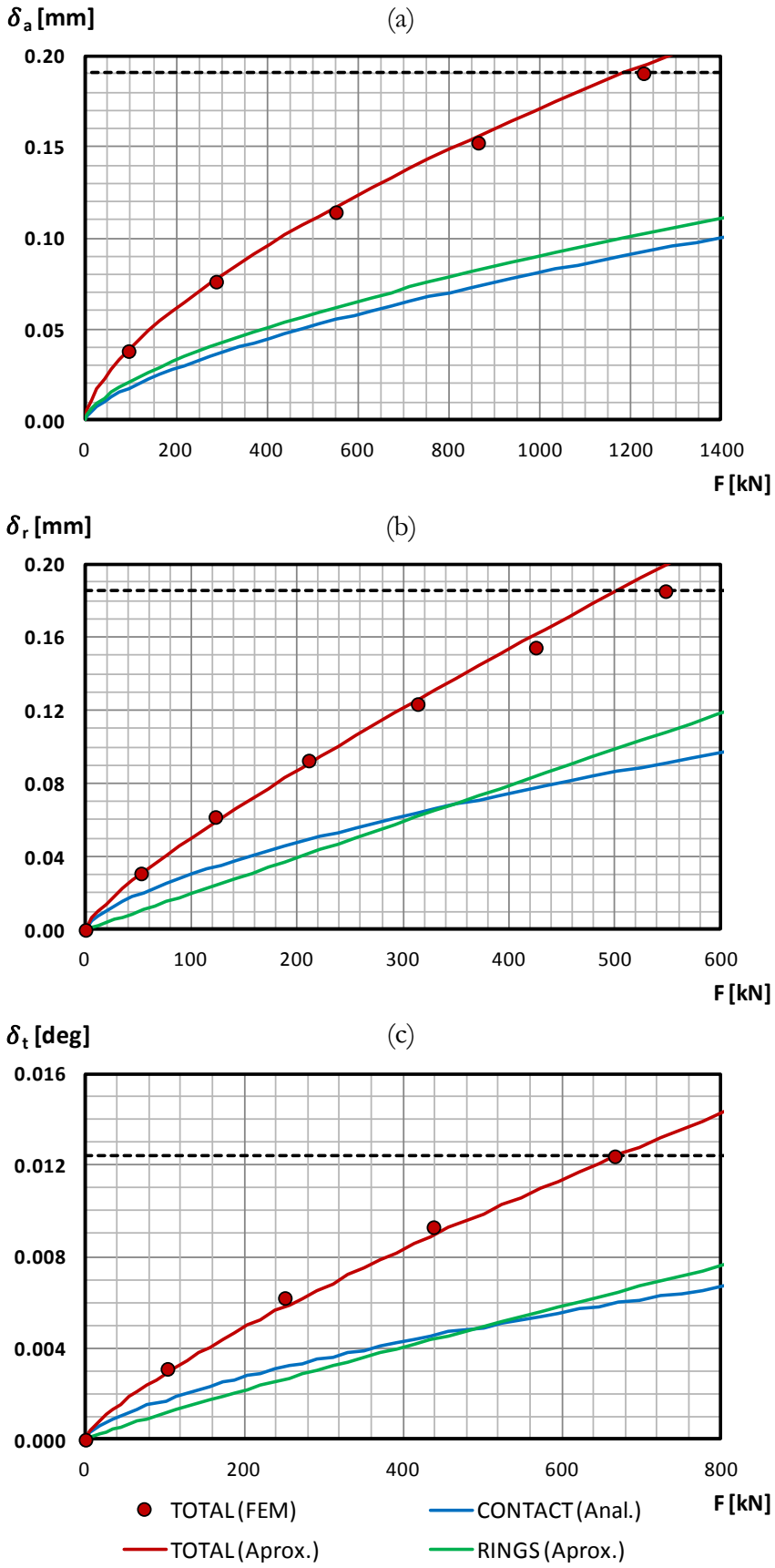

Figure A.5. Analytical model results (blue curve), functional approximation for rings deformation (green curve), the summation of both curves (red curve) and FE results (red dots) for DP5: (a) for axial load; (b) radial load; (b) tilting moment.

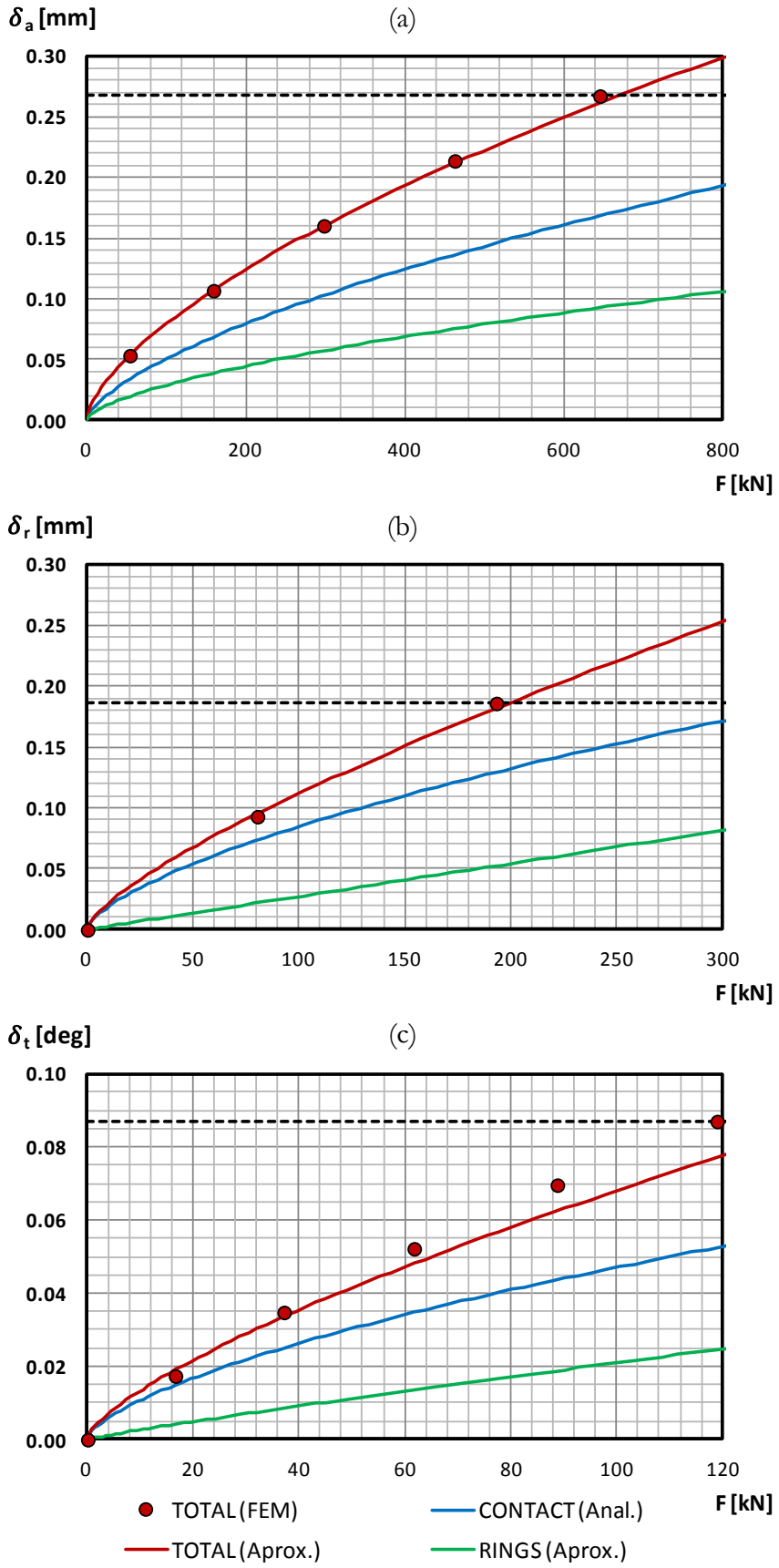

Figure A.6. Analytical model results (blue curve), functional approximation for rings deformation (green curve), the summation of both curves (red curve) and FE results (red dots) for DP6: (a) for axial load; (b) radial load; (b) tilting moment.

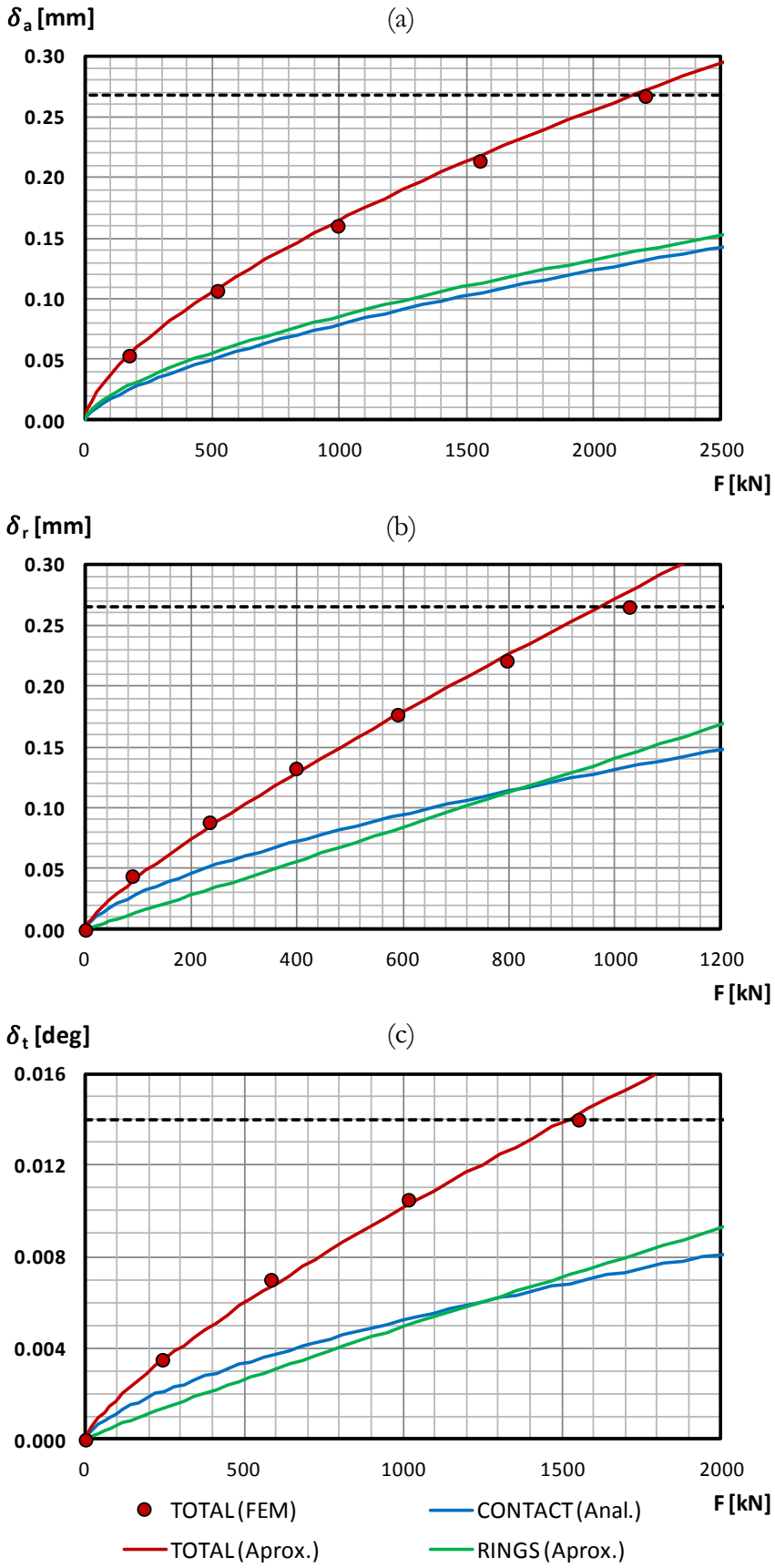

Figure A.7. Analytical model results (blue curve), functional approximation for rings deformation (green curve), the summation of both curves (red curve) and FE results (red dots) for DP8: (a) for axial load; (b) radial load; (b) tilting moment.

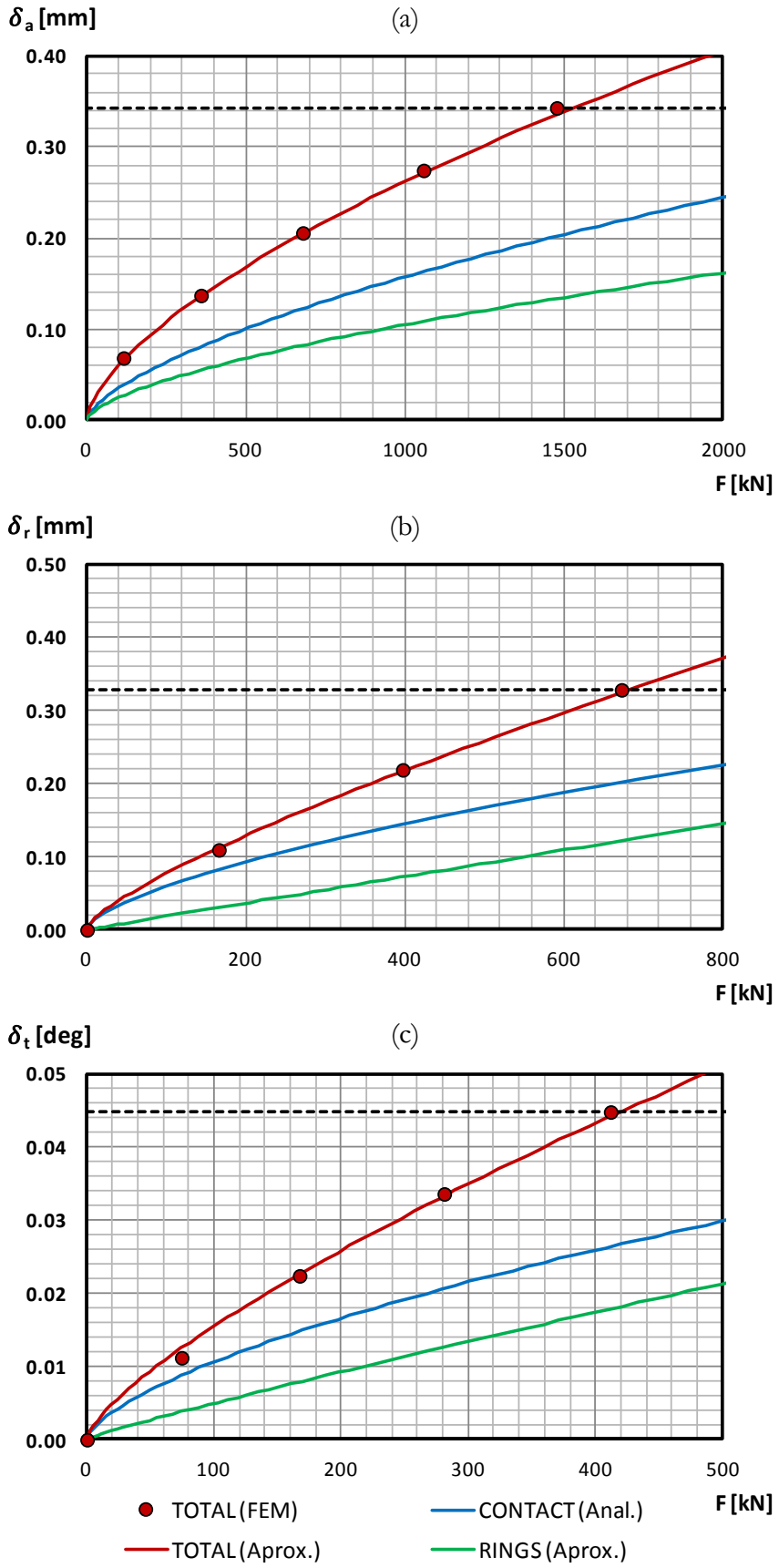

Figure A.8. Analytical model results (blue curve), functional approximation for rings deformation (green curve), the summation of both curves (red curve) and FE results (red dots) for DP9: (a) for axial load; (b) radial load; (b) tilting moment.

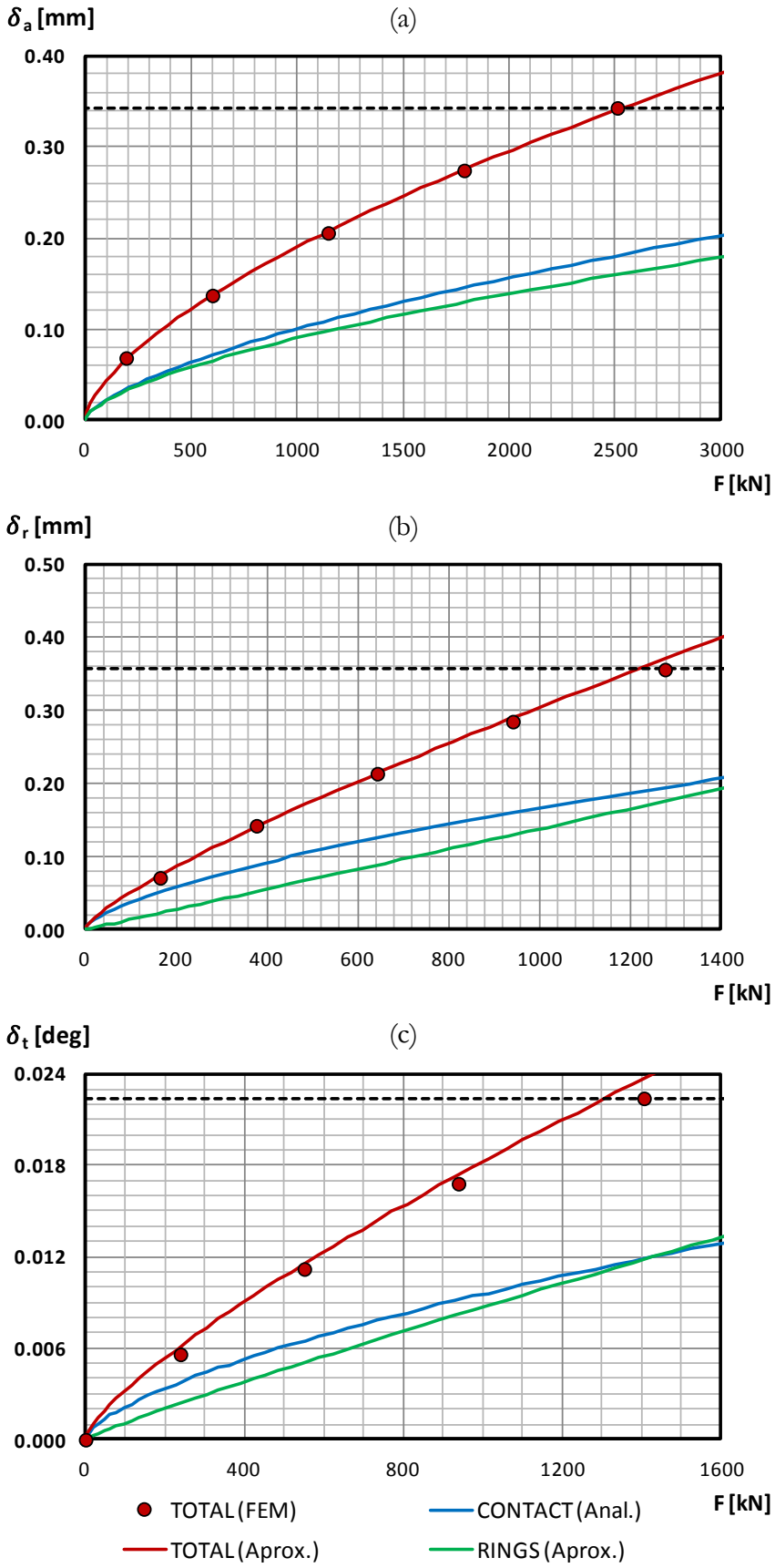

Figure A.9. Analytical model results (blue curve), functional approximation for rings deformation (green curve), the summation of both curves (red curve) and FE results (red dots) for DP10: (a) for axial load; (b) radial load; (b) tilting moment.

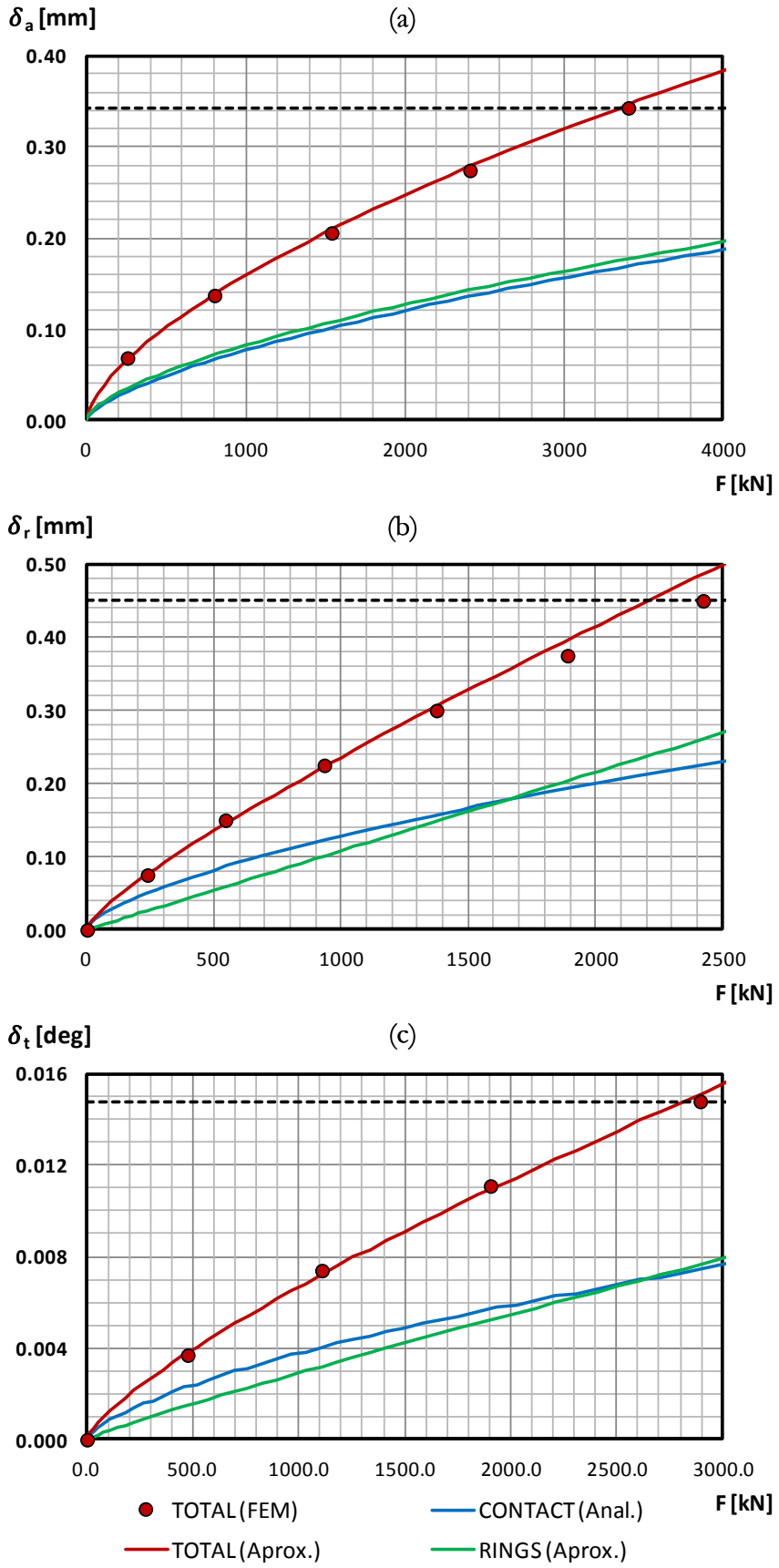

Figure A.10. Analytical model results (blue curve), functional approximation for rings deformation (green curve), the summation of both curves (red curve) and FE results (red dots) for DP11: (a) for axial load; (b) radial load; (b) tilting moment.

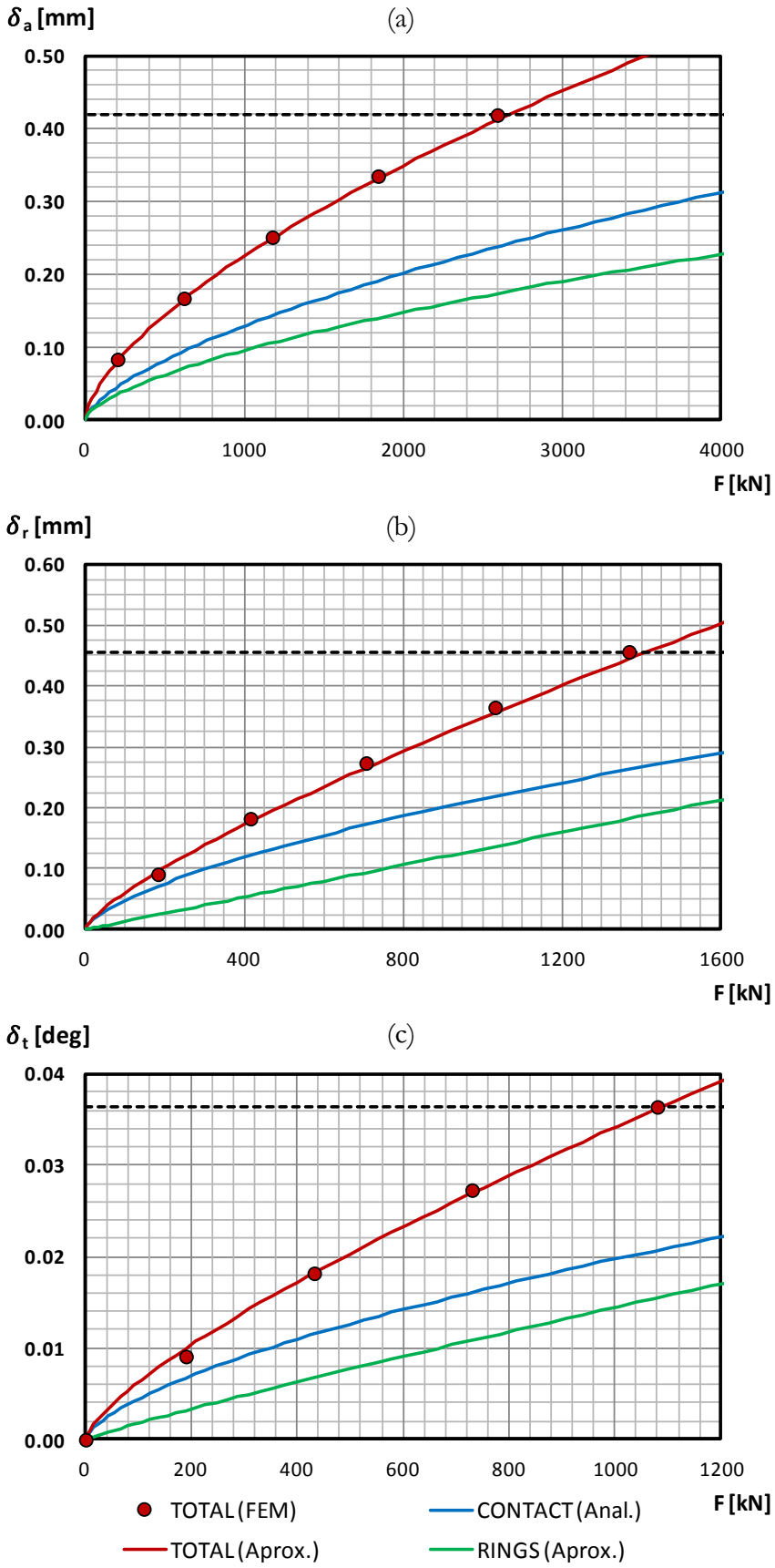

Figure A.11. Analytical model results (blue curve), functional approximation for rings deformation (green curve), the summation of both curves (red curve) and FE results (red dots) for DP12: (a) for axial load; (b) radial load; (b) tilting moment.

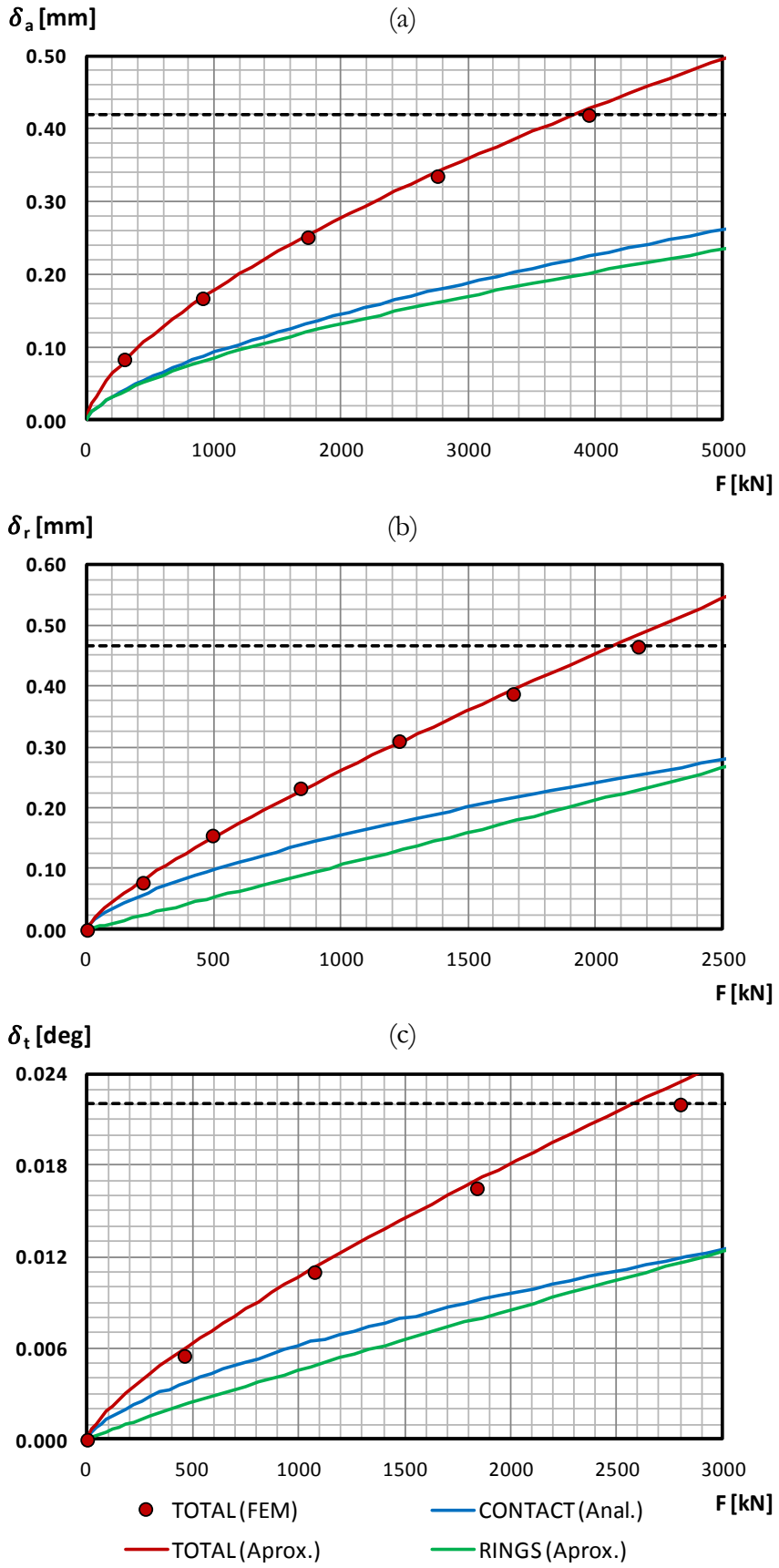

Figure A.12. Analytical model results (blue curve), functional approximation for rings deformation (green curve), the summation of both curves (red curve) and FE results (red dots) for DP13: (a) for axial load; (b) radial load; (b) tilting moment.

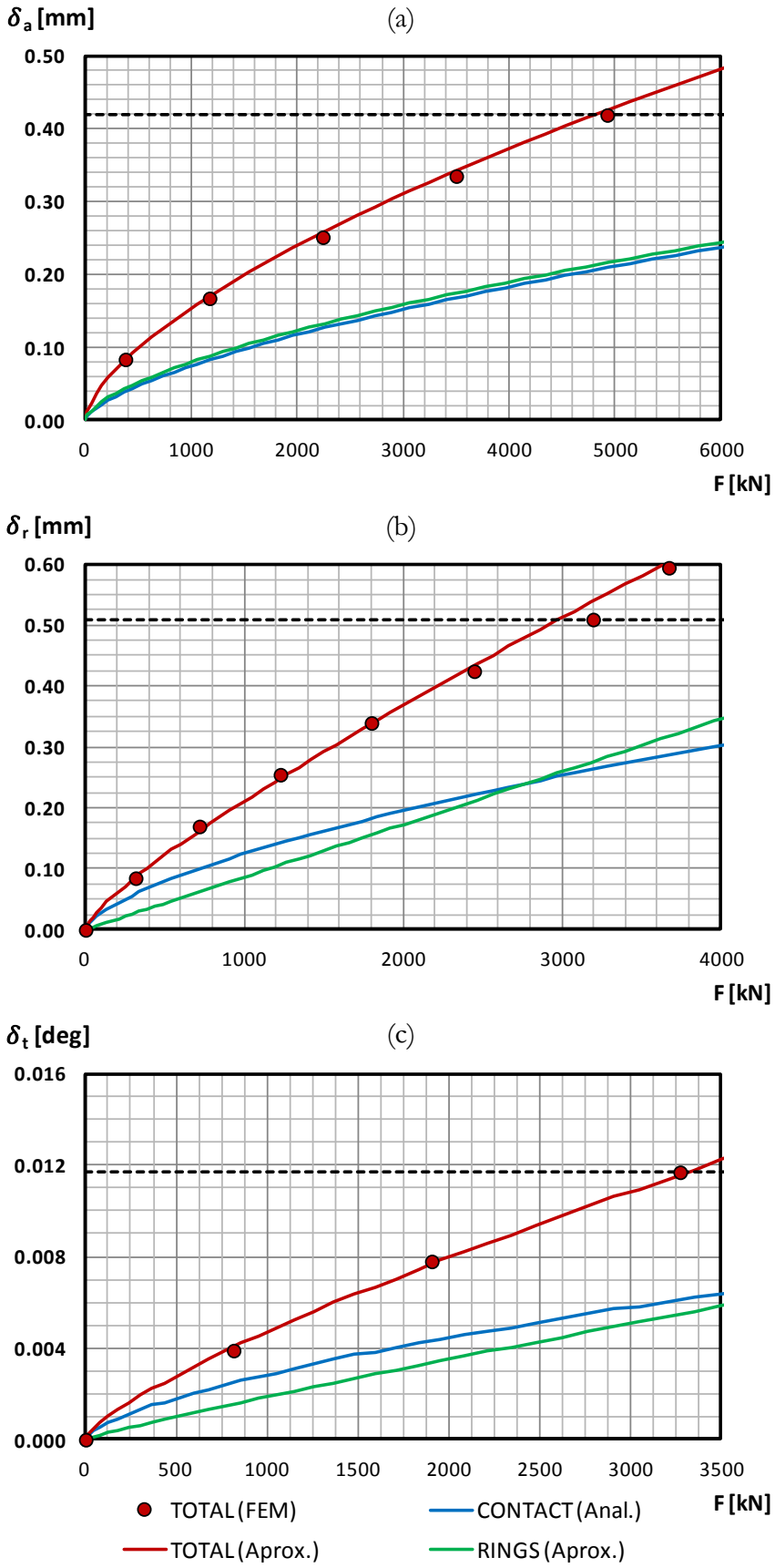

Figure A.13. Analytical model results (blue curve), functional approximation for rings deformation (green curve), the summation of both curves (red curve) and FE results (red dots) for DP14: (a) for axial load; (b) radial load; (b) tilting moment.

Appendix B: tools planes

In this appendix, the planes of the tools designed and manufactured for the experimental tests are presented. The object of these tools is explained in Chapter 6 (Figure 6.5 and Figure 6.7).

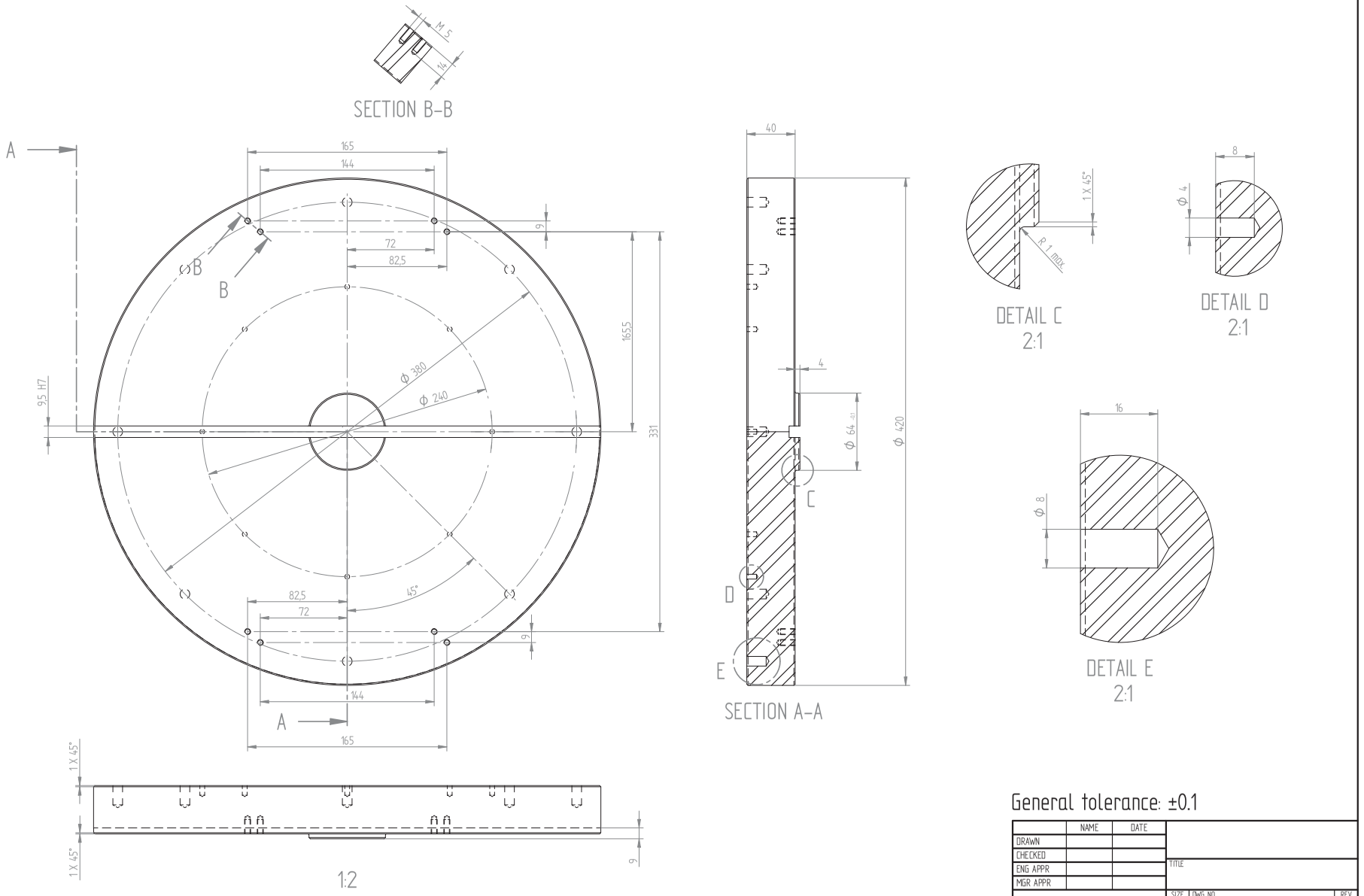
SECTION B–B
M 5
14
A
165
144
72
82,5
B
9
165,5
331
Φ 380
Φ 240
9,5 H7
45°
A
1 X 45°
9
1:2
40
4
Φ 64
Φ 420
C
D
E
SECTION A–A
1 X 45°
R 1 max.
DETAIL C
2:1
8
Φ 4
DETAIL D
2:1
16
Φ 8
DETAIL E
2:1
General tolerance: ±0.1
NAME
DATE
DRAWN
CHECKED
ENG APPR
MGR APPR
TITLE
SIZE
A2
DWG NO
REV
FILE NAME: Plate_Up_Tool.dft
SCALE:
WEIGHT:

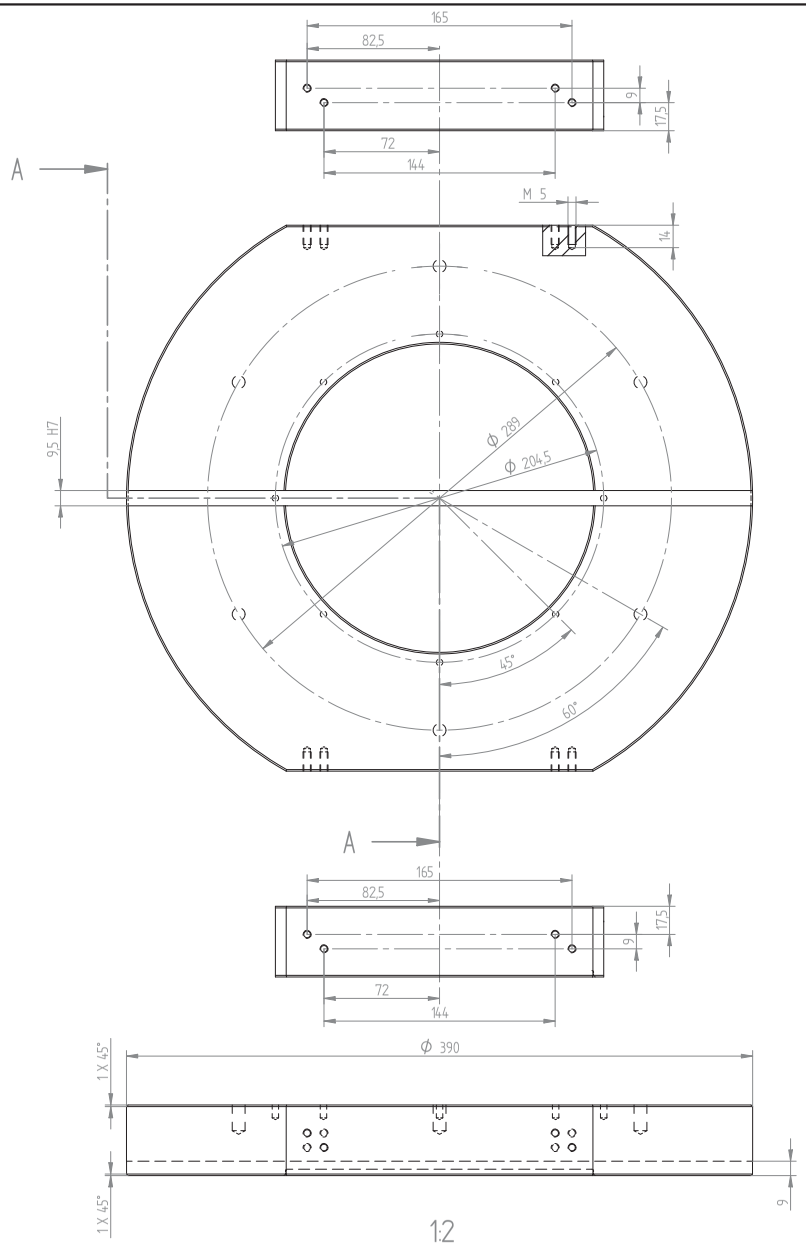

1:2

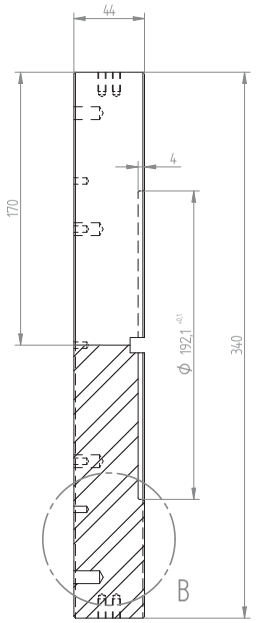

SECTION A-A

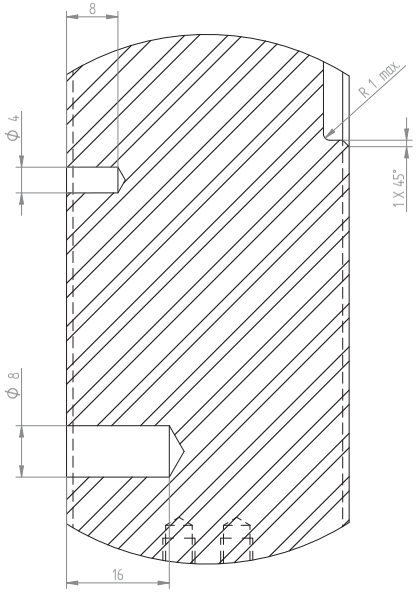

DETAIL B
2:1

General tolerance: ±0.1

	NAME	DATE
DRAWN		
CHECKED		
ENG APPR		
MGR APPR		

TITLE

SIZE A2 | DWG NO | REV

FILE NAME: Plate_Down_Tool.dft

SCALE: | WEIGHT: